



## City Research Online

### City, University of London Institutional Repository

---

**Citation:** Pancholi, M. (2010). Towards an Intelligent Intervertebral Disc Prosthesis for the Assessment of Spinal Loading. (Unpublished Doctoral thesis, City University London)

This is the submitted version of the paper.

This version of the publication may differ from the final published version.

---

**Permanent repository link:** <https://openaccess.city.ac.uk/id/eprint/12072/>

**Link to published version:**

**Copyright:** City Research Online aims to make research outputs of City, University of London available to a wider audience. Copyright and Moral Rights remain with the author(s) and/or copyright holders. URLs from City Research Online may be freely distributed and linked to.

**Reuse:** Copies of full items can be used for personal research or study, educational, or not-for-profit purposes without prior permission or charge. Provided that the authors, title and full bibliographic details are credited, a hyperlink and/or URL is given for the original metadata page and the content is not changed in any way.

# **Towards an Intelligent Intervertebral Disc Prosthesis for the Assessment of Spinal Loading**

**A thesis submitted to the graduate faculty in partial fulfilment of the requirements  
for the degree of Doctor of Philosophy in Biomedical Engineering**

**MEHUL PANCHOLI**

**School of Engineering and Mathematical Sciences  
Electrical, Electronic and Information Engineering  
City University London**

**Dec 2010**



**THE FOLLOWING HAVE BEEN REDACTED AT THE  
REQUEST OF THE UNIVERSITY:**

**PAGE 31, FIGURE 2.3**

**PAGE 32, FIGURE 2.4**

**PAGE 33, FIGURE 2.5**

**PAGE 34, FIGURE 2.6**

**PAGE 35, FIGURE 2.7**

**PAGE 52, FIGURES 4.1 & 4.2**

**PAGE 55, FIGURE 4.6**

**PAGE 77, FIGURE 6.6**

**PAGE 78, FIGURE 6.7**

# ABSTRACT

---

Low back pain is an economic and social burden to society. Low back pain is considered to be a chronic problem when the causes are due degenerative disc diseases and damaged vertebrae. The main causes for degenerative disc are extremely complex and still not well understood, although in their majority are strongly related to the acute and frequent mechanical loading on the spine. Knowledge that might shed more light on such pathologies is the availability of *in vivo* human spinal disc loading data, which at the moment does not exist. Many efforts had been made by researchers to investigate and understand the *in vivo* loading of the human spinal disc. All such techniques were not true *in vivo* techniques and hence, their findings are questionable. Not only a full understanding of the *in vivo* loading of the human spine, but also the distribution of the loading on the spinal disc are of prime importance in order to comprehensively understand the biomechanics of the human spine. Such new knowledge will also be helpful in the treatment of vertebrae compression fractures and also aid in the further improvement of current implantable spinal technologies. The aim of this work was to engage in such investigation by developing a prototype intelligent artificial spinal disc with the capability of mapping the loads applied to the disc when it's loaded in an *in vitro* and *ex vivo* environment. In this research, for the first time a commercial artificial intervertebral disc prosthesis was used as a base for a load-cell. Following a critical review of possible suitable sensors to be embedded within the artificial spinal disc, it was concluded that strain gauges and piezoresistive thin layer sensors were the most appropriate for incorporation within the body of the artificial spinal disc. The loading cell has been successfully designed and developed comprising of eight strain gauges and two piezoresistive sensors encapsulated inside the body of the artificial spinal disc. Further instrumentation and software were developed in order to interface the loading cell with a data acquisition system. A universal testing machine was used for all loading experiments. *In vitro* and *ex vivo* (using an animal spine) experiments were conducted in order to evaluate the developed technology and also to rigorously investigate the loading behaviour of the new loading cell. Following the *in vitro* and *ex vivo* experiments, it can be concluded that all the sensors' outputs are almost identical in characteristics. All results are very much predictable with moderate level of tolerances, uncertainty, accuracy and repeatability. Such results suggest that this new intelligent artificial intervertebral disc prosthesis could allow the *in vivo* investigation of loading on the human spine in the lumbar region and therefore enable the continuous postoperative assessment of patients that had a spinal disc surgical intervention.

# ACKNOWLEDGEMENT

This thesis is for the research work on "Towards an Intelligent Artificial Intervertebral Disc Prosthesis for the Assessment of Spinal Loading". This is a team effort towards the solution of low back problem and chronic spinal diseases in particular Disc Degenerated Diseases (DDD). The low back pain is a considerable burden on economy and human society. This all started and happened under the leadership and guidance from my supervisor Prof. P.A. Kyriacou and I offer my gratitude and respect for that. It all began in 2004, when I met my supervisor Prof. P.A. Kyriacou at his office at City University, London. I wish to express my utmost appreciation for his navigation and help without that I might have been lost in the biomedical research space.

I am very much grateful to my clinical supervisor Dr. John Yeh, Consultant Neurosurgeon at The Royal London Hospital, for his clinical support and guidance. Specifically, I am indebted to him for long discussions on crucial aspect of this research in spite of his extreme busy schedule.

I am very much thankful to Mr. Jim Hooker and Mr. John Carry for their help to develop the Experimental set-up and state-of-the-art tools.

I would like to acknowledge the financial support to this project from Emerald Technology Transfer Organization.

Last but not least, I am very much thankful to my colleagues in the "Bio-medical Engineering Research Group", Victor, Kamran, Shafiq, Mitchell, Tina Sashka and Justin. All of them extend their unwavering support and help as and when and as many times I needed.

Finally, I am indebted and thankful to my parents Prof. Pinakin Pancholi and Mrs. Lila Pancholi, my beloved wife Keta, my lovely kids Keval and Dhairya without their sacrifice & patience my education & achievement are impossible.

# LIST OF FIGURES

Figure 2-1: Three different anatomical views of the spine showing all its parts (backpain-guide.com, 2011). ..... 29

Figure 2-2: Detail anatomical view of the lumbar vertebra of the spine showing all its parts (indyspinemd.com, 2011). ..... 30

Figure 2-3: Facet joints motion during forward and backward movement of the body as part of the two vertebrae (spineuniverse.com, 2011). ..... 31

Figure 2-4: Neural foramina in the unit of two vertebrae with the spinal disc in-between (patientsites.com, 2011). ..... 32

Figure 2-5: The two different views of the spinal cord showing its position in the spine and cross-sectional view (health.com, 2011). ..... 33

Figure 2-6: The nerve roots run out of the spinal cord in the unit of two vertebrae with the disc in-between (mcm.edu, 2011). ..... 34

Figure 2-7: First two views from the left showing the intervertebral disc with its location in the spine and right most view showing cross-sectional view from the top (spineuniverse.com, 2011). ..... 35

Figure 2-8: Nucleus pulposus and annulus fibrosis in the intervertebral disc (Nuchiro, 2011).. 36

Figure 3-1: Colour Bar-graph showing discal Pressure in terms of Disc Load for Normal body Weight & different Positions of the Body (Nachemson and Morris, 1964) (Nachemson, 1966). ..... 42

Figure 4-1: Schematic sagittal anatomic sections of a normal young healthy disc (Left), an annular tear (radial tear in this case) and a disc herniation (Right) (Milette, 1997). ..... 52

Figure 4-2: Focal herniation involves less than 25% (90°) of the disc circumference (Left).Broad-based herniation involves between 25% and 50% (90–180°) of the disc circumference (Right) (Milette, 1997). ..... 52

Figure 4-3: Symmetrical presence (or apparent presence) of disc tissue “circumferentially” (50–100%) (Left), Asymmetrical bulging of the disc margin (50–100%) (Right) (Fardon and Millet, 2001). ..... 53

Figure 4-4: Types of Herniated discs – protrusion (Left), extrusion (Right), based on the shape of the displaced material (Fardon and Millet, 2001). ..... 53

Figure 4-5: Schematic representation of various types of posterior central herniation. (A) A herniation (or protrusion) without significant disc material migration. (B) A herniation with downward migration of disc material under the posterior longitudinal ligament (PLL). (C) A herniation with downward migration of disc material and sequestered fragment (arrow) (Milette, 2000). ..... 54

Figure 4-6: Schematic sagittal anatomic sections of the normal disc, spondylosisdeformans, and intervertebral osteochondrosis (Milette, 1997). ..... 55

Figure 6-1: One of the first artificial disc replacements (simple metal ball) designed by Fernström (Burton Report , 2010) ..... 70

Figure 6-2: One of the early designed artificial spinal disc with two metal end-plates hinged posteriorly and interposed with metal spring in between by Kostuik (Kotsuik, 1997). ..... 71

Figure 6-3: Artificial spinal disc designed by Hedman and colleagues (Hedman et al., 1991). .. 71

Figure 6-4: Artificial disc designed by Lee and Langrana (L) and SB CHARITÉ® III artificial spinal disc prosthesis (R) both cited in (Bono and Garfin, 2004) ..... 73

Figure 6-5: (a) Parts of SB CHARITÉ® I artificial spinal disc by (b) SB CHARITÉ®II disc with its parts. Both discs were by DePuy Spine, Raynham, MA. Cited in (Bono and Garfin, 2004). ..... 74

Figure 6-6: Integra - eDisc (L) (Slack Inc.-Orthosupersite, 2008) and Stryker Spine - Flexicore® spinal disc (R) (Murtagh et al., 2010). ..... 77

Figure 6-7: Medtronic-Prestige® spinal disc with lateral flexion and extension radiographs after implantation. (Boulder neurosurgical associates, 2010). ..... 78

Figure 6-8: Medtronic - Bryan® spinal disc (R) (Medtronic Inc., 2010). ..... 78

Figure 6-9: Zimmer Spine - Dynardi® artificial spinal disc (Zimmer Inc., 2010) (Neurocirguia Contemporanea, 2010). ..... 79

Figure 6-10: DePuy Spine (Johnson and Johnson) - SB CHARITÉ® Artificial spinal disc (Neurocirguia inc., 2010) (Microspine inc., 2010). ..... 79

Figure 6-11: Synthase spine – Prodisc II (L), Medtronic – Maveric (Murtagh et al., 2010). ..... 79

Figure 6-12: NuVasive XL-TDR (Nuvasive inc., 2010). ..... 80

Figure 6-13: B.Braun Spine disc - Active-L spinal disc prosthesis (Top Left), Superior end-plate (Top Right), Inferior end-plate with UHMWPE inlay material (Bottom Left) and Outer side of end-plates with anchor studs and porous titanium & Calcium phosphate layer for enhancing osseous induction process (Bottom Right). (B.Braun Inc., 2010) ..... 80

Figure 7-1: Applications of Piezoelectric effect: Categorized on basis of Direct Effect or Converse Effect (Gautschi, 2002). ..... 85

Figure 7-2: Working schematic of the capacitor with important parameters like d, A etc. .... 89

Figure 7-3: Detail schematic view of the strain gauge..... 90

Figure 7-4: Schematics of the strain - equal to the change in length per original length due to the applied force,  $\delta = \Delta L/L$ ..... 91

Figure 7-5: Detail schematic view of the design of the load cell using optical sensor ..... 92

Figure 7-6: Surface Acoustic Wave Sensor-SAW Sensor-Schematic diagram explaining its working principle ..... 94

Figure 8-1: Artificial Disc Prosthesis, Aesculap (B.Braun), Active®-L (Size M) (Aesculap, B.Braun Ltd. , 2005). .... 96

Figure 8-2: Different types of Strain Gauges with attached leads (HBM Ltd., 2005). .... 97

Figure 8-3: Flexiforce® sensor (Piezoresistive thin layer) (Tekscan Inc., 2007). .... 98

Figure 8-4: (A; top left)Superior end-plate of the prototype artificial spinal disc prosthesis with four strain gauges in place (B; top right) Inferior end-plate of the prototype artificial spinal disc prosthesis with four strain gauges in place (C; bottom left) Piezoresistive sensor (Flexiforce® sensor) placed on top of the inlay material set on the inferior end-plate (D; bottom right) Piezoresistive sensor (Flexiforce® sensor) placed at the bottom of the inlay material set on the inferior end-plate. .... 100

Figure 9-1: Photographs of the Experimental Set-Up. (A) Mechanical system: UT machine with tools& accessories (B) Signal conditioning, data acquisition and processing system hardware (C) Two Portable PC: one for display and running data acquisition software and another for controlling the UT machine as a console. .... 103

Figure 9-2: Photograph of mechanical loading experimental set-up with designed tools & accessories like fixtures and platens..... 104

Figure 9-3: Artificial lumbar spinal disc prosthesis (wedge shape) (Aesculap, B.Braun Ltd. , 2005). .... 105

Figure 9-4: Artificial spinal disc prosthesis – load cell holding fixtures for compressive loading upto 4 kN with important dimensions. .... 106

Figure 9-5: Photograph of the piezoresistive sensor (Flexiforce®) (Tekscan Inc., 2007). .... 107

Figure 9-6: Piezoresistive sensor (Flexiforce®) calibration compressive loading tool with important dimensions. (A) 3D view from the top (B) 3D view from the bottom (C) View from the top (D) View from the bottom..... 107

Figure 9-7: X-Y movable compression platen for proper alignment of the upper and lower compressive loading parts with important dimensions. .... 108

Figure 9-8: Strain gauge quarter bridge completion diagram ..... 110

Figure 9-9: Block diagram of signal conditioning, data acquisition and processing system..... 111

Figure 9-10: Connection diagram for strain gauges with the signal conditioning modules NI 9944 and NI 9237 (National Instruments Corporation, 2010)..... 113

Figure 9-11: Strain Gauge Analog Input Module (NI 9237) (National Instruments Corporation, 2010). ..... 114

Figure 9-12: Piezoresistive thin layer sensor-Flexi Force signal conditioning circuit (Tekscan Inc., 2007). ..... 118

Figure 9-13: Analogue voltage input module (NI 9215) (National Instruments Corporation, 2010). ..... 120

Figure 9-14: cRIO-9215 input circuitry of single channel with BNC connection (National Instruments Corporation, 2010). ..... 120

Figure 9-15: Photograph of USB data acquisition chassis (NI cDAQ9172) (National Instruments Corporation, 2010)..... 121

Figure 9-16: Front connection lay-out of USB data acquisition chassis (NI cDAQ9172) (National Instruments Corporation, 2010). ..... 122

Figure 9-17: NI cDAQ-9172 Block Diagram (National Instruments Corporation, 2010). ..... 122

Figure 9-18: Graphical symbol of “DAQmx start task” sub VI (National Instruments Corporation, 2010). ..... 125

Figure 9-19: Graphical symbol of “while loop” sub VI (National Instruments Corporation, 2010). ..... 125

Figure 9-20: Labview front panel of the VI called “Spinestresses” ..... 126

Figure 9-21: Labview block diagram of the VI called “Spinestresses” ..... 127

Figure 9-22: Graphical symbol of “DAQmx read” sub VI (National Instruments Corporation, 2010). ..... 128

Figure 9-23: Graphical symbol of “resample waveforms” sub VI (National Instruments Corporation, 2010)..... 129

Figure 9-24: Graphical symbol of “case structure” sub VI (National Instruments Corporation, 2010). ..... 129

Figure 9-25: Graphical symbol of “append waveforms” sub VI (National Instruments Corporation, 2010)..... 130

Figure 9-26: Graphical symbol of Split Signal sub VI (National Instruments Corporation, 2010). ..... 130

Figure 9-27: Graphical symbol of “merge signal” sub VI (National Instruments Corporation, 2010). ..... 130

Figure 9-28: Graphical symbol of “IIR cascade filter” sub VI (National Instruments Corporation, 2010). ..... 131

Figure 9-29: Graphical symbol of “Bessel coefficient” sub VI (National Instruments Corporation, 2010). ..... 131

Figure 9-30: Left-Graphical symbol for Block Diagram & Right- Front panel appearance of waveform graphs sub VI (National Instruments Corporation, 2010). ..... 131

Figure 9-31: Graphical symbol of “DAQmx stop task” sub VI (National Instruments Corporation, 2010). ..... 132

Figure 9-32: Graphical symbol of “open data storage” express VI (National Instruments Corporation, 2010)..... 132

Figure 9-33: Graphical symbol of “simple error handler” sub VI (National Instruments Corporation, 2010)..... 133

Figure 9-34: Graphical symbol of “file dialog” sub VI (National Instruments Corporation, 2010). ..... 133

Figure 9-35: Graphical symbol of “set properties” express VI (National Instruments Corporation, 2010)..... 134

Figure 9-36: Graphical symbol of “Write data” express VI (National Instruments Corporation, 2010). ..... 134

Figure 9-37: Graphical symbol of “close data storage” express sub VI (National Instruments Corporation, 2010)..... 134

Figure 9-38: Graphical symbol of “write labview measurement file” express VI (National Instruments Corporation, 2010). ..... 135

Figure 10-1: Graphical representation of Experiment 1 ..... 137

Figure 10-2: Graphical representation of Experiment 2 ..... 137

Figure 10-3: Graphical representation of Experiment 3 ..... 138

Figure 10-4: Graphical representation of Experiment 4 ..... 138

Figure 10-5: Graphical representation of Experiment 5 ..... 139

Figure 10-6: Graphical representation of Experiment 6 ..... 139

Figure 10-7: Graphical representation of Experiment 7 ..... 140



Figure 10-8: All eight strain gauge’s outputs, two piezoresistive-Flexiforce® sensor’s outputs and applied compressive load in Newton with respect to time in seconds. (Experiment protocol: Exp\_4k\_500NPS\_LH300S). ..... 142

Figure 10-9: All eight strain gauge’s outputs and two piezoresistive-Flexiforce® sensor’s outputs with respect to applied compressive load in Newton. (Experiment protocol: Exp\_4k\_500NPS\_LH300S). ..... 143

Figure 10-10: Raw Data with lots of typical noise of one typical strain gauge’s output (SG 0 Vs Time) with respect to time..... 144

Figure 10-11: Filtered data of one typical strain gauge’s output (SG 0 Vs Time) with respect to time. Low pass 3rd order Butterworth IIR filter-with cutoff frequency 5 Hz is used for filtering. .... 145

Figure 10-12: Front panel of Labview code Noise Statistics.vi. This can select any one channel of signal by just one change in block diagram. The two charts “signal” and “Chart” show statistical analysis of signal. The minimum value, maximum value, mean value, standard deviation, variance and range of values are also saved in spreadsheet format (.lvm) in memory. .... 147

Figure 10-13: Block diagram of the Labview code named “Noise Statistics.vi”, Front panel shown in Figure 11-5..... 148

Figure 10-14: Graphical representation of statistical analysis of noise of output of SG 0 when compressive loading is applied from 0 to 4 kN (1st part of the graph). ..... 149

Figure 10-15: Graphical representation of statistical analysis of noise of output of SG 0 when load kept constant at 4 kN (2nd part of the graph). ..... 150

Figure 10-16: Graphical representation of statistical analysis of noise for the output of SG 0 when unload from 4 to 0 kN (3rd part of the graph)..... 150

Figure 10-17: Typical strain gauge output and applied load graph with respect to time (SG 0 Vs Time and Load Vs Time). ..... 152

Figure 10-18: Outputs from two Flexiforce® sensors and applied load graph with respect to time. .... 153

Figure 10-19: All SG output (Microstrain) and two Flexiforce® sensor’s output (Volt) & Load (N) Vs Time (S), Experiment protocol:Exp\_4k\_500NPS\_300LHS. .... 154

Figure 10-20: All SG output (Microstrain) two Flexiforce® sensor’s output (Volt) & Load (N) Vs Time (S) without signal processing, Experiment protocol: Exp\_4k\_500 NPS\_300 LHS..... 155

Figure 10-21: The 1st part of the graph for all strain gauge’s output when loading from 0 to 4 kN. .... 156

Figure 10-22: The 3rd part of the graph for all strain gauge’s output when unloading from 4 to 0 kN. .... 156

Figure 10-23: All strain gauges outputs with respect to applied compressive load. .... 158

Figure 10-24: Two Flexiforce® sensors’ output with respect to applied compressive load. .... 158

Figure 10-25: All eight strain gauge’s outputs, two piezoresistive-Flexiforce® sensor’s outputs and applied compressive load in Newton with respect to time in seconds. (Experiment protocol: Exp\_4k\_500NPS\_PH300S). .... 160

Figure 10-26: All eight strain gauge’s outputs and two piezoresistive-Flexiforce® sensor’s outputs with respect to applied compressive load in Newton. (Experiment protocol: Exp\_4k\_500NPS\_PH300S). .... 161

Figure 10-27: Raw Data with lots of typical noise of one typical strain gauge’s output (SG 0 Vs Time) with respect to time. .... 163

Figure 10-28: Filtered data of one typical strain gauge’s output (SG 0 Vs Time) with respect to time. Low pass 3rd order Butterworth IIR filter-with cutoff frequency 5 Hz is used for filtering. .... 163

Figure 10-29: Typical strain gauge output and applied load graph with respect to time (SG 0 Vs Time and Load Vs Time). .... 164

Figure 10-30: Outputs from the two Flexiforce® sensors and applied compressive load with respect to time. .... 165

Figure 10-31: All SG output (Microstrain) & Load (N) Vs Time (S). .... 166

Figure 10-32: The 1st part of the graph for all strain gauge’s output when loading from 0 to 4 kN. .... 167

Figure 10-33: The 3rd part of the graph for all strain gauge’s output when unloading from 4 to 0 kN. .... 167

Figure 10-34: All strain gauges outputs with respect to applied compressive load. .... 168

Figure 10-35: Two Flexiforce® sensor’s output with respect to applied compressive load. .... 169

Figure 10-36: All eight strain gauge’s outputs, two piezoresistive-Flexiforce® sensor’s outputs and applied compressive load in Newton with respect to time in seconds. (Experiment protocol: Exp\_4k\_500NPS\_NOH). .... 170

Figure 10-37: All eight strain gauge’s outputs and two piezoresistive-Flexiforce® sensor’s outputs with respect to applied compressive load in Newton. (Experiment protocol: Exp\_4k\_500NPS\_NOH). ..... 171

Figure 10-38: Raw Data with lots of typical noise of one typical strain gauge’s output (SG 0 Vs Time) with respect to time..... 172

Figure 10-39: Filtered data of one typical strain gauge’s output (SG 0 Vs Time) with respect to time. Low pass 3rd order Butterworth IIR filter-with cutoff frequency 5 Hz is used for filtering. .... 173

Figure 10-40: Typical strain gauge output and applied load graph with respect to time (SG 0 Vs Time and Load Vs Time)..... 174

Figure 10-41: Outputs from two Flexiforce® sensors and applied load graph with respect to time. .... 175

Figure 10-42: All SG output (Microstrain) & Load (N) Vs Time (S)..... 176

Figure 10-43: The 1st part of the graph for all strain gauge’s output when loading from 0 to 4 kN. .... 176

Figure 10-44: The 2nd part of the graph for all strain gauge’s output when unloading from 4 to 0 kN. .... 177

Figure 10-45: All strain gauges outputs with respect to applied compressive load. .... 178

Figure 10-46: Two Flexiforce® sensor’s output with respect to applied compressive load. .... 178

Figure 10-47: All eight strain gauge’s outputs, two piezoresistive-Flexiforce® sensor’s outputs and applied compressive load in Newton with respect to time in seconds. (Experiment protocol: Exp\_4k\_100NPS\_NOH)..... 180

Figure 10-48: All eight strain gauge’s outputs and two piezoresistive-Flexiforce® sensor’s outputs with respect to applied compressive load in Newton. (Experiment protocol: Exp\_4k\_100NPS\_NOH). .... 181

Figure 10-49: Raw Data with lots of typical noise of one typical strain gauge’s output (SG 0 Vs Time) with respect to time..... 182

Figure 10-50: Filtered data of one typical strain gauge’s output (SG 0 Vs Time) with respect to time. Low pass 3rd order Butterworth IIR filter-with cutoff frequency 5 Hz is used for filtering. .... 183

Figure 10-51: Typical strain gauge output and applied load graph with respect to time (SG 0 Vs Time and Load Vs Time). .... 184

Figure 10-52: Outputs from two Flexiforce® sensors and applied load graph with respect to time..... 185

Figure 10-53: All SG output (Microstrain) & Load (N) Vs Time (S), Experiment protocol: Exp\_4k\_100NPS\_NOH. .... 185

Figure 10-54: The 1st part of the graph for all strain gauge’s output when loading from 0 to 4 kN. .... 186

Figure 10-55: The 2nd part of the graph for all strain gauge’s output when unloading from 4 to 0 kN. .... 187

Figure 10-56: All strain gauges outputs with respect to applied compressive load..... 187

Figure 10-57: Two Flexiforce® sensor’s output with respect to applied compressive load. .... 188

Figure 10-58: All eight strain gauge’s outputs, two piezoresistive-Flexiforce® sensor’s outputs and applied compressive load in Newton with respect to time in seconds. (Experiment protocol: Exp\_4k\_10NPS\_NOH)..... 190

Figure 10-59: All eight strain gauge’s outputs and two piezoresistive-Flexiforce® sensor’s outputs with respect to applied compressive load in Newton. (Experiment protocol: Exp\_4k\_10NPS\_NOH). .... 191

Figure 10-60: Raw Data with lots of typical noise of one typical strain gauge’s output (SG 0 Vs Time) with respect to time..... 192

Figure 10-61: Filtered data of one typical strain gauge’s output (SG 0 Vs Time) with respect to time. Low pass 3rd order Butterworth IIR filter-with cutoff frequency 5 Hz is used for filtering. .... 193

Figure 10-62: Typical strain gauge output and applied load graph with respect to time (SG 0 Vs Time and Load Vs Time)..... 194

Figure 10-63: Outputs from two Flexiforce® sensors and applied load graph with respect to time. .... 195

Figure 10-64: All SG output (Microstrain) & Load (N) Vs Time (S) ..... 196

Figure 10-65: The 1st part of the graph for all strain gauge’s output when loading from 0 to 4 kN. .... 196

Figure 10-66: The 2nd part of the graph for all strain gauge’s output when unloading from 4 to 0 kN. .... 197

Figure 10-67: All strain gauges outputs with respect to applied compressive load..... 197

Figure 10-68: Two Flexiforce® sensor’s output with respect to applied compressive load. .... 198

Figure 10-69: All eight strain gauge’s outputs, two piezoresistive-Flexiforce® sensor’s outputs and applied compressive load in Newton with respect to time in seconds. (Experiment protocol: Exp\_4k\_step1k\_500NPS\_LH30S)..... 200

Figure 10-70: All eight strain gauge’s outputs and two piezoresistive-Flexiforce® sensor’s outputs with respect to applied compressive load in Newton. (Experiment protocol: Exp\_4k\_step1k\_500NPS\_LH30S). .... 201

Figure 10-71: Raw Data with lots of typical noise of one typical strain gauge’s output (SG 0 Vs Time) with respect to time..... 202

Figure 10-72: Filtered data of one typical strain gauge’s output (SG 0 Vs Time) with respect to time. Low pass 3rd order Butterworth IIR filter-with cutoff frequency 5 Hz is used for filtering. .... 203

Figure 10-73: Typical strain gauge output and applied load graph with respect to time (SG 0 Vs Time and Load Vs Time)..... 204

Figure 10-74: Outputs from two Flexiforce® sensors and applied load graph with respect to time..... 204

Figure 10-75: All SG output (Microstrain) & Load (N) Vs Time (S) ..... 205

Figure 10-76: The 1st part of the graph for all strain gauge’s output when loading from 0 to 4 kN. .... 206

Figure 10-77: The 2nd part of the graph for all strain gauge’s output when unloading from 4 to 0 kN. .... 206

Figure 10-78: All strain gauges outputs with respect to applied compressive load. .... 207

Figure 10-79: Two Flexiforce® sensor’s output with respect to applied compressive load. .... 207

Figure 10-80: All eight strain gauge’s outputs, two piezoresistive-Flexiforce® sensor’s outputs and applied compressive load in Newton with respect to time in seconds. (Experiment protocol: Exp\_4k\_step1k\_10NPS\_LH30S)..... 209

Figure 10-81: All eight strain gauge’s outputs and two piezoresistive-Flexiforce® sensor’s outputs with respect to applied compressive load in Newton. (Experiment protocol: Exp\_4k\_step1k\_10NPS\_LH30S). .... 210

Figure 10-82: Raw Data with lots of typical noise of one typical strain gauge’s output (SG 0 Vs Time) with respect to time..... 211

Figure 10-83: Filtered data of one typical strain gauge’s output (SG 0 Vs Time) with respect to time. Low pass 3rd order Butterworth IIR filter-with cutoff frequency 5 Hz is used for filtering. .... 212

Figure 10-84: Typical strain gauge output and applied load graph with respect to time (SG 0 Vs Time and Load Vs Time). ..... 213

Figure 10-85: Outputs from two Flexiforce® sensors and applied load graph with respect to time. .... 214

Figure 10-86: All SG output (Microstrain) & Load (N) Vs Time (S), Experiment protocol: Exp\_4k\_step1k\_10NPS\_LH30S. .... 214

Figure 10-87: The 1st part of the graph for all strain gauge’s output when loading from 0 to 4 kN. .... 215

Figure 10-88: The 2nd part of the graph for all strain gauge’s output when unloading from 4 to 0 kN. .... 216

Figure 10-89: All strain gauges outputs with respect to applied compressive load. .... 216

Figure 10-90: Two Flexiforce® sensor’s output with respect to applied compressive load. .... 217

Figure 11-1: Photographs of the preparation of the animal spinal vertebrae for experimentation at the Royal Veterinary College clinical lab, UCL, Potters’ Bar, UK (A) Cleaning of harvested animal spine (B) Freshly harvested unclean animal spine (C) Cross-section view of spinal vertebra ..... 220

Figure 11-2: Photographs of the specially designed and developed spinal vertebrae holding mechanical tool (A) Top and bottom view of the tool (B) Three parts of the tool-(1) main holding body with positioning and locking screws (2) simple round plate (3) Plate supporting tool ..... 221

Figure 11-3: *Ex vivo* experimental set-up with photographs of the main components like load cell, Universal Testing machine, vertebrae holding tool etc..... 222

Figure 11-4: Schematic diagram of the spinal vertebrae holding tool including all three parts and necessary dimensions. .... 223

Figure 11-5: Photographs of the mechanical experimental set-up (A) UT machine with all required mechanical tools & accessories (B) Zoom in view of the animal spinal vertebrae with mounted load cell end-plates fixed in specially designed holding tool (C) Zoom in view at the time of the load cell loading during experiment. .... 224

Figure 11-6: Schematic 3-D views of the round plate vertebrae holding tool..... 225

Figure 11-7: Event description diagram of Experiment 1. .... 226

Figure 11-8: Event description diagram of Experiment 2. .... 227

Figure 11-9: Even description diagram of Experiment 3 ..... 227

Figure 11-10: All eight strain gauge’s outputs, two piezoresistive-Flexiforce® sensor’s outputs and applied compressive load in Newton with respect to time in seconds. (Experiment protocol: Exp_1k_10NPS_NOH).....	229
Figure 11-11: All eight strain gauge’s outputs and two piezoresistive-Flexiforce® sensor’s outputs with respect to applied compressive load in Newton. (Experiment protocol: Exp_1k_10NPS_NOH). ....	230
Figure 11-12: Raw Data with lots of typical noise of one typical strain gauge’s output (SG 0 Vs Time) with respect to time.....	231
Figure 11-13: Filtered data of one typical strain gauge’s output (SG 0 Vs Time) with respect to time. Low pass 3rd order Butterworth IIR filter-with cutoff frequency 5 Hz is used for filtering. ....	231
Figure 11-14: Typical strain gauge output and applied load graph with respect to time (SG 0 Vs Time and Load Vs Time). ....	232
Figure 11-15: Outputs from two Flexiforce® sensors and applied load graph with respect to time. ....	233
Figure 11-16: The 1st part of the graph for all strain gauge’s output when loading from 0 to 4 kN. ....	234
Figure 11-17: The 3rd part of the graph for all strain gauge’s output when unloading from 4 to 0 kN. ....	235
Figure 11-18: The 3rd part of the graph for all strain gauge’s output when unloading from 4 to 0 kN. ....	235
Figure 11-19: All strain gauges outputs with respect to applied compressive load. ....	236
Figure 11-20: Two Flexiforce® sensors’s output with respect to applied compressive load....	237
Figure 11-21: All eight strain gauge’s outputs, two piezoresistive-Flexiforce® sensor’s outputs and applied compressive load in Newton with respect to time in seconds. (Experiment protocol: Exp_1k_100NPS_NOH).....	239
Figure 11-22: All eight strain gauge’s outputs, two piezoresistive-Flexiforce® sensor’s outputs and applied compressive load in Newton with respect to time in seconds. (Experiment protocol: Exp_1k_100NPS_NOH).....	240
Figure 11-23: Typical strain gauge output and applied load graph with respect to time (SG 0 Vs Time and Load Vs Time). ....	241
Figure 11-24: Outputs from two Flexiforce® sensors and applied load graph with respect to time. ....	241

Figure 11-25: All strain gauge's output when loading from 0 to 1 kN. ....	242
Figure 11-26: The 1st part of the graph for all strain gauge's output when loading from 0 to 1 kN. ....	243
Figure 11-27: The 3rd part of the graph for all strain gauge's output when unloading from 1 to 0 kN. ....	243
Figure 11-28: All strain gauges outputs with respect to applied compressive load. ....	244
Figure 11-29: Two Flexiforce® sensor's output with respect to applied compressive load. ....	244
Figure 11-30: All eight strain gauge's outputs, two piezoresistive-Flexiforce® sensor's outputs and applied compressive load in Newton with respect to time in seconds. (Experiment protocol: Exp_750N_step250N_10NPS_LH10S). ....	246
Figure 11-31: All eight strain gauge's outputs, two piezoresistive-Flexiforce® sensor's outputs and applied compressive load in Newton with respect to time in seconds. (Experiment protocol: Exp_750N_step250N_10NPS_LH10S). ....	247
Figure 11-32: Typical strain gauge output and applied load graph with respect to time (SG 0 Vs Time and Load Vs Time) ....	248
Figure 11-33: Outputs from two Flexiforce® sensors and applied load graph with respect to time. ....	249
Figure 11-34: All strain gauges outputs with respect to applied compressive load. ....	250
Figure 11-35: The 1st part of the graph for all strain gauge's output when loading from 0 to 750 N. ....	250
Figure 11-36: The 3rd part of the graph for all strain gauge's output when unloading from 750 to 0 N. ....	251
Figure 11-37: shows the outputs from all strain gauges with respect to the applied compressive load. The applied compressive load in Newton is along the X-axis and strain gauges output in Microstrain are along the Y-axis. ....	251
Figure 11-38: Two Flexiforce® sensors's output with respect to applied compressive load. ....	252



# LIST OF TABLES

★ Table 3-1: Intradiscal Pressure Measured in the Spine at the time of Different Postures (Quinnel and Stockdale, 1983).....	43
★ Table 3-2: Showing ranges of motion of the lumbar spinal vertebrae in angle of degree in XYZ direction of axis during different physical movements of the body (White and Punjabi, 1990).....	46
★ Table 3-3: Different researcher’s experimented data on the ranges of the motion of the lumbar spine vertebrae during different physical movement of the body (White and Panjabi, 1978) (Pearcy et al., 1984) (Hayes et al., 1989) (Yamamoto et al., 1989) (White and Punjabi, 1990). ....	48
★ Table 6-1: Spinal market competitors by market share in 2009 .....	78
★ Table 6-2: The rest of spine technology companies (worldwide).....	81
★ Table 9-1: Connection diagram details .....	112
★ Table 10-1: Statistical analysis summary of whole graph (SG 0) .....	151
★ Table 10-2: Correlation analysis between applied compressive load and sensor’s output. ....	157

# TABLE OF CONTENTS

---

<b>ABSTRACT</b>	<b>2</b>
<b>ACKNOWLEDGEMENT</b>	<b>3</b>
<b>LIST OF FIGURES</b>	<b>4</b>
<b>LIST OF TABLES</b>	<b>17</b>
<b>1 INTRODUCTION</b>	<b>24</b>
<b>2 ANATOMY AND BIOMECHANICS OF THE SPINE</b>	<b>28</b>
2.1 Introduction	28
2.2 The Spine: Its Parts and Functions	28
2.2.1 Vertebra	30
2.2.2 Facet Joints (Zygopophysial Joints or Synovial Joints)	31
2.2.3 Neural Foramina	32
2.2.4 Spinal Cord	33
2.2.5 Nerve Roots	34
2.2.6 Para-Spinal Muscles	34
2.2.7 Intervertebral Disc	35
<b>3 PHYSICAL PROPERTIES AND FUNCTIONAL BIOMECHANICS OF THE INTERVERTEBRAL SPINAL DISC</b>	<b>38</b>
3.1 Introduction	38
3.2 Physical Properties of the Intervertebral Disc	38

3.2.1	Elastic characteristics of the disc	38
3.2.2	Visco-Elastic characteristics of the disc	40
3.2.3	Fatigue tolerance of the disc	41
<b>3.3</b>	<b>Functional Biomechanics of the Spine</b>	<b>41</b>
3.3.1	Measurement of <i>in vivo</i> loads on the spine	42
3.3.2	Measurement of the spinal disc degeneration	43
3.3.3	Effects on the mechanical properties of the spinal disc	43
3.3.4	Intervertebral spinal disc stresses	43
<b>3.4</b>	<b>Spine Kinematics</b>	<b>46</b>
3.4.1	Range of motion of the lumbar region of the spine	46
<b>3.5</b>	<b>Conclusion</b>	<b>48</b>
<b>4</b>	<b>PATHOLOGY AND SURGICAL INTERVENTION OF THE INTERVERTEBRAL SPINAL DISC</b>	<b>50</b>
<b>4.1</b>	<b>Introduction</b>	<b>50</b>
<b>4.2</b>	<b>Spinal Disc Pathology</b>	<b>50</b>
4.2.1	Normal	51
4.2.2	Congenital/Developmental variation	51
4.2.3	Degenerative/Traumatic	51
4.2.4	Infectious/Inflammatory	55
4.2.5	Neoplasia	56
4.2.6	Morphological variation of unknown significance	56
<b>4.3</b>	<b>Surgical intervention for the lumbar spinal disc</b>	<b>56</b>
4.3.1	Facetectomy	57
4.3.2	Foraminotomy	57
4.3.3	Laminoplasty	57
4.3.4	Laminotomy/Leminectomy	58
4.3.5	Corpectomy	58
4.3.6	Disc disectomy/ Disc micro-disectomy	58
4.3.7	Disc annuloplasty	58
4.3.8	Spinal fusion (Arthrodesis)	59
4.3.9	Total Disc Replacement (TDR)/Disc Arthroplasty	61
<b>4.4</b>	<b>Conclusion</b>	<b>62</b>

<b>5</b>	<b>HISTORICAL REVIEW OF THE RESEARCH ON MEASUREMENT OF <i>IN VIVO</i> SPINAL LOADING</b>	<b>63</b>
5.1	Introduction	63
5.2	Literature Review	63
5.3	Conclusion	67
<b>6</b>	<b>ARTIFICIAL SPINAL DISC PROSTHESIS</b>	<b>69</b>
6.1	Introduction	69
6.2	History and evolution of the Spinal Disc Prosthesis	69
6.2.1	All Metal Disc	69
6.2.2	All non-metallic disc	72
6.2.3	Combination of metal and non-metal discs	73
6.2.4	Artificial joint capsule	75
6.2.5	Nucleus replacement	76
6.3	Artificial Spinal Disc market today	77
<b>7</b>	<b>INVESTIGATION OF SENSING MODALITIES</b>	<b>82</b>
7.1	Introduction	82
7.2	Sensing Modalities	83
7.2.1	Piezoelectric: Sensing Modality	83
7.2.2	Rare Earth Permanent Magnets:	87
7.2.3	Capacitive Sensor	88
7.2.4	Strain gauges	90
7.2.5	Optical sensors	92
7.2.6	Surface Acoustic Wave (SAW) Sensors	93
7.3	Conclusion	94
<b>8</b>	<b>DESIGN AND DEVELOPMENT OF THE ARTIFICIAL SPINAL DISC PROSTHESIS LOADING CELL</b>	<b>95</b>
8.1	Introduction	95
8.2	Sensing element	95

<b>8.3</b>	<b>Sensors</b>	<b>97</b>
8.3.1	Strain gauge sensor	97
8.3.2	Piezoresistive thin layer sensor	98
<b>8.4</b>	<b>Fabrication of the load cell</b>	<b>100</b>
<b>9</b>	<b>DESIGN AND DEVELOPMENT OF THE MECHANICAL TOOLS, ACCESSORIES AND ELECTRONICS DATA ACQUISITION SYSTEM</b>	<b>102</b>
<b>9.1</b>	<b>Introduction</b>	<b>102</b>
<b>9.2</b>	<b>Experimental set-up</b>	<b>102</b>
<b>9.3</b>	<b>Loading machine (UTM-Universal testing machine)</b>	<b>103</b>
<b>9.4</b>	<b>Mechanical tools and accessories</b>	<b>104</b>
9.4.1	Load cell holding fixtures	105
9.4.2	Mechanical calibration tool for Piezoresistive Sensor	106
9.4.3	X-Y movable compression platen with 2-degrees of freedom	108
<b>9.5</b>	<b>Signal Conditioning &amp; Data acquisition system - Hardware</b>	<b>109</b>
9.5.1	Quarter bridge completion module (NI 9944)	110
9.5.2	Strain gauge analogue input module (NI 9237)	113
9.5.3	Signal conditioning circuit for Flexiforce® (Piezoresistive Thin Layer) sensor	118
9.5.4	Voltage analogue input module (NI 9215)	119
9.5.5	USB data acquisition chassis (NI c-DAQ 9172)	121
<b>9.6</b>	<b>Data acquisition and processing - Labview Software</b>	<b>123</b>
9.6.1	Source code in Labview	124
<b>10</b>	<b>STUDY PROTOCOL AND RESULTS FOR THE <i>IN VITRO</i> LOADING OF THE ARTIFICIAL SPINAL DISC PROSTHESIS – LOADING CELL</b>	<b>136</b>
<b>10.1</b>	<b>Introduction</b>	<b>136</b>
<b>10.2</b>	<b>Study protocol</b>	<b>136</b>
10.2.1	Experiment 1: Exp_4k_500NPS_LH300S	137
10.2.2	Experiment 2: Exp_4k_500NPS_PH300S	137
10.2.3	Experiment 3: Exp_4k_500NPS_NOH	138
10.2.4	Experiment 4: Exp_4k_100NPS_NOH	138
10.2.5	Experiment 5: Exp_4k_10NPS_NOH	138

10.2.6	Experiment 6: Exp_step1k_500NPS_LH30S	139
10.2.7	Experiment 7: Exp_step1k_10NPS_LH30S	139
<b>10.3</b>	<b>Results of the <i>in vitro</i> experiments</b>	<b>140</b>
10.3.1	Results of experiment 1: Exp_4k_500NPS_LH300S	141
10.3.2	Results of experiment 2: Exp_4k_500NPS_PH300S	159
10.3.3	Results of Experiment 3: Exp_4k_500NPS_NOH	169
10.3.4	Results of Experiment 4: Exp_4k_100NPS_NOH	179
10.3.5	Results of Experiment 5: Exp_4k_10NPS_NOH	189
10.3.6	Result of Exp. 6: Exp_4k_step1k_500NPS_LH30S	198
10.3.7	Result of Exp. 7: Exp_4k_step1k_10NPS_LH30S	208
<b>10.4</b>	<b>Summary</b>	<b>217</b>
<b>11</b>	<b>EXPERIMENTAL SET-UP, PROTOCOLS AND RESULTS FOR THE <i>EX VIVO</i> LOADING OF THE ARTIFICIAL SPINAL DISC PROSTHESIS – LOADING CELL WITH ANIMAL SPINE</b>	<b>219</b>
<b>11.1</b>	<b>Introduction</b>	<b>219</b>
<b>11.2</b>	<b>Experimental set-up and study protocols</b>	<b>219</b>
11.2.1	Selection of animal spine	219
11.2.2	Preparation of the animal spinal vertebrae	220
11.2.3	<i>Ex vivo</i> experimental set-up	221
11.2.4	<i>Ex vivo</i> study protocols	226
<b>11.3</b>	<b>Results of the <i>ex vivo</i> experiments</b>	<b>227</b>
11.3.1	Results of Exp. 1: Exp_1k_10NPS_NOH	228
11.3.2	Results of Exp. 2: Exp_1k_100NPS_NOH	237
11.3.3	Results of Exp. 3: Exp_750N_step250N_10NPS_LH10S	245
<b>11.4</b>	<b>Summary</b>	<b>253</b>
<b>12</b>	<b>DISCUSSIONS, CONCLUSIONS AND FUTURE WORK</b>	<b>254</b>
<b>12.1</b>	<b>Introduction</b>	<b>254</b>
<b>12.2</b>	<b>Discussion and conclusion</b>	<b>254</b>
<b>12.3</b>	<b>Future work</b>	<b>258</b>

<b>REFERENCES</b>	<b>259</b>
<b>PUBLICATIONS AND PATENTS</b>	<b>271</b>
<b>GLOSSARY</b>	<b>272</b>

# 1 INTRODUCTION

---

Low Back pain is one of the most common reasons for chronic disability and incapacity for work in the western world. In the UK, the National Health Service (NHS) spends £512 million on hospital costs for back pain patients, £141 million on GP (General Practitioner) consultation for back pain related matters and £150.6 million on back pain physiotherapy treatment. The total spending due to back pain is more than £1 billion per year (Maniadakis and Gray, 2000). Up to 4.9 million working days were lost due to back pain in year 2003-04 and up to half a million people received a long term state incapacity benefit because of back pain. In addition to the impact on individuals and their families, back pain is estimated to cost the UK economy up to £ 5 billion a year (Health and Safety Executive, 2006). Moreover, the US demand for implantable medical devices will increase nearly 11% annually which has touched \$24.4 billion in 2007 (Lewis, 2007). According to Stryker, the global market size for spinal implants is worth a total of US \$4.2 billion. Worldwide growth of such implants is expected to average around 16%. However, it is expected that the Asian spinal implants market will grow at a rate of between 20-25% (Lewis, 2007).

The total solution of low back pain – the second most common health problem after headache and common cold, requires a multi-disciplinary research study of the biomechanics, kinematics and physical properties of the spine, specifically the lumbar spine. In most of the cases, low back pain normally occurs in the lower region of the spine – lumbar region. One of the common diseases for chronic low back pain is Disc Degeneration Disease (DDD). In this disease, spinal intervertebral disc loses its ability to safely handle the mechanical stresses. Moreover, the relationship between Disc Degeneration Disease (DDD) and loading of the spine has been well documented (Stokes and Iatridis, 2004) (Liuke et al., 2005) (Nachemson, 1981). Repetitive loading and acute overloading both have been correlated with high incidence of degenerative disease. Therefore, *in vivo* data on spine loading are vital and essential for the understanding of the visco-elasticity of the spine which may lead to the optimisation of treatment and



management of low back pain. Also, such knowledge will facilitate the better and more efficient design of spinal implants such as artificial disc prosthesis and also, will enable the surgeons to optimize their spinal surgical procedures.

*In vitro* data on spine loading only are not sufficient, although many physical properties of the spinal parts like intervertebral disc, vertebra, facet joints, ligaments, etc., are based on the *in vitro* testing. *In vitro* test data can be used as a predictor of *in vivo* test data, if and only, when the *in vitro* environment is the same as the *in vivo* environment. In the case of the lumbar spine, there is no common consensus on *in vitro* mechanical testing environment similarity (McGill, 1992). Without *in vivo* mechanical test data, validity of predictive models and *in vitro* results are questionable. Different mathematical models and various *in vitro* data records show that loads on the lumbar spine vary from around 30% of body weight in a relaxed position to around 5300% of body weight during lifting of heavy loads (Nachemson and Morris, 1964) (Nachemson, 1966) (Leskinen et al., 1983) (Granhed et al., 1987) (Cholewicki et al., 1991). This large variation in values of spinal loads puts a big question mark over its validity. In the forward bending position, particular weight carried by the person increases the loading on the spinal disc ranging from by five times to twenty times (Waris, 1948) (Perey, 1957) (Nachemson, 1965). These results reconfirm the inevitable need for *in vivo* spinal loading measurements. Over the past few decades, many researchers have tried to collect *in vivo* experimental data on spinal loading; however, despite of all efforts and approaches it has not yet been possible to do this for the human spine. Therefore, there is a strong need for the development of new technologies that will allow the *in vivo* investigation of spinal stresses and enable the understanding of the visco-elastic characteristic properties of the human spine.

The hypothesis underlying this project is the development of a prototype intelligent implantable spinal disc prosthesis with the capability of monitoring *in vivo* spinal loading information. One of the notable uniqueness of the project is its contribution towards new knowledge in the field of spinal loading plus the technical developments will contribute in the development of the next generation intelligent artificial spinal disc prosthesis. By enabling correct measurement of *in vivo* load mapping on the spinal disc (which is

still unknown), it opens up many avenues of further research in this area. The development of such new technology it will significantly aid in post-surgery management of patients as such an intelligent implant will continuously monitor the patients activities (bending, lifting). There can be many other advantages, such as providing real-time warning to the patient when performing physical activities which are dangerous to the spine.

More specifically this thesis describes the design and development of a prototype intelligent artificial spinal disc loading cell and processing system, which were developed to investigate the *in vitro* and *ex vivo* spinal loading. The details of both the hardware and software required to fabricate the loading cell will be the subject of the following chapters. Additionally, this thesis details the test methods at all development stages as well as the comprehensive data analysis following the *in vitro* and *ex vivo* methods. A brief description of the subjects that are covered in the following chapters is presented below.

Chapter 2 describes the anatomy of the human spine. It also, covers the structure and the various parts of the spine such as intervertebral disc, vertebra, nerve roots, spinal cord, etc.

Chapter 3 covers relevant material on the physical properties and functional biomechanics of the intervertebral disc with focus on the lumbar region as it will be the area of interest in this research.

Chapter 4 covers the details relating to the pathology and surgical intervention of the human spinal disc. Such details, especially the limitations of the surgical procedures will identify more clearly the main drivers for this research.

Chapter 5 covers a comprehensive and systematic review of the literature on *in vivo* measurements of spinal loading.

Chapter 6 technically explores the commercial evolution of the artificial spinal disc prosthesis. It also describes the currently available models and designs. This knowledge will be helpful in the designing of new generation artificial spinal disc prosthesis with *in vivo* load measuring capability, which is one of the ultimate aims of this project.

Chapter 7 explores relevant sensing modalities which might be suitable for this project. A comparison between the modalities is also presented justifying the selection of sensing modalities used in this study.

Chapter 8 describes the detailed design and development of the sensor loaded artificial spinal disc prosthesis for the *in vitro* and *ex vivo* experiments.

Chapter 9 explains the experimental set-up, including the design of mechanical tools, electronics for the signal conditioning and data acquisition systems along with required software.

Chapter 10 covers the different study protocols used in the *in vitro* experiments of this research project and presents the results and data analysis of the *in vitro* experiments conducted.

Chapter 11 describes the animal *ex vivo* experimental set-up with the specifically designed mechanical tools. The chapter discusses the study protocols and presents all results and data analysis from the *ex vivo* study.

Chapter 12 presents the discussions and conclusions along with suggestions for future work.

## **2 ANATOMY AND BIOMECHANICS OF THE SPINE**

---

### **2.1 INTRODUCTION**

---

The knowledge of the anatomy, the physical properties and biomechanics of the human spine are fundamental for this research project and this is the subject of this chapter.

Clinical Biomechanics is defined as;

“Body of Knowledge that employs mechanical facts, concepts, principles, terms, methodologies, and mathematics to interpret and analyze normal and abnormal human anatomy and physiology” (White and Punjabi, 1990).

### **2.2 THE SPINE: ITS PARTS AND FUNCTIONS**

---

The spine is very difficult to define as a structure. Mainly, it is a mechanical structure which supports the body and hence, allows the body to perform normal physical activities like standing, sitting, running, sleeping, etc (White and Punjabi, 1990). During normal postures and physical activities, the spinal stability from a biomechanical point of view is crucial and very complex as well. The stability of the spine is due to a number of factors, such as ligamentous support and a very sophisticated dynamic neuromuscular control system. Another important function of the spine is to protect the very delicate spinal cord – the main information bus of the body. The spine is also mechanically supported by the rib cage. So, in total the spine has three fundamental biomechanical functions.

- ★ To transfer the weight and the resultant bending moments to the pelvis and to support the human posture.
- ★ To allow the adequate physiological movement of the body and their main parts – head, trunk and pelvis.
- ★ To protect the delicate spinal cord.

The spine mainly consists of 32-33 vertebrae. It is further sub-divided into cervical (C1-C7), thoracic (T1-T12), lumbar (L1-L5), fused sacral (S1-S5) and 3 or 4 fused coccygeal vertebrae.

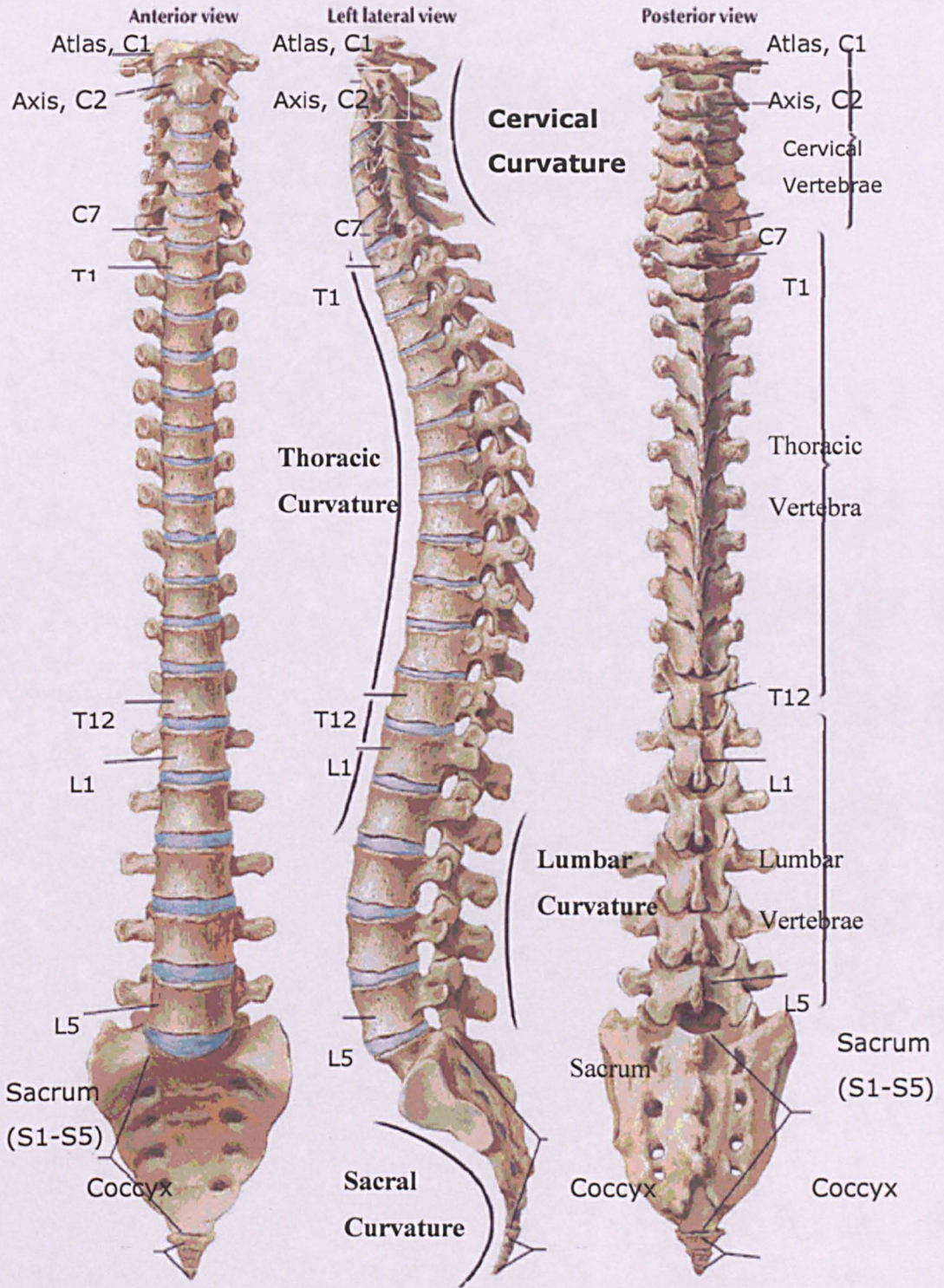


Figure 2-1: Three different anatomical views of the spine showing all its parts (backpain-guide.com, 2011).



As shown in Figure 2-1, from the left lateral view the human spine is an s-type structure. This shape supports the normal body postures and provides enhanced flexibility and shock absorbing capability to the body. This shape also provides the required stability and stiffness. In the frontal plane it looks generally straight and symmetrical. The shapes of the thoracic and sacral curvature are due to the higher heights of the posterior borders than of the anterior borders. The shapes of the cervical and lumbar regions are due to the wedge-shaped intervertebral disc (White and Punjabi, 1990). In detail the spine comprises of:

- ✳ Vertebra
- ✳ Facet Joint
- ✳ Neural Foramina
- ✳ Spinal Chord
- ✳ Nerve Root
- ✳ Para-spinal Muscle
- ✳ Intervertebral Disc.

### 2.2.1 Vertebra

---

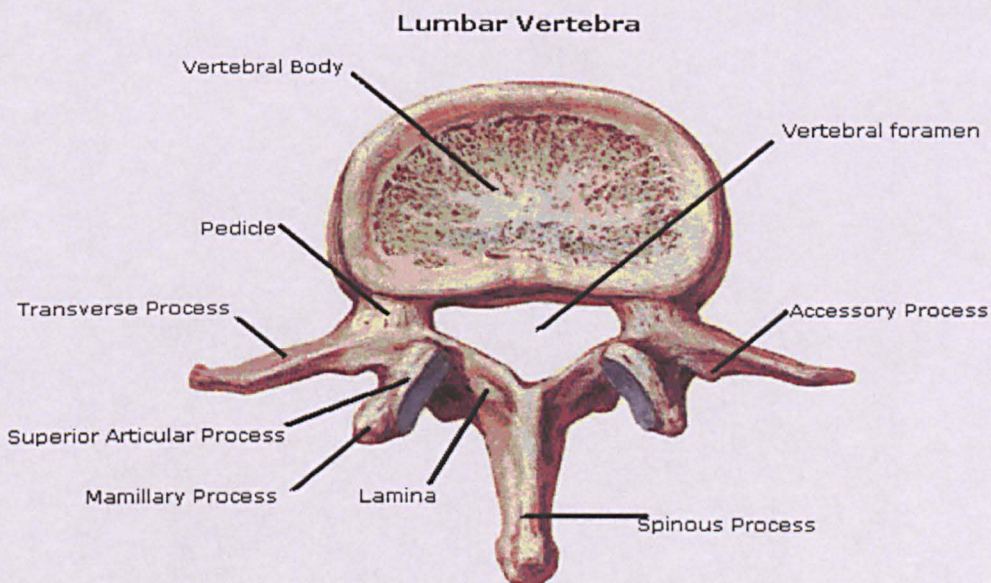


Figure 2-2: Detail anatomical view of the lumbar vertebra of the spine showing all its parts (indyspinemd.com, 2011).



The vertebral body is made up of the outer hard and strong shell known as cortical bone, the inner soft and spongy material known as cancellous bone and the end-plates (Superior and Inferior) (Virgin, 1951). It bears the majority of the spinal loading and protects the delicate spinal cord. As shown in figure 2-2, it consists of vertebral body, spinous process, mamillary process, articular process, transverse process, vertebral foramen, pedicle and lamina. The top and bottom surfaces of the vertebral body are known as cartilaginous end-plates or simply, end-plates. The size and mass of the vertebra are increasing from the first cervical to the last lumbar. This is due to the fact that the vertebrae are subjected to increasing load from the first cervical to the last lumbar. The L-5 vertebra is the biggest vertebra in the spine and this is due to its location and its function of transmitting load to the sacrum. The vertebral compression strength, at slow loading rate also, increases from the first cervical to the last lumbar and the value range is from 1000 N to slightly more than 8000 N. The L-4 vertebra has highest compressive strength, which is slightly more than 8000 N (Perey, 1957) (Bell et al., 1967).

### **2.2.2 Facet Joints (Zygopophysial Joints or Synovial Joints)**

---

The spinal column has real joints, like the knee and the elbow, called facet joints or zygapophysial joints or synovial joints (Figure 2-3).



Figure 2-3: Facet joints motion during forward and backward movement of the body as part of the two vertebrae (spineuniverse.com, 2011).



These facet joints link all the vertebrae together and give them the adequate flexibility to move against each other. The facets are the "bony knobs" that meet between each vertebra. There are two facet joints between each pair of vertebrae, one on each side. They extend and overlap to each other to form a joint between the neighbouring vertebrae. The facet joints provide the required flexibility and mechanical stability to the spine. At the same time they are one of the main causes for the back pain (White and Punjabi, 1990). The total compressive load to the vertebrae shares between facet joints and spinal disc. The facet joints share 18% of the compressive load on the lumbar spine vertebrae (Nachemson, 1960) and this share varies from 0 to 33% depending upon spine postures (Kings et al., 1975). As shown in Figure 2.3, in flexion (bending forward) the facet joints experience tension as shown by the arrow and the spinal disk experiences compression on its' anterior part where as in extension (bending backward) the facet joints experience compression as shown by the arrows (Figure 2-3) and the spinal disk experiences tension on its' anterior part. Hence, these biomechanics help to understand the variations in the sharing of load between the facet joints and the spinal disk due to different spine postures.

### 2.2.3 Neural Foramina

---

The spinal cord branches off into 31 pairs of nerve roots that they exit the spine through small openings on each side of the vertebra called neural foramina (Figure 2-4).

Figure 2-4: Neural foramina in the unit of two vertebrae with the spinal disc in-between (patientsites.com, 2011).



The two nerve roots in each pair go in opposite directions when travelling through the foramina. One goes out through the left foramina and the other goes out through the right foramina. The nerve root allows nerve signals to travel between the brain and the rest of the body (Bogduk and Twomey, 1991).

#### 2.2.4 Spinal Cord

---

The spinal cord is a column of millions of nerve fibres that carries messages from the brain to the rest of the body. It starts from the brain to the area between the end of the first lumbar vertebra and the top of the second lumbar vertebra (Figure 2-5). Each vertebra has a hole in the centre, so when they stack on top of each other they form a hollow tube (spinal canal) that holds and protects the entire spinal cord and its nerve roots (Bogduk and Twomey, 1991). The spinal cord only goes down to the second lumbar vertebra and below this level, a group of nerve fibres, called the cauda-equine start. This group of nerves goes to the pelvis and lower limbs. A protective membrane, called the dura-mater covers the spinal cord. The dura mater forms a watertight sac around the spinal cord and the spinal nerves. Inside this sac, the spinal cord is surrounded by spinal fluid.

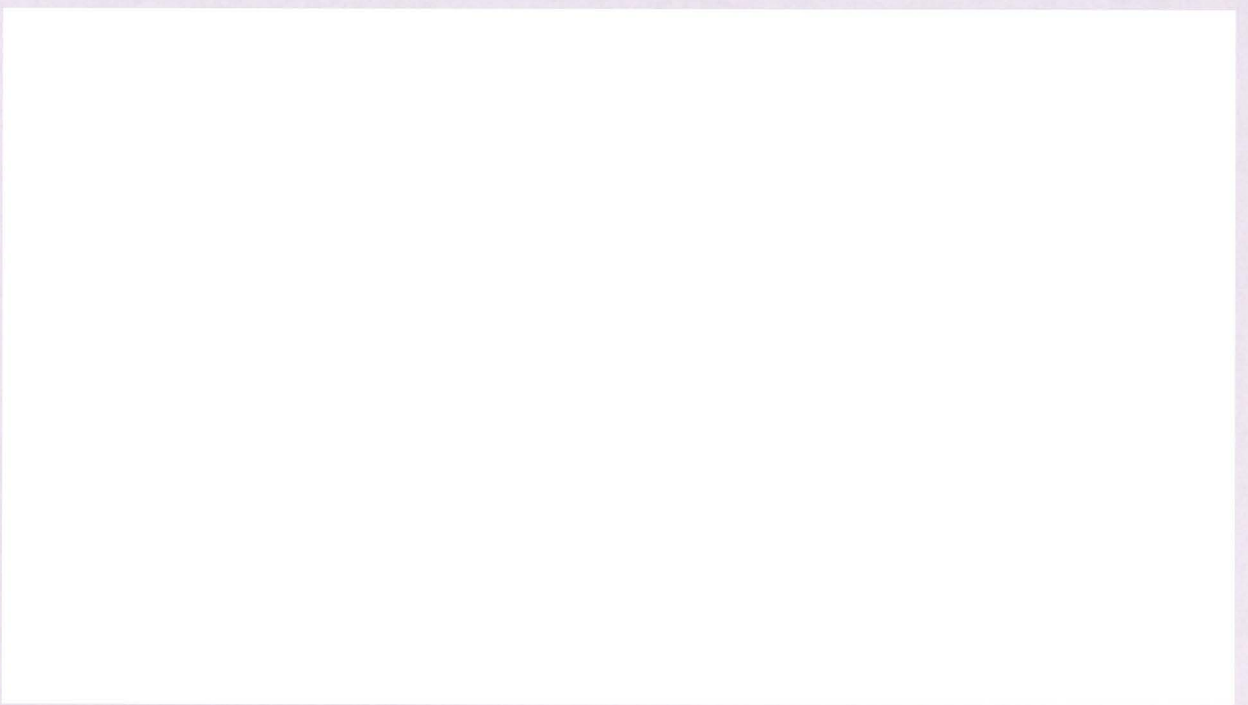


Figure 2-5: The two different views of the spinal cord showing its position in the spine and cross-sectional view (health.com, 2011).

### 2.2.5 Nerve Roots

---

The nerve fibres branch off from the spinal cord to form pairs of nerve roots that travel through the small openings between the vertebrae (Figure 2-6).

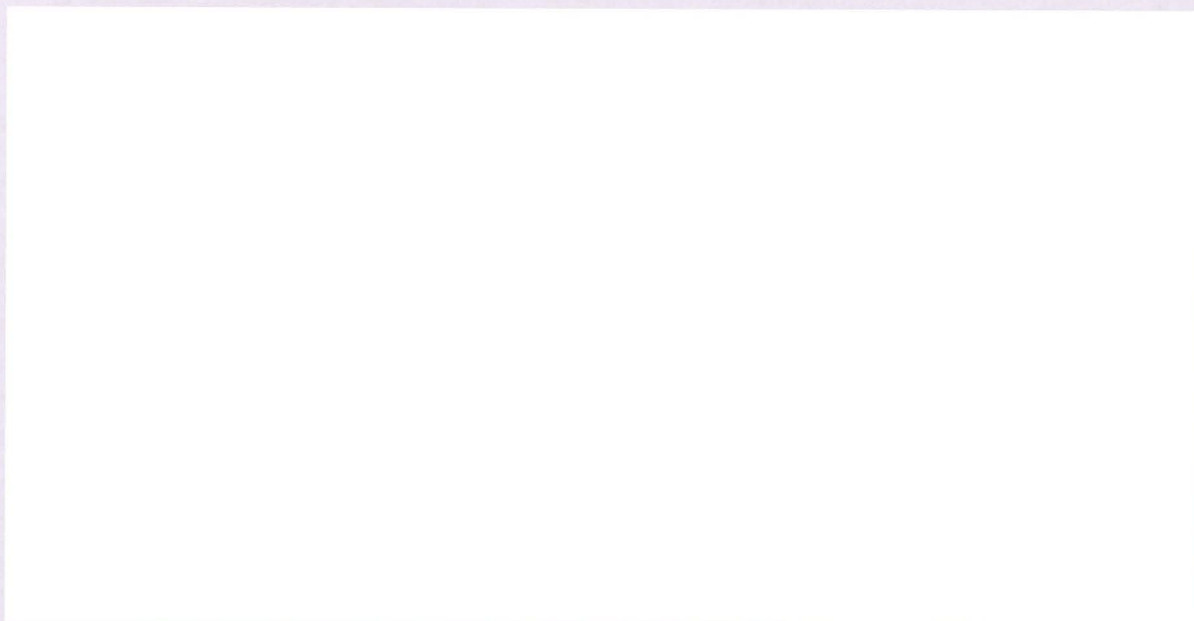


Figure 2-6: The nerve roots run out of the spinal cord in the unit of two vertebrae with the disc in-between (mcm.edu, 2011).

The nerves in each area of the spinal cord connect to specific parts of the body. This is the reason why damage to the spinal cord can cause paralysis in only specific areas depending on which spinal nerves are affected (White and Punjabi, 1990). The nerves of the cervical spine go to the upper chest and arms whereas the nerves of the thoracic spine go to the chest and abdomen, and the nerves from the lumbar spine reach the legs, pelvis, bowel, and bladder. These nerves coordinate and control all organs, muscles and other parts of the body.

### 2.2.6 Para-Spinal Muscles

---

The muscles next to the spine are called the para-spinal muscles. They support the spine and provide the motor for movement of the spine (Bogduk and Twomey, 1991). There are many small muscles in the back and each of these muscles control some part of the total movement between the vertebrae and the rest of the skeleton.



When muscles contract, the small blood vessels travelling through the muscles are pinched off (like a tube pinched between thumb and finger), which causes the building up of lactic acid. If the muscle cells cannot relax and too much lactic acid builds up, it causes a painful burning sensation. The muscle relaxes as the blood vessels open up, and the lactic acid is eventually washed away by fresh blood flowing into the muscle. This mechanism helps to prevent possible severe damage to muscles.

### 2.2.7 Intervertebral Disc

---

An intervertebral disc is located between two consecutive vertebrae as shown in Figure 2-7 and Figure 2-8. It is subjected to different types of forces and bending moments. It is responsible for carrying all compressive loads to which the trunk is subjected along with the sharing of load with the facet joints (Hirsch, 1955) (Prasad et al., 1974). The force on a lumbar disc in a sitting position is more than three times the value of the force due to the weight of the trunk (Nachemson, 1965) (Nachemson, 1966). The reason for such a high force is muscular control forces acting on the spine for achieving spinal stability. The intervertebral disc is also subjected to dynamic loads depending of the human activity (e.g. jumping and trauma).

The actual load on the disc during an active event is perhaps up to twice as high as those in the static position.



From a study of 600 lumbar intervertebral discs, it was found that;

- ✿ Disc degeneration first appears in males in the second decade and in females a decade later.
- ✿ By the age of 50, 97% of the lumbar discs are degenerated.
- ✿ The most degenerated segments are L3-L4, L4-L5 and L5-S1. (Miller et al., 1988).

The intervertebral disc constitutes to 20-33% of the entire height of the vertebral column (White and Punjabi, 1990) and comprises of three distinct parts;

- ✿ Nucleus Pulposus
- ✿ Annulus Fibrosis
- ✿ Cartilaginous End-plate

All three parts of the intervertebral disc will be discussed in brief below.

**Nucleus Pulposus:** It is a centrally located area composed of very loose and translucent network of fine fibrous strands that lie in a mucoprotein gel containing various mucopolysaccharides as shown in Figure 2-8. The cross sectional of the nucleus area is 30-50% of the total disc cross sectional area in the lumbar spine (Panagiotacopoulos et al., 1987). The water content ranges from 70%-90%, highest at birth and tends to decrease with age. The size of the nucleus and its capacity to swell are greater in the lumbar and the cervical regions (White and Punjabi, 1990).

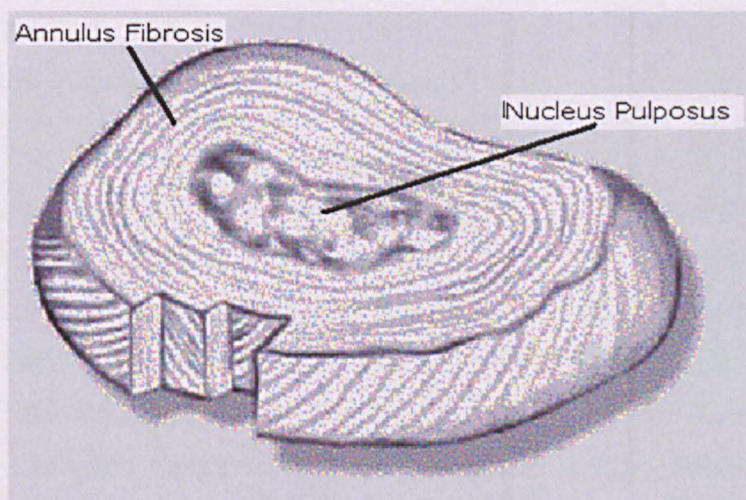


Figure 2-8: Nucleus pulposus and annulus fibrosis in the intervertebral disc (Nuchiro, 2011)

**Annulus Fibrosis:** Annulus fibrosus is a portion of the disc that gradually becomes differentiated from the periphery of the nucleus and forms the outer boundary of the disc enclosing the nucleus pulposus as shown in Figure 2-8. Its structure is composed of fibrous tissue in concentric laminated bands and the fibres are arranged in helicoids manner. They run in the same direction, in the same band but in the opposite direction in the two adjacent bands oriented at 30 degrees to the disc plane, and so 120 degrees with each other in two adjacent bands (White and Punjabi, 1990). This typical structural arrangement provides it with an ability to withstand loads in different directions and at different angles.

**Cartilaginous End-Plates:** Cartilaginous end-plates are composed of hyaline cartilage that separates the other two components of the disc, nucleus pulposus and annulus fibrosis from the vertebral body. It changes with age (approximately, 0-37 years) (Bernick and Cailliet, 1982). It starts with an active growth cartilage and the change in age results in irregularly arranged growth cartilage that disappears with time and is replaced by bone (White and Punjabi, 1990).

# **3 PHYSICAL PROPERTIES AND FUNCTIONAL BIOMECHANICS OF THE INTERVERTEBRAL SPINAL DISC**

---

## **3.1 INTRODUCTION**

---

This chapter covers the physical properties and basic biomechanics of the intervertebral disc along with the kinematics specifically for the lumbar region. The physical properties and the basic biomechanics of the intervertebral disc are fundamental for this research.

## **3.2 PHYSICAL PROPERTIES OF THE INTERVERTEBRAL DISC**

---

Knowledge of the physical properties of the intervertebral discs is essential in the understanding of the behaviour of the lumbar spine including basic biomechanics, including the kinematics, of the lumbar spine. The disc is mainly a visco-elastic structure; therefore its biomechanical characteristics can be divided into three parts, elastic characteristic, visco-elastic characteristic and fatigue. All three types of characteristics will be described below.

### **3.2.1 Elastic characteristics of the disc**

---

The disc is a visco-elastic structure, therefore to observe its elastic characteristics a test should be performed at a slow mechanical loading rate to neglect the visco elastic effect. It is very important to note here, that it makes a lot of difference on the consideration of applied load. It means that the applied load is considered to be applied to the whole structure or to an individual material or part. As the disc is not made up of homogeneous material the applied loads to the whole spine causes different types of stresses to the disc at different locations. For example, when a compressive load is applied to the disc, the disc experiences the compressive stresses on the area of the nucleus pulposus and the tensile stresses on the outer area

of the annulus fibrosus. Elastic characteristics can be divided into Compression, Tensile, Bending, Torsional and Shear characteristics.

**Compression characteristics of the disc:** A study of the load-displacement curve of the disc has revealed that the disc provides little resistance at low loads, but as the load increases it becomes stiffer, and that makes the disc an intelligent shock-absorbing device in the human body. In load displacement curve, the higher the loading rate the steeper the resulting curve. As the disk exhibits visco-elastic behaviour, during the loading and unloading cycle the disk loses energy in the form of temperature called hysteresis. This study also showed that although the disc is subjected to very high loads and a permanent deformation on removal of the load is shown, there was no indication of herniation of the nucleus pulposus. This finding suggests that disc herniation is not due to the excessive compressive loading. It was also found that, no failure of the disc ever took place but the first component of failure was the vertebra, in which the end-plates fractured (Virgin, 1951) (Brown et al., 1957). One surprise was that the disc did not damage under pure compressive load (Farfan, 1973).

**Tensile characteristics of the disc:** The disc nucleus is never subjected to tensile loads under normal physical activities. Moreover, the anterior and posterior regions of the disc are stronger than the lateral and central regions as well, as the central region is the weakest of all. One typical characteristic of the disc is that it is found to be stiffer in tension than under compression and that attributed to the build-up of fluid pressure within the nucleus under compression loading (Markolf, 1970). Moreover, more stiffness in tension restricts the movement of the spine and less stiffness in compression absorbs the loading shocks.

**Bending characteristics of the disc:** The bending characteristics are of great interest because that causes more damage to the disc. Many experiments were done on the disc to understand the bending characteristics of the disc. The disc has more chance to get damaged when subjected to a combined bending and torsional load. It was found that after removal of the posterior element of the disc and with 15 degrees of bending (anterior flexion); consequently disc failure occurred (Brown et al., 1957).

In this case the disc bulged anteriorly during flexion and posteriorly during extension.

**Torsional characteristics of the disc:** Like bending, torsional characteristics are of equal interest. It was found that the average failure torque for non-degenerated disc was 25% higher than that for the degenerated discs (Farfan et al., 1970). The average angle of failure is 16 degrees for non-degenerated disc and 14.5 degrees for degenerated disc (White and Punjabi, 1990).

**Shear characteristics of the disc:** Shear characteristics are of very much importance because torsional characteristics do not provide exact information on the distribution of stresses on all cross sectional area of the disc. Shear stiffness in the horizontal plane was found to be about 260 N/mm (Markolf, 1970). This value was found to be significant in clinical terms and had good impact on biomechanically relevant damage to the disc, particularly in trauma. Moreover, it is relatively rare for the annulus to fail clinically because of the pure shear loading, and most likely clinical evidences of annular disruption implies that the disc has failed due to some combination of bending, torsion and tension (White and Punjabi, 1990).

### 3.2.2 Visco-Elastic characteristics of the disc

---

The visco-elastic characteristic is generally defined as "The time dependent property of a material (e.g. hysteresis, creep and relaxation) to show sensitivity to the rate of loading or deformation" (White and Punjabi, 1990).

The visco-elastic property can be described by a combination of two properties, creep/relaxation and hysteresis. The disc, as mentioned before, is a visco-elastic element, therefore, the detail study of the visco-elastic characteristics of the disc is very much required.

**Creep and Relaxation characteristics of the disc:** White and Punjabi found that the higher the disc the greater the deformation and faster the rate of creep. Experimentally, it was also proved that non-degenerated discs creep slowly and achieve their final deformation value after considerable time as compared to that of the degenerated discs (Kazarian, 1975). Furthermore, the process of degeneration makes the disc less visco-elastic, hence, degeneration results in loss of its capability to attenuate



shocks and to distribute the load uniformly over the entire end-plate (White and Punjabi, 1990).

**Hysteresis characteristics of the disc:** Hysteresis is a phenomenon associated with energy loss exhibited by visco-elastic materials when they are subjected to loading and unloading cycles (White and Punjabi, 1990). In a load versus deformation curve, the area under the curve represents the energy of deformation. Therefore, if the loading and unloading curve has some gap between them, then the energy is lost during loading and unloading. This is of great importance for the spine because shock is absorbed in the disc when the spine is subject to loading and hence, that provides a unique mechanism which protects the spine. The hysteresis depends on the age, magnitude of the applied load and the level of degeneration of the disc. Therefore, more hysteresis is desirable for shock absorption and hence, a younger person's disc exhibits more hysteresis than that of an older person. The lower lumbar discs exhibit more hysteresis than the lower thoracic and upper lumbar discs. Also, it has been observed that the hysteresis decreases on repetitive loading of the disc (Virgin, 1951).

### 3.2.3 Fatigue tolerance of the disc

---

*In vitro* experiments of the disc for finding out the fatigue tolerance will help to estimate the life of the disc in terms of the number of loading cycles. Loading cycles are two per second and the value of load ranges from 400 N to 1800 N. The fatigue tolerance of the disc defines the number of load cycles that can be tolerated before radial and circumferential tears develop. This has been investigated and had been proven experimentally that the disc showed signs of failure after only 200 cycles of forward bending at 5 degrees and it completely failed after 1000 cycles (Brown et al., 1957). Moreover, the *in vivo* real fatigue tolerance is not yet known and that is why it is very less explored and fewer facts are known on fatigue tolerances.

## 3.3 FUNCTIONAL BIOMECHANICS OF THE SPINE

---

Along with the physical properties, the functional biomechanics are also of great importance. Knowledge of the functional biomechanics helps to

develop proper design of implants and get a better understanding of the spine pathology. It is also very much useful in physiotherapy, which is used for the treatment of low back pain.

### 3.3.1 Measurement of *in vivo* loads on the spine

One of the objectives of this research is to measure the *in vivo* load on the lumbar spinal disc, and details on this topic are covered in later chapters. Nachemson and Morris (1964) for the first time found out the actual *in vivo* disc load. They found, with the help of *in vitro* experiments, that fluid pressure within the nucleus is directly related to the axial compression applied to the disc. They measured the pressure by inserting a needle with a miniature electronic pressure gauge at its tip. By this method they measured the loads when a person was performing different physical activities (Nachemson and Morris, 1964) (Nachemson, 1966). The results of this study are shown in Figure 3-1. Many scientists worked in this area and their work is explained in the next chapter.

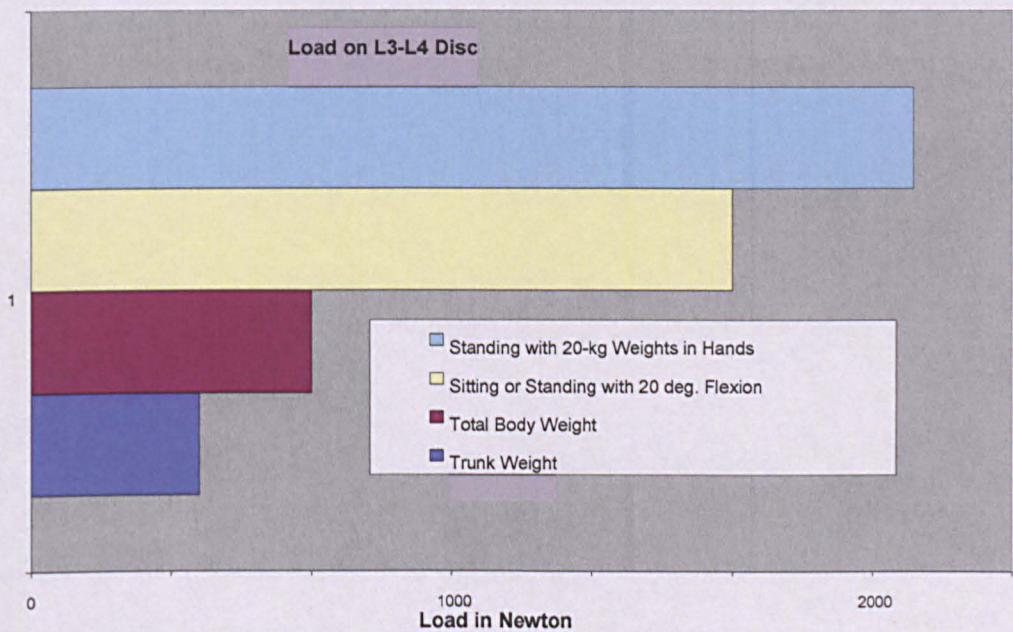


Figure 3-1: Colour Bar-graph showing discal pressure in terms of disc load for normal body weight and different positions of the body (Nachemson and Morris, 1964) (Nachemson, 1966).

### 3.3.2 Measurement of the spinal disc degeneration

---

The Intradiscal Pressure which represents the spine loading has a relationship with the disc degeneration (Punjabi et al., 1988). Disc degeneration was measured by adapting a methodology where the quantity of the discography showed the value of intradiscal pressure (Quinnel and Stockdale, 1983). The lumbar discography is an injection technique used to evaluate patients with back pain who have not responded to extensive conservative care regimens. The most common use of discography is for surgical planning prior to a lumbar fusion. The recorded intradiscal pressure at different postures are shown in Table 3-1.

Table 3-1: Intradiscal pressure measured in the spine at the time of different postures (Quinnel and Stockdale, 1983).

Postures	Pressure (kPa)
Sitting	700
Prone	154
Standing	550

### 3.3.3 Effects on the mechanical properties of the spinal disc

---

The fluid within the intervertebral disc has a relationship with the level of degeneration and obviously, it has a relationship with the mechanical properties of the disc. Researchers conducted experiments by injecting fluid into the intervertebral disc and measured the mechanical properties of the disc before and after the injection of the fluid. The fluid retained specimen's showed more stiffness and they found no changes in stiffness in cases of non-fluid retained specimens (Andersson and Schultz, 1979).

### 3.3.4 Intervertebral spinal disc stresses

---

The stresses are very important characteristics of functional biomechanics for the development of the artificial disc. That is the main interest of this research. During different physical activities like standing, sitting, and running, the intervertebral disc is subjected to different types of loads. Due

to these loads (different magnitudes and directions), the disc accordingly develops stresses in different directions and magnitudes. These stresses may be tensile, compressive, shear or a combination of them and are known as the disc stresses. Stress is defined as "The force per unit area of a structure and a measurement of the intensity of the force" (White and Punjabi, 1990). The Intervertebral disc has an anisotropic structure, so it is very difficult to measure the stresses and its directions. Mathematical models such as FEM- Finite Element Models are also used to find out the stresses in the disc (Shirazi-Adl et al., 1984). A brief description of the various spinal disc stresses can be found below.

**Spinal disc stresses under compression:** Compression is an important type of spine load from the biomechanical point of view. Compression load is transferred from the upper vertebral disc to the lower vertebral disc to the pelvis. The shock is mainly absorbed by various discs due to their visco-elastic characteristics. Due to the compressive load, the nucleus pulposus develops pressures and hence, it applies a force in all the directions away from the centre (Rolander and Blair, 1975) (Brinckmann et al., 1983).

Obviously, these loads/forces generate the stresses in the annular ring. Axial and circumferential stresses are compressive and at the same time the annular fibre stresses are tensile. Typical  $\pm 30$  degree arrangements of the fibres are best suitable to absorb the tensile stresses. The biomechanical characteristics of the spine, in terms of absorbing shocks generated by the loading, are mainly affected by the fluid contents of the nucleus pulposus. In cases of lesser fluid (degenerated disc), due to compressive loading, the nucleus cannot develop pressure inside it and therefore, the vertebrae end-plates experience more pressure at the outer periphery and less at the centre. Experiments and various mathematical models suggest that no intervertebral disc failure takes place only due to the compressive loading (Broberg, 1983) (Shirazi-Adl et al., 1984).

**Spinal disc stresses under tension:** When the intervertebral disc is subjected to tensile load, normal and shear stresses are developed. Due to the typical arrangement of the annular fibres, the normal stresses are absorbed comfortably but the shear stresses cannot be absorbed. The shear stresses are a major portion of these two stresses. Therefore, the intervertebral disc is at more risk due to shear stresses in tensile loading

when compared to compressive loading. It is also important to mention that due to the Poisson effect, the disc bulges during compression and contracts during tension (White and Punjabi, 1990).

**Spinal disc stresses with bending:** During bending, the spine experiences tension in the thoracic and the sacral region and compression in the cervical and the lumbar regions of the spine due to its typical s-type structure. Therefore, one part of the disc experiences compression and the other part experiences tension that in turn, generates the tensile and the compressive stresses accordingly (White and Punjabi, 1990).

**Spinal disc stresses with torsion:** The stresses in the intervertebral disc, whilst the disc is subjected to axial force, depend on the level of degeneration and the condition of the posterior element of the disc. Experiments were conducted (White and Punjabi, 1990) to examine the disc stresses with five options, and they are as under; (with 60 Nm torque)

Option – 1: Non-Degenerated Disc

Option – 2: Non-Degenerated Disc with 2000 N compression

Option – 3: Non-Degenerated Disc with loss of Intradiscal pressure.

Option – 4: Non-Degenerated Disc with posterior portion removed.

Option –5: Non-Degenerated Disc with 2000 N compression & posterior element removed.

The results of the above experiments are as under;

- ★ In all above options, the tensile stresses in the direction of torque were of maximum value in the anterior part of the disc.
- ★ In option 1, 2, and 3, the stresses were found in the posterior and the posterolateral parts of the disc.
- ★ The stresses increased at the periphery after removal of the posterolateral part of the disc.
- ★ Without intradiscal pressure the stresses decreased.
- ★ Increasing compressive load did not have any major impact on the stresses.

**Spinal disc stresses under shear:** The shear force is parallel to the plane of the vertebrae end-plate (transverse plane) and perpendicular to the long spinal axis. It probably generates shear stresses equally over the annulus and nil on the surface. Therefore, the failure of the disc due to shear stresses can be easily understood by the biomechanical and the anatomical disc characteristics (White and Punjabi, 1990).

### 3.4 SPINE KINEMATICS

There are more incidences of spinal diseases at the lumbar vertebrae L4-L5 and L5-S1, which shows strong relationship between the mechanics and the disc diseases. Moreover, these two locations bear the highest loading and undergo the most motion in the sagittal plane (Bogduk and Twomey, 1991). Therefore, the study of the kinematics is essential for the study of the spine related diseases.

“Kinematics is that phase of mechanics concerned with the study of motion of rigid bodies with no consideration of the forces involved” (White and Punjabi, 1990).

As per above definition, the lumbar spine kinematics is needed to be considered for this study because of its direct relevance.

#### 3.4.1 Range of motion of the lumbar region of the spine

The knowledge of the range of motion for the lumbar region is essential for the better understanding of spine kinematics. Table 3-2 shows the range of rotations for the lumbar spine.

Table 3-2: Ranges of motion of the lumbar spinal vertebrae in angle of degree in XYZ direction of axis during different physical movements of the body (White and Punjabi, 1990).

	Combined flex./ext. (+/- x-axis rotation)		One side lateral bending (+/- z-axis rotation)		One side axial rotation (+/- y-axis rotation)	
	Limits of Ranges (Degrees)	Representative angle (Degrees)	Limits of Ranges (Degrees)	Representative angle (Degrees)	Limits of Ranges (Degrees)	Representative angle (Degrees)
Interspace						
L1-L2	5--16	12	3--8	6	1--3	2
L2-L3	8--18	14	3--10	6	1--3	2
L3-L4	6--17	15	4--12	8	1--3	2
L4-L5	9--21	16	3--9	6	1--3	2
L5-L6	10--24	17	2--6	3	0--2	1



Looking at the table 3-2, it is very clear that the flexion/extension range of motion is higher than the lateral bending and axial rotation. Looking at the structure and kinematics of the lumbar spine, the saggital plane translation is important and that's why it is used as a tool to determine the instability. The lumbar area L4-L5 and L5-S1 are subjected to more loading and high motion in the saggital plane. Therefore, it looks appropriate to consider the biomechanics of the lumbar region since is more related to low back pain and spine diseases. In the lumbar region, it is found that the upper vertebra plate has significantly high range of motion than the lower vertebra plate. The summarized results by many researchers on the range of motion of the lumbar spine are shown in Table 3-3. The relationship between the disc degeneration and the kinematics is very important. Many researchers' findings are controversial on this point. It was found that the disc degeneration did not restrict the motion range of L5 facet with respect to the sacrum (Hirsch and Lewin, 1968), rather, the disc degeneration and the low back problems can be predicted by the increased saggital plane translation (Knutsson, 1944) (Gertzbein et al., 1988) (Woody et al., 1988). In contradiction with the above point, it was pointed out that, only 1-2 mm of translation in the frontal and the saggital plane and increased translation is not connected with the degenerative discs (Rolander, 1966). Therefore, the detection of the significant increase in the saggital translational can be considered as the symptoms of the disc degeneration. In one experiment, it was found that, after the study of the motion of the lumbosacral joint in 527 patients, only 15% of the normal control group showed absence of the mobility and 43% of the patients with low back pain due to various diseases showed no motion of L4-L5 (Mensor and Duvall, 1959). In another study it was found that 11% to 20% of the normal persons without back pain have restriction of the spinal movement at L4-L5 and L5-S1 (Tanz, 1953) (Jirout, 1957). In general, many measuring techniques with questionable reliability end up with more contradictory results, and hence, no practical solution can be achieved in predicting low back pain or understanding the related disease.

Table 3-3: Different researcher’s experimental data on the ranges of the motion of the lumbar spine vertebrae during different physical movement of the body (White and Panjabi, 1978) (Pearcy et al., 1984) (Hayes et al., 1989) (Yamamoto et al., 1989) (White and Punjabi, 1990).

FLEXION PLUS EXTENSION															
Yamamoto, 89			Hayes, 89			Pearcey, 84			Dvorak, 89			White & Panjabi 78			
ISSLS, KYOTO			SPINE 14/3:327-331			SPINE 9/3:294-297			ISSLS, KYOTO						
in vitro			in vivo/active			in vivo/active			in vivo/passive						
MEAN	LOWER	UPPER	MEAN	LOWER	UPPER	MEAN	LOWER	UPPER	MEAN	LOWER	UPPER	MEAN	LOWER	UPPER	
L1/2	10.7	5	13	7	1	14	13	3	23	11.9	8.6	17.9	12	9	16
L2/3	10.8	8	13	9	2	16	14	10	18	14.5	9.5	19.1	14	11	18
L3/4	11.2	6	15	10	2	18	13	9	17	15.3	11.9	21	15	12	18
L4/5	14.5	9	20	13	2	20	16	8	24	18.2	11.6	25.6	17	14	21
L5/S1	17.8	10	24	14	2	27	14	4	24	17	6.3	23.7	20	18	22

LATERAL BENDING (ONE SIDE)															
Yamamoto, 89			Pearcey, 84			Dvorak, 89									
ISSLS, KYOTO			SPINE 14/3:327-331			SPINE 9/3:294-297									
in vitro			in vivo/active			in vivo/PASSIVE			White & Panjabi 78						
MEAN	LOWER	UPPER	MEAN	LOWER	UPPER	MEAN	LOWER	UPPER	MEAN LOWER UPPER						
L1/2	4.9	3.8	6.5	5.5	4	10	7.9	14.2	6 3 8						
L2/3	7	4.6	9.5	5.5	2	10	10.4	16.9	6 3 9						
L3/4	5.7	4.5	8.1	5	3	8	12.4	21.2	8 5 10						
L4/5	5.7	3.2	8.2	2.5	3	6	12.4	19.8	6 5 7						
L5/S1	5.5	3.9	7.8	1	1	6	9.5	17.6	3 2 3						

AXIAL ROTATION (ONE SIDE)															
Yamamoto, 89			Pearcey, 84												
ISSLS, KYOTO			SPINE 14/3:327-331												
in vitro			in vivo/active			White & Panjabi 78									
MEAN	LOWER	UPPER	MEAN	LOWER	UPPER	MEAN LOWER UPPER									
L1/2	2.1	0.9	4.5	1	-1	2	6 3 8								
L2/3	2.6	1.2	4.6	1	-1	2	6 3 9								
L3/4	2.6	0.9	4	1.5	0	4	8 5 10								
L4/5	2.2	0.8	4.7	1.5	0	3	6 5 7								
L5/S1	1.3	0.6	2.1	0.5	-2	2	3 2 3								

### 3.5 CONCLUSION

The knowledge and information gained from the study of physical properties, kinematics, anatomy, functional biomechanics of the spine is



essential for the correct design of an artificial spinal disc prosthesis capable of measuring the correct *in vivo* loading on the spine.

The important points to note are,

- ★ Subjected to extremely high compression force, the spinal disc end-plates fracture first without apparent damage to the spinal disc.
- ★ The intervertebral disc exhibits visco-elastic behaviour which helps absorbing the shock to the spine and provides flexibility to the spine and body to do different physical activities at ease.
- ★ Bending and torsional forces are more effective reasons for disc problems and in turn, back pain problems than compressive forces.
- ★ The loads on the spinal disc are extremely high *in vivo* than *in vitro*.
- ★ Compressive strength of vertebrae increases from the cervical to the lumbar region of the spine.
- ★ The facet joints share on average 18% compressive load with the spinal disc and go upto as high as 45%.
- ★ Muscles and tissues around the spine are very important for maintaining the posture of the spine and to bear extremely high *in vivo* compressive loading to the spine.

## **4 PATHOLOGY AND SURGICAL INTERVENTION OF THE INTERVERTEBRAL SPINAL DISC**

---

### **4.1 INTRODUCTION**

---

This chapter covers the details relating to the pathology and surgical intervention of the spinal disc with a specific focus on the lumbar region of the spine. Details on spinal disc pathology and surgical intervention foster the better understanding of this research project. Most of spinal disc pathologies lead to spinal pain and hence, back pain, which results in the restriction of mobility of the whole body. The study of spinal biomechanics and kinematics (discussed in the previous chapters) also help to better understand the roots of the diseases and treatments. The nomenclature and terms used here are supported and endorsed by the North American Spine Society (NASS), the American Association of Neurological Surgeons (AANS), the Congress of Neurological Surgeons (CNS) and American Academy of Orthopaedic surgeons).

### **4.2 SPINAL DISC PATHOLOGY**

---

The Merriam-Webster dictionary defined pathology as,

"The study of essential nature of diseases especially of the structural and functional changes produced by them".

The spinal disc pathology classified here on the basis of diagnosis categories of the disc and each lumbar disc falls into one or more of the following categories.

- ★ Normal
- ★ Congenital/Developmental variation
- ★ Degenerative/Traumatic
- ★ Infectious/Inflammatory
- ★ Neoplasia
- ★ Morphologic variation of unknown significance.

#### 4.2.1 Normal

---

Normal spinal disc means morphologically normal disc. This does not mean that clinically normal disc is morphologically normal as well. For example, when the disc is degenerated due to aging, the disc is still considered clinically normal but it is not morphologically normal. The same way degenerative, developmental or adaptive changes due to scoliosis, spondylolisthesis, etc are considered clinically normal but not morphologically normal (Fardon and Millet, 2001).

#### 4.2.2 Congential/Developmental variation

---

This category includes the congenital/developmental variation in disc morphology in order to adapt abnormal growth of the spine such as spondylolisthesis or scoliosis (Fardon and Millet, 2001).

#### 4.2.3 Degenerative/Traumatic

---

Degeneration is known as “the loss of shock absorbing power of the spinal disc”. Degenerated disc contains less water portion than normal healthy disc. Hence, the more degeneration of the disc the less it exhibits visco-elastic characteristics (Fardon and Millet, 2001). This category is subdivided into,

- ★ Annulus tears/Fissures
- ★ Herniation
- ★ Degeneration

##### **Anulus tears/fissures:**

Anular tears, also known as anular fissures, defined as uncommon spaces between fibres and/or tear away fibres from their vertebral body insertions, and/or tear away broken fibres that pop out concentrically, radially and/or transversely. The terms “tear” or “fissure” which represents lesions not necessarily mean that it is due to the trauma (Figure 4-1) (Fardon and Millet, 2001). The tears or fissures could be there for any reasons like biological or trauma, etc. This is one of the common types of pathology for spine disc related problems.




Figure 4-1: Schematic sagittal anatomic sections of a normal young healthy disc (Left), an annular tear (radial tear in this case) and a disc herniation (Right) (Milette, 1997).

**Herniation:** An extension of the disc material beyond the normal periphery of the intervertebral disc space is known as herniation of the disc (slipped disc) (Figure 4-1). This extension of material is due to extension of any part or more than one part of the spinal disc like cartilage, apophyseal bone, outer tissue, and/or nucleus pulposus. The herniation of the disc is further subdivided in focal herniation and broad-based herniation (Figure 4-2) (Fardon and Millet, 2001).




Figure 4-2: Focal herniation involves less than 25% (90°) of the disc circumference (Left). Broad-based herniation involves between 25% and 50% (90–180°) of the disc circumference (Right) (Milette, 1997).

Bulging is defined as extension of circumferential disc tissue (50-100%) outside the edges of the ring apophyses (Figure 4-3). The "bulging" and "herniation" are different types of spinal disc pathology. If extension of circumferential disc tissue is symmetrical all around then it is known as

"symmetrical bulging". If extension of the circumferential disc tissue is not symmetrical, then is known as "asymmetrical bulging" of the disc (Figure 4-3). This type of asymmetrical bulging is present in scoliosis or spondylolisthesis. The "bulging" is a descriptive term for the shape of the disc contour and not a diagnostic category (Fardon and Millet, 2001).

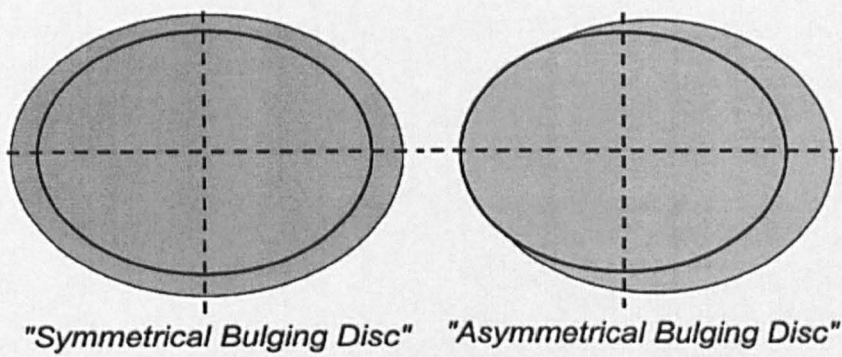


Figure 4-3: Symmetrical presence (or apparent presence) of disc tissue "circumferentially" (50–100%) (Left), Asymmetrical bulging of the disc margin (50–100%) (Right) (Fardon and Millet, 2001).

Herniation is morphologically subdivided into,

- ✦ Protrusion
- ✦ Extrusion
- ✦ Intervertebral

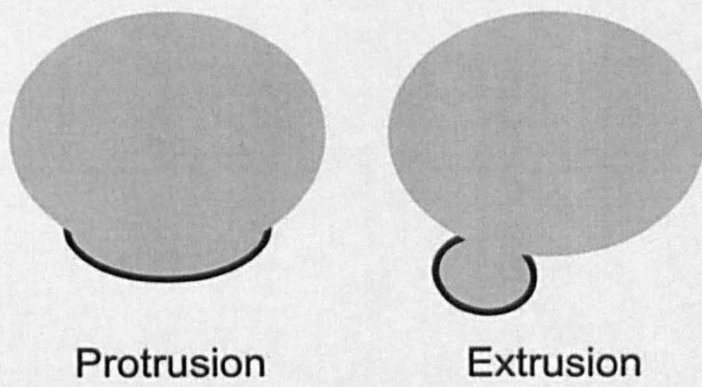


Figure 4-4: Types of Herniated discs – protrusion (Left), extrusion (Right), based on the shape of the displaced material (Fardon and Millet, 2001).

**Protrusion:** The protrusion is defined as; "If the greatest distance, in any plane, between the edges of the disc material beyond the disc space is less than the distance between the edges of the base, in the same plane". The base is defined as the cross-sectional area of disc material at the outer margin of the disc space of origin, where disc material displaced beyond the

disc space is continuous with disc material within the disc space. In the cranio-caudal direction, the length of the base cannot exceed, by definition, the height of the intervertebral space (Figure 4-4) (Fardon and Millet, 2001).

**Extrusion:** Extrusion is defined as “When, in at least one plane, any one distance between the edges of the disc material beyond the disc space is greater than the distance between the edges of the base, or when no continuity exists between the disc material beyond the disc space and that within the disc space (Figure 4-4)” (Fardon and Millet, 2001).

**Sequestration** is a type of extrusion. It is defined as – “If displaced material is not in any physical contact with the disc” (Figure 4-5) (Fardon and Millet, 2001).

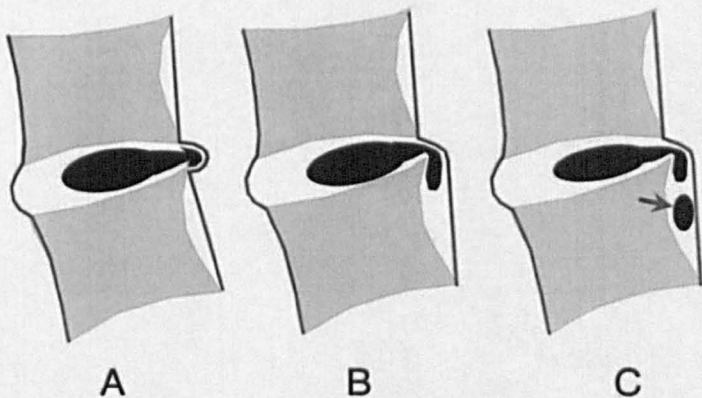


Figure 4-5: Schematic representation of various types of posterior central herniation. (A) A herniation (or protrusion) without significant disc material migration. (B) A herniation with downward migration of disc material under the posterior longitudinal ligament (PLL). (C) A herniation with downward migration of disc material and sequestered fragment (arrow) (Milette, 2000).

**Intravertebral:** Intravertebral herniation is defined as “If displaced disc material is in the cranio-caudal (vertical) direction through a break in the vertebral body endplate” (Fardon and Millet, 2001).

Disc herniation may be further specifically described as contained or uncontained. Contained herniation is defined as “If the displaced disc material is under the cover of circumferential anulus fibres”. Uncontained herniation defined as “If the displaced disc material is pops out of the circumferential anulus fibres means no outer cover of anulus fibres is present”. Displaced disc tissues may also be described by location, volume, and content (Fardon and Millet, 2001).



**Degeneration:** Degenerated disc is defined in simple words as, “The spinal disc which losses its ability to absorb the shocks”.

It may include, apparent desiccation, fibrosis, narrowing of the disc space, diffuse bulging of the anulus beyond the disc space, extensive fissuring (i.e. numerous anular tears), and mucinous degeneration of the anulus, defects and sclerosis of the endplates, and osteophytes at the vertebral apophyses (Fardon and Millet, 2001). This is further divided into two subcategories,

**Spondylosisdeformans:** It is defined as changes in the disc associated with a normal aging process (Figure 4-6).

**Intervertebral osteochondrosis:** It is defined as changes in the disc due to the pathologic process (Figure 4-6) (Fardon and Millet, 2001).

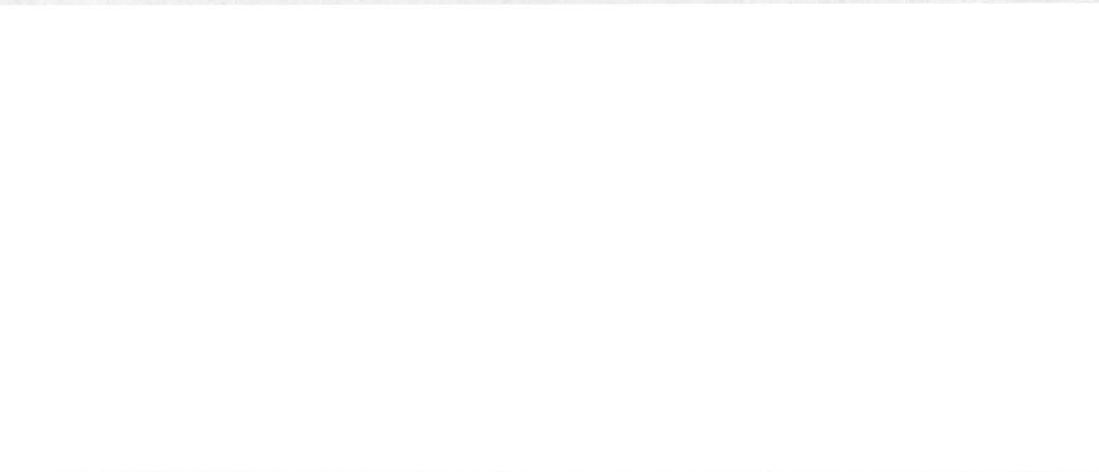


Figure 4-6: Schematic sagittal anatomic sections of the normal disc, spondylosisdeformans, and intervertebral osteochondrosis (Milette, 1997).

4.2.4 **Infectious/Inflammatory**

This category is defined as the changes in the spinal disc due to infection and/or infection-like inflammatory discitis, and/or inflammatory due to spondyloarthropathy. The inflammatory spondylitis of subchondral endplate and bone marrow manifested as Modic Type 1 magnetic resonance imaging (MRI) changes. This can be further subcategorised as per appropriate specificity (Fardon and Millet, 2001).

#### **4.2.5 Neoplasia**

---

Primary or metastatic morphologic changes of disc tissues caused by neoplasia are categorized as Neoplasia, with sub categorization for appropriate specificity (Fardon and Millet, 2001).

#### **4.2.6 Morphological variation of unknown significance**

---

Instances in which data suggest abnormal morphology of the disc but are not complete enough to warrant a diagnostic categorization can be categorized as morphologic variant of unknown significance (Fardon and Millet, 2001).

### **4.3 SURGICAL INTERVENTION FOR THE LUMBAR SPINAL DISC**

---

In one of the national health and nutrition examination survey, it is mentioned that back pain is the second most frequently reported reason for visiting a doctor, the fifth most frequent cause of hospitalization and the third most frequent reason for surgery (American association of neurological surgeons, 2010). Back pain is due to many reasons like trauma, diseases, etc. Many types of treatments are available and the most important and common types are:

- ★ Drug-therapy
- ★ Epidural steroidal injections
- ★ Physiotherapy
- ★ Acupuncture
- ★ Chiropractic
- ★ Ayurvedic
- ★ Surgical

The surgical treatment option is selected after trying all or many of the other non-surgical treatment options. The clinical symptoms which also give indication for lumbar spinal surgery are cauda equine syndrome, radiculopathy and instability. The severe discogenic back pain is also an indication of surgery. Most lumbar surgical approaches use the posterior approach. In cases of major surgery like spinal fusion and total disc replacement (TDR) the anterior surgical approach is used. In cases of highly



unstable spine or when there is a requirement of severe deformity corrections, the circumferential approach is used (Bartleson and Gordon Deen, 2010). There are many types of surgical treatments available (White and Punjabi, 1990). The typical surgical procedures are,

- ★ Facetectomy
- ★ Foraminotomy
- ★ Laminoplasty
- ★ Laminotomy
- ★ Corpectomy
- ★ Disc Disectomy/Micro-disectomy
- ★ Disc Annuloplasty
- ★ Disc Arthroplasty
- ★ Spinal leminectomy
- ★ Spinal fusion
- ★ Total disc replacement

A brief description of each procedure is given below.

#### **4.3.1 Facetectomy**

---

Facetectomy is defined as "Excision of a facet especially of a vertebra" (Merriam-Webster Inc., 2010). In this surgery, the spinal nerve root is decompressed by removing some part of the facet of the spinal vertebrae.

#### **4.3.2 Foraminotomy**

---

Foraminotomy is defined as "A medical operation used to relieve pressure on nerves that are being compressed by the intervertebral foramina, the passages through the bones of the vertebrae of the spine that pass nerve bundles to the body from the spinal cord" (Benzel, 2005).

#### **4.3.3 Laminoplasty**

---

Laminoplasty is defined as "A surgical procedure for treating spinal stenosis by relieving pressure on the spinal cord. The procedure involves cutting the lamina on both sides of the affected vertebrae (cutting through on one side and merely cutting a groove on the other) and then "swinging" the freed flap of bone open thus relieving the pressure on the spinal cord. The spinous process may be removed to allow the lamina bone flap to be swung

open. The bone flap is then propped open using small wedges or pieces of bone such that the enlarged spinal canal will remain in place” (Benzel, 2005).

#### **4.3.4 Laminotomy/Laminectomy**

---

Laminotomy is defined as “A surgical division of a vertebral lamina”. (Merriam-webster Inc., 2010).

This is one of the most commonly performed spinal surgical procedures (Benzel, 2005). A Laminotomy is a neurosurgical procedure that removes part of a lamina of the vertebral arch in order to decompress the corresponding spinal cord and/or spinal nerve root. This was originally performed as a hemilaminectomy, consisting in the removal of either the left or right half of the lamina, but is now more commonly carried out as the removal of a portion of both sides of the lamina (while retaining the rest to preserve vertebral stability as much as possible). Laminotomy is also often accompanied by Facetectomy.

#### **4.3.5 Corpectomy**

---

Corpectomy is a surgical procedure that involves removing part of the vertebral body usually as a way to decompress the spinal cord and nerves. Corpectomy is often performed in association with some form of disectomy (Wikimedia Foundation Inc., 2008). Anterior Corpectomy and stabilization is most often indicated for treatment of trauma or spinal tumours. It is less frequently, it is indicated for chronic instability, pseudoarthrosis, disc herniation or disc degeneration (Bradford and Zdeblick, 2004).

#### **4.3.6 Disc disectomy/ Disc micro-disectomy**

---

A disectomy is a surgical procedure in which the central portion of an intervertebral disc, the nucleus pulposus, which is causing the pain by stressing the spinal cord or radiating nerves, is removed. (Wikimedia Inc., 2010).

#### **4.3.7 Disc annuloplasty**

---

The term intervertebral disc annuloplasty indicates any procedure aimed at repairing the annulus of a bulging intervertebral disc before it herniated.

IDET ("Intradiscal-Electro thermal-Annuloplasty") is a recently developed minimally invasive form of annuloplasty. In this technique, local anaesthesia and conscious monitored sedation is given to the discogenic patient. A 17 gauge needle is inserted in the affected disc under multiplane fluoroscopic guidance. Then it is heated to 90°C (corresponding to adjacent tissue temperature of 72 degree) for approximately fifteen minutes. The heat is intended to seal any ruptures in the disc wall and may also burn nerve endings, which can make the area less sensitive to pain. A survey of complications were noted a 6 per 1,750 incidence of reversible nerve injury due to needle puncture and a 1 per 1,750 incidences of discitis (Hsiu et al., 2000).

#### **4.3.8 Spinal fusion (Arthrodesis)**

---

As per Medline Plus-Meriam Webster dictionary, the spinal fusion (Arthrodesis) defined as,

"A surgical fusion of two or more vertebrae for remedial immobilization of the spine"

It is first introduced by Albee and Hibbs in 1911 (Albee, 1911) (Hibbs, 1911). Spinal fusion is also known as spondylodesis or spondylosyndesis. There are many fusion operation procedures and many of them can be found in the literature (Wu, 1975). Supplementary bone tissue (like autograft, allograft) is used along with the natural osteoblastic processes. This procedure is used to eliminate the pain caused by abnormal motion of the vertebrae by restricting minimum motion of the vertebrae themselves. Today, about 250,000 spinal fusion surgeries are performed each year in the USA with a steady growth rate as almost all surgeries require bone graft material (Bono and Grafin, 2004).

Spinal fusion is done most commonly in the lumbar region of the spine, but it is also used to treat cervical and thoracic problems. Conditions where spinal fusion surgery may be considered are:

- ★ Degenerative disc disease
- ★ Discogenic pain
- ★ Spinal tumour
- ★ Vertebral fracture

- ★ Scoliosis
- ★ Kyphosis (i.e. Scheuermann's disease)
- ★ Spondylolisthesis
- ★ Spondylitis
- ★ Following Osteotomy of the spine
- ★ Posterior Rami Syndrome
- ★ Other degenerative spinal conditions.
- ★ Any condition that causes instability of the spine

(Herkowitz et al., 2004) (White and Punjabi, 1990), (Wikimedia Foundation Inc., 2010).

**Types of spinal fusion:** There are two main types of lumbar spinal fusion. *Posterolateral-intertransverse-fusion*; in this type of fusion the bone graft is placed between the transverse processes in the back of the spine. These vertebrae are then fixed in place using screws, metal rods, wire, etc. This process is an old process. The process was modified by no fixation of screws and introduce silver instead of bone graft. This modification was very successful (92% union) (Truchly and Thompson, 1970).

*Inter-body fusion*; in this type of fusion the bone graft is used to fuse the two vertebrae and a bone graft is placed between two vertebrae after removing the spinal disc. A plastic or titanium device may be placed between the vertebra to maintain spine alignment and disc height. The fusion then occurs between the endplates of the vertebrae. If both types of fusion are used then this is known as a 360-degree fusion. Fusion rates are higher with inter-body fusion. There are mainly three types of inter-body fusions and are, briefly described below.

- ★ **Anterior lumbar interbody fusion (ALIF):** The disc is approached from an anterior abdominal incision and this is the most common approach. It is particularly useful when posterior elements are destroyed or attempts failed or clinically not possible (Sijbrandij, 1962).
- ★ **Transforaminal lumbar inter-body fusion (TLIF)** - the disc is accessed from a posterior incision on one side of the spine. It is a minimally invasive surgery. It has very low chances of nerve root

damage when compared to the posterior lumbar inter-body fusion (White and Punjabi, 1990).

- ★ **Posterior lumbar inter-body fusion (PLIF)** - In this technique the disc is approached from a posterior part of the body. This technique is advisable due to the non-exposure of the sacral sympathetic fibre, and the risk of impotency for male patient is nil. The disadvantage of this procedure is the probability of protrusion of graft material (White and Punjabi, 1990). The fusion process typically takes 6–12 months after surgery. During this time external bracing (orthotics) may be required. External factors such as extensive fusion, large bone graft, osteoporosis, certain medications, wound healing, and heavy activity can prolong the fusion process. Due to some observations of increased stress, degenerative changes, spinal stenosis and fracture dislocation at the adjacent segments, some newer technologies are being introduced which avoid fusion and preserve spinal motion. Procedures, such as artificial disc replacement, are being offered as alternatives to fusion, but have not yet been adopted on a widespread basis (Hunter et al., 1980) (Eismont and Simeone, 1981) (Lee and Langrana, 1984) (Herkowitz et al., 2004).

#### **4.3.9 Total Disc Replacement (TDR)/Disc Arthroplasty**

---

Artificial Disc Replacement (ADR), or Total Disc Replacement (TDR), is a type of Arthroplasty. It is a surgical procedure to remove vertebral discs and replaced them with artificial devices in the lumbar (lower) or cervical (upper) spine. The procedure is used to treat chronic, severe low back pain and cervical pain resulting from degenerative disc disease. The aim of the invention of artificial spinal disc is to achieve more natural biomechanics and kinematics, after surgery than after fusion, for the spine. It is also protecting the adjacent level discs against the non-physiologic loading, as in the case of fusion. Artificial disc replacement has been developed as an alternative to spinal fusion, with the goal of pain elimination or reduction, while still allowing motion throughout the spine. Another possible benefit is the prevention of premature breakdown in adjacent levels of the spine, a potential risk in fusion surgery. More details and explanation for this is provided in the chapter-6.

## 4.4 CONCLUSION

---

Spine diseases are mainly related to abnormal physical changes, degeneration, infections, bone deformity and metastatic morphological changes in the spine and its parts such as discs, vertebrae and related muscles and tissues. Laminotomy/Laminectomy is the most commonly performed surgical procedure for the spine. There is always a great debate on "Which surgical procedure is more successful Fusion or Total Disc Arthroplasty?" Most probably, Total Disc Arthroplasty has a more bright future when aiming for a better solution of disc degeneration diseases.

## **5 HISTORICAL REVIEW OF THE RESEARCH ON MEASUREMENT OF *IN VIVO* SPINAL LOADING**

---

### **5.1 INTRODUCTION**

---

This chapter summarizes chronologically the work done on measurements of *in vivo* spinal loading, including a discussion on their limitations. Despite the many attempts and techniques used in measuring the *in vivo* loading of the spine, still, these results are required to be validated.

### **5.2 LITERATURE REVIEW**

---

The oldest work in the measurement of *in vivo* spinal loading in human was done in the 1957 by Perey. In this work, a simplistic indirect estimation model was used. In this model, the spine load was calculated on the basis of the bodyweight above the particular spinal flexible unit in terms of body weight percentage e.g. 50%, 60%, and 45% (Perey, 1957). For example, when the total body weight is 100 kg it means that will generate  $100 \times 9.81$  (Gravitation constant) = 981 N. At a particular spinal flexible unit the body weight above that flexible unit is 50% of the total body weight (i.e. 50 kg (Equivalent to 490.50 N force)). This model had limitations as it did not consider the musculature forces, externally applied forces (like load due to weight lifting), the intra-abdominal forces and other complex forces like stabilizing forces, in the calculation. In other words, the work did not properly include the kinematics of the spine and its effects on the loading. Also, this study did not perform any real time *in vivo* direct load measurement experiments on the spine (Rohlmann et al., 2000). This model had many limitations and it is very far from providing information on the actual loading of the spine.

About a decade later in 1966, Waugh measured the spinal load by implanting a sensor loaded device into the human spine. Waugh used a strain gauge loaded Harrington rod (Waugh, 1966). The main limitation of

Waugh's research was that the Harrington rod was implanted parallel to the spine, therefore the load was shared between the spine and the device, hence, the actual real time *in vivo* loading measurement of the spine could not be achieved. Moreover, after the surgical operation, the load bearing capacity of the spine kept on changing, hence, the load sharing between the spine and the Harrington rod also kept changing. Therefore, the above technique it is also not a proper method for measuring the *in vivo* spinal loading.

Nachemson et al. in 1964, inserted a pressure transducer loaded needle into the nucleus of the disc to measure the *in vivo* pressure while the patients were performing various tasks. He collected data from more than 100 patients over a period of 20 years. The recorded data, as mentioned above, were measured during different physical activities like standing, sitting, lying supine and at the same time with forward flexion of 20° and rotation of 20° whilst lifting a weight (Nachemson and Morris, 1964) (Nachemson, 1966) (Nachemson and Elfstrom, 1970). The main limitation is that this technique measured pressure instead of force. They derived the force data from the recorded pressure data by using an empirical function (Farfan, 1995). This function is also based on the *in vitro* data collected from experiments on a cadaveric spine. Nachemson himself discussed this limitation in 1981 (Nachemson, 1981).

In 1977, Olsson and his team conducted a precise motion analysis by using roentgen-stereo-photogrammetry and found that the implant was subject to motion and loads even after solid fusion (Olsson et al., 1977). The work did not produce direct *in vivo* real time data of the spinal loading. Also, this method has an inherent erroneous relationship between motion measurements with the actual load measurement of the spine.

In the 1980's many other researchers have also used external spinal fixator devices in order to investigate *in vivo* spinal loading. Their research methods had the same limitations as some of the studies conducted earlier like Waugh (described above), where the loading was shared between the spine and the fixator devices placed parallel to the spine (Schlapfer et al., 1980) (Wilke, 1992). Schultz and his team have measured the *in vivo* pressure inside the disc and measured the electrical outputs using Electromyography (EMG). The measurements were made during resting



periods, during lifting of 8 kg of weight and during twisting and bending of the spine (Schultz et al., 1982a) (Schultz et al., 1982b). The limitations of this work are again the same as those discussed before. They managed to measure the *in vivo* pressure instead of the *in vivo* loading. Moreover, they used the EMG technique which involves direct measurement of the electrical parameters due to muscle activities and that can be correlated to the different forces of the muscles applied on the spine in different directions (Farfan, 1995) (Patwardhan et al., 1999). EMG measurements also vary from one human subject to another.

In 1983, Leskinen and his team have used the simplified 5 cm bending moment model. The 5 cm bending moment model was based on certain assumptions. In this model, 5 cm is a rough distance from the processes to the centre of the disc space. An assumption was made that the spine is positioned in bending and connected tissues can be considered as a single vector working in opposite direction of the loads on the spine. They experimented with the condition of lifting 15 kg weight and due to that the extension tissues were working against the loads of the spine. The 5 cm is a rough distance from the processes to the centre of the rotation of the disc space (Leskinen et al., 1983). This model does not consider the intra-abdominal forces during lifting. If such forces were considered then the load would have been very low [ (McGill, 1990) cited in (Goel and Weinstein, 1990)]. Looking at the typical spine anatomy and its very complex structure, it is highly unlikely that the mathematical models based on some simple methodology can actually achieve the result which is very near to the original.

An indirect method of the dynamic chain model that uses the kinematics representation of the musculoskeletal system coupled with the experimental measures of the applied loads and the ground reaction forces to predict the loading at each joint in the resulting dynamic chain has been used by some researchers (Kromodihardjo and Mital, 1987) (Granhed et al., 1987) (Cholewicki et al., 1991). The model does not consider the forces exerted by the muscles for the stabilization of the spine and that may be a significant contributor to the reactionary forces applied to the spine (Cholewicki et al., 1999).

Han and McGill have used the EMG technique and the dynamic chain model. McGill has used the lateral bending and, Han and his team used the lifting up to 180 N as a condition (McGill, 1992) (Han et al., 1995). The limitations of these techniques are the same as the ones described above.

Dolan and Adams in 1998 have also used the EMG technique again under the condition of the repetitive lifting of 10kg weight (Dolan and Adams, 1998). Morlock and others, in 1998, used the dynamic chain technique while performing everyday activities (Morlock and Schneider, 1998). Dolan and team members have used a smart but complex model of combination of the EMG and the dynamic chain model while lifting of weight. Again the limitations of these techniques are the same as the ones described above.

Rohlmann and his team, in 1997 and 2000, made a significant contribution in achieving the objective of obtaining the real time *in vivo* data of the spine loading but they have used the internal fixator devices which have limitations of the parallel load sharing with the spine as discussed before (Rohlmann et al., 1997) (Rohlmann et al., 2000).

Ledet and his team, in 2000 and 2005, have perfectly measured the real time load on the lumbar spine. The location of the sensor/implant and the design of the load cell were excellent in serving the required purpose. They did experiments on a baboon (Ledet et al., 2000) (Ledet et al., 2005). The baboon's body posture and the structure are different from the human and the muscular structure is also different, specifically the hip extensors and the gluteal are more powerful in the human than the baboon (Farfan, 1995). Therefore, these data can be used as near estimates to the human.

In 2007 Linders and Nuckley used the strain on a vertebral surface to measure the loading on the spinal disc. To measure the strain on the vertebral surface they have installed rosette strain gauges on the vertebral surface. For this experiment they have used L4-L5 vertebrae of a macaque monkey model (Linders and Nuckley, 2007). The limitations of this work are:

- ✱ Vertebrae is not made up of homogeneous mechanical characteristic material like steel or any metal, so, the strain is not uniform across the vertebrae's outer surface.

- ★ Due to improper and lasting adhesion between contact surfaces of the strain gauge and vertebrae the validity of the strain measurement by strain gauges is always questionable.
- ★ It is done on a macaque monkey model, so, it is not biomechanically the same as a human.

Rohlmann and his team in 2008 have used a vertebral body replacement (VBR) as an inter-body load-cell to measure the *in vivo* loading in the spine. This is a very good experiment however it has a limitation. The main limitation is that the implanted vertebral body replacement (VBR) is surrounded by bone material from the iliac crest and the respective rib. After osseous healing process this becomes as strong as the vertebrae itself and hence, the load on the spine is shared between telemeterized VBR and fusion bone. So, as discussed before this approach will still not provide the accurate measurement of *in vivo* loading on the spine (Rohlmann et al., 2008).

In 2009, Demetropoulos and others have used the inter-body fusion cage as an inter-body load-cell to measure the *in vivo* loading on the lumbar spine. The technique is good for measuring the correct *in vivo* loading on the spine. They have installed the strain gauges on four load bearing pillars of the cage, so, whatever load comes to the inter-body fusion cage is transmitted further by those four pillars. This technique has a main limitation that the load is shared between the cage and the surrounding solid osseous fusion material between the two vertebrae, and hence, cannot actually measure the correct *in vivo* loading on the spine. Moreover, this is the only design they have still not used. The device based on this design has never been used as a load-cell to measure actual *in vivo* loading on the human spine (Demetropoulos et al., 2009).

### 5.3 CONCLUSION

---

The results from all attempts to measure the *in vivo* spinal loading from the above researchers have shown a lot of variation in values. Some contradicting results create even more uncertainty on the subject. For example;

- ★ Waugh measured the range of load on the disc as % of body weight and found it to be 20 to 99 where Nachemson measured the same and found it to be 29 to 386 and later on Nachemson & Elfstrom measured it and found it to be 97 to 369 (Waugh, 1966) (Nachemson, 1966) (Nachemson and Elfstrom, 1970).
- ★ Schultz and others have measured spinal load while lifting a weight of 8 Kg and found it to be 343% of the body weight (70 Kg subject) where Leskinen and others measured spinal load during lifting of 15 Kg weight and found it to be 1145% of body weight with again a 70 Kg subject. Finally Dolan in 1998 performed a similar experiment while using a 15.7 Kg weight for lifting and found the spinal load to be 364-656 % of body weight with a 70 Kg subject (Schultz et al., 1982b) (Leskinen et al., 1983) (Dolan and Adams, 1998).
- ★ Granhed and others have measured spinal load as much as 2741 to 5306 % of body weight with 70 Kg subject during very heavy lifting (maximum of 335 Kg) (Granhed et al., 1987).

Therefore, such results and techniques do not generate much confidence either in their accuracy or in their methodology for measuring *in vivo* spinal loading. Thus, there remains the need for a more reliable approach which will generate accurate *in vivo* spinal loading results and this will be the subject and the main focus of this research.

## 6 ARTIFICIAL SPINAL DISC PROSTHESIS

---

### 6.1 INTRODUCTION

---

In chapter 5, it was mentioned that there are mainly three surgical procedures for disc degenerated disease (DDD). They are as under,

- ★ Decompression of disc by removing part of the spinal vertebrae like neural-foramina
- ★ Fusion of vertebrae
- ★ Total disc replacement (TDR) or Nucleus replacement

In Total Disc Replacement surgery, the original disc is removed and replaced by an artificial disc prosthesis. The total disc replacement allows physio-motion (backpain-guide.com, 2011) between the two adjacent vertebrae unlike fusion. Moreover, it also provides shock-absorbing capability to the spine unlike fusion. This chapter describes the evolution of the artificial spinal disc prosthesis and describes the current commercial state of the art artificial discs.

### 6.2 HISTORY AND EVOLUTION OF THE SPINAL DISC PROSTHESIS

---

The spinal disc prosthesis is divided into,

- ★ All metal disc
- ★ All non-metallic disc
- ★ Combination of metal and non-metal disc
- ★ Artificial joint capsule
- ★ Nucleus replacement

#### 6.2.1 All Metal Disc

---

The first obvious choice of material for making an artificial spinal disc are metals like steel, titanium, Cobalt-Chromium-Molybdenum (Co-Cr-Mo) alloys, etc. The principle reason for the choice is its proven biocompatibility

and superior strength to withstand high compressive loading. The artificial spinal disc prosthesis was first implanted in the 1950s'. As shown in Figure 6-1, only a single metallic ball was used as the spinal disc prosthesis and it was developed by Fernström (Fernström, 1966). In 1954, Knowles filed a patent for an all metal disc prosthesis (Knowles, 4th May, 1954). The metal disc spacer is wedge shaped and was designed to be placed between spinous processes. This disc did not provide a physio-motion between the spinal vertebrae and that's why it was not considered as successful spinal disc prosthesis.



Figure 6-1: One of the first artificial disc replacements (simple metal ball) designed by Fernström (Burton Report , 2010)

On the other hand, Fernström's metal ball can provide sagittal and posterior movement like today's ball-joint type artificial spinal disc. The failure of this design is due to the subsidence over the ball. The reason for subsidence is the concentration of compressive load at the point of contact between the ball and the vertebrae end-plates. The shear forces between ball and a vertebra also contribute to the cause of the failure. In about 88% of the cases the restored height is lost within 4 to 7 years (Fernström, 1966). In 1950s', Nachemson placed silicon rubber into the cadaveric spinal disc. From 1973, almost every year a new patent filing on spinal disc prosthesis occurred (Szpalski et al., 2002). Fassio and Ginestie's designed an artificial spinal disc which was the first to be implanted in 3 patients. The nucleus part of the disc was made up of a silastic ball and constrained by a horse-shoe designed non-compressible plate. In 4 years all 3 patients exhibited migration of the disc (Fassio and Ginestie, 1978). As shown in Figure 6-2, Kostuik designed a disc prosthesis that had a hinge on the posterior part



and a spring was placed between the two endplates to absorb the shock. This disc prosthesis exhibited good results in laboratory testing but failed in animal trials (Kotsuik, 1997).

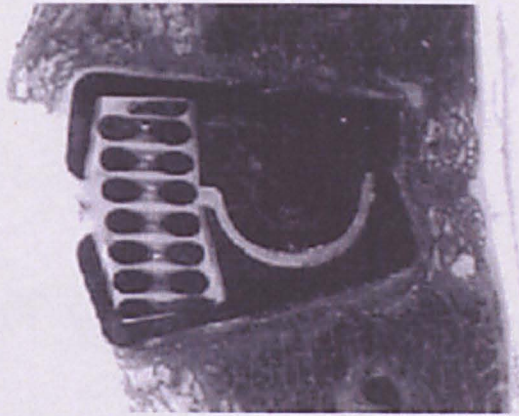


Figure 6-2: One of the early designed artificial spinal discs with two metal end-plates hinged posteriorly and interposed with metal spring in between (Kotsuik, 1997).

In 1982, Patil developed a disc with two cup shape end-plates and in between stainless springs of 12 lb load bearing capacity. The plates anchored by spikes on the outer surface of the vertebrae (Patil, 12th January, 1982).

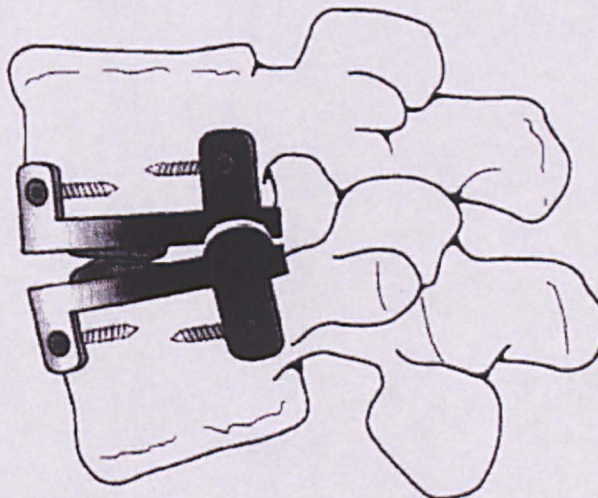


Figure 6-3: Artificial spinal disc designed by Hedman and colleagues (Hedman et al., 1991).

As shown in Figure 6-3, Hedman and his team developed posteriorly hinged end plates with coil springs in between. This facilitates flexion and extension of the body (Hedman et al., 1991).

Mathews and his team used Cobalt-Chromium (Co-Cr) alloys for the end-plates. The disc is known as the Maverick®. The central fins were used for proper anchoring of the disc. The bottom plate had concave inside surface in the centre which was matched by the same concave inside surface on the upper plate (Bono and Garfin, 2004). Gill and associates have developed an all stainless steel disc known as the Prestige®. For stability after surgery, screws were provided to fix with the vertebrae body. This disc exhibited good results in preliminary trials in 20 patients (Cummins et al., 1998).

### **6.2.2 All non-metallic disc**

---

The landmark development in disc design is the introduction of synthetic-on-synthetic articulating surfaces. The advantage of this design is the natural like visco-elastic behaviour of the disc.

In 1956, Van Steenbrugghe designed a disc with many components. It was made-up of intermediate cushions in layers with plastic bodies of varying shapes (Van Steenbrugghe, 28th May, 1956). In 1975, Stubstad and associates developed a disc with kidney shape silicone or polyurethane elastomer and elastomeric end plates. The nucleus of the disc was made-up of fluid contained within weave of Dacron® fibres (Stubstad et al., 25 February, 1975). Downey developed a disc with rigid silicone end plates where the nucleus consisted of soft polymeric foam. For immediate stability the disc was provided with screws (Downey, 17 October, 1989) (Downey, 30 July, 1991).

In 1978, Weber developed a modern like 3-piece disc comprising two end plates with concave cavities and a bio-ceramic spacer (Weber, 6 February, 1978) (Weber, 21 June, 1980).

Many different non-metallic disc designs were developed and most of them are described by;

- ★ Edeland (Edeland, 1989)
- ★ Fischers (Fischer, 8 December, 1987).
- ★ Tadano and associates (Tadano et al., 1992).
- ★ Dove and his team (Dove et al., 27 February, 1990).
- ★ Monson (Monson, 5 September, 1989)



One of the non-metallic discs was developed by Stone in 1992. The uniqueness of this design is its design to regenerate the disc. Regeneration of the disc is achieved by biocompatible and bio-resorbable fibre (glycosaminoglycans) scaffold. The dry, porous volume matrix is made by using the scaffold. This type of disc has not yet been tried on humans (Stone, 28 April, 1992). In a latest development, the Cadisc<sup>TM</sup> developed by Ranier Technologies (Cambridge, UK), is an all polymer disc with the advantage of MRI compatibility. It means the patients can be scanned under MRI.

### 6.2.3 Combination of metal and non-metal discs

---

This contemporary disc is made up of two metal end plates with a non-metallic spacer in between. It is a ball-joint type of design. This design has the advantage of the high compressive strength of metal (the end plates) and the visco-elastic biomechanical characteristic of the non-metallic materials like rubber, polyethylene, polyurethane, etc. The main limitation of this design is the adverse effect of wear debris of the polyethylene material generated due to friction between the end plates and the polyethylene spacer. As shown in Figure 6-4, Lee and colleagues have developed an elastomeric disc spacer with hydroxyapatite coated surfaces to encourage in-growth. It gave good *in vitro* results but the core migrated with canine implantation (5 of 12 cases). No human trials have been done until today (Langrana et al., 1994) (Vuono-Hawkins et al., 1994).

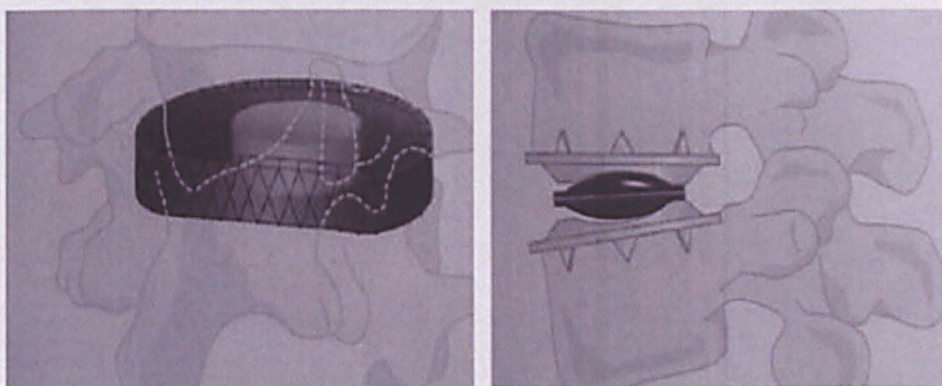


Figure 6-4: Artificial disc designed by Lee and Langrana (L) and SB CHARITÉ® III artificial spinal disc prosthesis (R) both cited in (Bono and Garfin, 2004)



Enker and colleagues in 1993 published the results of experiments when using a disc called Acroflex® (DePuy Spine). The disc is made up of two porous coated titanium end plates. The rubber spacer is placed between the end plates and vulcanised to the inner surfaces of end-plates. The implant was suddenly discontinued because benzene was being used by the vulcanising process. Benzene is probably responsible for carcinogenicity (Enker et al., 1993).

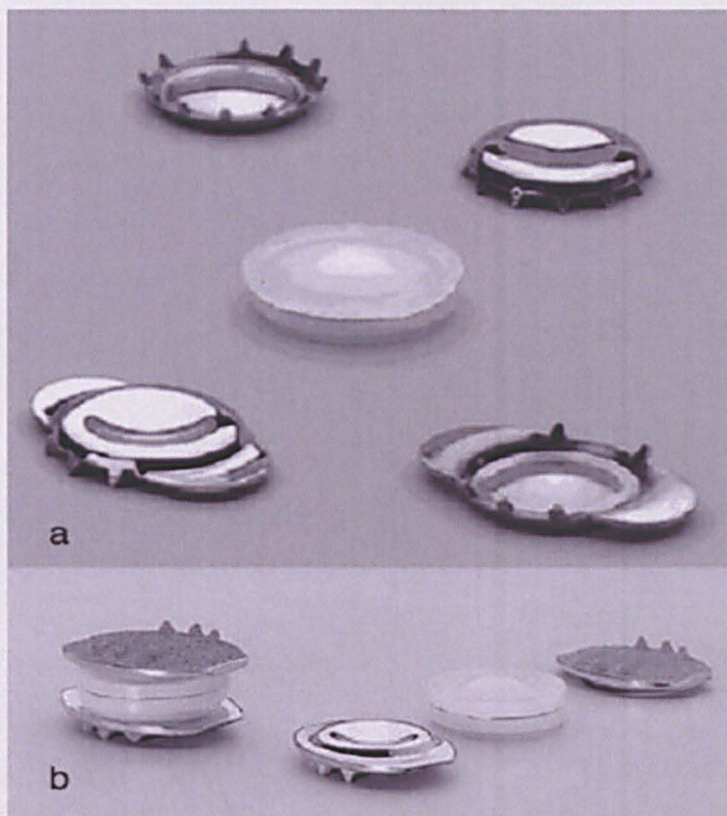


Figure 6-5: (a) Parts of SB CHARITÉ® I artificial spinal disc by (b) SB CHARITÉ® II disc with its parts. Both discs were by DePuy Spine, Raynham, MA. Cited in (Bono and Garfin, 2004).

In 1980s, the SB CHARITÉ® disc was developed by DePuy Spine, Raynham, MA. It was designed by Shellnack and Buttler-Janz. They have used sliding core of UHMWPE (Ultra High Molecular Weight Poly-Ethylene). With this design, its instantaneous axis of rotation could translate anterior and posterior to the mid-point of the disc during the extension and flexion, respectively. The first introduced disc called SB CHARITÉ® I had shell like plates having a diameter smaller than the polyethylene core (Figure 6-5).

Due to that higher concentration of compressive force migration of the disc occurred after implantation. In a revised design of the disc, called SB CHARITÉ® II, which produced a flat extension on the left and right side of the disc stopped the problem of significant migration of the disc but caused fatigue fracture of the end plates resulting in failure of the disc. In 1987, the SB CHARITÉ® III disc was introduced with broadened flat end plates to reduce the subsidence of the disc. To reduce the polyethylene wear, the end plates were made up of Cobalt-Chromium-Molybdenum alloy. To enhance the process of osseous integration the end plates were coated with porous titanium and a layer of calcium phosphate was applied on it.

The Prodisc® disc was designed by Marnay in the late 1980s. This disc has a polyethylene core fixed to the inferior plate and the articulating surface is on the superior plate only enabling a fix axis of rotation. Due to the fix axis of rotation the facet joints experienced abnormally high force in their direction which lead to dimensional changes in neuro-foramina during motion.

Many different combinations of metallic and non-metallic disc designs developed and few examples are as under,

- ★ Pisharodi (Pisharodi, 23 June, 1992)
- ★ Frey and Koch (Frey and Koch, 17 April, 1990) (Frey, 12 June, 1990) (Frey, 11 September, 1990).
- ★ Oka and associates (Oka et al., 24 May, 1994).
- ★ Hirayama and colleagues (Hirayama et al., 7 August, 1990).
- ★ Khvisyak and colleagues (Khvisyuk et al., 7 January, 1982.).
- ★ Main and his team (Main et al., 12 june, 1990).
- ★ Fuhrmann and associates (Fuhrmann et al., 26 March, 1991).

#### **6.2.4 Artificial joint capsule**

---

The metal end plates and the polyethylene spacer design generated a lot of wear debris of polyethylene. To overcome this limitation a new disc was designed, called artificial joint capsule. In this design, a flexible rubber membrane spanned between the two end plates sealed the articulating surfaces from surrounding tissues. The saline fluid was filled inside the membrane which served as a lubricant. That reduced the amount of the

wear of polyethylene debris significantly. This was also used to reconstruct the cervical spine after anterior disectomy for myelopathy (Sekhon, 2003).

### **6.2.5 Nucleus replacement**

---

The principle difference between nucleus replacement and total disc replacement is that total disc replacement replaces the whole disc including the end plates whereas nucleus replacement does not include end plate replacement. The main concern is which procedure to apply to the patient. If the patient has end plate defects and/or high Body Mass Index (30 or over) and/or high disc collapse (residual height less than 5 mm), then nucleus replacement is not advisable (Ray, 2002).

Ray designed many related prosthetic disc-nucleus (PDN) (Ray, 2002). The toughest problem in the case of PDN is to position it properly and strongly in the annular disc. The core made up of hydrophobic gel is contained by a cover of polyethylene mesh like fabric. The hydrophobic gel absorbs the water and expands but it is constrained by the polyethylene mesh to prevent overexpansion. One of the major advantages of PDN over total disc replacement is the ease in the surgical approach. PDN can be very easy to operate due to the posterior approach laminotomy and standard disectomy. It has shown good clinical results after 1-year follow-up (Bertagnoli and Schonmayr, 2002), however some migration of the disc was reported. Therefore, the surgical approach was changed from posterior to lateral. In another design of PDN, a coiled spiral implant was designed (Korge et al., 2002). In 1975, Stubstad and colleagues has patented a helicoid disc implant, however this design was never used in humans (Stubstad et al., 25 February, 1975) (Urbaniak et al., 1973).

Many different nucleus replacement disc designs were developed and many are described in the following sources,

- ★ Kuntz (Kuntz, 21 september, 1982).
- ★ Fernström (Fernström, 1964) (Fernström, 1965) (Fernström, 1966).
- ★ Ashida and associates (Ashida et al., 1990)
- ★ Bao and Higham (Bao and Higham, 10 September, 1991) (Bao and Higham, 9 March, 1993).
- ★ Schneider and Oyen (Schneider and Oyen, 1974a) (Schneider and Oyen, 1974b).



- ✿ Hou (Hou, 1994).
- ✿ Roy Camille and associates (Roy-Camille et al., 1978)
- ✿ Reitz-Joubert (Reitz and Joubert, 1964).
- ✿ Froning (Froning, 8 April, 1975).
- ✿ Ray and Corbin (Ray and Corbin, 20 September, 1988).

### 6.3 ARTIFICIAL SPINAL DISC MARKET TODAY

---

In 2008, the global spinal implant market was valued at around £6 bn, which includes all types of spinal surgery from the minimally invasive to disc replacement. This market is predicted to rise because of the growth in the aging population, and the increasing preference of surgeons to carry out invasive surgery for back problems. Non-fusion technologies have emerged as the most significant factor driving growth in the spinal implant market.

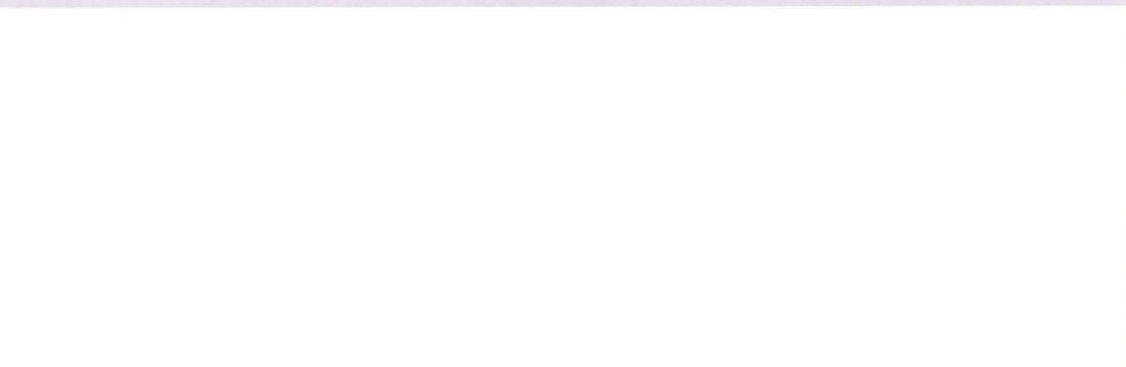


Figure 6-6: Integra - eDisc (L) (Slack Inc.-Orthosupersite, 2008) and Stryker Spine - Flexicore® spinal disc (R) (Murtagh et al., 2010).

Today, there are five main companies focussing on releasing clinical data that demonstrate the efficacy and economic benefits of spinal non-fusion surgery. Most notably, no comprehensive data exists which predicts what happens when they fail. Additionally, compared with conventional approaches, health authorities and insurers are still sceptical of the cost and risk of the replacement surgery. Five companies have dominated the spinal implant market, which equals around 78% of the market (Table 6-1). They are Zimmer Spine (Figure 6-9), Stryker Spine (Figure 6-6), DePuy Spine (Johnson and Johnson, Figure 6-10), Synthes Spine and Medtronic Spinal. Medtronic is the market leader with over 40% market share. It acquired Kyphon in 2007 to improve its market position. DePuy held a 16% share of



the market in 2007, followed by Synthes on 13% and Stryker on 9% (Figure 6-6, 6-10 and 6-11). Zimmer signalled its intentions, in 2008, with the acquisition of Abbott Spine, giving the company a 6% share of the market. The major spinal manufacturers have all seen their positions in the market decline in recent years, as numerous new companies enter the spinal market with proprietary technology aimed at improving current surgical approaches.



Figure 6-7: Medtronic-Prestige® spinal disc with lateral flexion and extension radiographs after implantation. (Boulder neurosurgical associates, 2010).



Figure 6-8: Medtronic - Bryan® spinal disc (R) (Medtronic Inc., 2010).

Table 6-1: Spinal market competitors by market share in 2009

Company	Medtronic	Synthes	J&J	Stryker	Nuvasive	Zimmer	Other
Market share	39%	14%	14%	9%	4%	4%	16%





Figure 6-9: Zimmer Spine - Dynardi® artificial spinal disc (Zimmer Inc., 2010) (Neurocirugia Contemporanea, 2010).

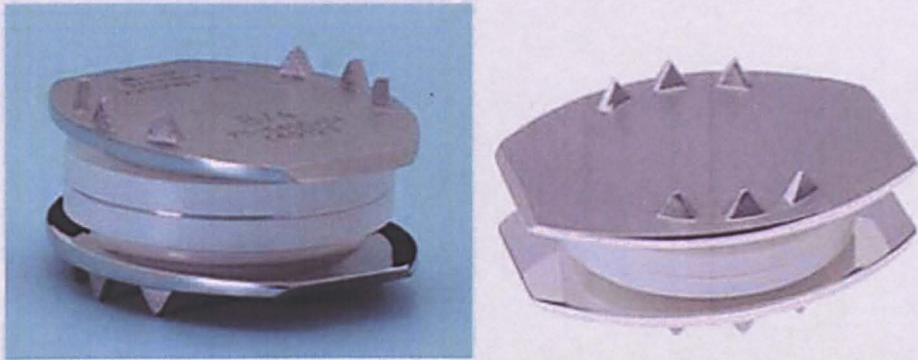


Figure 6-10: DePuy Spine (Johnson and Johnson) - SB CHARITÉ® Artificial spinal disc (Neurocirugia inc., 2010) (Microspine inc., 2010)

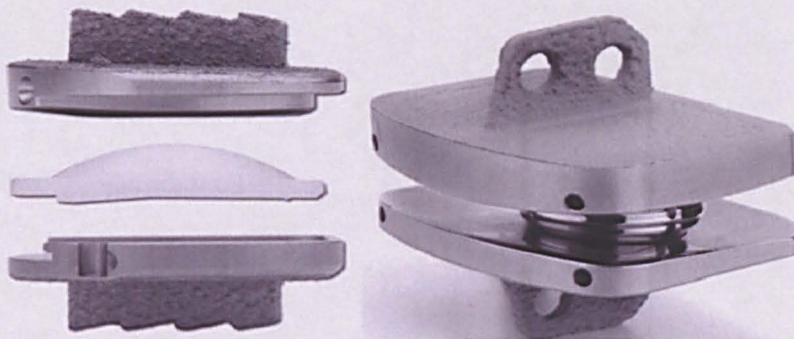


Figure 6-11: Synthase spine - Prodisc II (L), Medtronic - Maveric (Murtagh et al., 2010).

Companies including SpinalMotion and NuVasive (Figure 6-12) are mounting challenges to the big five companies with alternatives to the non-fusion devices. These two companies have developed alternative artificial discs for orthopaedic surgeons, such as SpinalMotion's Kineflex and Kineflex-C as well as Cervitech/NuVasive's PCM. NuVasive's innovation PCM and NeoDisc were both reported entering into clinical trials in 2009. The new entry aims



to target the market share of several current products including Medtronic's Prestige and Bryan XL-TDRs as well as Synthes, Inc.'s ProDisc - TDR.

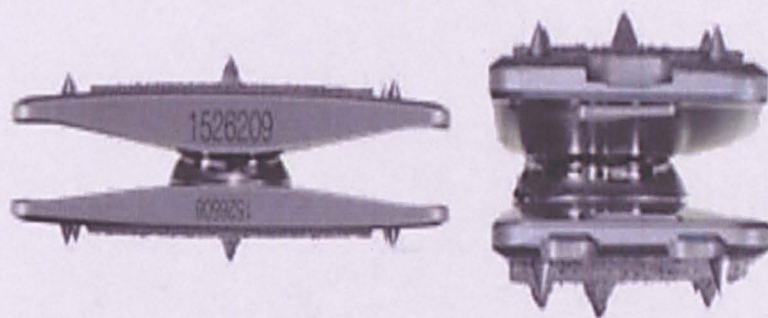


Figure 6-12: NuVasive XL-TDR (Nuvasive inc., 2010).



Figure 6-13: B.Braun Spine disc - Active-L spinal disc prosthesis (Top Left), Superior end-plate (Top Right), Inferior end-plate with UHMWPE inlay material (Bottom Left) and Outer side of end-plates with anchor studs and porous titanium & Calcium phosphate layer for enhancing osseous induction process (Bottom Right). (B.Braun Inc., 2010)

The multinational company B.Braun also acquired Aesculap Spine Company and its product Active-L lumbar spinal disc (Figure 6-13) is very well placed in Europe. Integra Spine (Figure 6-6) is a leading manufacturer of spinal disc implants, currently aiming to commercialise an implantable disc with sensors by 2013. There are around 90 spine bioengineering companies worldwide summarised in Table 6-2.

Table 6-2: The rest of spine technology companies (worldwide)

Abbott Spine	Technologies	Signus Medical
Acuña y Fombona	Interbody Innovations	Sintea Biotech
Aesculap Implant Systems	ITEM Implant	Soelim International
Allez Spine	Japan Medical Materials	Solco Biomedical
AlloSource	Jemo Spine	Specialty Spine Products
Alphatec Spine	K2M	Spinal Edge
Altiva	Kiscomedica	Spinal Elements
Amedica	Lafitt	Spinal USA
ASpine USA	Lanx	SpineArt
Atlas Spine	LDR Spine	SpineSmith
Australian Surgical Innovations	LifeLink Foundation	SpineVision
AustSpine	LifeNet Health	Spine Wave
Axiomed Spine	Life Spine	SpineWorks
Biomet Spine	MBA Grupo	Surgi C
Choice Spine	MEDICREA	Surgical House
Custom Spine	Mizuho Medical	Surgicraft
Device Technologies Australia	Musculoskeletal Transplant Foundation	SURGIVAL
Dieter Marquardt Medizintechnik	NeuroMax	Theken Spine
Eden Spine	NuVasive	Titan Spine
Elite Surgical Supplies	Ortho Development	TranS1
Encore Medical	Orthofix Spinal Implants	ulrich medical
ESM Technologies	OrthoTec	US Spine
Eurosurgical	permedica	Vertebration
Flexuspine	Peter Brehm	VERTEBRON
Getz Bros. & Co.	PINA MedizintechnikVertriebs	X-spine Systems
Global Orthopaedic Technology	Pioneer Surgical Technology	YufuItonag
Globus Medical	Quadrant Medical	
GS Medical	Regeneration Technologies Inc. Biologics	
Inland Spine	Scient'x	
Innovasis	SeaSpine	
Innovative Spinal	Shinwoo Medical	

# 7 INVESTIGATION OF SENSING MODALITIES

---

## 7.1 INTRODUCTION

---

The main objective of this research is to develop an intelligent artificial spinal disc for measuring the loading/stresses on the lumbar disc; hence, the selection of an appropriate sensing modality (sensors) which can correctly measure the force on the lumbar disc is critical. The force is defined as:

“An action that will cause acceleration or a certain reaction of a body and is a vector quantity” (Elbestawi, 1999).

Many different approaches to measure forces are possible but there are some limiting factors in selecting applicable sensing modalities. The limiting factors in selecting the sensor are compactness, reliability, accuracy, biocompatibility, robustness, and suitability for appropriate signal conditioning electronic circuitry with ultralow power consumption. Due to the recent developments in sensors, electronics, circuits, material science, there are many sensing modalities that can be explored for this application.

The fundamental of the force measurement depends on the physical behaviour of the body subjected to external forces. So, mechanical behaviour of the body/material is crucial for force measurement. The relation between stress and strain is defined by Hooke’s law and that is fundamental for force measurement for the body in static equilibrium and in elastic region (Elbestawi, 1999). The measurement of the force regime more or less overlaps or directly connected by the other regimes of measurement of other measurands like pressure, strain, displacement, load and even acceleration. According to Newton’s fundamental law, the force is equal to the multiplication of the mass ( $m$ ) of the body and the acceleration ( $a$ ) of the same body due to that force ( $F = m \times a$ ). Hence, the force ( $F$ ) causes the change in bending moments of the body.

The force can be measured by different principles and they are as under,

- ★ By comparing the unknown force with the known reference force when the body is in equilibrium (according to Newton's Law).
- ★ By measuring the pressure on the known area of the surface.
- ★ By measuring the acceleration of the known mass.
- ★ By measuring the displacement between the known objects.
- ★ By measuring various electrical, magnetic, optical quantities which changes due to the applied forces like resistance, capacitance, magnetic field, luminance, etc.  
(Brodgesell et al., 2003).

## 7.2 SENSING MODALITIES

---

Having the above in mind, different sensing modalities have been reviewed for consideration in this research. A description of these modalities is the subject of this section.

### 7.2.1 Piezoelectric: Sensing Modality

---

When the piezoelectric material is subjected to a force, it deforms asymmetrically and develops an electric potential across the material. This phenomenon is known as the piezoelectric effect (Gautschi, 2002). This reversible phenomenon means that when an electrical potential is applied across the piezoelectric material it deforms. Hence, the piezoelectric effect can be of two forms, one is a direct effect and the other is a converse effect (reversible phenomenon). Due to its typical characteristics, the piezoelectric material is also known as the electro-restrictive material (Gautschi, 2002) (Elbestawi, 1999).

The magnitude and polarity of induced charge are proportional to the applied force to the piezoelectric material.

$$Q = d \times F \dots\dots\dots(1)$$

Where, Q = Electric Charge induced (Coulomb)

F = Applied force (Newton)

d = Charge sensitivity (constant for particular material)



The force causes variation in thickness of material,  $\Delta T$  meters,

$$F = \frac{AY}{T} \cdot \Delta T \dots \dots \dots (2)$$

Where, A = Area of material

T = Thickness of the material

Y = Young's modulus

Voltage developed across material is,

$$V = \frac{Q}{C} \dots \dots \dots (3)$$

Where, C = Capacitance (Farad),

$$= (\epsilon \cdot A) / T$$

$\epsilon$  = Absolute permittivity of the material

Hence,

From equation...(1) and equation...(3),

$$V = \frac{dF}{\epsilon A / T}$$

The voltage sensitivity =  $E = d / \epsilon$ , in Volt.m/N,

$$V = E \cdot (T/A) \cdot F$$

$$V = E \cdot T \cdot P, \dots \dots \dots (4)$$

Where, E = Voltage sensitivity (Volt.m/N)

T = Thickness (m)

P = Pressure (N/m<sup>2</sup>)

(Elbestawi, 1999).

The applications of the piezoelectric effect can be classified as in Figure 7-1.

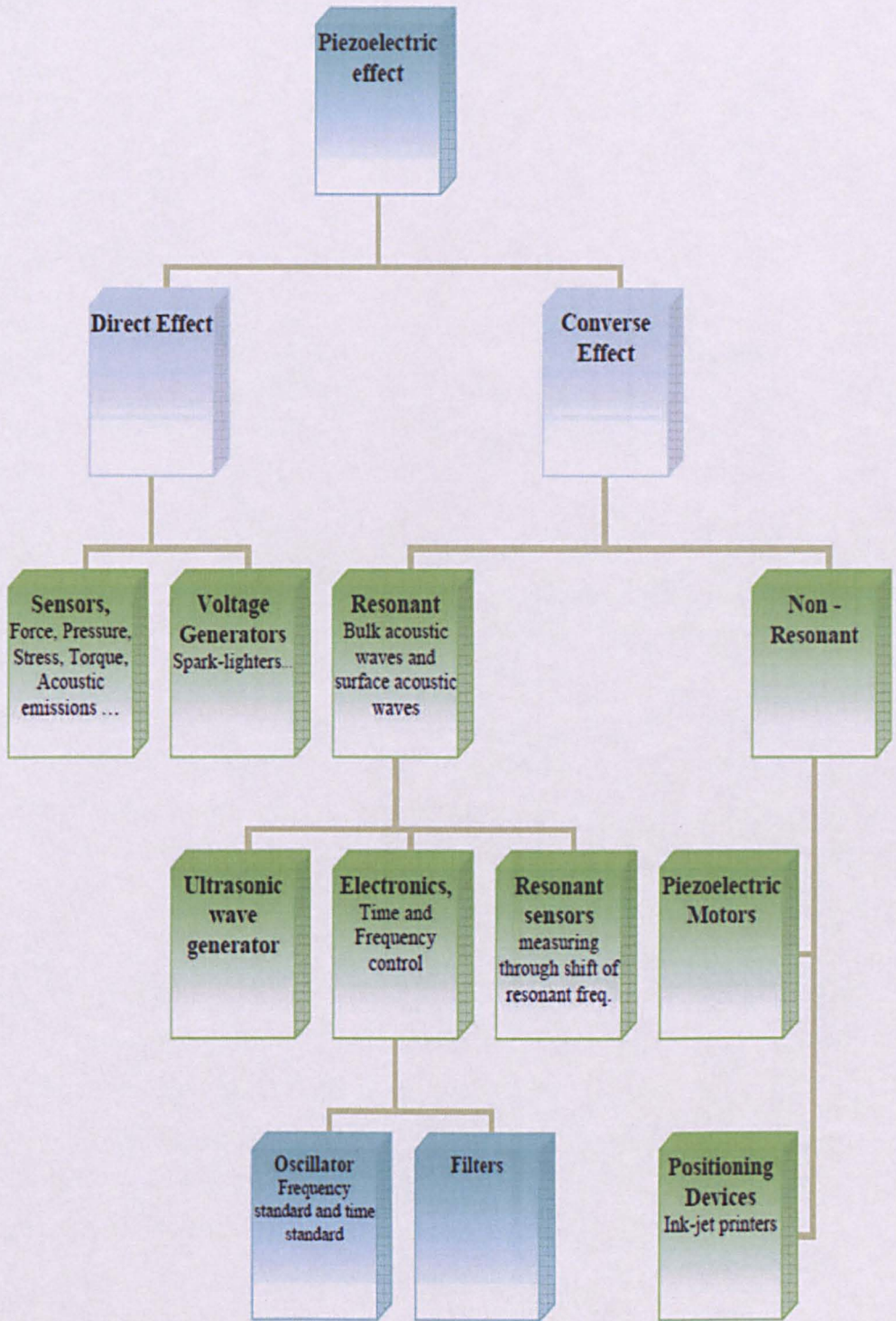


Figure 7-1: Applications of Piezoelectric effect: Categorized on basis of Direct Effect or Converse Effect (Gautschi, 2002).

## Piezoelectric Materials

The important piezoelectric materials are:

- ★ **Quartz:** This is the most common type of piezoelectric material. It's chemical formula is  $\text{SiO}_2$ . In this type, the other common quartz materials are  $\alpha$ -quartz,  $\beta$ -quartz and synthetic quartz (Gautschi, 2002), (Arnau, 2004).
- ★ **Tourmaline:** It is an aluminum borosilicate material. It has high mechanical strength and possesses good resistance against acid and alkali. It is proprietarily used by the AVL Company (Gautschi, 2002).
- ★ **Gallium Orthophosphate:** This material has high temperature stability and that's why it is used in high temperature application (Gautschi, 2002).
- ★ **Crystals of Ca-Ga-Ge Group:** It is synthesized crystals with compound  $\text{Ca}_3\text{Ga}_2\text{Ge}_4\text{O}_{14}$ . It has high electromechanical coupling and used mainly for frequency control applications it is more resistive than quartz (Gautschi, 2002).
- ★ **Lithium Tetra Borate:** its chemical formula is  $\text{Li}_2\text{B}_4\text{O}_7$ . High piezoelectric co-efficient  $d_{33}$  and high electromechanical coupling of lithium tetra borate makes it very attractive for surface wave acoustic application (SAW). This seems one of the very promising modalities required to be explored for this application (Gautschi, 2002), (Arnau, 2004).
- ★ **Piezoelectric Ceramics (PZT):** It is also, very promising material for this application as a sensor. When electric potential applied to piezo-ceramics, it generates an elastic strain. The relationship between strain and applied electric potential is normally linear, but in some material like PMN (lead manganese niobate) the relationship is non-linear. This can be used as a force sensor but its most popular use is as a force actuators and oscillators in electronic watches and tuning devices. It may be possible to use it after some modifications as a sensor for this application but such an approach will require a significant contribution in the development of a new material which is beyond the scope of this research. Moreover, it has limited life and stability. It is sensitive to temperature as well. It has lower resistivity hence; it is less likely to be used for the quasi-static measurement.

In total this is avoided for further exploration in this research (Gautschi, 2002).

- ★ **Piezoresistive Thin Film:** This modality is very useful in this research application. This sensor is made-up of semiconducting material, usually carbon. When it is subjected to force the distance between carbon particles are changed and that changes the overall resistance of the sensor. Hence, when load/force is applied to Piezoresistive sensors, the resistance or conductance changes accordingly (Elbestawi, 1999). The positive part of this sensing modality is its thin film type structure and its load Vs conductance relationship which is linear. Moreover, it consumes very low power. The Piezoresistive sensor measures force not strain as in the strain gauge and due to that force the resistance/conductance of the sensor is proportional to the applied load to the sensor (Gautschi, 2002).

In total, piezoelectric materials look very promising modalities for this research because they are active sensors. As mentioned before, the piezoelectric material's output decays with time on application of the compressive load. That's why it cannot be used to measure the static forces. Hence, it will not be selected for further exploration in this research project except from the piezoresistive thin film. Moreover, it needs to be calibrated often which is next to impossible for this application. Moreover, it is mainly useful in dynamic applications. It is also, not useful in continuous loading condition, as in this application the disc is always in loading condition at any point of time. However, there is lot of research in this material for force sensing applications. The magneto restrictive material is more useful in actuators rather than sensors. The shape memory material like PLZT (Lanthanum-doped lead zirconatetitanate) is looking very promising because it can be activated by an electric charge instead of heat. But still it is in its primary phase of development for being used as a sensor in this application. The amorphous iron alloys also known as metallic glasses is very interesting material for this application (Fletcher, 1996).

### 7.2.2 Rare Earth Permanent Magnets:

---

The newly discovered rare earth permanent magnetic material like NdFeB can also be used as a force sensor but it is mainly used as an actuator. The

magnetic actuators made from this material can generate forces as high as 2712 Joules over a 0.6096 m stroke (Fletcher 1996). In this research the requirement is just opposite to it as the loading range 0 – 4 kN is what is needed to be measured instead of generating high force from a small input change.

### 7.2.3 Capacitive Sensor

---

This is one of the most promising sensing modalities for this research application. It has high accuracy, precision, low drift, compactness, repeatability, stability, ruggedness. It also, with proper design and fabrication, has negligible effect of temperature and humidity. One of the main advantages is that it has very good resistance against mechanical misalignment and it also possesses good shielding ability against stray electric fields. Due to these reasons it is very popular in instrumentation industries, after strain gauges, in measuring pressure. In this application, it is very much possible to develop the whole measurement system with the requirement of ultralow power signal conditioning circuitry (Elbestawi, 1999), (Liptak, 2003).

The capacitive sensor measures the capacitance between conductors in a dielectric environment. For excellent performance of the sensor, the diaphragm material of the sensor should be elastic for a designated force range. The commonly available materials are steel, inconel, Ni-span C, quartz, silicon, etc (Liptak, 2003).

The capacitive sensor works on Coulombs Law,

$$F = (Q1.Q2) / (4.\pi.\epsilon_0.r^2)$$

Where,

F = electrostatic force between two charges (N)

Q1 and Q2 = Electrical Charges of two conductors (C)

r = Distance between two conductors (m)

$\epsilon_0$  = Permittivity of free space ( $F.m^{-1}$ )

$\pi$  = Const. = 3.1412

The capacitance between two parallel plates is (as shown in Figure 7-2),



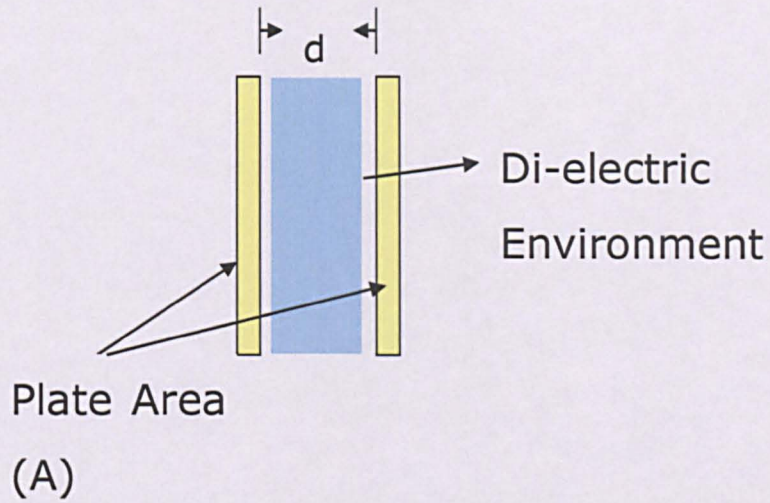


Figure 7-2: Working schematic of the capacitor with important parameters like  $d$ ,  $A$  etc.

$$C = (\epsilon \times A)/d$$

Where,

$C$  = Capacitance between two parallel plates (F)

$A$  = Area of plates ( $\text{m}^2$ )

$d$  = Distance between two plates (m)

$\epsilon$  = Dielectric Constant ( $\text{F.m}^{-1}$ )

There are mainly two main designs of capacitive sensors. One is a single plate and other is a two/multiple plate design. In the single plate design, the force is applied to the diaphragm and that deflects the diaphragm. Hence, the capacitance is changed between the fixed plate and the diaphragm due to the change in the distance between them. The change in capacitance is converted to dc current in milli-ampere range or in dc voltage form (Liptak, 2003).

In this research, it is possible to use this approach but design it in somewhat different way. The proposal is that the change in capacitance is connected with a fix value inductor to make an LC circuit. Hence, the change in resonance frequency of the LC circuit indicates the applied pressure/force.



The two/multi plate design is operated in two different methods. In the first method, the change in capacitance between diaphragm and plate changes the capacitance in the other arm of the bridge circuit to balance the bridge. Hence, the null point indicates the applied pressure/force. In the second method, the applied pressure/force is the ratio of the output voltage to the supply voltage. The multiple plate design is used to avoid the effect of stray capacitance on the measurement (Liptak, 2003).

The capacitive Pressure sensor has accuracy in the range of  $\pm 0.1\%$  to  $\pm 0.2\%$  of the span. The range of the applied pressure can be as low as vacuum pressure and as high as 35 MPa (Liptak, 2003).

#### 7.2.4 Strain gauges

The strain gauge is a sensor which measures strain in an elastic region. Strain is defined as the amount of deformation due to the applied load. The strain gauge is made-up of a finite length of gauge wire placed in designed pattern like a flat coil as shown in Figure 7-3. This coil is then cemented or bonded between two insulating material sheets. The gauge wire is of resistance such as 120  $\Omega$ , 300 $\Omega$ , 1000  $\Omega$  etc. Due to the strain the cross sectional area of the grid wire changes due to the change in length of the conductor, as shown in Figure7-4.

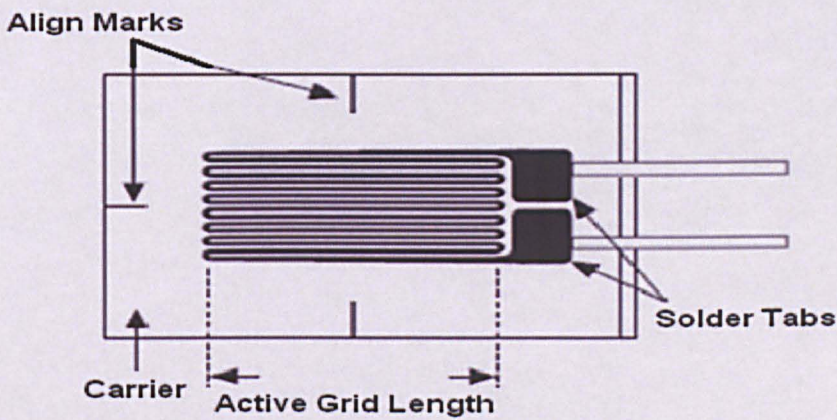


Figure 7-3: Detail schematic view of the strain gauge



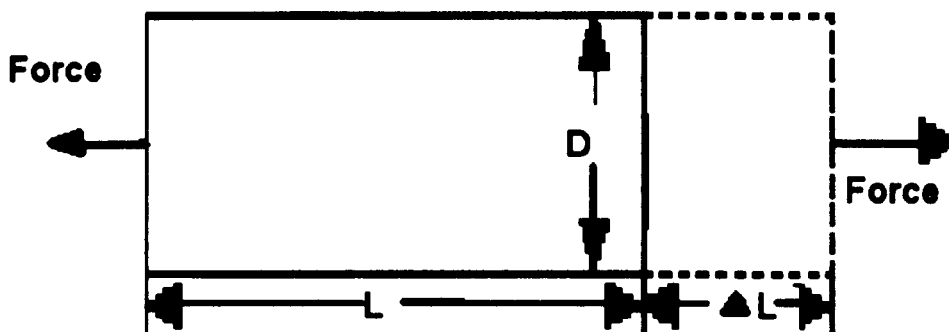


Figure 7-4: Schematics of the strain - equal to the change in length per original length due to the applied force,  $\delta = \Delta L/L$

Due to the compressive force, the length  $L$  is changed to  $L - \Delta L$  and due to tensile force the length is changed to  $L + \Delta L$ . Although dimensionless, the strain is sometimes expressed in units such as in/in or mm/mm. In practice, the magnitude of the measured strain is very small. Therefore, the strain is often expressed as micro strain ( $\mu \delta$ ), which is  $\delta \times 10^{-6}$ .

When a bar is strained with an uni-axial force, as in Figure 7-4, a phenomenon known as the Poisson Strain causes the girth of the bar,  $D$ , to contract in the transverse, or perpendicular, direction. The magnitude of this transverse contraction is a material property indicated by its Poisson's Ratio.

The Poisson's Ratio  $n$  of a material is defined as the negative ratio of the strain in the transverse direction (perpendicular to the force) to the strain in the axial direction (parallel to the force),

or

$$n = - e_T/e,$$

Where,  $e_T$  = Strain in transverse direction,  $e$  = Strain in axial direction

Poisson's Ratio ( $n$ ) for steel, for example, ranges from 0.25 to 0.3 (National Instruments Corporation, 2010).

Therefore, the total resistance of the grid wire changes i.e. strain gauge. This is most common, highly reliable and widely used method of measuring strain and hence loading/force. There are mainly two types of strain gauges available, one is made up of metal and other is made up of semiconductor

material. The semiconductor strain gauges are more sensitive than metal strain gauges but they are also very much sensitive to temperature.

The metallic strain gauges consist of metallic foil arranged in a grid pattern as shown in figure 7-3. This grid of metallic foil is bonded to thin backing material which is known as a carrier. This carrier is directly adhering to specimen whose strain is to be measured. Due to the applied load to the specimen, the strain develops on the specimen which transferred to the carrier and then to the grid of the strain gauge. The commonly used carrier materials are polyimide and resins like glass reinforced phenolic resin. For better accuracy the grid metal is selected to match the temperature response of the specimen material (National Instruments Corporation, 2010). Due to its ruggedness, reliability, precision and easy to develop ultralow power signal conditioning circuitry, it is selected for further exploration in this research. More details about the selected strain gauge are provided in chapter-8 (section 8.3.1).

#### 7.2.5 Optical sensors

This is a new and innovative way of accurately, without the significant effect of hysteresis and temperature, measuring the force/pressure. The simplified cross-sectional view of an optical sensor is shown in Figure 7-5.

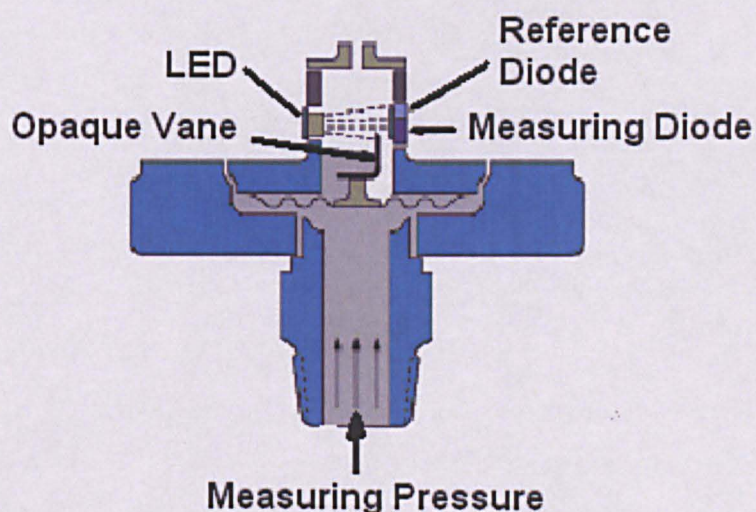


Figure 7-5: Detail schematic view of the design of the load cell using optical sensor

The measured pressure deflects the diaphragm; hence, the vane connected to the diaphragm deflects accordingly. Due to the movement of the vane it

blocks the light incident on the measuring diode. In this sensor, the light emitting diode (LED) is used as a source of light. On the other side the two diodes are located in a straight line as shown in the figure. One diode is a measuring diode and other is a reference diode. The reference diode is placed to eliminate the error due to the change in light energy incident on the diodes. The reference diode is fitted in such a way that light incident on this diode will never be blocked by the vane due to the diaphragm movement. The optical transducer is immune to temperature effects because the temperature affects both the diodes equally. Moreover, the optical transducer has  $\pm 0.1\%$  accuracy and has good response time as well. The pressure measurement range is 35 kPa to 413 MPa. Due to the very little deflection of the diaphragm it has very low hysteresis and good stability. When compared with the capacitive sensor and the strain gauge sensor, it is less mechanically stable, rugged and it requires frequent calibration. Overall measurement system require more space and power in comparison with capacitive and strain gauge sensor. For these reasons, it will not be considered in this research project.

#### **7.2.6 Surface Acoustic Wave (SAW) Sensors**

---

It is one of the most promising sensing modalities for further exploration in further development of this research project. This sensing modality detects the acoustic waves (mechanical wave), hence, it is named as surface acoustic wave sensor. When any acoustic wave propagates on the surface of the material, a little change in the material's surface due to any reason like loading, stress, strain etc., affects the velocity and/or amplitude of the wave. Hence, the measurements of velocity, frequency, phase, amplitude, indirectly become the measurement of corresponding physical quantities being measured.

Figure 7-6 shows a schematic diagram of the SAW sensor. When alternating signals with some frequency approach the input sensor it is converted to an acoustic wave which propagates on the sensor surface. The device also comprises of an IDT (Inter Digital Transducer) which converts acoustic wave to the electric signal by using the piezoelectric effect of the material. Due to the stresses, its amplitude and velocity changes and hence that represents the applied load or force to the sensor indirectly. The manufacturing process



of the sensor includes the common technology as used in the integrated silicon circuits. Almost all acoustic wave devices use piezoelectric materials for generating acoustic waves. Many piezoelectric materials discussed before in this chapter are used in making surface acoustic wave sensors. The selection of the material is dependent upon many criteria like temperature dependence, attenuation and propagation velocity and other required relevant mechanical characteristics. Typical SAW sensors operate from 25 to 500 MHz.

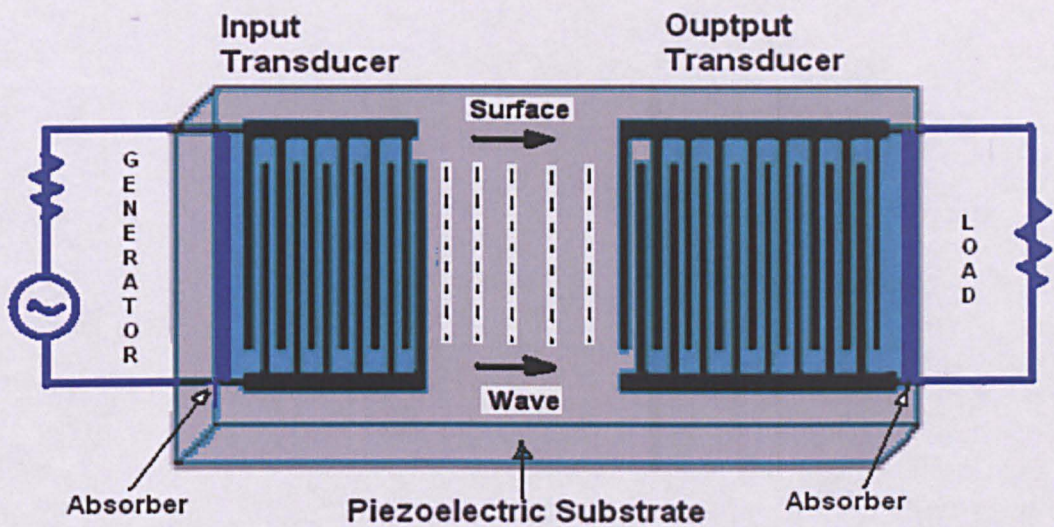


Figure 7-6: Surface Acoustic Wave Sensor-SAW Sensor-Schematic diagram explaining its working principle

A SAW pressure sensor weighs less than 1 gram and has a resolution of 0.73 PSI. One of the disadvantages of SAW sensor is its sensitivity to mass deposition. The only solution to this problem is to fix it in hermetically seal enclosures and that can make it very difficult to use in this research project as space is of paramount importance. Though, its application in this project is interesting enough to explore (Drafts, 2000).

### 7.3 CONCLUSION

Following the review of different relevant sensors for measuring load/stress/strain/force it has been decided that the two sensors that will be used in this application will be the strain gauge and the piezoresistive sensor.

# **8 DESIGN AND DEVELOPMENT OF THE ARTIFICIAL SPINAL DISC PROSTHESIS LOADING CELL**

---

## **8.1 INTRODUCTION**

---

Following the discussion on sensing modalities in the previous chapter, this chapter describes the design of the load-cell for measuring the correct *in vivo* spinal loading using the two selected sensors (strain gauges and piezoresistive sensor). The load measuring range for this experiment is 0 to 4 kN. One of the authentic *in vivo* spinal load measurement experiments was done by Nachemson and the maximum load measured with 20-kg weights in hands was a little more than 2 kN (Nachemson, 1966). Moreover, normal physical activities never cross more than 1 kN. Hence, when considering a heavy patient the range is set to 4 kN maximum with a 5% tolerance margin.

## **8.2 SENSING ELEMENT**

---

The sensing element's size, shape and material determine the range of measuring force. Usually to measure the force the sensing element is of the following types of shape,

- ★ Beam
- ★ Proving ring
- ★ Diaphragm
- ★ Column

Unfortunately, in this application there are no possibilities of using any of the above types. To measure the correct *in vivo* loading on the spinal disc the lumbar artificial spinal disc prosthesis is chosen as a sensing element (Figure 8-1). In the case of using strain gauge sensors, the strain gauges are installed on the surfaces of the sensing element where maximum strains



occur. For example, in a cantilever beam type sensing element the maximum strains occur on the opposite end of the free end of the beam.

In this research a commercial artificial lumbar spinal disc prosthesis is used as a sensing element in order to develop the load-cell to measure the loading on the lumbar spine. After consulting clinical partners for this research, an Active-L lumbar disc from Aesculap- B.Braun is used (Figure 8-1). The main specifications of the disc used are:

- ✳ Company: Aesculap – Braun, Germany
- ✳ Brand: Active - L
- ✳ Size: Medium - 6°
- ✳ Inlay Size: 10 mm

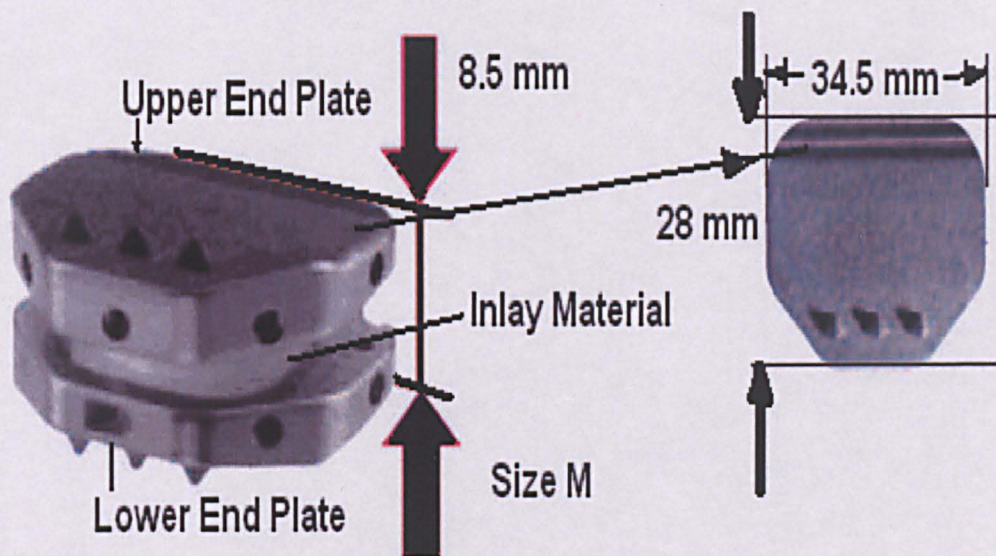


Figure 8-1: Artificial Disc Prosthesis, Aesculap (B.Braun), Active®-L (Size M)  
(Aesculap, B.Braun Ltd. , 2005).

✳ Materials:

ISODUR®F Cobalt wrought alloy CoCr29Mo acc. To 5832-12 (End-plates), PLASMAPORE®  $\mu$ -Cap surface coating made of pure titanium acc. to ISO 5832-2, with an additional calcium phosphate coating Ultra-high molecular low-pressure polyethylene acc. to ISO 5834-2 (ISODUR® and PLASMAPORE® are registered trademark of Aesculap AG & Co. KG, 78532, Tuttlingen / Germany.). Inlay material is



Polyethylene UHMWPE (Ultra High Molecular Weight Poly-Ethylene) ISO 5834-2.  
(Aesculap, B.Braun Ltd. , 2005).

## 8.3 SENSORS

---

As discussed before, in this experiment two types of sensors are used to measure the loading/force on the disc. They are strain gauges and piezoresistive sensors.

### 8.3.1 Strain gauge sensor

---

The strain gauges are most commonly used in the development of load cells with an aim to translate the detected force into an electrical signal. The oldest strain gauge design is the foil-type strain gauge, which have been widely used in 4- to 20-mA transmitters. The foil strain gauges are available with normal resistances from 120, 350, 1000, to 5000  $\Omega$ . The thin foil (0.0001 in., or 0.0025 mm in thickness) is bonded to the sensing element surface where maximum strain occurs using speciality adhesive.



Figure 8-2: Different types of Strain Gauges with attached leads (HBM Ltd., 2005).

The specifications of the Strain Gauges used in this research (examples shown in Figure 8-2) are as follows:

- ✳ Company: HBM \_ Germany
- ✳ Order No: K-LY41-3/120-3-2M
- ✳ Type: Linear Strain Gauge with Teflon wire and 2-measuring grids



- ✳ Temperature response match to steel with  $\alpha = 10.8 \text{ (} 10^{-6} / ^\circ\text{C)}$
- ✳ Resistance:  $120\Omega \pm 0.35\%$
- ✳ Gauge-factor:  $2.00 \pm 1\%$
- ✳ Transverse sensitivity:  $0.2\%$
- ✳ Temperature coefficient of gauge factor:  $104 \pm 10 \text{ (} 10^{-6} / ^\circ\text{C)}$   
(-10+ 45°C)  
(HBM Ltd., 2005).

### 8.3.2 Piezoresistive thin layer sensor

The Piezoresistive sensor measures force not strain (as measured by the strain gauge). The compressive force which needs to be measured passes through the piezoresistive sensor and due to that force the resistance/conductance of the sensor is changed. This change is proportional to the applied load to the sensor. The Piezoresistive sensor is a load bearing sensor. For this experiment the Flexiforce® (Tekscan Inc) sensor as shown in Figure 8-3 is used, which is a thin-film and flexible sensor with better linearity, repeatability, hysteresis, drift and temperature sensitivity than any other thin-film sensor available on the market today.

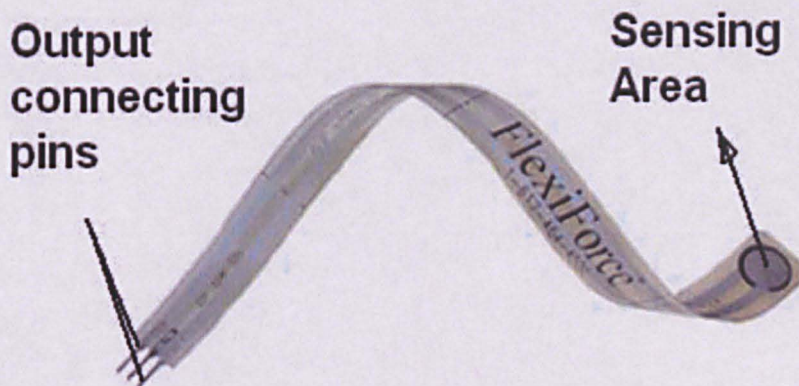


Figure 8-3: Flexiforce® sensor (Piezoresistive thin layer) (Tekscan Inc., 2007).

The sensors are constructed of two layers of substrate. This substrate is composed of polyester film. On each layer, a conductive material (silver) is applied, followed by a layer of pressure sensitive ink. Adhesive is then used to laminate the two layers of substrate together to form the sensor. The

silver circle on top of the pressure-sensitive ink defines the “active sensing area.” Silver extends from the sensing area to the connectors at the other end of the sensor, forming the conductive leads.

When the sensor is unloaded, its resistance is very high (greater than 5 M $\Omega$ ); when a force is applied to the sensor, the resistance decreases. Connecting an ohmmeter to the outer two pins of the sensor connector and applying a force to the sensing area can read the change in resistance. One important fact about this sensor is that the applied load Vs resistance relationship is non-linear but the applied load Vs conductance (1/R) relationship is very much linear.

The specifications of the sensor are:

- ★ Company: Tekscan Inc.-USA
  - ★ Brand: Flexiforce®
  - ★ Model: A201-100 (0-100 lb range or 0-445 N ), can be extended up-to 0-1000 lb (0-4448 N) range by using low drive voltage and less feedback resistance in drive circuit (as given in signal conditioning section).
  - ★ Sensor life: Over 1-million load cycle with 50 lb force
  - ★ Operating temperature range: 15°F (-9°C) to 140°F (60°C)
  - ★ Linearity (error): <+/- 5%
  - ★ Repeatability: <+/- 2.5% of full scale (conditioned sensor, 80% force applied)
  - ★ Hysteresis: <4.5% of full scale (conditioned sensor, 80% force applied)
  - ★ Drift: <3% per logarithmic time scale (constant load of 90% sensor rating)
  - ★ Temperature sensitivity: Output variance up to 0.2% per degree F (approximately 0.36% per degree C). For loads >10 lbs (44 N)., operating temperature can be increased to 165°F (74°C).
- (Tekscan Inc., 2007)



## 8.4 FABRICATION OF THE LOAD CELL

The two types of sensors, strain gauge and piezoresistive (Flexiforce®-Tekscan), were mounted on the superior (upper) and the inferior (lower) end-plates of the artificial spinal disc at the locations as shown in Figure 8-4(A), 8-4(B), 8-4(C) and 8-4(D). The location and size of the strain gauges were selected according to the available and suitable space on the surface of the end plates by carefully placing them so they will not have any effect in the loading process.

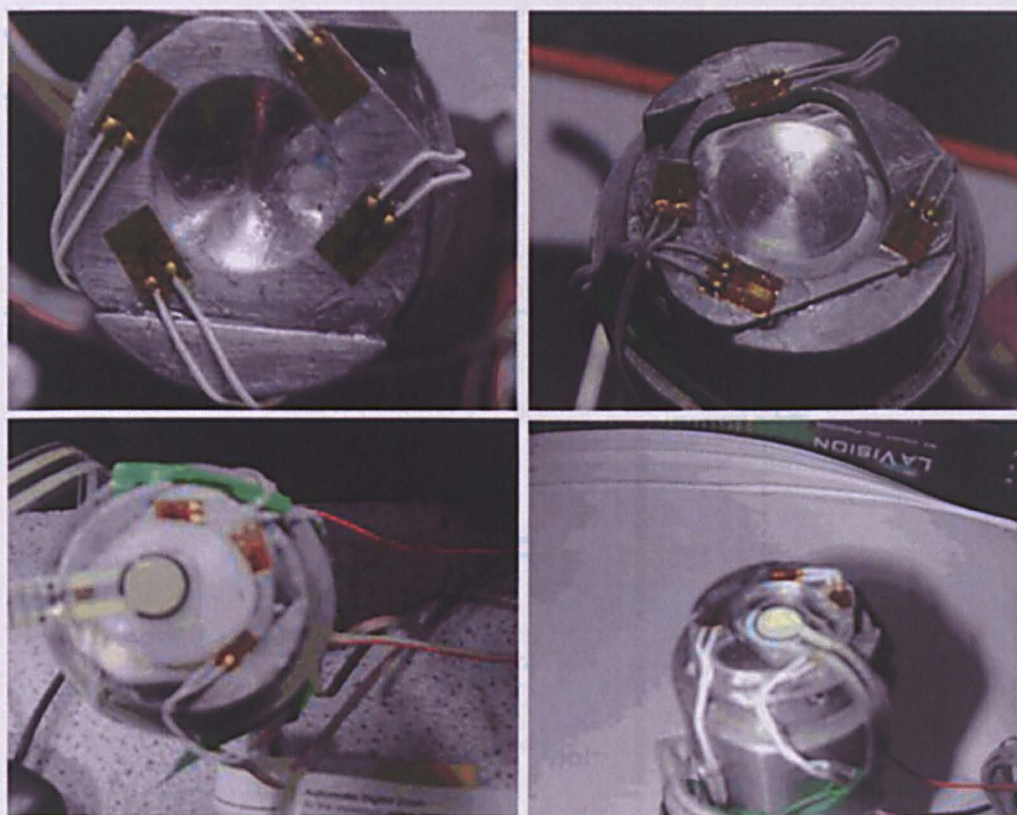


Figure 8-4: (A; top left)Superior end-plate of the prototype artificial spinal disc prosthesis with four strain gauges in place (B; top right) Inferior end-plate of the prototype artificial spinal disc prosthesis with four strain gauges in place (C; bottom left) Piezoresistive sensor (Flexiforce® sensor) placed on top of the inlay material set on the inferior end-plate (D; bottom right) Piezoresistive sensor (Flexiforce® sensor) placed at the bottom of the inlay material set on the inferior end-plate.

Figure 8-4(A) shows four strain gauges mounted on the upper end-plate of the disc. Figure 8-4(B) shows four strain gauges mounted on the inferior end-plates of the disc. The strain gauges are installed as per BSSM (The British Society for Strain Measurement) standard for code and practice. The

installation procedure begins with the preparation of the surface for installation. The strain gauges are installed on that surface with quick-drying cyanoacrylate adhesive. This adhesive builds a stiff bond instantly that transfers the strain with minimal loss from the application surface to the strain gauge carrier surface. Thereafter, constant pressure is applied for 1 minute with thumb or hand, and then is left for 30 minutes to 60 minutes for curing. Figure 8-4(C) shows the piezoresistive sensor (Flexiforce®-Tekscan) mounted on the top of the inlay material and Figure 8-4(D) shows piezoresistive sensor (Flexiforce®-Tekscan) kept on the inferior end-plate of the disc placed at the bottom of the inlay material.

As said above the Piezoresistive (Flexiforce®- Tekscan) sensors are load bearing sensors for measuring force and will be used for measuring the compressive forces subjected to the disc. The sensors will be placed above and below the inlay material in order to observe the visco-elastic behaviour of the inlay material and hence of the disc.

Therefore, the placement of all sensors securely on the artificial spinal disc completes the design and fabrication of the load-cell which will be used in this research for measuring the forces on the disc during loading.

# **9 DESIGN AND DEVELOPMENT OF THE MECHANICAL TOOLS, ACCESSORIES AND ELECTRONICS DATA ACQUISITION SYSTEM**

---

## **9.1 INTRODUCTION**

---

This chapter describes the *in vitro* experimental set-up including required mechanical tools, jigs and fixtures, signal conditioning, data acquisition and processing system with both hardware and software. The signals produced by the sensors located on the load cell are further conditioned and all acquired data are stored in a PC based data acquisition system in the form of .lvm, .xl, and .bin files for further analysis. This chapter also covers the software, filtering and graphical presentation of the data. It also, includes description of the fabrication of the mechanical tools, jigs and fixtures used in the performing of the *in vitro* loading experiments on the artificial spinal disc prosthesis.

## **9.2 EXPERIMENTAL SET-UP**

---

Experimental set-up consists of,

1. Artificial intervertebral lumbar disc prosthesis with sensors as a load-cell
2. Loading machine (UT)
3. Mechanical tools and accessories.
4. Signal conditioning, data acquisition and processing system

The artificial spinal disc prosthesis with sensors as a load cell is explained in chapter-8. In order to apply the required compressive loading to this load cell, a certain amount of mechanical tools, jigs and fixtures were required. The compressive load for this experiment is applied by a Universal Testing Machine (UTM). In this research experiment, as two different types of sensors are used (strain gauge and piezoresistive), two different types of signal conditioning circuits were also required. To compare the output of the



two different sensors the same data acquisition system has been used and the results were plotted against the same time axis on the same graph. The description of all parts of the experiments is provided in the following sections.

### 9.3 LOADING MACHINE (UTM-UNIVERSAL TESTING MACHINE)

---

In this experiment, the compressive loading is applied using the Dartec®, Universal Testing Machine (UTM) with computer controlling software provided by Instron® as shown in the Figure 9-1-A and Figure 9-1-C. As discussed previously, in this primary stage of experiments only compressive loading up to 4 KN is applied in a normal direction at the disc.

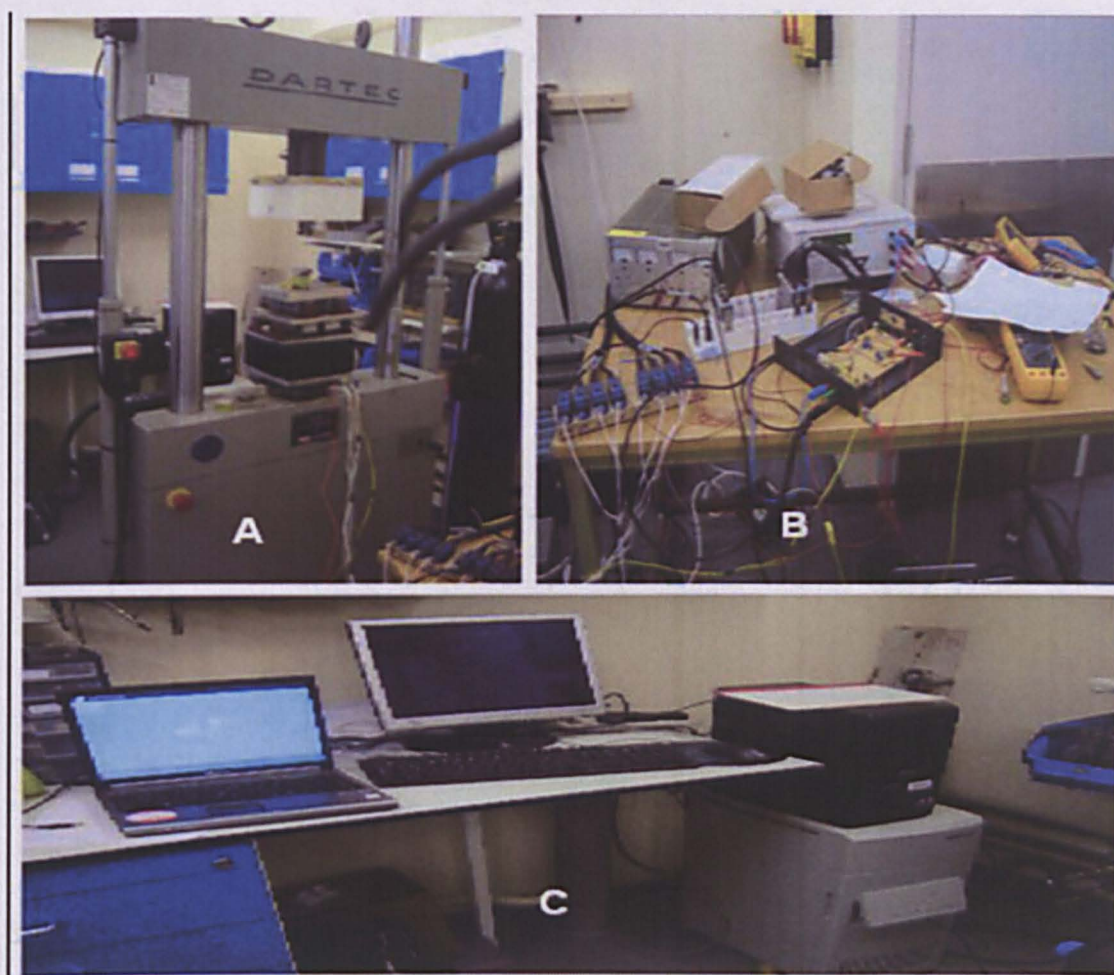


Figure 9-1: Photographs of the Experimental Set-Up. (A) Mechanical system: UT machine with tools & accessories (B) Signal conditioning, data acquisition and processing system hardware (C) Two Portable PC: one for display and running data acquisition software and another for controlling the UT machine as a console.



## 9.4 MECHANICAL TOOLS AND ACCESSORIES

The precise design and development of mechanical tools and accessories that will support the loading of the artificial disc are very crucial for this experiment. In this *in vitro* experiment, as explained in chapter-8, the load cell based on the artificial lumbar spinal disc prosthesis is developed. The signals from all the sensors and the analogue output of the applied compressive load produced by the loading machine are sampled by the data acquisition system at every 0.01 seconds. In order to apply compressive load in a normal direction to the load cell using the UT machine proper mechanical tools and accessories like fixtures and platens are needed.

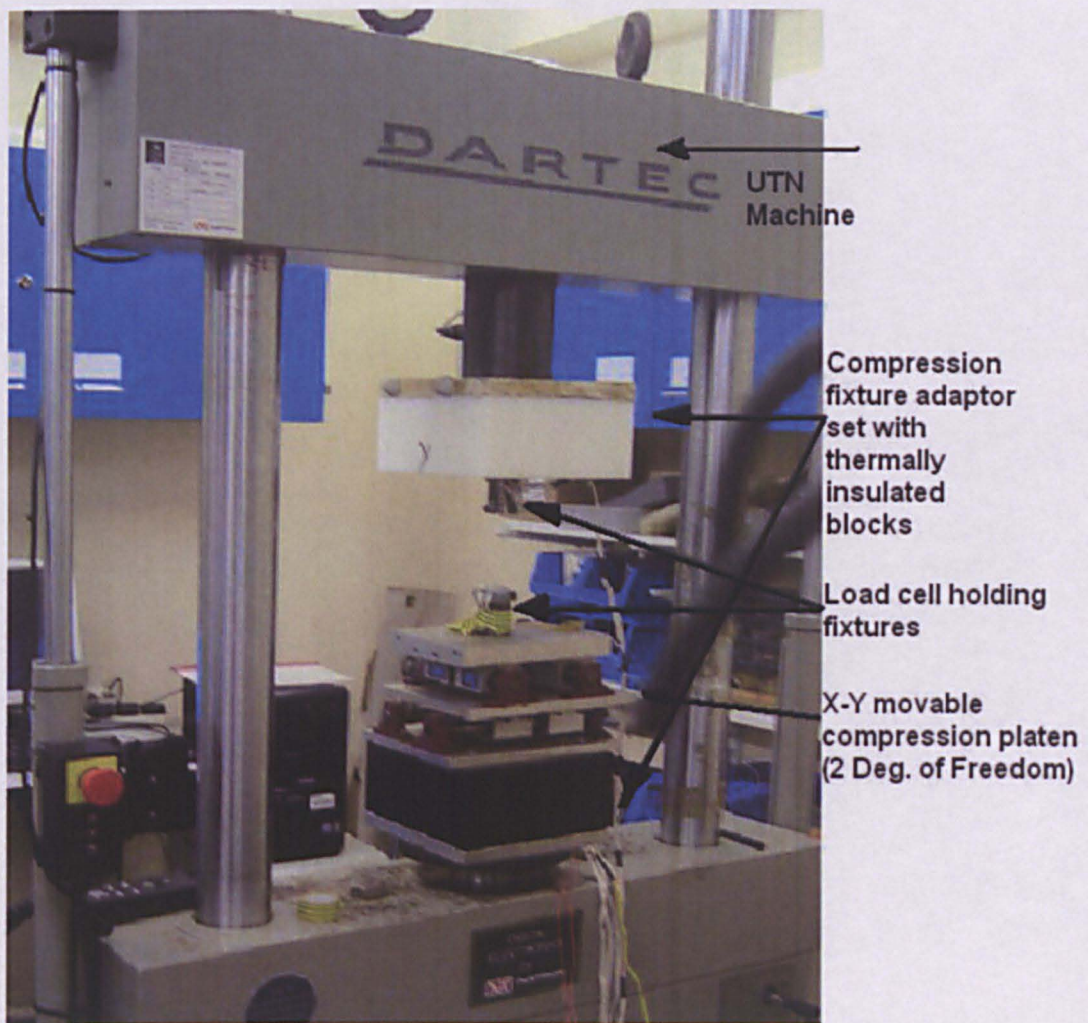


Figure 9-2: Photograph of mechanical loading experimental set-up with designed tools & accessories like fixtures and platens.



Figure 9-2 shows the total mechanical compressive loading experimental set-up for the *in vitro* experiments on the load cell. It consists of the UT machine, a compression fixture adaptor set with thermally insulated blocks, load cell holding fixtures and X-Y movable compression loading platen with 2-degrees of freedom. Each of these parts will be described below.

#### 9.4.1 Load cell holding fixtures

This is one of the very challenging mechanical tools that was developed. To properly understand the design and development of this load cell holding fixture, we need to first look at the artificial lumbar spinal disc. As explained in chapter-2, in the lumbar region of the human spine the spinal disc is wedge shaped. Hence, as shown in Figure 9-3, the artificial lumbar spinal disc prosthesis is also wedge shaped in order to maintain the original biomechanics of the human spine. This is one of the design constrain for load cell holding fixtures. In order to apply compressive loading by the UT machine in a normal direction to the load cell, it requires complementary wedge shaped fixtures with proper mechanical holding of the end-plates of the load cell. That's why, the mechanical load cell holding fixture surface is kept taper (Figure 9-3).

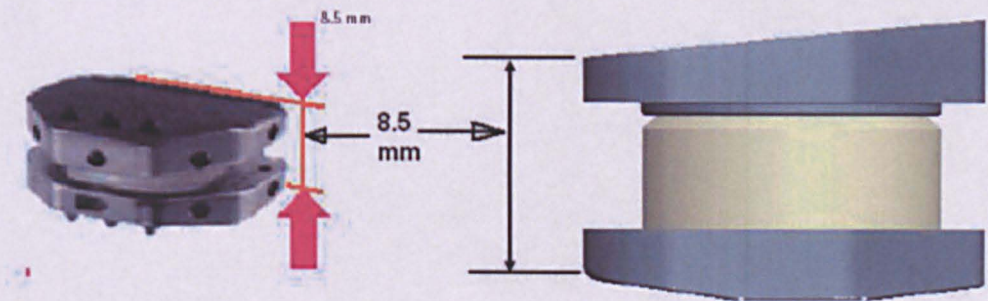


Figure 9-3: Artificial lumbar spinal disc prosthesis (wedge shape) (Aesculap, B.Braun Ltd. , 2005).

The end-plate of the load cell is strongly fixed with the fixture by two sets of 3 mm diameter screws from opposite sides. The outer surface of the end-plates have a very rough layer of calcium phosphate for enhancing osteo-induction. Moreover, it also has three studs (anchors) and three horizontal grooved lines. In this design the external surface of the top endplate and inner contact surface of the top tool are not making strong enough grip to



withstand the compressive force of upto 4 kN. Hence, to solve this problem, the fixture surface is layered with a 2-part epoxy self-hardening putty and that was covered with a layer of cling film. Then, the load cell end plates were kept in place in the self hardening putty under uniform load for 12 hours. After 12 hours, the end-plates of the

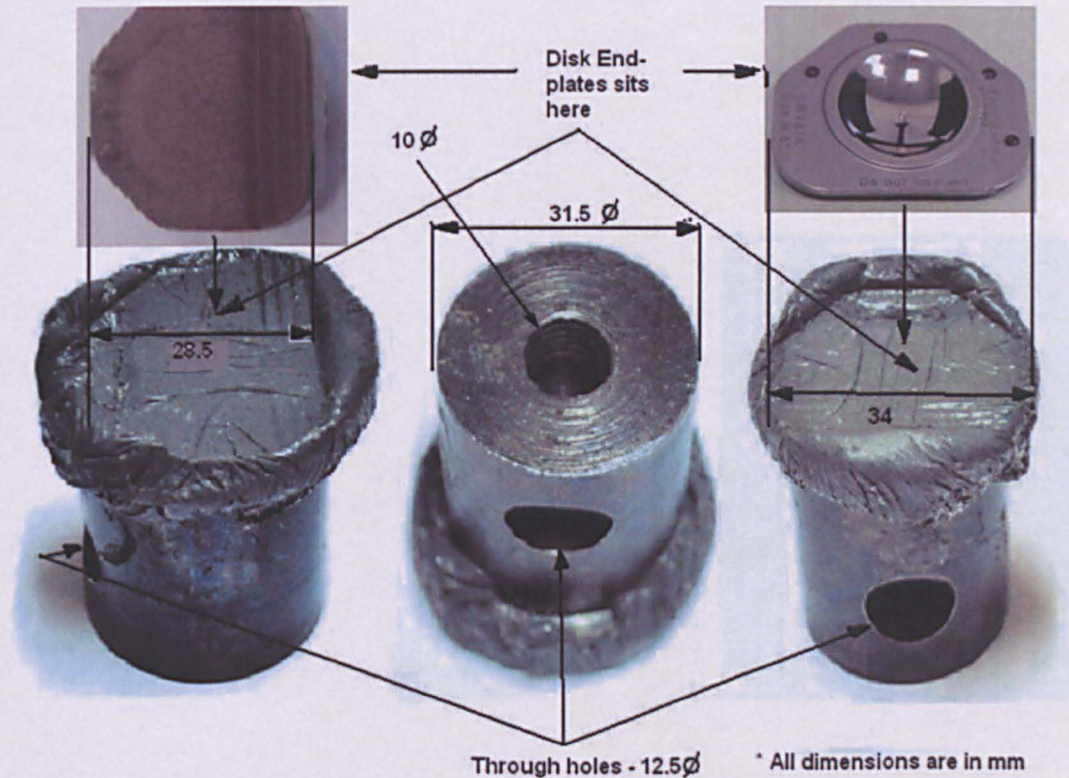


Figure 9-4: Artificial spinal disc prosthesis – load cell holding fixtures for compressive loading upto 4 kN with important dimensions.

load cell were removed and the putty became very hard. The solid putty can be seen in Figure 9-4. The load cell holding fixture is now ready for applying compressive loading in the accurate normal direction to the load cell.

#### 9.4.2 Mechanical calibration tool for Piezoresistive Sensor

For consistent and accurate results the piezoresistive sensor (Flexi force) needed to be calibrated properly. As shown in Figure 9-5, the total load applied to the entire sensing area is considered as a single point of loading. The sensor must be loaded consistently, or in the same way each time. If the load applied surface of the tool or specimen is smaller than the circular sensing area of the sensor then the output of the sensor is incorrect.



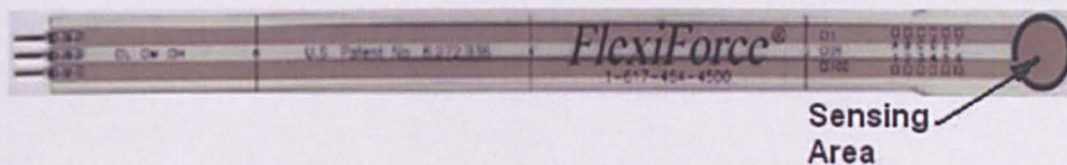


Figure 9-5: Photograph of the piezoresistive sensor (Flexiforce®) (Tekscan Inc., 2007).

Hence, as shown in Figure 9-6, the load application tool tip surface diameter is designed as 11mm. This area is equal to the inner circular area of the sensing circle on the sensor. The sensor is mounted on the surface with a tape (Tekscan Inc., 2007).

### Sensor conditioning

The Flexiforce® sensor must be conditioned before calibration for accurate results. Such conditioning reduces the effects of drift and hysteresis. Conditioning is required for new sensors, and for sensors that have not been used for a long time. To condition a sensor 110% of the test weight was placed on the sensor then the sensor allowed to be stabilized. Thereafter the weight was removed. This process was repeated four or five times (Tekscan Inc., 2007).

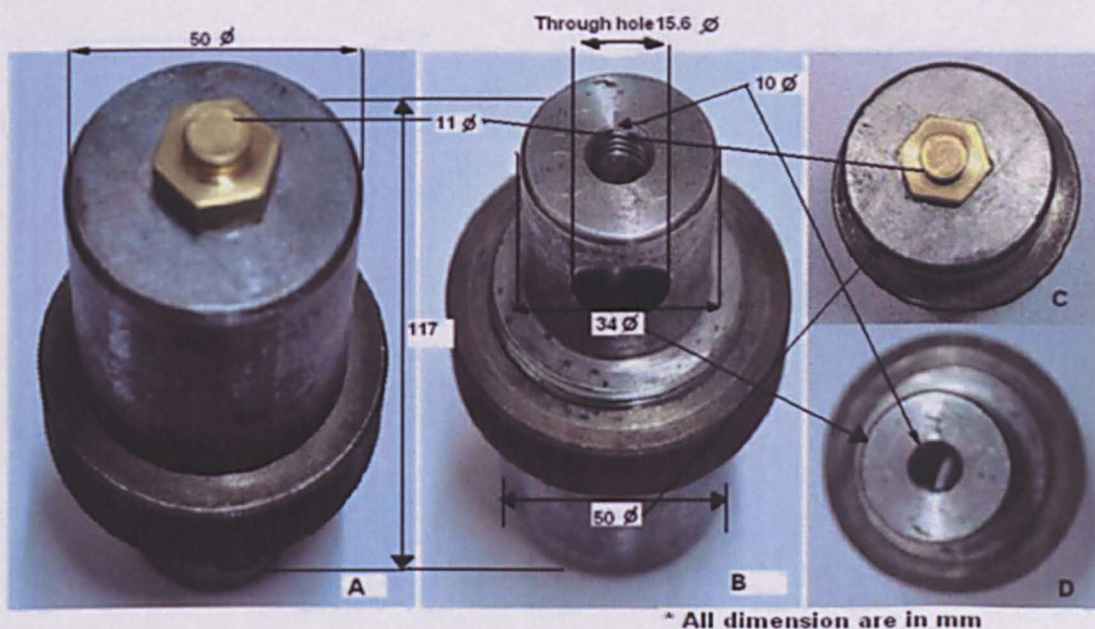


Figure 9-6: Piezoresistive sensor (Flexiforce®) calibration compressive loading tool with important dimensions. (A) 3D view from the top (B) 3D view from the bottom (C) View from the top (D) View from the bottom.



### Sensor calibration

The calibration procedure was performed by applying a known load like 100N, 200N, 2kN, etc, while the sensor's resistance output was recorded. The process was repeated with a number of known forces upto the maximum range. Then, the Force Vs Conductance (inverse of resistance) graph was plotted. The linear curve was found by plotting the load values from zero to the maximum range of force. Here the range of compressive loading was 0-4 kN.

### 9.4.3 X-Y movable compression platen with 2-degrees of freedom

In a compressive loading experiment with the non-flat surface of the test specimen, the accurate alignment of the two parts (upper and lower) of the UT machine is very crucial otherwise experimental results can be incorrect.

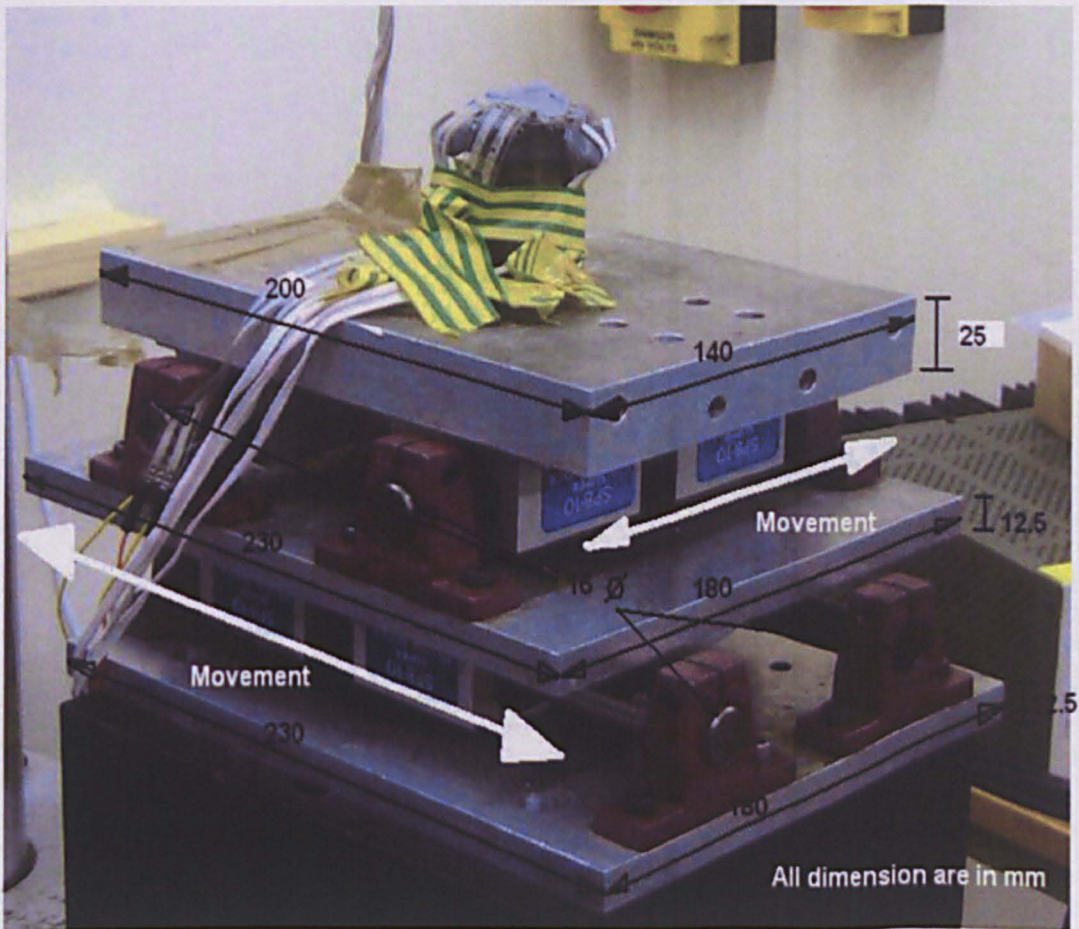


Figure 9-7: X-Y movable compression platen for proper alignment of the upper and lower compressive loading parts with important dimensions.

As the top surface of the inlay material is semi-circle (dome type) and the inner surface of the upper end-plate of the load cell is concave with glass finish, the compressive loading direction must be perfectly normal in direction.

Hence, for proper alignment of the two parts (upper and lower) of the UT machine requires some movement of the two parts (upper and lower) of the UT machine in the X-Y directions. To facilitate movement of the X-Y directions of the two parts of the UT machine, the X-Y movable compression platen was designed and developed (Figure 9-7). The whole platen is made-up of three metal plates. The dimensions of all three plates are shown in the Figure 9-7. The bottom surfaces of the top and middle plate are fitted with guiding 4-jigs each for movement in particular directions of the respective plates. The top surfaces of the middle and bottom plates are fitted with 4-holding brackets each for the 16mm diameter four metal shafts as shown in Figure 9-7. Therefore, it is assumed that the top plate moves in the Y-direction and the middle plate moves in the X-direction. The bottom plate is meant for providing the base for the upper two plates and is used for securing the shaft holders of the middle plate using by screws and nuts.

## **9.5 SIGNAL CONDITIONING & DATA ACQUISITION SYSTEM - HARDWARE**

---

The block diagram (Figure 9-9) shows the layout of the signal conditioning and data acquisition system of the experiment. As shown in chapter-8, the four strain gauges mounted on the superior end-plate and four strain gauges mounted on the inferior end-plate are connected to a quarter bridge completion modules (NI 9944). The outputs from the quarter bridge completion modules are connected to two Strain gauge-analogue input modules (NI 9237) each with a 4-channel through cable with RJ-50 connector. The two Flexiforce® (Piezoresistive) sensors are also connected to the signal conditioning circuit (Figure 9-9). The outputs of the signal conditioning circuit are analogue voltages (0-10V). One analogue output (0-10V) for loading (0-4 kN) was taken from the UT machine and was connected to the 4-channel analogue input voltage module (NI 9215) through cables with a BNC connector. The three analogue input modules



(two NI 9237 and one NI 9215) were positioned in three slots of an 8-slot data acquisition chassis (NI 9172) through a direct 15-pin D-sub (VGA) connection. The output of the data acquisition chassis was connected to a personal computer (Laptop) through a cable with USB (2.0) pin connector. The required code written in Labview software was loaded on a laptop computer. The above explained set-up completes the whole signal conditioning and data acquisition hardware of the experiment.

### 9.5.1 Quarter bridge completion module (NI 9944)

The quarter bridge completion modules are used to complete the single sensor i.e. strain gauge quarter bridge circuit to the full bridge circuit as shown in Figure 9-8 and 9-10. The quarter bridge completion circuit is very useful for better accuracy, precision, repeatability and it also nullifies the effect of temperature, noise pick-up in the lead wires and the effect of contact resistance. Figure 9-8 shows the diagram for connecting a single quarter bridge (strain gauge) to a quarter bridge completion module NI9944/9945. The Quarter bridge completion module (NI9944/9945) is made-up of all circuitry except from an external single resistance – in this case the strain gauge (Figure 9-3).

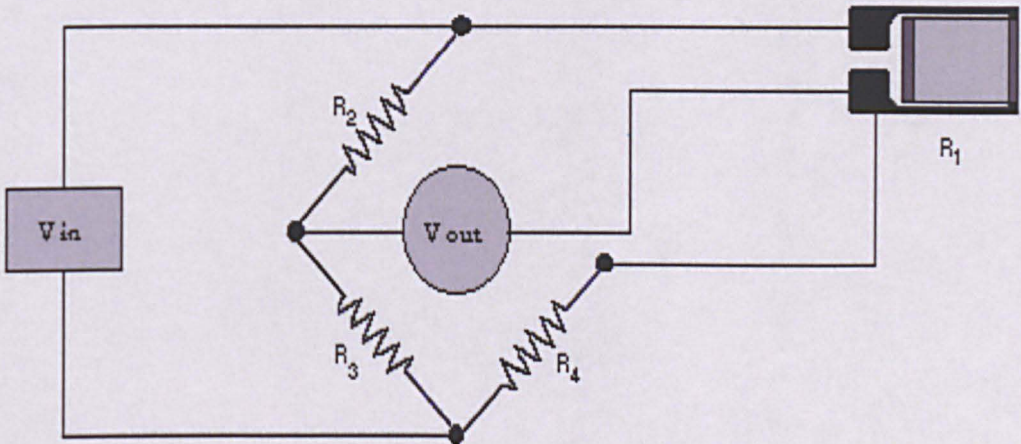


Figure 9-8: Strain gauge quarter bridge completion diagram



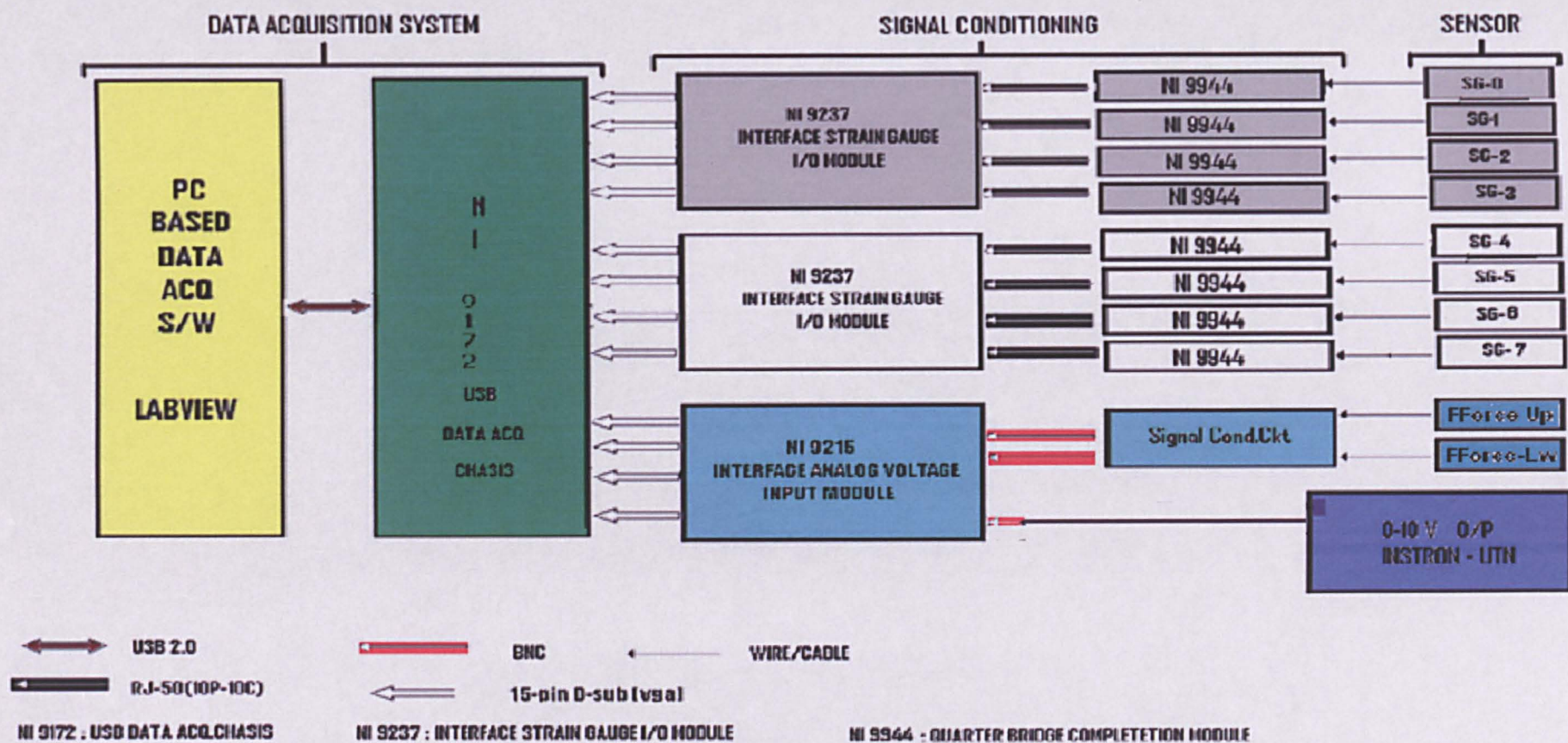


Figure 9-9: Block diagram of signal conditioning, data acquisition and processing system



Table 9-1: Connection diagram details

Connection Diagram Report			
Task Name: Myalltask			
Channel Name	Physical Channel	Device Type	Measurement Type
<a href="#">Strain0</a>	cDAQ1Mod7/ai0	NI 9237	Strain
<a href="#">Strain1</a>	cDAQ1Mod7/ai1	NI 9237	Strain
<a href="#">Strain2</a>	cDAQ1Mod7/ai2	NI 9237	Strain
<a href="#">Strain3</a>	cDAQ1Mod7/ai3	NI 9237	Strain
<a href="#">Strain4</a>	cDAQ1Mod8/ai0	NI 9237	Strain
<a href="#">Strain5</a>	cDAQ1Mod8/ai1	NI 9237	Strain
<a href="#">Strain6</a>	cDAQ1Mod8/ai2	NI 9237	Strain
<a href="#">Strain7</a>	cDAQ1Mod8/ai3	NI 9237	Strain
FForce_Up	cDAQ1Mod1/ai0	NI 9215 (BNC)	Voltage
FForce_Lw	cDAQ1Mod1/ai1	NI 9215 (BNC)	Voltage
Load-N	cDAQ1Mod1/ai2	NI 9215 (BNC)	Voltage
<a href="#">Strain0 (Back to Top)</a>			
Point 1		Point 2	
Strain Gage Quarter Bridge 1/CH+		NI-9237_qtr/CH0/IN+	
Strain Gage Quarter Bridge 1/EX+		NI-9237_qtr/CH0/EX+	
Strain Gage Quarter Bridge 1/QTR		NI-9237_qtr/CH0/QTR	

Figure 9-10, shows how straingauge-0 can be connected and this connection is similar with the remaining of the strain gauges used with the other seven modules (NI9944/9945). The complete connection diagram report is shown in Table 9-1.



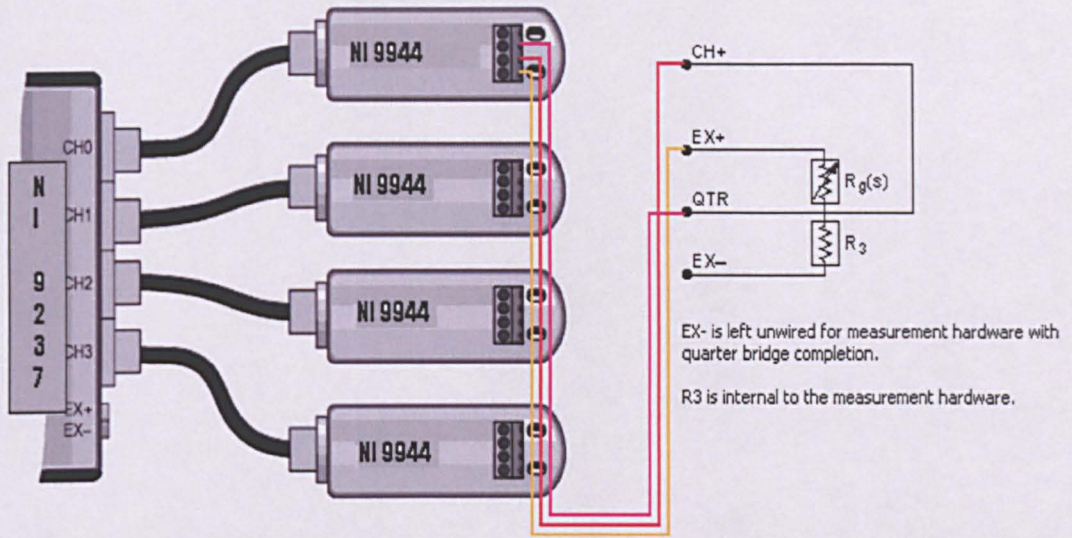


Figure 9-10: Connection diagram for strain gauges with the signal conditioning modules NI 9944 and NI 9237 (National Instruments Corporation, 2010).

The specifications for NI 9944 are as under,

- ✧ Weight .....32 g (1.1 oz)
- ✧ Operating temperature .....-40 to 70 °C
- ✧ Resistor value.....120  $\Omega$
- ✧ Resistance drift.....0.012  $\Omega/^\circ\text{C}$
- ✧ Resistor tolerance (at 25 °C).....0.1% max
- ✧ Resistor power .....0.25 W max

### 9.5.2 Strain gauge analogue input module (NI 9237)

As shown in Figure 9-10, all eight strain gauges are connected to a strain gauge analogue input module (NI 9237) of signal conditioning circuit through a quarter bridge completion module NI 9944/45.

The NI 9237 (Figure 9-11) includes remote sensing to compensate the error due to the connection to wire resistances. Remote sense wires are connected to the point where the excitation voltage wires connect to the bridge circuit.





Figure 9-11: Strain Gauge Analog Input Module (NI 9237) (National Instruments Corporation, 2010).

In this load cell design all strain gauges are connected in the quarter bridge completion module. The outputs from the bridge completion modules are connected to the NI 9237 module. This module has an in-built shunt calibration circuitry. It also has filtering, alias free bandwidth and for the low power consumption, sleep-mode facilities. The details of these features and specifications are explained in the following sections.

## Shunt calibration

Shunt calibration is required to eliminate the errors due to the resistance of wiring/cabling to the excitation and individual resistors of the bridge. It is very much required in the case of quarter-bridge sensors.

The NI 9237 shunt calibration circuitry has a precision 100 k $\Omega$  resistor and a software-controlled switch. The shunt calibration can be done by applying or removing resistances from the software i.e. Labview. While remote sensing corrects for resistances from the EX terminals on the NI 9237 to the sensor, shunt calibration corrects for these errors and for errors caused by wire resistance within an arm of the bridge. Shunt calibration is done by simulating the change in strain by changing the known value of the resistance in the bridge. The difference between expected values and measured values are used to correct the entire errors.

### Excitation voltages

The NI 9237 is able to supply 2.5 V, 3.3 V, 5 V, or 10 V of excitation voltage, and maximum excitation power is 150 mW, unless you supply external excitation voltage. Recommended total power should be less than

or equal to 150 mW. The NI 9237 automatically reduces internal excitation voltages as needed to stay below 150 mW. The power consumed by a single bridge is P and denoted by,

$$P = (V_{ex})^2 / R$$

Where, R is the total resistance of the bridge.

For a full bridge, R is equal to the resistance of the each element. For a half or quarter bridge, R is equal to the two times the resistance of each element. The 150 mW limit allows you to power full and half bridges as follows:

- ★ Four 350  $\Omega$  half bridges at 5.0 V
- ★ Four 350  $\Omega$  full bridges at 3.3 V
- ★ Four 120  $\Omega$  half bridges at 2.5 V

### **NI 9237 circuitry**

The NI 9237 is isolated from the earth-ground. However, the individual channels are not isolated from each other. The EX+, EX–, and T– signals are common among all channels. You can connect the NI 9237 to a device that is biased at any voltage within the NI 9237 rejection range of earth ground. Refer to the specification section for more information. You also can connect floating signals to the NI 9237. If you connect floating signals to the NI 9237, National Instruments recommends you connect the EX– signal to the earth ground or shield for better noise rejection. Each channel on the NI 9237 has an independent 24-bit ADC and input amplifier that enables you to sample signals from all four channels simultaneously. The NI 9237 also includes filters to prevent aliasing. The filters on the NI 9237 filter according to the sampling rate.

### **NI 9237 filtering**

The filtering is basically used to attenuate the noise signals from the data signals, in other words to filter out the noise. The NI 9237 uses a combination of analogue and digital filtering to provide an accurate representation of desirable signals while rejecting out-of-band signals. The filters discriminate between signals based on the frequency range, or bandwidth, of the signal. The three important bandwidths to consider are the pass band, the stop band, and the alias-free bandwidth.

The NI 9237 represents signals within the pass band as accurately as possible, as quantified primarily by pass band flatness and phase non linearity. The filters reject frequencies within the stop band as much as possible, as quantified by stop band rejection. All signals that appear in the alias-free bandwidth are either un-aliased signals or signals that have been filtered by at least the amount of the stop band rejection.

- ★ **Pass band:** The signals within the pass band have frequency-dependent gain or attenuation. The small amount of variation in gain with frequency is called the pass band flatness. The filters of the NI 9237 adjust the frequency range of the pass band to match the data rate.
- ★ **Stop band:** The filter significantly attenuates all signals above the stop band frequency. The primary goal of the filter is to prevent aliasing. Therefore, the stop band frequency scales precisely with the data rate. The stop band rejection is the minimum amount of attenuation applied by the filter to all signals with frequencies that would be aliased into the alias-free bandwidth.

### **Alias-Free bandwidth**

Any signal that appears in the alias-free bandwidth of the NI 9237 is not an aliased artefact of signals at a higher frequency. The alias-free bandwidth is defined by the ability of the filter to reject frequencies above the stop band frequency and equals the data rate minus the stop band frequency.

### **Sleep mode**

This module supports a low-power sleep mode. Support for sleep mode at the system level depends on the chassis that the module is plugged into. Refer to the chassis documentation for information about support for sleep mode. You can enable sleep mode in software. Refer to the driver software documentation for more details. Typically, when a system is in sleep mode, you cannot communicate with the modules. In sleep mode, the system consumes minimal power and may dissipate less heat than it does in normal mode. Refer to the specification section for more information about power consumption and thermal dissipation.

**Binary data**

Some devices in the system return un-calibrated binary data. For these devices, you can apply calibration coefficients and convert the data to engineering units in software. Refer to the software documentation for information about converting data. Some devices, such as those that use NI-DAQmx software, return calibrated data by default. Refer to the software documentation for more information.

**Specifications**

The following specifications are typical for the range -40 to 70 °C unless otherwise noted.

**Input Characteristics**

- ★ Number of channels.....4
- ★ Bridge completion Full and half..... Internal
- ★ Quarter.....External
- ★ ADC resolution.....24 bits
- ★ Type of ADC.....Delta-sigma (with analogue pre-filtering)
- ★ Sampling mode .....Simultaneous
- ★ Data rates (fs)..... n = 1, 2 ... 31.
- ★ Master time base (internal)
- ★ Frequency .....12.8 MHz
- ★ Accuracy.....± 100 ppm max
- ★ Nominal full-scale range.....± 25 mV/V
- ★ Scaling coefficient .....2.9802 nV/V per LSB
- ★ Over voltage protection between any two terminals ± 30V Accuracy
- ★ Gain drifts.....10 ppm/°C max Offset drift
- ★ 2.5 V excitation .....0.6 µV/V per °C
- ★ 3.3 V excitation .....0.5 µV/V per °C
- ★ 5 V excitation .....0.3 µV/V per °C
- ★ 10 V excitation .....0.2 µV/V per °C



### 9.5.3 Signal conditioning circuit for Flexiforce® (Piezoresistive Thin Layer) sensor

As explained earlier (Sec. 8.3.2 of chapter-8), the output of the Flexiforce® sensor is changed in conductance proportional to the change in applied load. The change in resistance is converted to the change in analogue voltage through the given signal conditioning circuit. The circuit (Figure 9-12) is a simple inverting amplifier circuit using MC34071 op-amp. The circuit has dual power sources,  $\pm 9V$  DC and  $-5V$  DC. The output is calculated as follows,

$$V_{out} = -V_D * (R_F/R_{S1})$$

Where,  $V_{out}$  = Output Voltage (V)

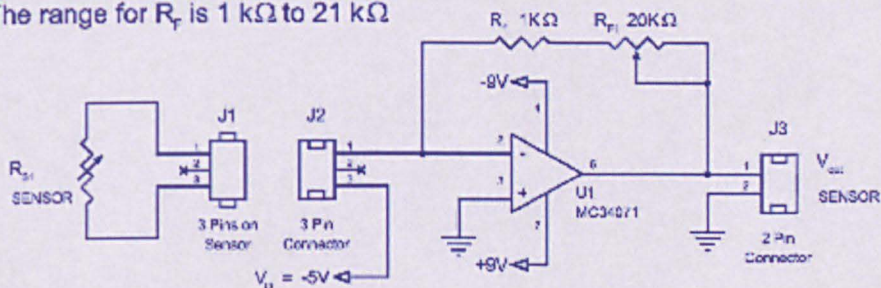
$$V_D = -5V \text{ DC}$$

$$R_F = \text{Feedback Resistor } (\Omega)$$

$$R_{S1} = \text{Resistance of Sensor } (\Omega)$$

$$V_{out} = -V_D * (R_F/R_{S1}); \text{ where } R_F = R_1 + R_{F1}$$

The range for  $R_F$  is 1 k $\Omega$  to 21 k $\Omega$



U1: MC34071AP (Plastic Dip Package)

OR

U1: MC34071AD (Surface Mount Package)

- Max recommended current: 2.5 mA
- No-Load Resistance = Approximately 20 M $\Omega$
- Full-Load Resistance  $\geq 20$  k $\Omega$
- Possible Overload Resistance  $\geq 5$  k $\Omega$
- The two supply voltages (+9V and -9V) and  $V_D$  (-5V) should remain constant

Figure 9-12: Piezoresistive thin layer sensor-Flexi Force signal conditioning circuit (Tekscan Inc., 2007).

In the unloaded condition the sensor's output is very high (greater than 5 M $\Omega$ ) and as load increases its resistance is decreasing sharply that's why the selection of op-amp is very important for proper required performance of the circuit. The Op-Amp MC34071AP/AD is a suitable op-amp for this application. The op-amp has,

- ★ Wide Bandwidth: 4.5 MHz
- ★ High Slew Rate: 13 V/ms
- ★ Fast Settling Time: 1.1 ms to 0.1%
- ★ Wide Single Supply Operation: 3.0 V to 44 V
- ★ Wide Input Common Mode Voltage Range: Includes Ground (VEE)
- ★ Low Input Offset Voltage: 3.0 mV Maximum (A Suffix)
- ★ Large Output Voltage Swing: -14.7 V to +14 V (with  $\pm 15$  V Supplies)
- ★ Large Capacitance Drive Capability: 0 pF to 10,000 pF
- ★ Low Total Harmonic Distortion: 0.02%
- ★ Excellent Phase Margin: 60°
- ★ Excellent Gain Margin: 12 dB
- ★ Output Short Circuit Protection

The sensitivity of the sensor can be adjusted as per requirement by changing the feedback resistance. The lower the feedback resistance the lower the sensitivity and the higher the force range. The output of this signal conditioning circuit is connected to an analogue input voltage of the module NI 9215.

#### **9.5.4 Voltage analogue input module (NI 9215)**

---

The output of the signal conditioning circuit of the piezoresistive Flexiforce® sensor is connected to the one BNC terminal of the NI cRIO-9215 module (Figure 9-13). The other two terminals of the NI cRIO-9215 module are also connected to the analogue outputs (0-10V) of the extension and loading/compressive force of the Instron UT machine. The NI cRIO-9215 is a 4-channel,  $\pm 10$ V, 16-bit simultaneous analogue input module with BNC connectors.





Figure 9-13: Analogue voltage input module (NI 9215) (National Instruments Corporation, 2010).

### cRIO 9215 circuitry

The cRIO 9215 channels share a common ground that is isolated from the other modules in compact RIO system. As mention in the specification, this module comes with over-voltage protection for each channel. As shown in Figure 9-14, after over-voltage protection circuit the conditioning circuit of the Instrumentation amplifier is connected.

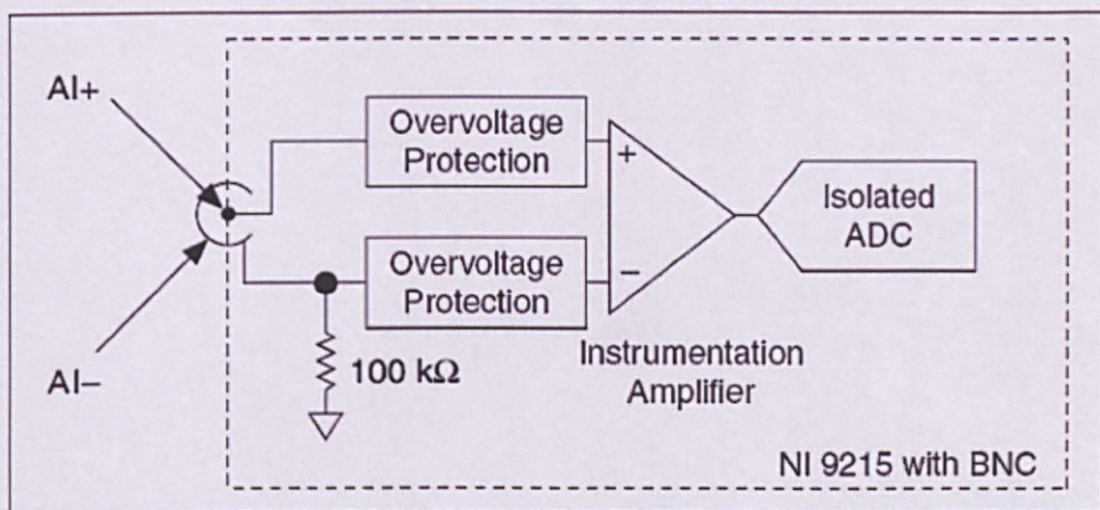


Figure 9-14: cRIO-9215 input circuitry of single channel with BNC connection (National Instruments Corporation, 2010).

The signals coming out of the instrumentation amplifier are sampled by a 16-bit ADC. Due to the availability of the independent track-and-hold amplifiers, this module has the ability of simultaneous sampling. The above module with BNC connectors has a resistor that ensures the input voltage



does not drift outside of the common mode range. This module also has sleep-mode facility.

**Specifications**

The electric and thermal specifications are as under,

**Power Requirements**

- ✧ Power consumption from chassis (full-scale input, 100 kS/s)
- ✧ Active mode .....560 mW max
- ✧ Sleep mode .....25  $\mu$ W max

**Thermal dissipation (at 70 °C)**

- ✧ Active mode .....560 mW max
- ✧ Sleep mode .....25  $\mu$ W max

**9.5.5 USB data acquisition chassis (NI c-DAQ 9172)**

---

The whole NI cDAQ9172 system (Figure 9-15 and 9-16) is made up of eight empty slots for C-series I/O modules, the cDAQ module interface, and the USB-STC2. This cDAQ9172 chassis with I/O modules made the complete signal conditioning and data acquisition system hardware required for connecting the sensor loaded load cell to PC/laptop.

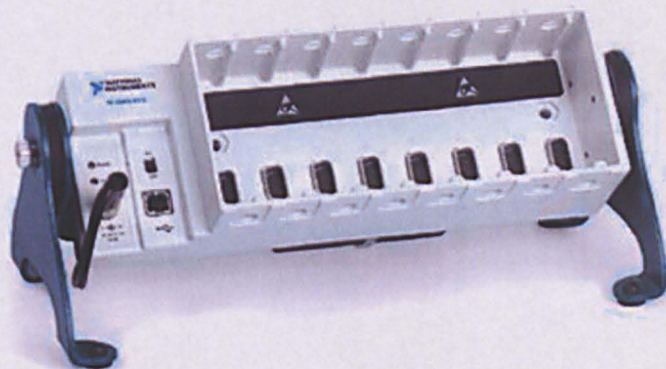


Figure 9-15: Photograph of USB data acquisition chassis (NI cDAQ9172) (National Instruments Corporation, 2010).



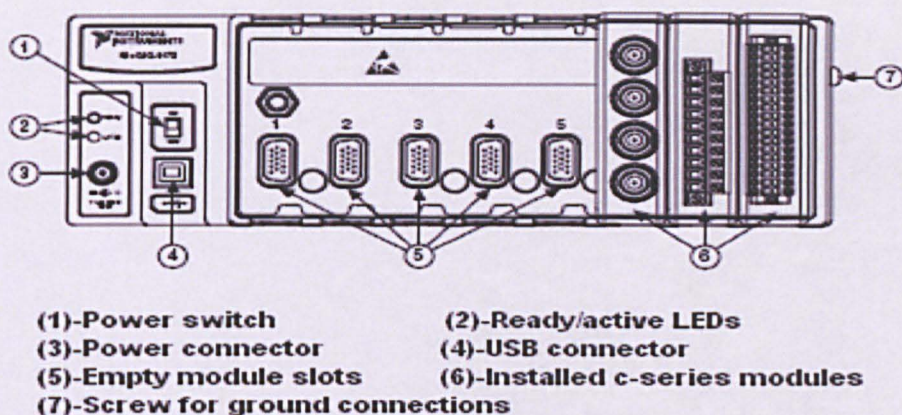


Figure 9-16: Front connection lay-out of USB data acquisition chassis (NI cDAQ9172) (National Instruments Corporation, 2010).

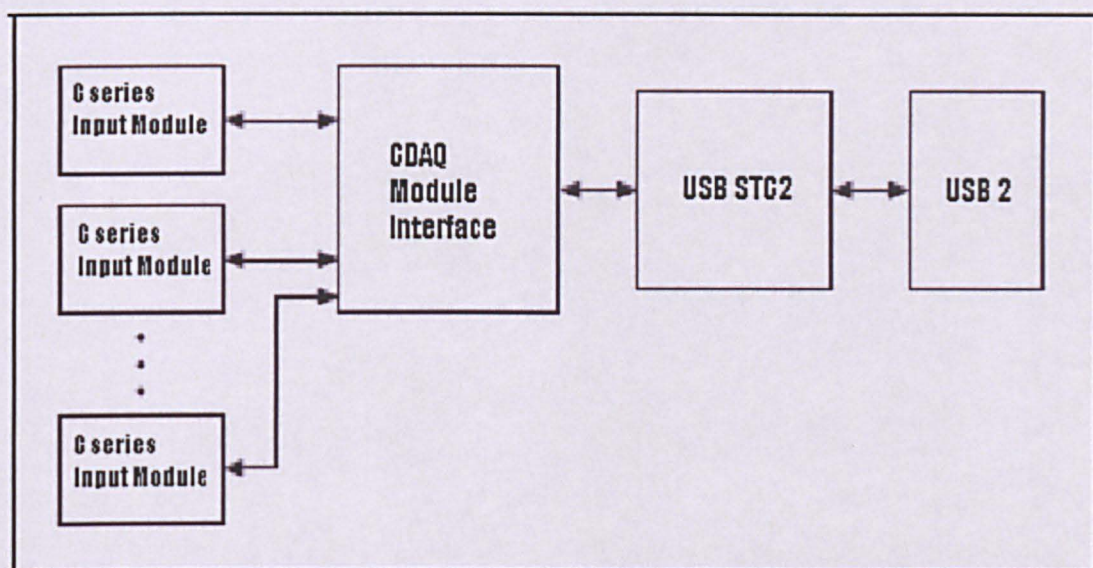


Figure 9-17: NI cDAQ-9172 Block Diagram (National Instruments Corporation, 2010).

Figure 9-17 shows the block diagram for NI cDAQ9172 data acquisition chassis. The details of the hardware parts are explained here.

### I/O modules

The I/O modules fulfil the requirements of signal conditioning circuit with proper connectors like screw terminal, spring terminal, BNC, D-SUB, or RJ-50 connectors.

As explained in the previous section, it is mainly used for the main signal conditioning system. It is hot swappable and able to provide access through

the Labview software to the sensor. The digital I/O module can also be used in the cDAQ chassis.

### **cDAQ module interface**

The cDAQ Module Interface manages data transfers between the USB-STC2 and the I/O modules. The interface also handles auto-detection, signal routing, and the synchronization.

### **USB-STC2**

The USB-STC2 features independent High-Speed data streams; flexible AI and AO sample timing; triggering; PFI signals for multi-device synchronization; flexible counter/timers with hardware gating; digital waveform acquisition and generation; and static DIO.

The cDAQ 9172 also supports different trigger modes and four independent high speed data streams. It is also equipped with PFI signals which enable cDAQ 9172 to perform advance functions like triggering, synchronization etc. The PFI pins have a digital filter circuit which prevents noise and other functions like bounces on switches. It includes two general purpose 32-bit counter/timers.

## **9.6 DATA ACQUISITION AND PROCESSING - LABVIEW SOFTWARE**

---

Labview™ software is a powerful common platform through which many applications like real time acquisition of signals can be done in a computer-based Virtual Instrumentation (VI) environment. This is a revolutionary graphic programming language from National Instruments (NI). The Virtual Instrumentation can be defined as,

“A layer of software and/or hardware added to a general purpose computer in such a fashion that users can interact with the computer as though it were their own custom designed traditional electronic instrument”.

Hence, in the Virtual Instrumentation, the traditional instrumentation can be developed and controlled through software. This inherent advantage makes the VI extremely portable and versatile according to requirement of the application. The modular and layered programming language is very much

reusable and reconfigurable. Normally the software is designed using text based high level languages like C, C++ or BASIC. In this case, the graphical user interface (GUI) required extra to complete the whole data acquisition system. In Labview this is not required because is already a graphical programming language. This also works in Windows, Macintosh and Sun workstations. Labview can perform simple data acquisition, signal processing, result analysis and instrument control over a GPIB (IEEE-488.2) interface. Analogue inputs and outputs can be incorporated by using A/D and/or D/A external hard-wares. The other peripheral products of NI help to develop the complete instrumentation system. It also, includes image acquisition board with digital signal processing capabilities. The Labview software also, includes different signal processing algorithms such as Fast Fourier Transform sub routines. This makes it possible to do frequency based analysis of results.

The Labview application programs are identified as Virtual Instruments and presented by .VI extension. The main source code can be developed in block diagram format in graphical language. Graphical icons are used for making IF...Then loop, For...Next loop and While....loop conditional statements like it is used in text based languages. Labview has very high flexibility and a complex program can be developed in a number of simple programs i.e. VIs. Many of these simple VIs are stored in the higher level VI library as an icon. One more advantage is the execution of such program. It is not run by line by line as in other languages like C, C++, but it is data flow driven. Hence, data processing never occurs unless the desired data is read from a data buffer.

#### **9.6.1 Source code in Labview**

---

A virtual instrument has been developed for acquiring in real time, processing, displaying and storing all data from the sensors located on the loading cell and the Instron machine.

#### **Description of VI**

As explained in the previous section, the signals coming from the sensors (strain gauges and Flexiforce@s) through the signal conditioning system are acquired by the data acquisition system. The name of this VI is "spine stresses" (Figure 9-20 and 9-21). The front panel of this VI is shown



in Figure 9-20 and the block diagram of the same VI is shown in Figure 9-21. This VI is made up from a number of sub-VIs. The following sub-VIs are used in this program and their details are explained below.

**DAQmx start task**



Figure 9-18: Graphical symbol of “DAQmx start task” sub VI (National Instruments Corporation, 2010).

The task starts automatically when this VI runs (Figure 9-18). This sub VI makes this code efficient by avoiding start and stop in a loop repeatedly. This sub VI also has facility of “error in” and “error out” which means any error occur before this VI is passed to error out and if error occur while running this VI, it functions normally but generate error status in error out. This helps very much in troubleshooting and using error handlers. The “Myalltask” represents the name of the task (Table 9-1).This VI symbol is used in the block diagram of the code only.

**While loop**

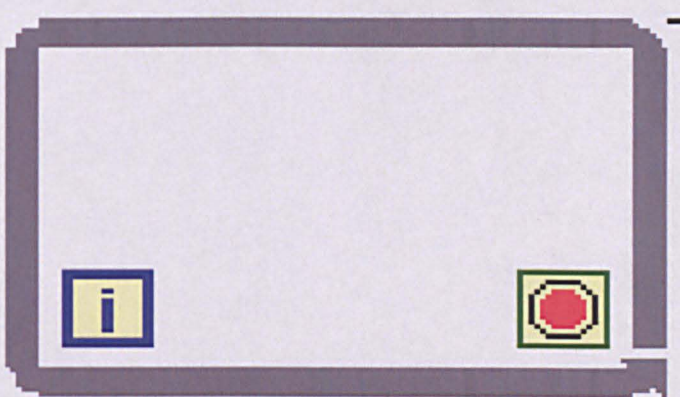


Figure 9-19: Graphical symbol of “while loop” sub VI (National Instruments Corporation, 2010).

This sub VI repeats the sub-diagram inside it until the conditional terminal, an input terminal, receives a particular Boolean value (Figure 9-19). The



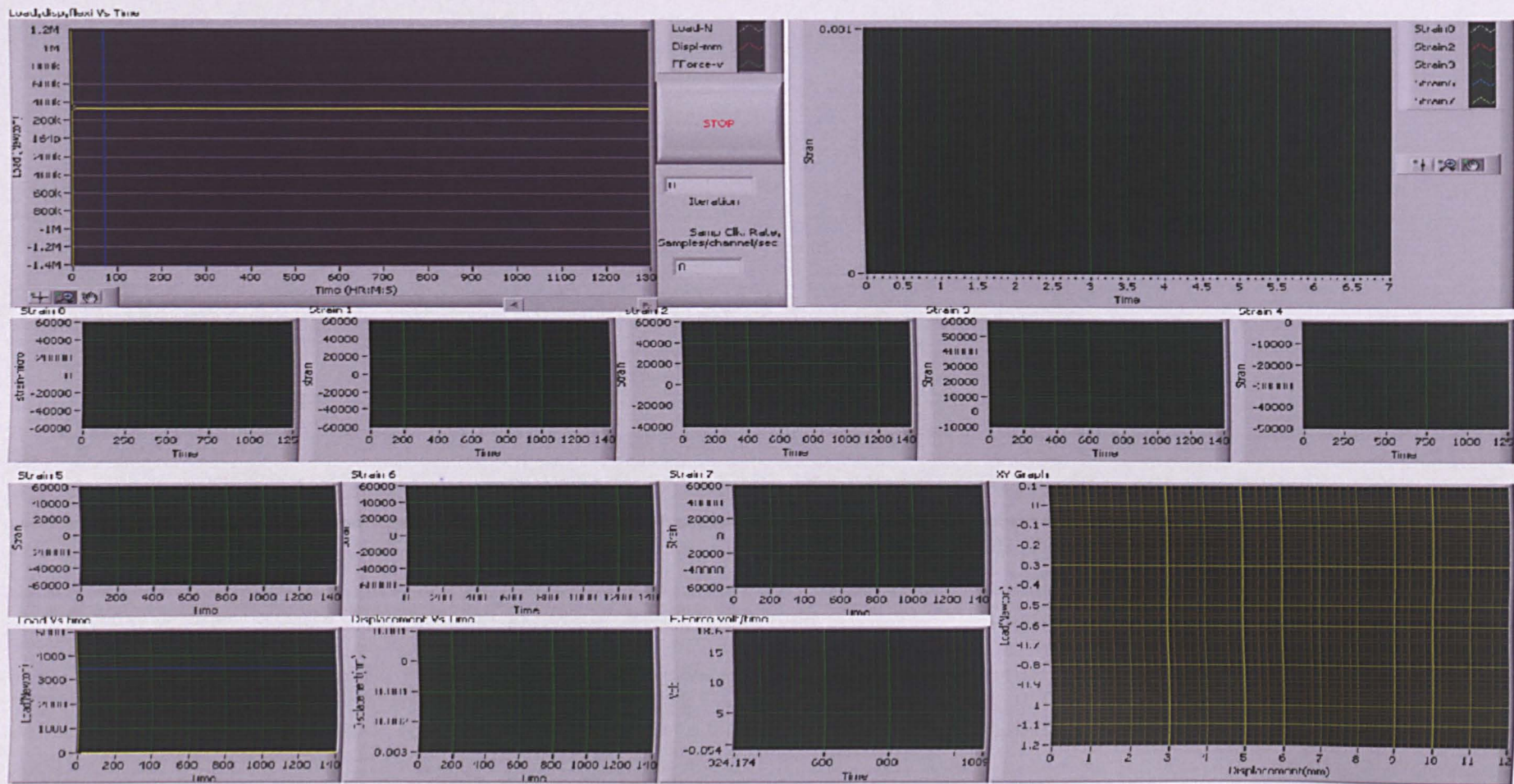


Figure 9-20: Labview front panel of the VI called "Spinestresses".







Boolean value depends on the continuation behaviour of the While Loop. Here, the "Stop if True" is selected from the shortcut menu. That means if true Boolean signal goes to RED button in the block diagram inside the while loop, the loop stops executing. In this VI, the RED button in the block diagram is connected to the error signal from DAQmx sub VIs and the STOP push button on the front panel through the OR sub VI. That means, when any or both of the signals from the error and the STOP button are TRUE the loop stop executing. In other words, either user press the STOP push button or an error occurs, the while loop stop executing. The While Loop always executes at least once. The iteration (i) terminal provides the current loop iteration count, which is zero for the first iteration and which is shown live on the front panel diagram. This VI symbol is used in the block diagram of the code only.

**DAQmx read:**

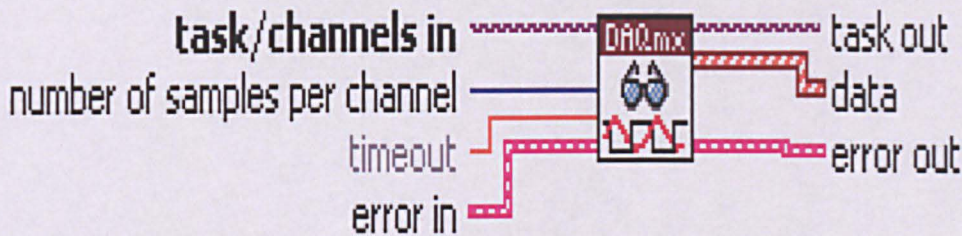


Figure 9-22: Graphical symbol of "DAQmx read" sub VI (National Instruments Corporation, 2010).

This sub VI reads samples from the task you specified in the "Myalltask" (Table 9-1) or from the virtual channels you specify. This is a polymorphic VI (Figure 9-22). This VI also specifies the format of sample to return, to read a single or multiple samples at once and whether to read from one or multiple channels. Here, the "Analog 1D waveform N channel N sample" is used that means it will read multiple samples from multiple virtual channels. This VI also has facility of "error in" and "error out", as explained above (2DAQmx start task). The 1000 shows the number of samples to read from each channel. This VI symbol is used in the block diagram of the code only.



### Resample waveform (continuous):

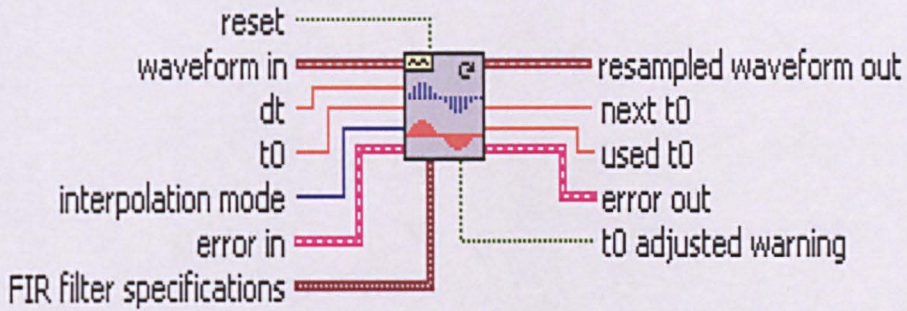


Figure 9-23: Graphical symbol of "resample waveforms" sub VI (National Instruments Corporation, 2010).

The data coming out of the "DAQmx Read" sub VI is connected to the "Resample waveform (continuous)" sub VI (Figure 9-23). The "dt" is the user-defined sampling interval for re-sampled waveform out, here; the "dt" is 0.01. This VI symbol is used in the block diagram of the code only.

### Case structure:

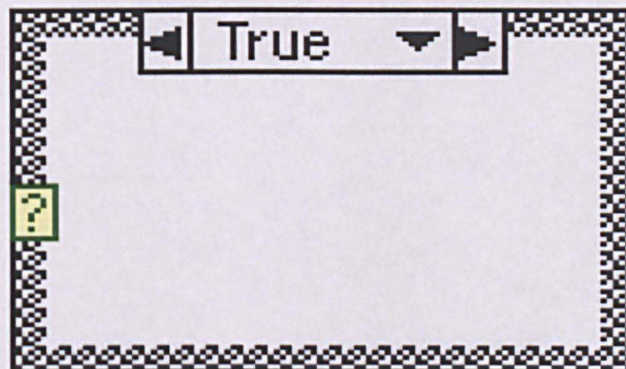


Figure 9-24: Graphical symbol of "case structure" sub VI (National Instruments Corporation, 2010).

Here, this sub VI is used for selecting two or more cases/sub diagrams on basis of different conditions or input value (Figure 9-24). IF....Then....Else or Switch statements are analogues to Case in text based programming language. For example in this code, if  $i=0$ , i.e. starting of iteration, it supplies samples as it is (TRUE case) else it execute other case sub diagram (FALSE case). In FALSE case, it uses Append waveform sub VI to append



waveforms original and re-sampled. This VI symbol is used in the block diagram of the code only.

### Append waveforms

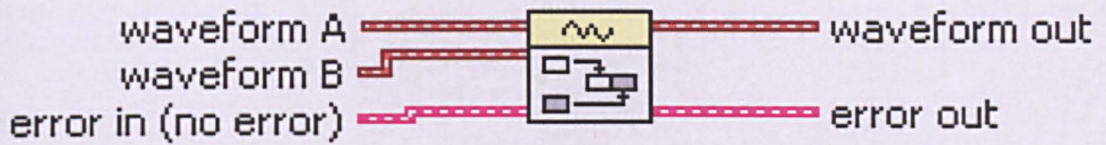


Figure 9-25: Graphical symbol of "append waveforms" sub VI (National Instruments Corporation, 2010).

This sub VI here appends the re-sampled signals at the end of the original signal (Figure 9-25). This sub VI also has facility of error in and error out. This VI symbol is used in the block diagram of the code only.

### Split signals

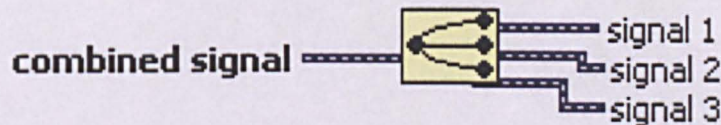


Figure 9-26: Graphical symbol of Split Signal sub VI (National Instruments Corporation, 2010).

This sub VI splits combined signal into the component signals (Figure 9-26). Here, the combined signal is a combination of all signals from all eight strain gauges, analogue o/p of applied load and displacement, and the flexi force sensors. This VI symbol is used in the block diagram of the code only.

### Merge signals

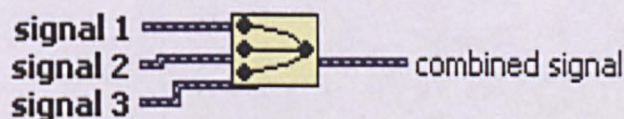


Figure 9-27: Graphical symbol of "merge signal" sub VI (National Instruments Corporation, 2010).

It merges or combines all component signals into one combined signal (Figure 9-27). This sub VI is used here to plot all signals including signals



from all strain gauges and piezoresistive sensor into one graph for better comparison. This VI symbol is used in the block diagram of the code only.

### IIR Cascade filter

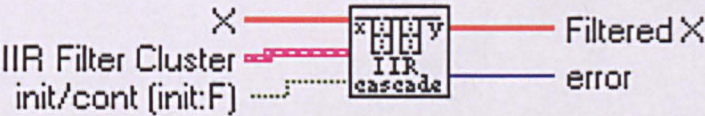


Figure 9-28: Graphical symbol of "IIR cascade filter" sub VI (National Instruments Corporation, 2010).

This sub VI is used to filter the data by using cascade IIR filter (Figure 9-28). This is specified by the IIR filter cluster. The cluster is the output from the Bessel coefficient design VI. This VI symbol is used in the block diagram of the code only.

### Bessel coefficient

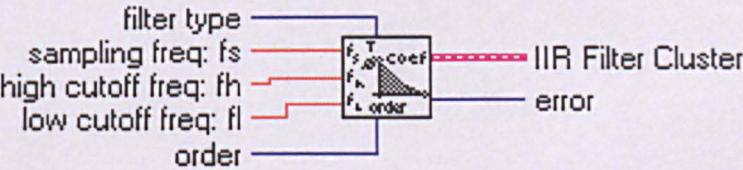


Figure 9-29: Graphical symbol of "Bessel coefficient" sub VI (National Instruments Corporation, 2010).

This sub VI produces set of coefficients to make the IIR filter based on the Bessel filter model (Figure 9-29). Here, a low pass filter is selected by using "0" as a filter type. "5" suggests the order of the IIR filter. This VI symbol is used in the block diagram of the code only.

### Waveform graphs

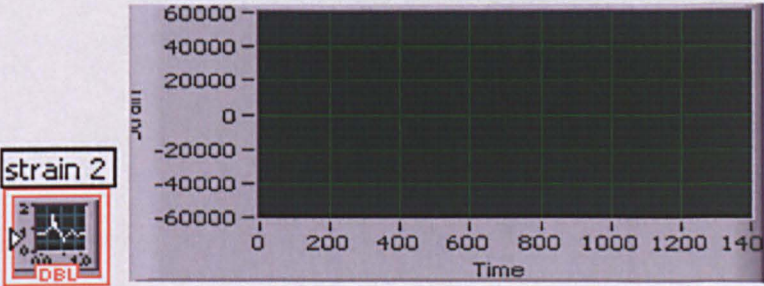


Figure 9-30: Left-Graphical symbol for Block Diagram & Right- Front panel appearance of waveform graphs sub VI (National Instruments Corporation, 2010).



This sub VI plots the graph of waveforms ion the front panel diagram (Figure 9-30). The graphical symbol shown in Figure 9-30 on the left is used in the block diagram of the VI where the wide graphical representation shown in Figure 9-30 on right shows on the front panel on the monitor of the PC.

**DAQmx stop task**

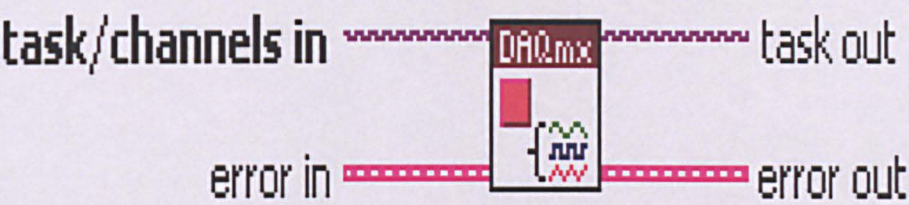


Figure 9-31: Graphical symbol of “DAQmx stop task” sub VI (National Instruments Corporation, 2010).

This sub VI stops the task and returns it to the state the task was in before the DAQmx Start Task VI ran or the DAQmx Write VI ran with the auto start input set to TRUE (Figure 9-31). Same as the DAQmx Start it increases efficiency of program execution by avoiding unnecessary start and stop in loop. This VI symbol is used in the block diagram of the code only.

**Open data storage**

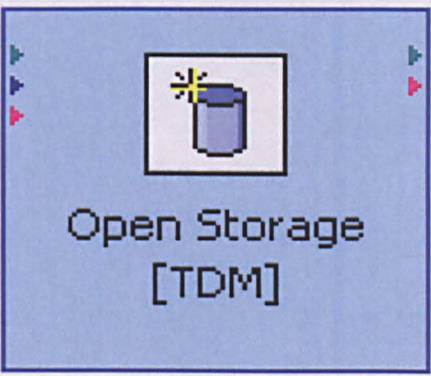


Figure 9-32: Graphical symbol of “open data storage” express VI (National Instruments Corporation, 2010).

This express VI opens an NI test Data Exchange Format (.tdm) file for reading or writing (Figure 9-32). This VI can be used to create a new file or



replace an existing file. Use the “Close Data Storage” VI to close the reference to the file. This VI symbol is used in the block diagram of the code only.

### Simple error handler

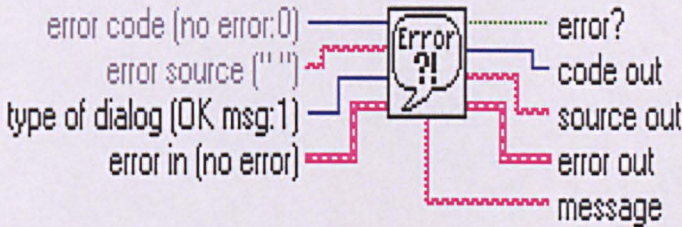


Figure 9-33: Graphical symbol of “simple error handler” sub VI (National Instruments Corporation, 2010).

This sub VI indicates whether an error occurred (Figure 9-33). If an error occurred, this VI returns a description of the error and optionally displays a dialog box. This VI calls the “General Error Handler” VI and has the same basic functionality as General Error Handler but with fewer options. This VI symbol is used in the block diagram of the code only.

### File dialog

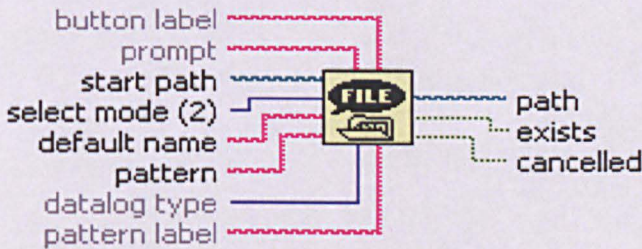


Figure 9-34: Graphical symbol of “file dialog” sub VI (National Instruments Corporation, 2010).

Displays a dialog box with which you can specify the path to a file or directory (Figure 9-34). This dialog box can be used to select existing files or directories or to select a location and name for a new file or directory. This VI symbol is used in the block diagram of the code only.

### Set properties

This express VI defines the properties of an existing file, channel group, or channel (Figure 9-35). If you configure this VI before you wire a refnum to



storage refnum, the configuration might change depending on the refnum you wire. For example, if you configure this VI for a channel and then wire a channel group refnum, the VI returns broken wires on the block diagram because the same properties are not available for a channel group. This VI symbol is used in the block diagram of the code only.



Figure 9-35: Graphical symbol of “set properties” express VI (National Instruments Corporation, 2010).

**Write data**



Figure 9-36: Graphical symbol of “Write data” express VI (National Instruments Corporation, 2010).

This express VI used to define channels or channel group and that also specify the same in file where to write data (Figure 9-36).This VI symbol is used in the block diagram of the code only.

**Close data storage**

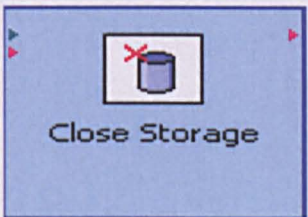


Figure 9-37: Graphical symbol of “close data storage” express sub VI (National Instruments Corporation, 2010).

This express VI saves the data to file and closes the file after reading from it or writing to it (Figure 9-37). This VI symbol is used in the block diagram of the code only.

**Write Labview measurement file**

This sub VI writes data to the Labview Measurement file (Figure 9-38). The graphical symbol used in block diagram of the code only. Here in this experiment the data, collected from the sensor at a rate of 100 samples per second. The recorded data can be helpful for further analysis of the results. It saves this data in file with extension .lvm.



Figure 9-38: Graphical symbol of “write labview measurement file” express VI (National Instruments Corporation, 2010).



# **10 STUDY PROTOCOL AND RESULTS FOR THE *IN VITRO* LOADING OF THE ARTIFICIAL SPINAL DISC PROSTHESIS – LOADING CELL**

---

## **10.1 INTRODUCTION**

---

Following the experimental set-up as described in chapter-9, this chapter describes the details of the study protocol and results of the *in vitro* loading of the artificial spinal disc prosthesis load cell. The following sections describe all the designed *in vitro* experiments and the results of the experiments according to the study protocols.

## **10.2 STUDY PROTOCOL**

---

The proposed experimental method satisfies the FDA standard F2346-05 for static and dynamic tests with axial load, shear load and torsion. The loading range for artificial lumbar spinal disc prosthesis is from 600 N to 2000 N. In this experiment, the compressive loading was applied in the normal direction to the artificial disc (with all sensors embedded) using a computer controlled Universal Testing Machine (Instron, Bucks, UK). The load that was applied to the disc was from 0 to 4 kN, which is the typical natural maximum range of load that the human spinal disc can be exposed (White and Panjabi, 1990). The study protocols are designed in such a way that the visco-elastic characteristics, i.e. creep and relaxation can also be investigated. In these experiments the applied load was also held constant at certain value for some time and in some protocols the position of the upper movable tool of the UT machine's position was also maintained for a specified period of time. In these protocols, the loading speed was also variable in order to study the effects of loading speed on the sensor's output. The following experimental methods are described below.

10.2.1 Experiment 1: Exp\_4k\_500NPS\_LH300S

Figure 10-1 describes the events in this experiment. In summary the experiment was conducted as follows:

- ✦ Loading range: 0 – 4 – 0 kN
- ✦ Loading speed: 500 Newton per second
- ✦ Holding interval: 300 seconds with load holding

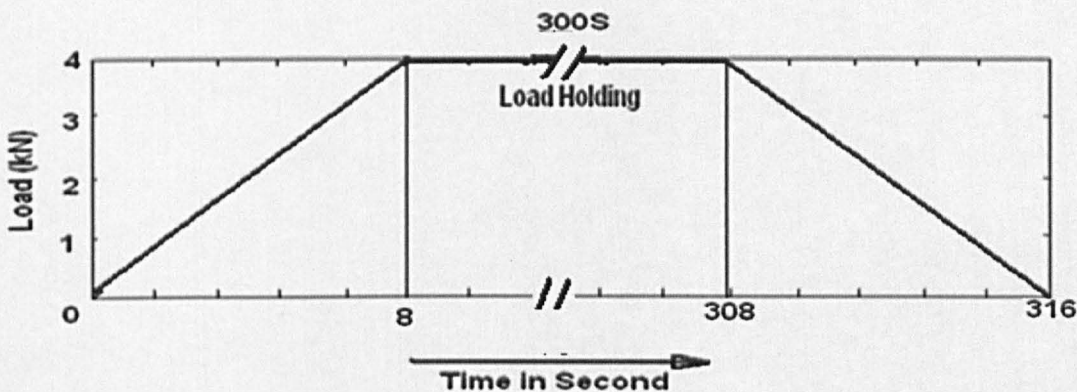


Figure 10-1: Graphical representation of Experiment 1

10.2.2 Experiment 2: Exp\_4k\_500NPS\_PH300S

Figure 10-2 describes the events in this experiment. In summary, the experiment was conducted as follows:

- ✦ Loading range: 0 – 4 – 0 kN
- ✦ Loading speed: 500 Newton per second
- ✦ Holding interval: 300 seconds with position holding

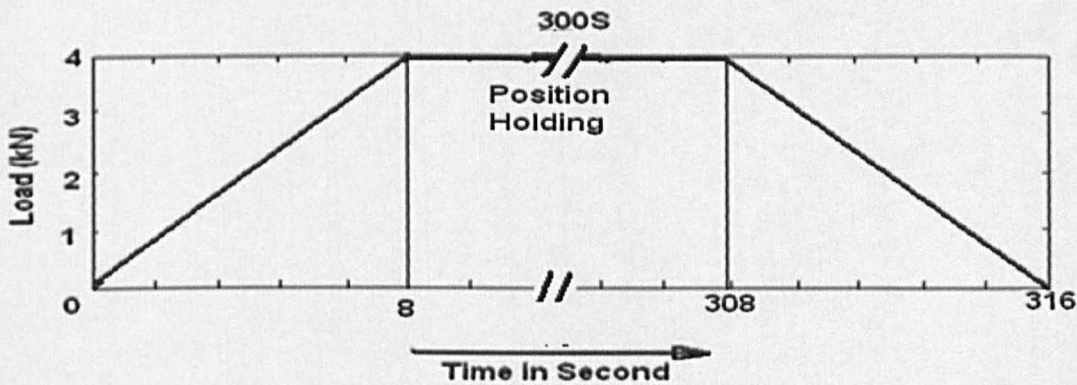


Figure 10-2: Graphical representation of Experiment 2

### 10.2.3 Experiment 3: Exp\_4k\_500NPS\_NOH

Figure 10-3 describes the events in this experiment. In summary the experiment was conducted as follows:

- ✦ Loading range: 0 – 4 – 0 kN
- ✦ Loading speed: 500 Newton per second
- ✦ No Holding interval

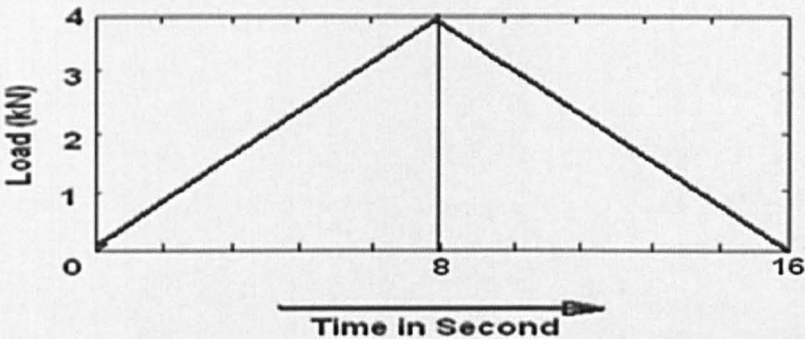


Figure 10-3: Graphical representation of Experiment 3

### 10.2.4 Experiment 4: Exp\_4k\_100NPS\_NOH

Figure 10-4 describes the events in this experiment. In summary the experiment was conducted as follows:

- ✦ Loading range: 0 – 4 – 0 kN
- ✦ Loading speed: 100 Newton per second
- ✦ No Holding interval

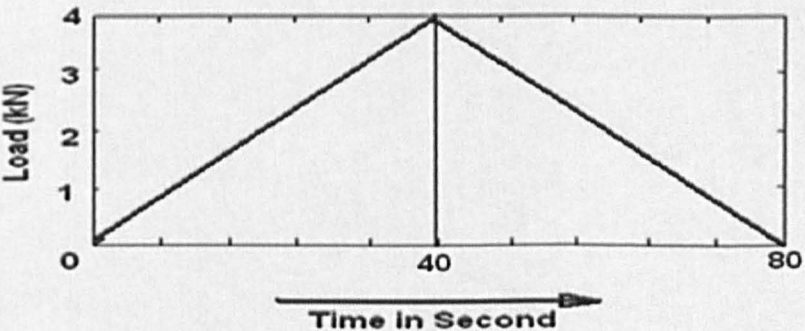


Figure 10-4: Graphical representation of Experiment 4

### 10.2.5 Experiment 5: Exp\_4k\_10NPS\_NOH

Figure 10-5 describes the events in this experiment. In summary the experiment was conducted as follows:



- ✦ Loading range: 0 – 4 – 0 kN
- ✦ Loading speed: 10 Newton per second
- ✦ No Holding interval

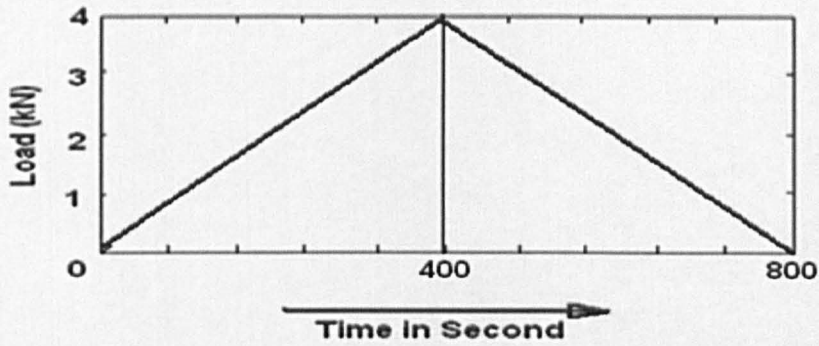


Figure 10-5: Graphical representation of Experiment 5

#### 10.2.6 Experiment 6: Exp\_step1k\_500NPS\_LH30S

Figure 10-6 describes the events in this experiment. In summary the experiment was conducted as follows:

- Loading range: 0 – 4 – 0 kN with a step of 1 kN
- Loading speed: 500 Newton per second
- Holding interval: 30 seconds at each step of 1 kN with load holding

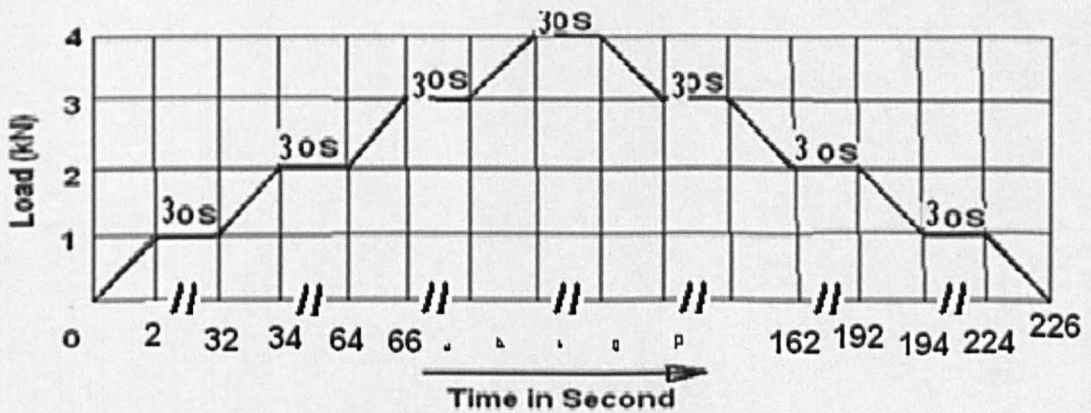


Figure 10-6: Graphical representation of Experiment 6

#### 10.2.7 Experiment 7: Exp\_step1k\_10NPS\_LH30S

Figure 10-7 describes the events in this experiment. In summary the experiment was conducted as follows:

- Loading range: 0 – 4 – 0 kN with a step of 1 kN
- Loading speed: 10 Newton per second
- Holding interval: 30 seconds at each step of 1 kN with load holding

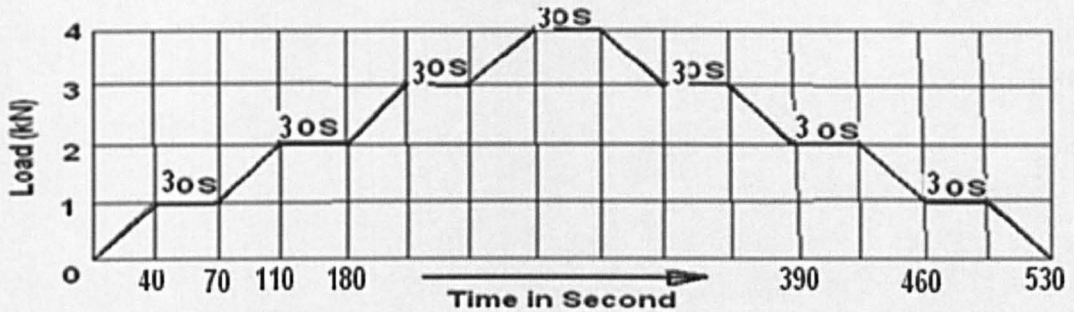


Figure 10-7: Graphical representation of Experiment 7

### 10.3 RESULTS OF THE *IN VITRO* EXPERIMENTS

In above section 10.2, the study protocols for experiments are described in details. This section covers the results of the experiments performed according to those study protocols. In summary the selected protocols are as under,

1. Experiment 1: Exp\_4k\_500NPS\_LH300S
2. Experiment 2: Exp\_4k\_500NPS\_PH300S
3. Experiment 3: Exp\_4k\_500NPS\_NOH
4. Experiment 4: Exp\_4k\_100NPS\_NOH
5. Experiment 5: Exp\_4k\_10NPS\_NOH
6. Experiment 6: Exp\_4k\_step1k\_500NPS\_LH30S
7. Experiment 7: Exp\_4k\_step1k\_10NPS\_LH30S

The results of these experiments will enable us to study the effects of loading/unloading speed, effects of different types of load holding i.e. load keep constant for particular duration, creep-relaxation of artificial spinal disc prosthesis by measuring load decay while keeping positions of loading jaws of universal testing machine constant (position holding) and many others. Each experiment's results are presented in the following sub-sections from 10.3.1 to 10.3.7.

### 10.3.1 Results of experiment 1: Exp\_4k\_500NPS\_LH300S

---

Experiment 1 was performed as described in the protocol (section 10.2.1). The results are shown in graphical format; see Figure 10-8 and Figure 10-9. The graphs in Figure 10-8 present the outputs from all eight strain gauges (s.gauge 0 to s.gauge 7) and the outputs from the two piezoresistive-Flexiforce® sensors (F.force\_upper and F.force\_lower) when a compressive load is applied (with respect to time). The last graph depicted in Figure 10-8 titled as "Load Vs Time" presents the analogue output of the applied compressive load by the universal testing machine. In the graphs, outputs from all strain gauges are presented in Microstrain ( $\text{Microstrain} = \text{strain} \times 10^{-6}$ ) and outputs from the two Flexiforce® sensors are in analogue dc volt (Y-axis). The time is in seconds (x-axis). The red colour portions in all graphs shows the noisy raw signal and the black line plots are the best fit lines.

Similarly in Figure 10-9, the graphs present the outputs from all eight strain gauges (s.gauge 0 to s.gauge 7) and the outputs from the two piezoresistive-Flexiforce® sensors (F.force\_upper and F.force\_lower) when a compressive load is applied (with respect to the applied compressive load). In the graphs, outputs from all strain gauges are presented in Microstrain ( $\text{Microstrain} = \text{strain} \times 10^{-6}$ ) and outputs from the two Flexiforce® sensors are in analogue dc volt (Y-axis). The applied compressive load is in Newton (x-axis). The black line plots are the best fit lines of the raw data.

The outputs from all the eight strain gauges look similar in characteristics and after repeating the same experiments 10 times it exhibits the same results with tight tolerances. That confirms the suitability of the use of strain gauges for this application. In Figure 10-8, a typical noise pattern is shown by the red colour portion and it can be seen in the graphs representing outputs from the all strain gauges. Most probably, it is mainly due to the vibration of the hydraulic motor and movement of the parts of the universal testing machine. Similarly, a different noise pattern can also be seen in the graphs representing outputs from the two Flexiforce® sensors. The difference in noise patterns are probably, due to the different sensitivity of the sensors in the particular experimental set-up.



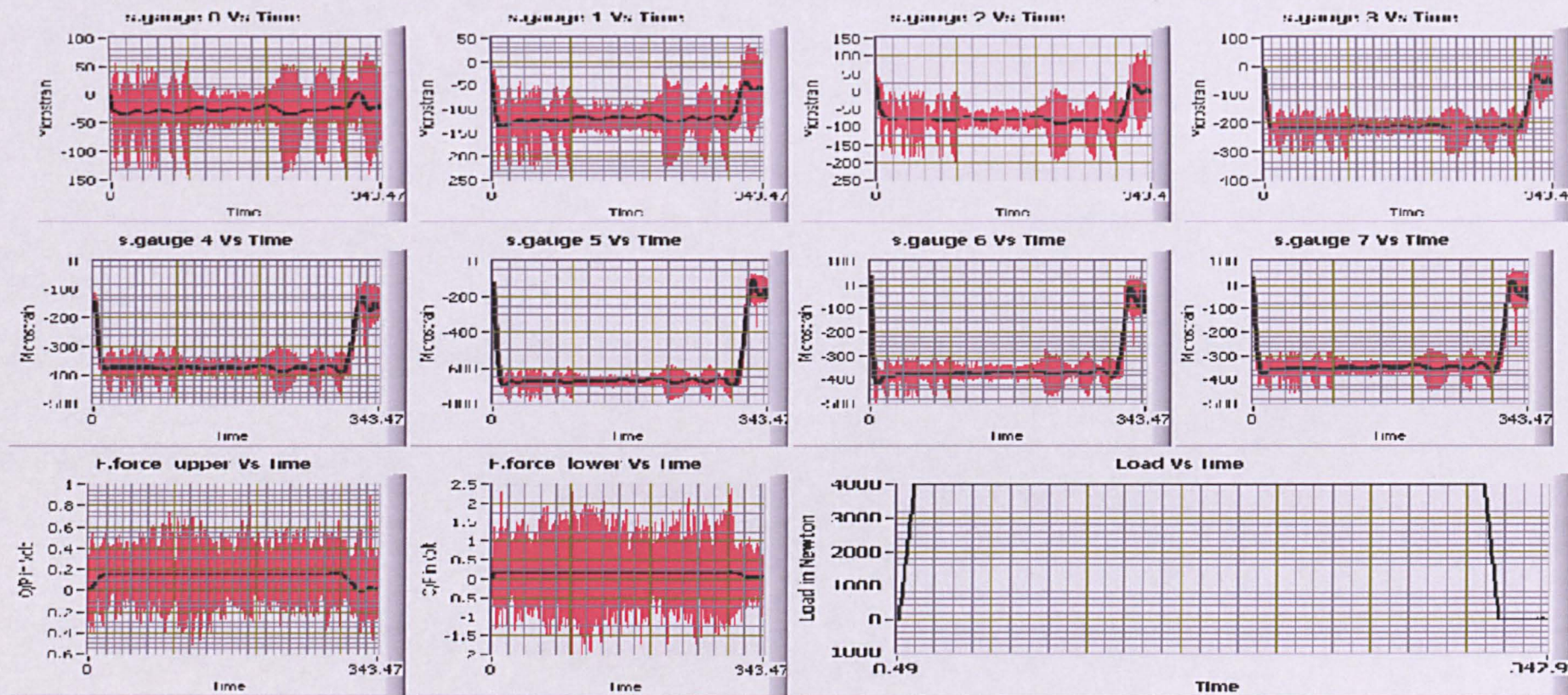


Figure 10-8: All eight strain gauge's outputs, two piezoresistive-Flexiforce® sensor's outputs and applied compressive load in Newton with respect to time in seconds. (Experiment protocol: Exp\_4k\_500NPS\_LH300S).



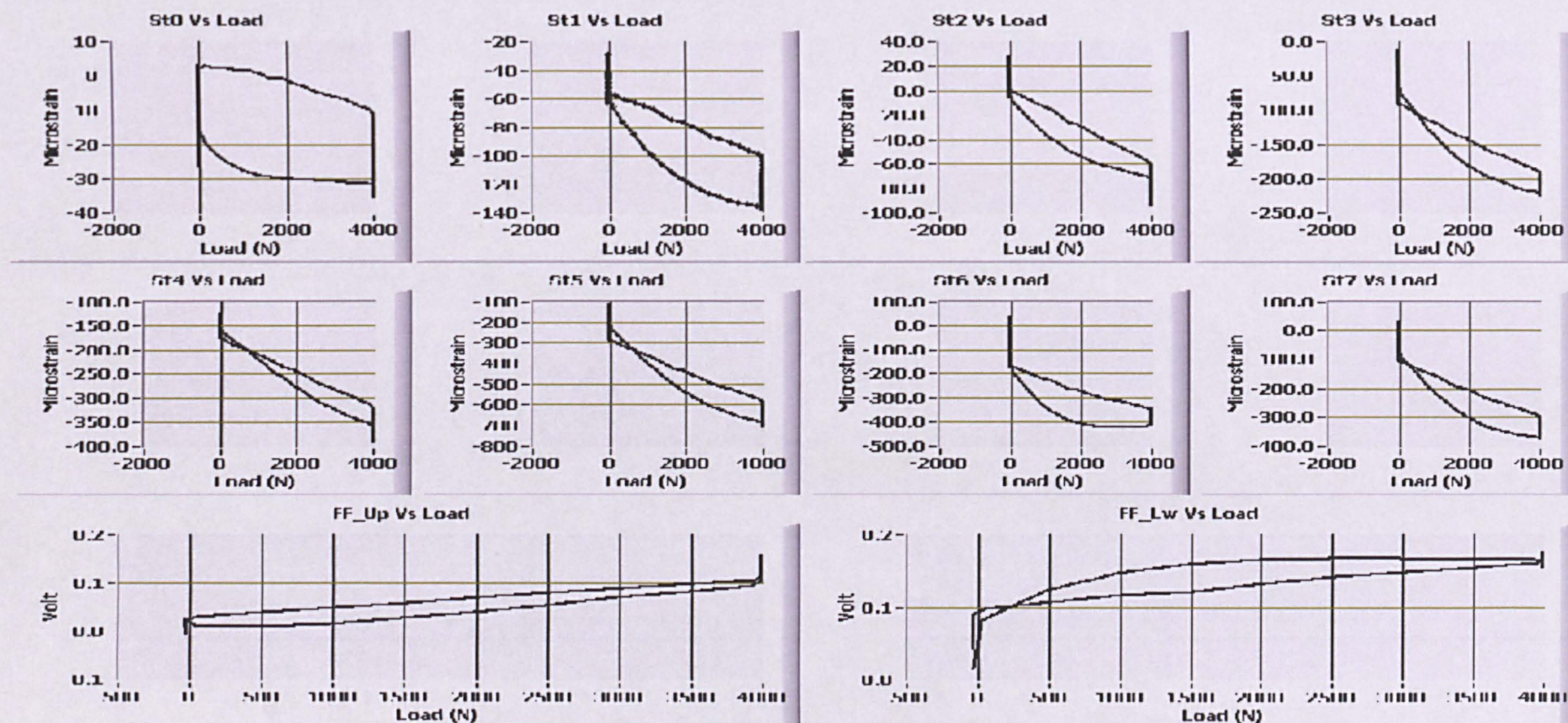


Figure 10-9: All eight strain gauge's outputs and two piezoresistive-Flexiforce® sensor's outputs with respect to applied compressive load in Newton.  
(Experiment protocol: Exp\_4k\_500NPS\_LH300S).



A significant effort has been put forward in analyzing the signals (and removing the noise) that were presented in Figure 10-8 and 10-9. Therefore, it was decided that it is something that needs to be explained and reported. This explanation will be done only for this first experiment and also for one typical strain gauge (here, s.gauge 0) as the same steps were followed for all subsequent experiments.

Figure 10-10 shows a magnified view from the output (Microstrain) of the one typical strain gauge out of all sensors (SG 0 Vs Time).

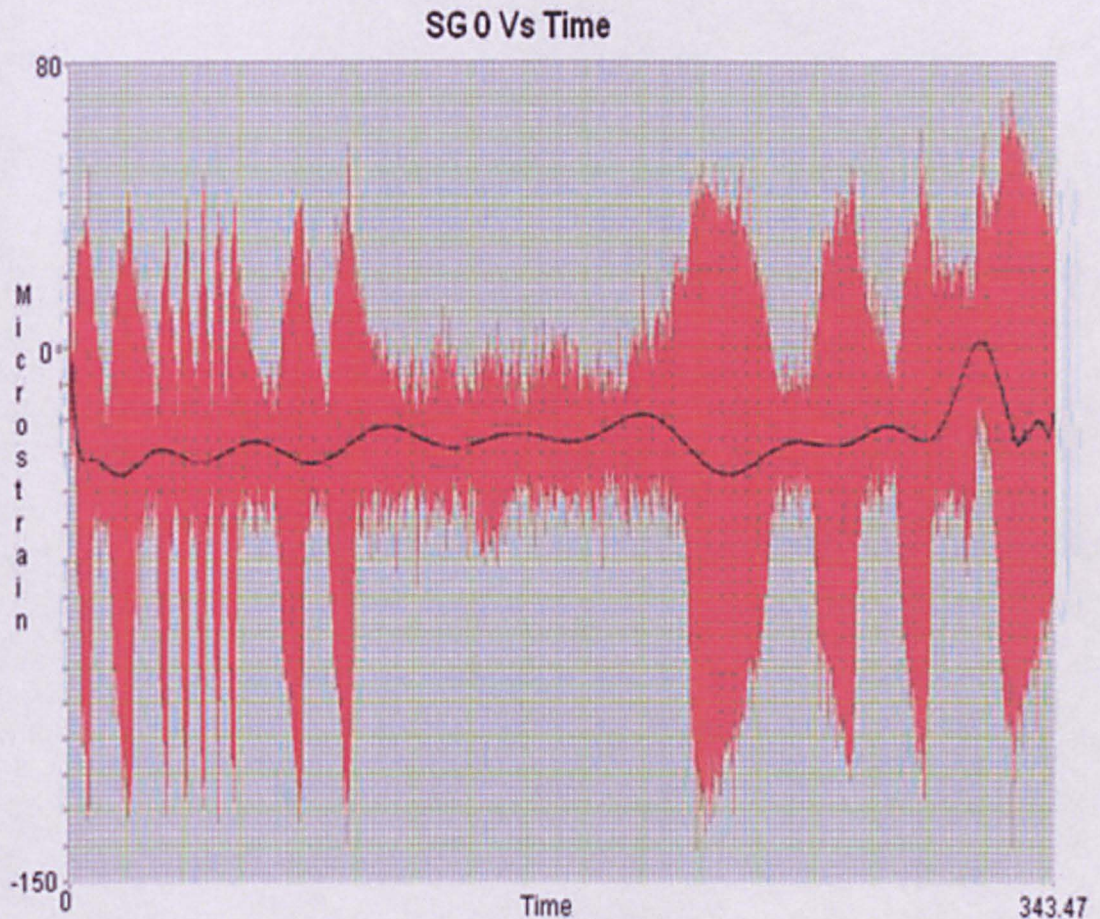


Figure 10-10: Raw Data with lots of typical noise of one typical strain gauge's output (SG 0 Vs Time) with respect to time.

The raw data coloured in red contain the output of s.gauge 0 (SG 0) together with noise, and therefore the challenge is to correctly filter out the actual strain gauge output. To filter the noise, a low pass 3rd order Butterworth IIR Filter is used with 5 Hz cut-off frequency. By applying FFT analysis the cut-off frequency of 5 Hz is selected here. The filtered signal is shown in Figure 10-11. In Figure 10-8, in the last row the last graph (Load



Vs Time) shows the analogue output of the applied compressive load and therefore the strain gauge output should be similar to this. In this experiment the artificial disc prosthesis is loaded from 0 to 4 kN and kept constant for finite time and again unloaded from 4 to 0 kN. Hence, in loading cycle and unloading cycle the signal is dynamic (non-stationary type), whereas in case of constant load cycle, the signal is stationary type. One of the challenging problems is the selection and application of the signal processing technique because the whole graph requires different signal processing techniques in different parts.

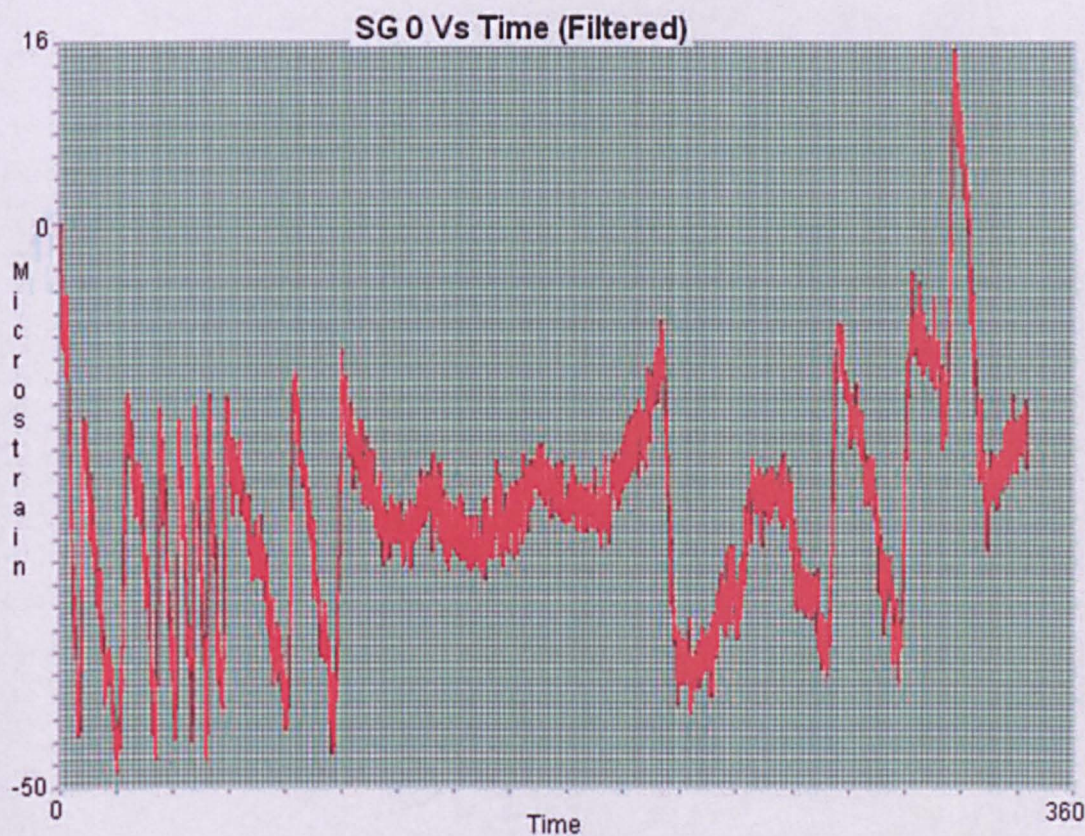


Figure 10-11: Filtered data of one typical strain gauge's output (SG 0 Vs Time) with respect to time. Low pass 3rd order Butterworth IIR filter-with cutoff frequency 5 Hz is used for filtering.

The first part is when loading from 0 to 4 kN, the second part is when load holding at around 4 kN for around 300 seconds and the third part is unloading from 4 to 0 kN. According to the experiment protocol, the compressive load is applied from 0 to 4 kN in the first part with 500 NPS (Newton per Second) loading speed. So, the duration of the first part is

around 8 seconds, the duration of the second part is of about 300 seconds and the duration of the third part is of around 8 seconds. So, in the first and the third part, the output signals from the sensors (during loading and unloading) are of non-stationary type of signal and in the second part (load holding) the output signal from the sensors are of stationary type. Stationary signal means the value of load do not changes with respect to time and non-stationary signal means the value of the load changes with respect to time. Hence, the same signal processing technique cannot be applied to whole waveform graph.

To better understand the signal and noise, a comprehensive noise analysis was implemented in Labview software where a custom made virtual instrument (VI) has been developed for this purpose. Figure 10-12, shows the front panel of the Labview-VI named "Noise Statistics.vi". This Labview-VI can analyze any signal from any sensor by connecting the particular sensor's channel with the rest of the statistical analysis code. In block diagram of this Labview-VI (Figure 10-13), the s.gauge 0 is connected by connecting channel 0 (First top channel). In front panel of the Labview-VI (Figure 10-12), the chart titled "Signal" shows the one packet/segment of retrieved data collected at every instance of sample scan from the output of the particular sensor, in this case s.gauge 0.

Each packet is a collection of samples from the sensor's output for 3 seconds. The sampling rate is 100 Hz, so the total number of samples in each packet/segment is 300. Similarly, the main chart shows the output of the s.gauge 0 for the duration of the whole experiment. The red coloured line represents the arithmetic mean value of the sensor's output samples for each packet/segment of data collected at every sample scan, here 300 samples. In the same way the maximum value of the sensor's output is represented by a blue coloured line and the minimum value represented by a green coloured line. Figure 10-13 shows the block diagram of the same Labview-VI. The left most symbol represents the "Read Measurement File" express VI. That VI reads the saved data file in any one of the formats like .lvm, .tdm and .tdms.

Here, (Fig. 10-13) the output of this VI contains signals from all sensors and the analogue output of applied compressive load with respect to time. By using the signal separating VI, all signals are separated for further



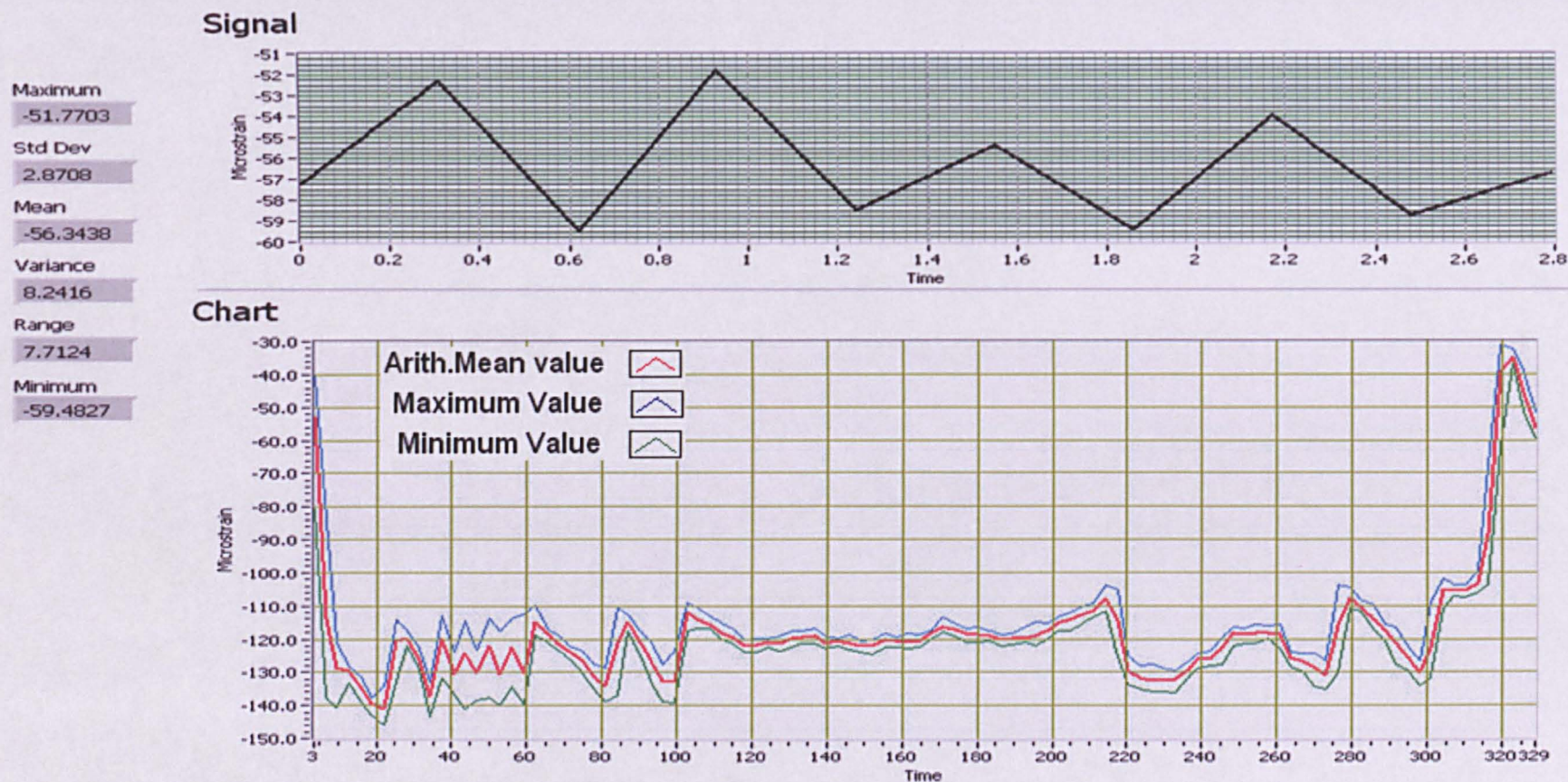


Figure 10-12: Front panel of Labview code Noise Statistics.vi. This can select any one channel of signal by just one change in block diagram. The two charts "signal" and "Chart" show statistical analysis of signal. The minimum value, maximum value, mean value, standard deviation, variance and range of values are also saved in spreadsheet format (.lvm) in memory.



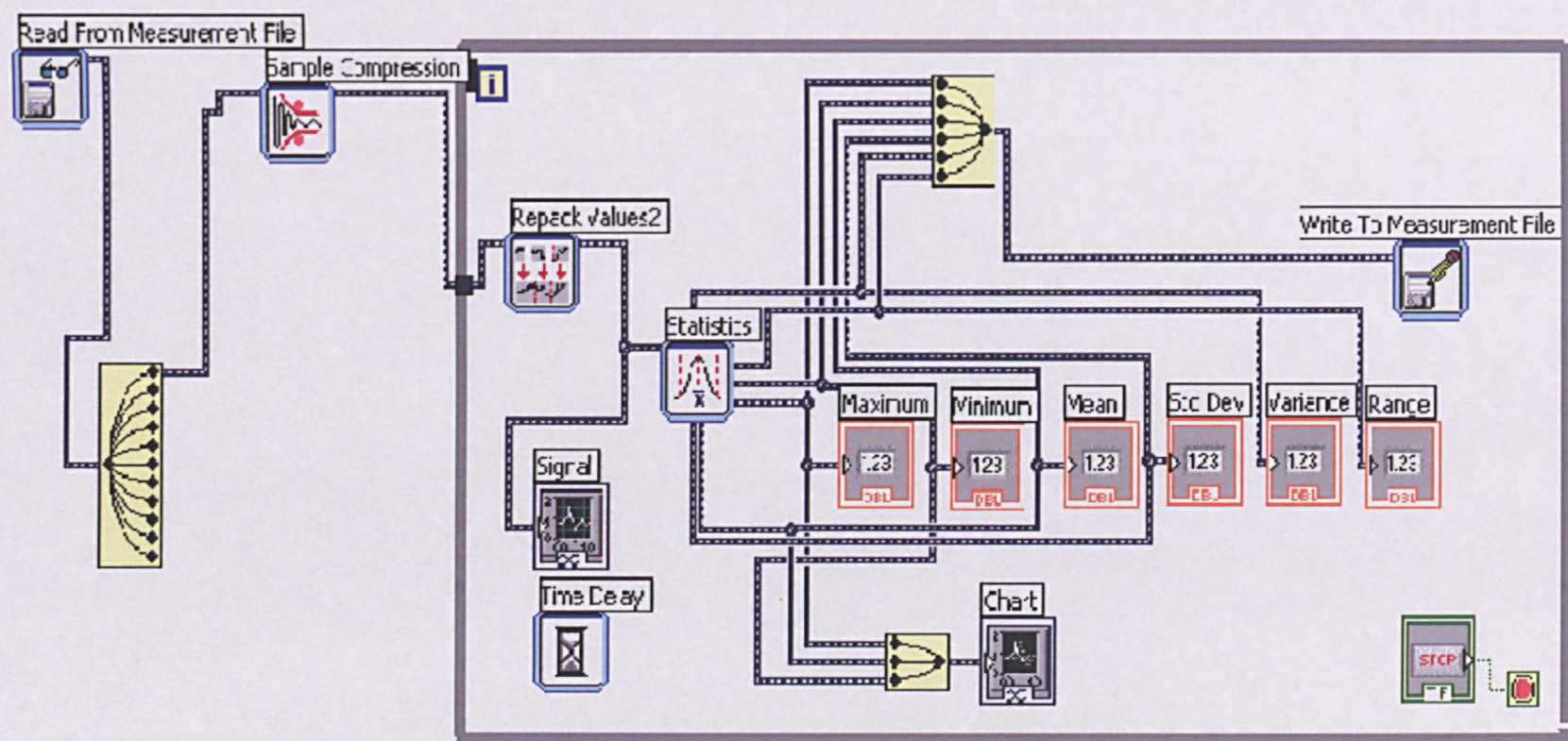


Figure 10-13: Block diagram of the Labview code named "Noise Statistics.vi", Front panel shown in Figure 11-5.



processing. A total 11 channels are there to represent all signals. The total number of data is compressed by 5 for simplification of data analysis by a "Data Compression" VI. Then, data is further statistically processed through each packet and represented by minimum value, maximum value, arithmetic mean value, standard deviation, range and variance. The same is saved in spreadsheet format file in the computer's memory.

The main chart shown in the front panel of the Labview-VI (Figure 10-12) is presenting statistical analysis of noise for the output from SG 0. The whole graph is divided into three parts as mentioned before. As the 1st and 3rd part of the graph is of duration 8-9 seconds (because loading speed = 500 NPS) in comparison to the 2nd part of the graph of which is of duration of 300 seconds, therefore, each part of the graph is represented separately in individual graphs.

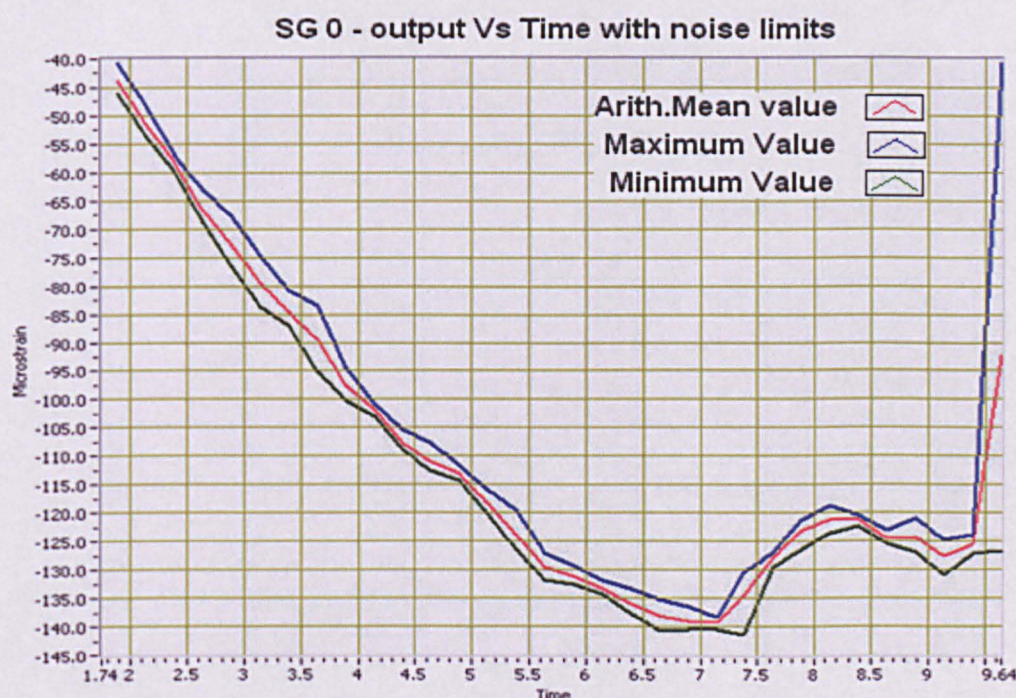


Figure 10-14: Graphical representation of statistical analysis of noise of output of SG 0 when compressive loading is applied from 0 to 4 kN (1st part of the graph).

Figure 10-14 shows the 1st part of the graph, Figure 10-15 shows 2nd part of the graph and Figure 10-16 shows the 3rd part of the graph.



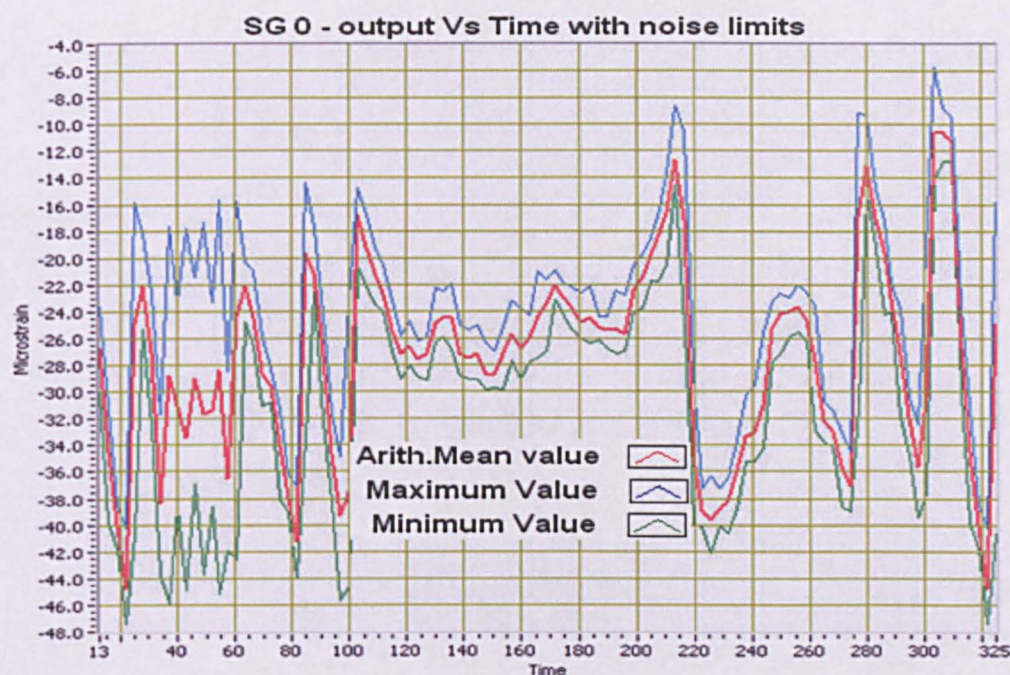


Figure 10-15: Graphical representation of statistical analysis of noise of output of SG 0 when load kept constant at 4 kN (2nd part of the graph).

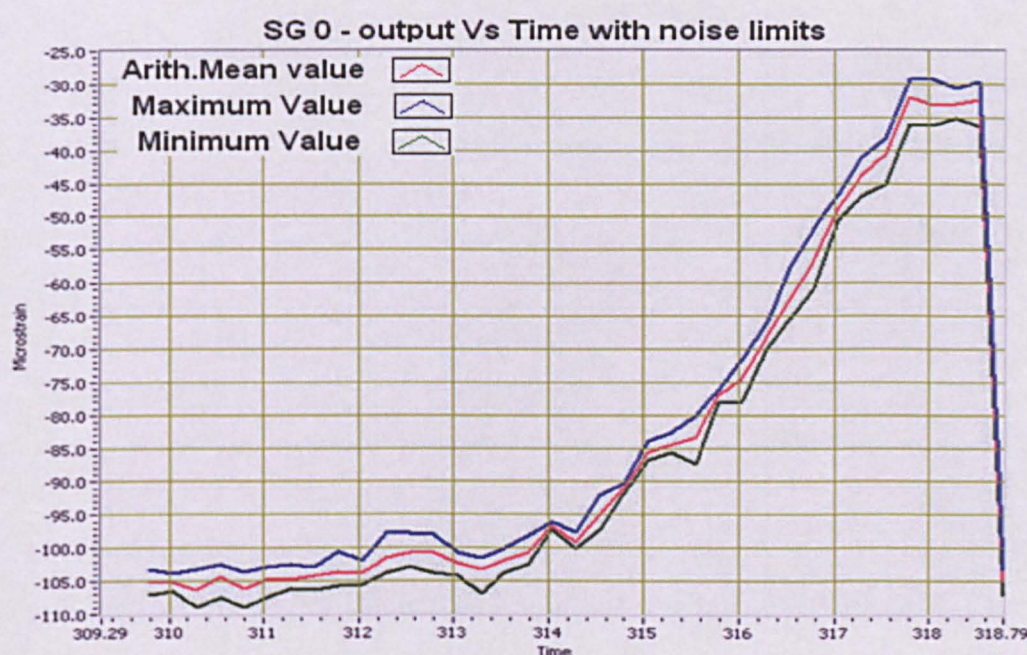


Figure 10-16: Graphical representation of statistical analysis of noise for the output of SG 0 when unload from 4 to 0 kN (3rd part of the graph).

The results in tabulated form, from running the above mentioned Noise Statistics.vi for the output of strain gauge SG 0, are shown in Table 10-1.



Table 10-1: Statistical analysis summary of whole graph (SG 0)

Microstrain	Std. Deviation	Variance	Range
Max	11.567	133.808	28.261
Min	0.642	0.412	1.979
Range	10.925	133.396	26.281
Mean	2.601	13.130	7.596

The above statistics mainly postulates that for the whole graph of the waveform the mean value of the standard deviation is 2.601, variance is 13.130 and range of values is 7.596.

The first part of the waveform graph which is 8-9 seconds with a sampling speed of 100 Hz, comprises of approximately 900 samples. So, the first 900 samples of the waveform graph are converted to the final plot using “curve fitting” signal processing techniques. The model of polynomial equation of order N is used here. For the second part of the waveform graph having approximately total samples of 30,000, is converted to the final plot of waveform using the same signal processing curve fitting tools as used in the first part, but may be of different value of N. The third part is the same as the first part with remaining number of samples till the end. So, after multipart parametric signal processing, the resultant waveform is shown in Figure 11-10, named “SG 0 Vs Time and Load Vs Time”. The time in second is shown along X-axis. The graph has two Y-axis, one is in Microstrain and other is in applied compressive load (Newton). The graph is very clear and very much similar in characteristics of the analogue output of applied compressive load. The strain gauge is experiencing compression that’s why the load Vs strain graph is inversely proportional as can be seen in Figure 10-17.

Similarly, Figure 10-18 shows the graphical presentation of the two Flexiforce® sensors with respect to time. The graph has two Y-axis similar to shown in Figure 10-17, one is in Microstrain and other is in applied compressive load (Newton).

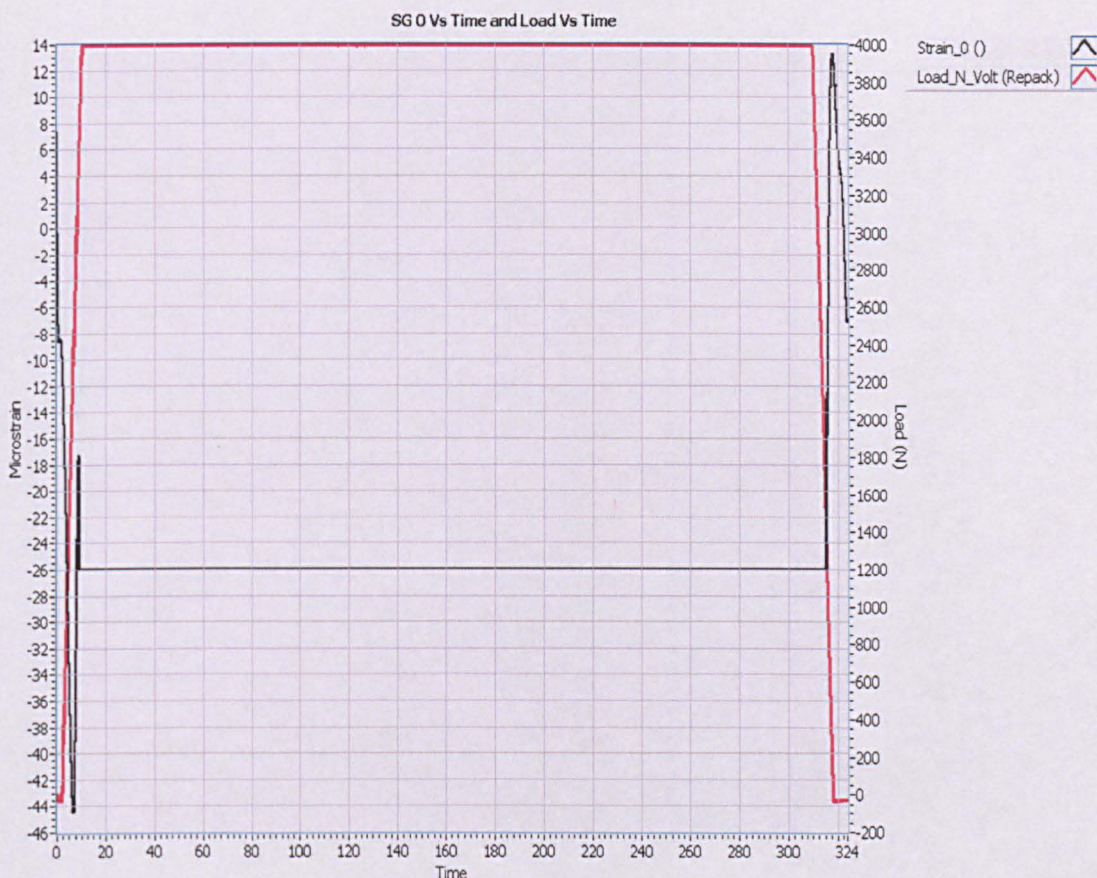


Figure 10-17: Typical strain gauge output and applied load graph with respect to time (SG 0 Vs Time and Load Vs Time).

The graphs are obtained using identical signal processing techniques for both the Flexiforce® sensors. The graphs are very clear and very similar in characteristics of the analogue output of the applied compressive load. The Flexiforce® sensor's output is directly proportional to the applied compressive load as can be seen in Figure 10-18. The signal processing techniques used in SG 0 Vs Time is used for plotting all outputs of all eight strain gauges (SG 0 to SG 7) and the two Flexiforce® sensors (Flexiforce®\_Upper and Flexiforce®\_Lower). For better comparison all outputs are plotted on the same graph as shown in Figure 10-19.



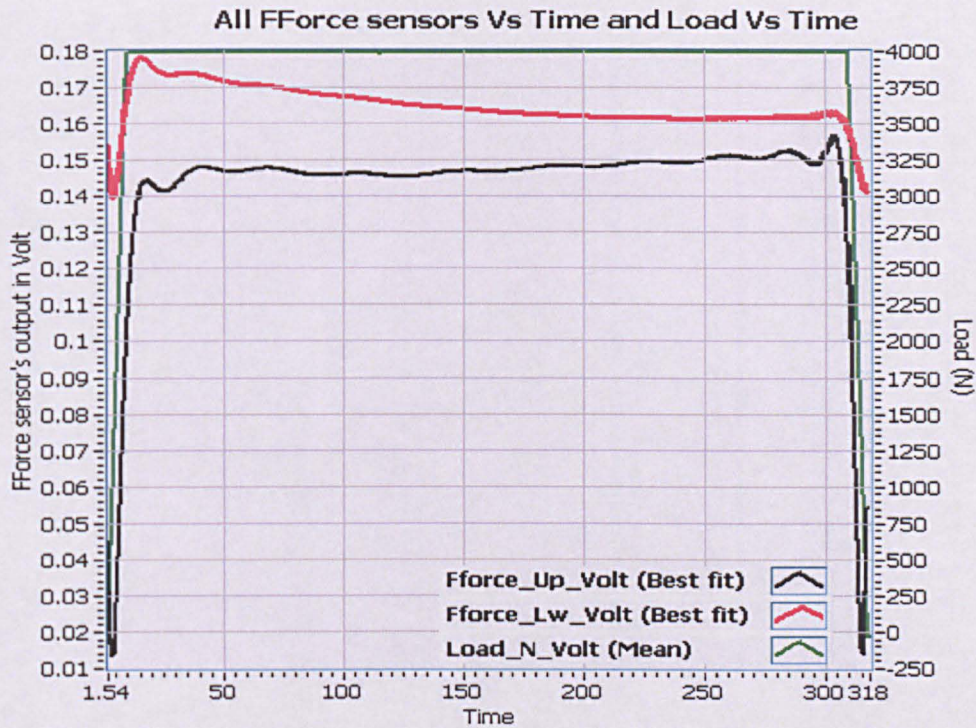


Figure 10-18: Outputs from two Flexiforce® sensors and applied load graph with respect to time.

The outputs from all sensors and the output from representing the applied compressive load look very similar in characteristics. The only noticeable difference is in the outputs from the strain gauges which exhibit a little non-linearity like quadratic or polynomial curve. Most probably this is due to the visco-elastic properties of the inlay material of the spinal artificial disc. That supports one of the main objectives of this research.

Figure 10-20 shows the same plots as Figure 110-19 but without applying signal processing as explained before. By comparing Figure 10-19 and Figure 10-20 it can be noticed that the output behaviour is not significantly modified due to the signal processing. Hence, the designed and used signal processing technique is suitable for this application.

As explained before, the 1st and 3rd part of the graph which represents the sensor's output when loading and unloading has a duration of 8-9 seconds only. This is much less compared to the 2nd part of the graph which is 300 seconds. Hence, to clearly present the graph, the 1st and 3rd part of the graph in Figure 10-19 is magnified and shown in Figure 10-21 and 10-22 respectively.



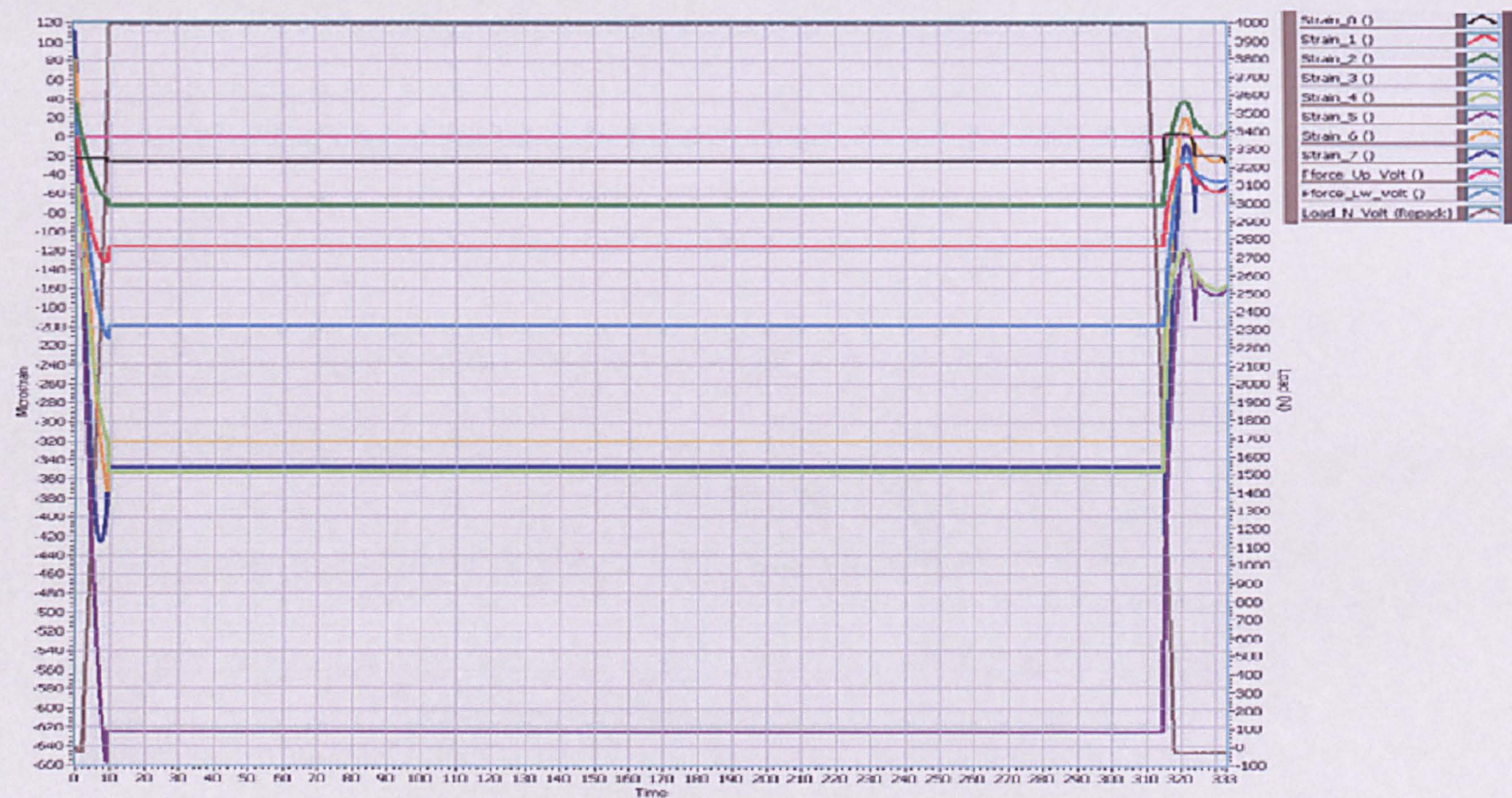


Figure 10-19: All SG output (Microstrain) and two Flexiforce® sensor's output (Volt) & Load (N) Vs Time (S), Experiment protocol: Exp\_4k\_500NPS\_300LHS.



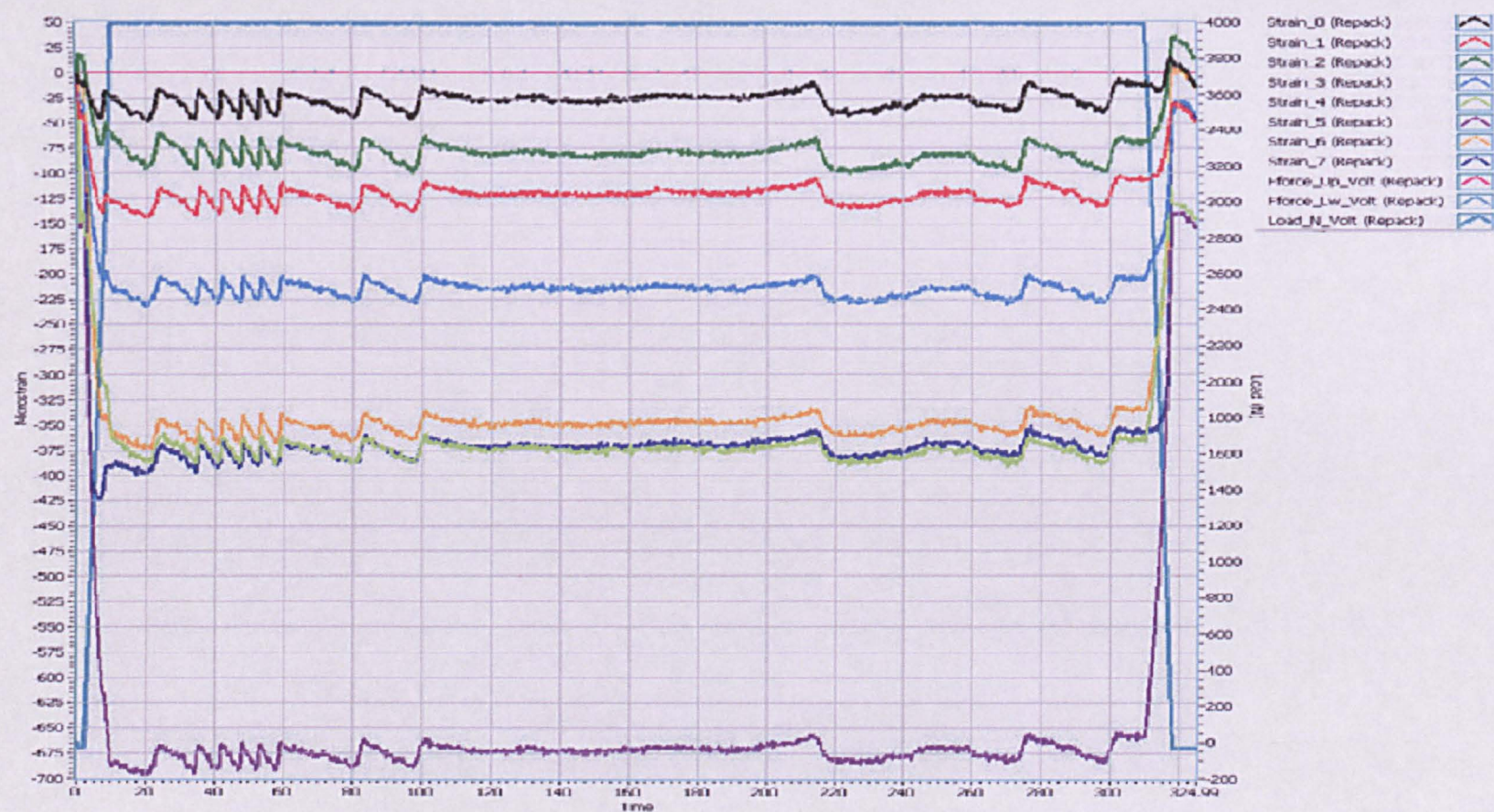


Figure 10-20: All SG output (Microstrain) two Flexiforce® sensor's output (Volt) & Load (N) Vs Time (S) without signal processing, Experiment protocol: Exp\_4k\_500 NPS\_300 LHS.



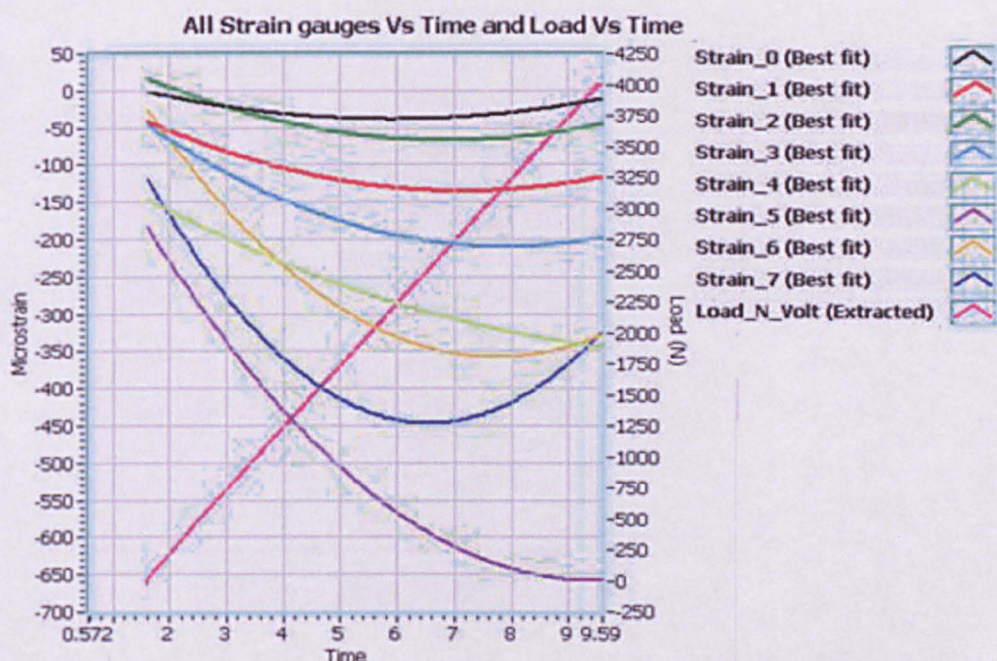


Figure 10-21: The 1st part of the graph for all strain gauge's output when loading from 0 to 4 kN.

It can be easily seen in the Figure 10-21 and Figure 10-22 that all strain gauge's outputs are a little non-linear in nature which is, as mentioned before due to the visco elastic inlay material of the disc. The positive results suggest that the strain gauges can be used in this application reliably.

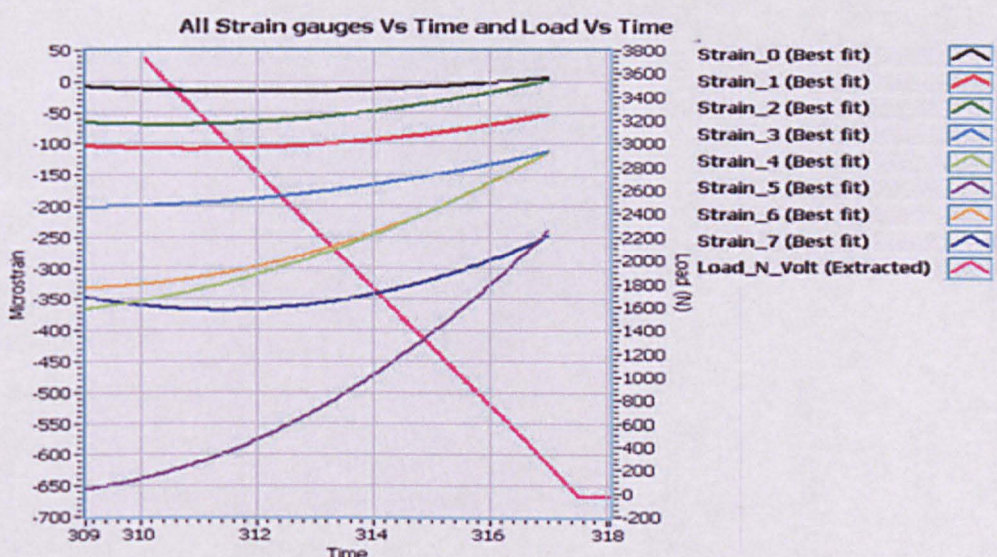


Figure 10-22: The 3rd part of the graph for all strain gauge's output when unloading from 4 to 0 kN.



So for, all graphs presented here are presented and discussed with respect to time. However, the ultimate objective of this research is to measure loading from the sensor's output. Therefore, the sensor's output Vs Applied load relationship is very important. Before exploring this relationship in detail, it is crucial to know how the sensor's output and the applied load are correlated. and for this reason statistical correlation techniques were used. The results are shown in Table 10-2.

### Correlation Coefficients

Table 10-2: Correlation analysis between applied compressive load and sensor's output.

Correlation Coefficients		
Overall Waveform	-0.598	Moderate and negative relationship
1 <sup>st</sup> part: 0 – 4 kN	-0.812	Strong and negative relationship
2 <sup>nd</sup> part: 4 kN const.	-0.027	Weak and negative relationship

Table 10-2 shows that in first part, when loading from 0-4 kN, the correlation coefficient is -0.812 which shows very strong and inverse relationship. In the second part when the load was kept constant for 4 kN the correlation coefficient is -0.027 which shows very weak or almost no relationship due to the presence of noise. In the second part the sensor's output signals the remain constant and effect of noise is very significant. That's why the signal to noise ratio reduces significantly. That is one of the principle reasons for very weak relationship in the second part of the signal.

Figure 10-23 shows the outputs from all strain gauges with respect to the applied compressive load. The applied compressive load in Newton is along the X-axis and the strain gauges output in Microstrain are along the Y-axis. The graph shows very clear and similar characteristics. This consistent repeatability in the outputs of the sensors suggest that the design of the load cell is suitable for further use for measuring load on the artificial lumbar spinal disc prosthesis.

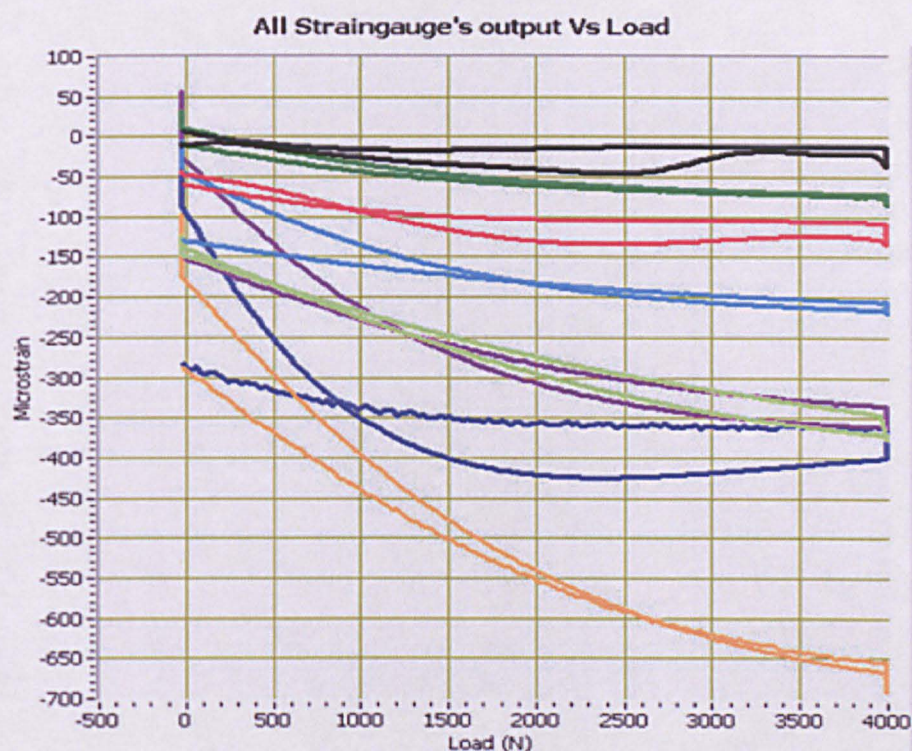


Figure 10-23: All strain gauges outputs with respect to applied compressive load.

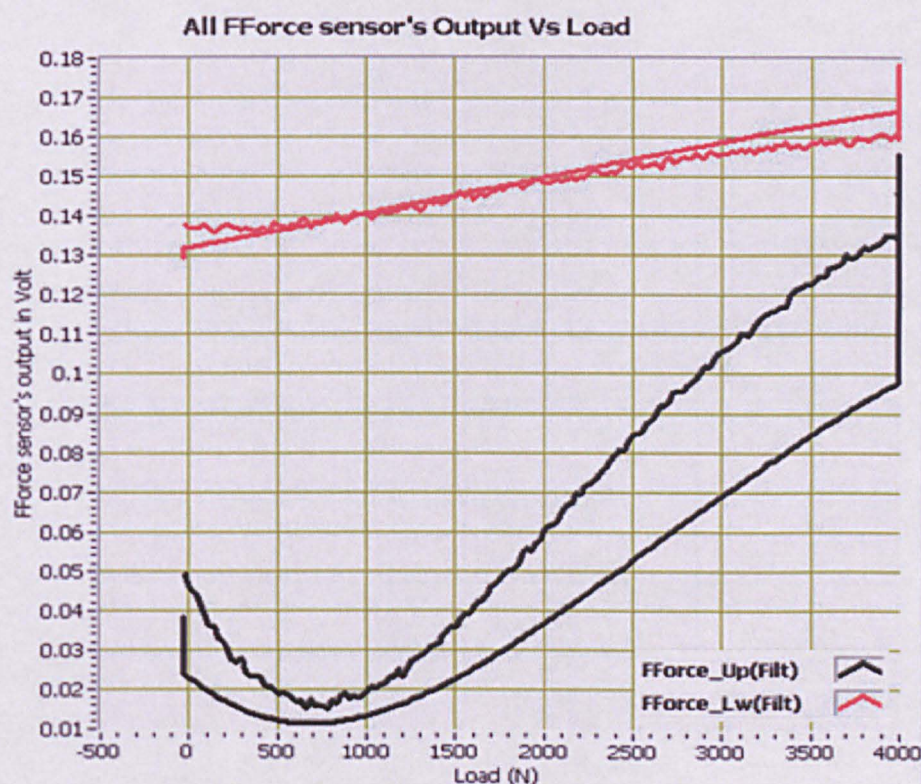


Figure 10-24: Two Flexiforce® sensors' output with respect to applied compressive load.

Figure 10-24 shows the outputs from the two Flexiforce® sensors with respect to the applied compressive load. The applied compressive load in Newton is along the X-axis and the Flexiforce® sensor's output in dc volt is along the Y-axis. The graph shows very clear and similar characteristics.

In both Figures, 10-23 and 10-24, the hysteresis can be observed between the plots of the loading and unloading cycle. Every sensor shows different hysteresis and this is possibly due to the vibrations of the hydraulic motor in the universal testing machine and due to the small movement of the inlay material in the bottom disc of the artificial spinal disc prosthesis. The movement is probably due to the misalignment of the upper and lower jaws of the universal testing machine at the beginning part of the loading.

### **10.3.2 Results of experiment 2: Exp\_4k\_500NPS\_PH300S**

---

Experiment 2 was performed as described in the protocol (section 10.2.2). The results are shown in graphical format; see Figure 10-25 and Figure 10-26. The graphs in Figure 10-25 present the outputs from all eight strain gauges (s.gauge 0 to s.gauge 7) and the outputs from the two piezoresistive-Flexiforce® sensors (F.force\_upper and F.force\_lower) when a compressive load is applied (with respect to time). The last graph depicted in Figure 10-25 titled as "Load Vs Time" presents the analogue output of the applied compressive load by the universal testing machine. In the graphs, outputs from all strain gauges are presented in Microstrain ( $\text{Microstrain} = \text{strain} \times 10^{-6}$ ) and outputs from the two Flexiforce® sensors are in analogue dc volt (Y-axis). The time is in seconds (x-axis). The red colour portions in all graphs shows the noisy raw signal and the black line plots are the best fit lines.

Similarly in Figure 10-26, the graphs present the outputs from all eight strain gauges (s.gauge 0 to s.gauge 7) and the outputs from the two piezoresistive-Flexiforce® sensors (F.force\_upper and F.force\_lower) when a compressive load is applied (with respect to the applied compressive load). In the graphs, outputs from all strain gauges are presented in Microstrain ( $\text{Microstrain} = \text{strain} \times 10^{-6}$ ) and outputs from the two Flexiforce® sensors are in analogue dc volt (Y-axis). The applied compressive load is in Newton (x-axis). The outputs from all the eight strain



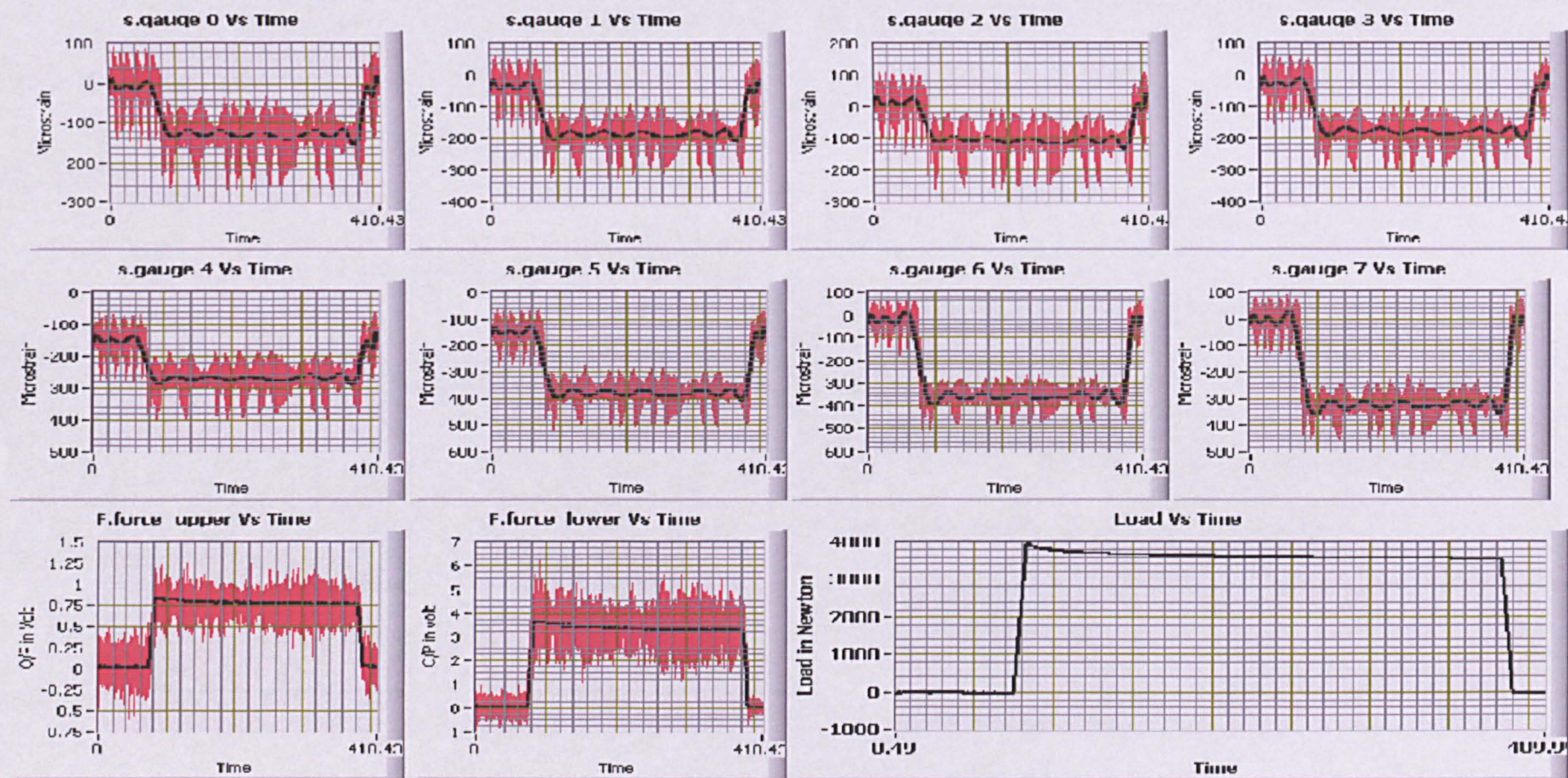


Figure 10-25: All eight strain gauge's outputs, two piezoresistive-Flexiforce® sensor's outputs and applied compressive load in Newton with respect to time in seconds. (Experiment protocol: Exp\_4k\_500NPS\_PH300S).



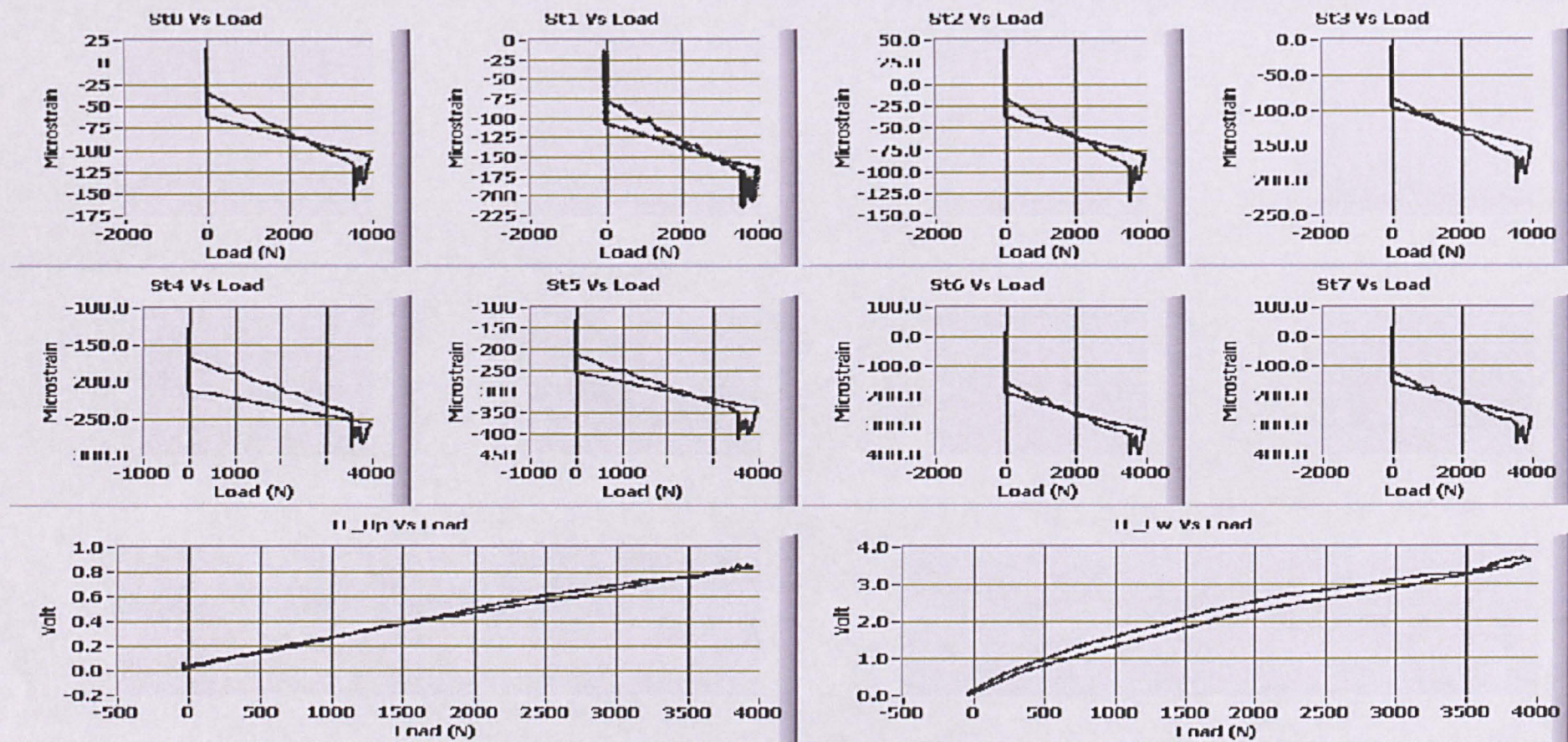


Figure 10-26: All eight strain gauge's outputs and two piezoresistive-Flexiforce® sensor's outputs with respect to applied compressive load in Newton. (Experiment protocol: Exp\_4k\_500NPS\_PH300S).

gauges look similar in characteristics as in the previous experiment. That reconfirms the suitability of the use of strain gauges for this application. In Figure 10-25, a typical noise pattern similar to the previous experiment can be seen in the graphs representing outputs from all strain gauges. Similarly, a different noise pattern can also be seen in the graphs representing outputs from the two Flexiforce® sensors. There is a significant difference in Flexiforce® sensor's output value range compare to the previous experiment. The difference is most probably due to the dislocation of the sensors due to loading and unloading cycles during the experimental trials. The lower Flexiforce® sensor sensing area is less than the bottom surface area of the inlay material. That is erroneous and may be causing fluctuations in the output values. As discussed in the previous experiment, the same steps were taken for further noise analysis. Figure 10-27 shows a magnified view from the output (Microstrain) of one typical strain gauge (SG 0 Vs Time). In figure 10-27, the raw data coloured in red contain the output of s.gauge 0 (SG 0) together with a typical noise which is similar as in the previous experiment as shown in Figure 10-10. To filter the noise the Low Pass 3rd order Butterworth IIR Filter is used with 5 Hz cutoff frequency. The filtered signal is shown in Figure 10-28 which is very much similar as in the previous experiment shown in Figure 10-11. Here, also the same signal processing techniques are used as mentioned in the previous experiment. The study protocol is very much similar as in experiment 1 except in the 2nd part of the graph the position of the two jaws of the universal loading machine are locked as the applied compressive load reaches 4 kN force. In this experiment the graph is divided in three parts; the first part is when loading was from 0 to 4 kN, the second part is when the load applying jaws position was held constant for 300 seconds and the 3rd part is unloading from 4 kN to 0 kN. According to the experiment protocol, the compressive load is applied from 0 to 4 kN in the first part with 500 NPS loading speed. So, the duration of the first part is of about 8 seconds, the duration of second part is of about 300 seconds and the duration of the third part is of around 8 seconds. All three parts of the graph are of non-stationary type.



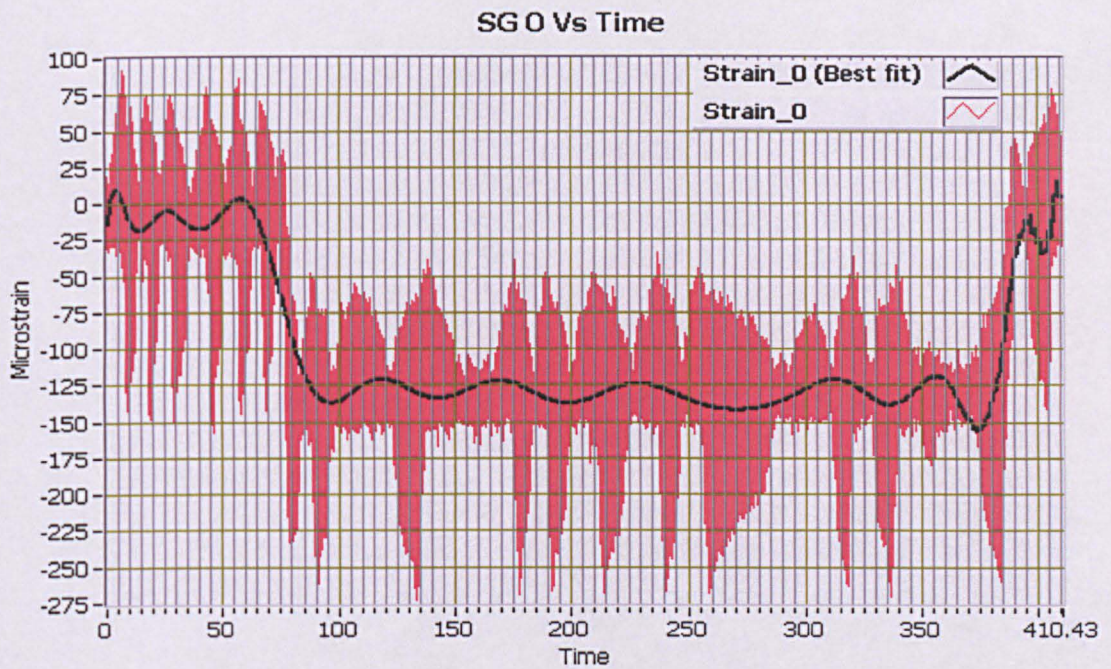


Figure 10-27: Raw Data with lots of typical noise of one typical strain gauge's output (SG 0 Vs Time) with respect to time.

The speed of loading and rate of change of the sensor's output is significantly different; hence, the same signal processing technique cannot be applied to the whole waveform graph.

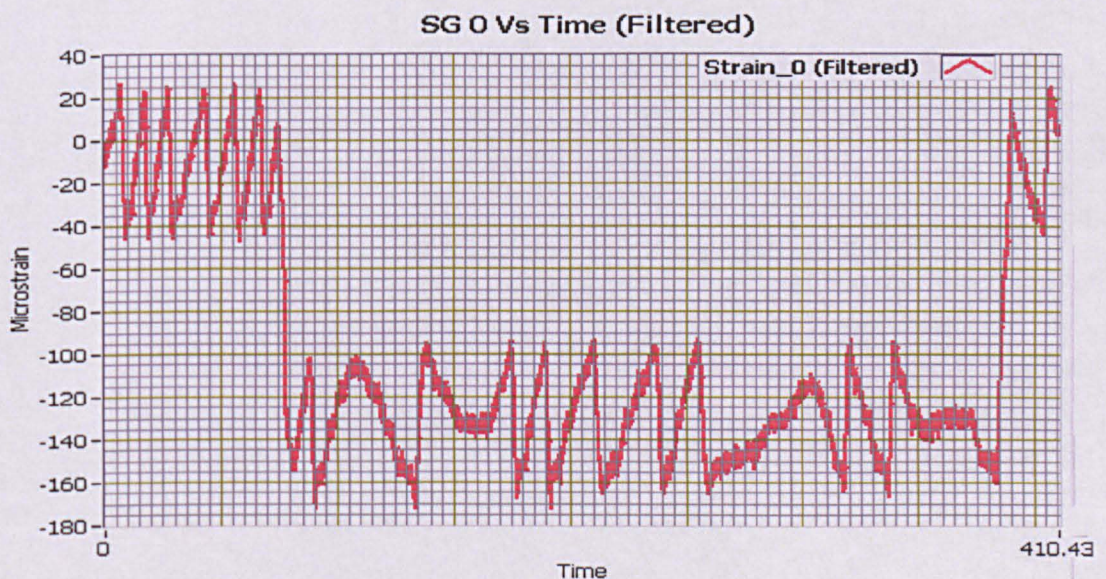


Figure 10-28: Filtered data of one typical strain gauge's output (SG 0 Vs Time) with respect to time. Low pass 3rd order Butterworth IIR filter-with cutoff frequency 5 Hz is used for filtering.

This type of experiment study protocol is useful to understand the creep-relaxation behaviour of the inlay material of the spinal disc prosthesis. That



is very crucial in this application because the original spinal disc in human is visco-elastic in nature and absorbs the shock as explained in details in the previous chapters. In this experiment within 300 seconds the load is reduced from 4000 N to around 3500 N exponentially.

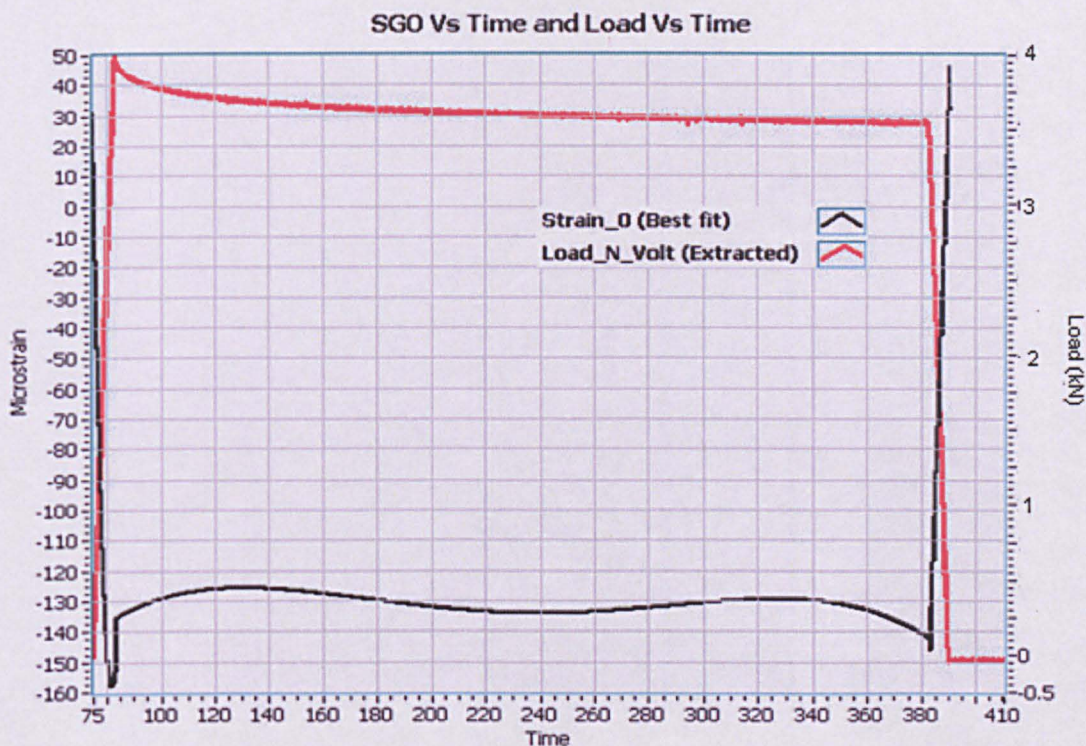


Figure 10-29: Typical strain gauge output and applied load graph with respect to time (SG 0 Vs Time and Load Vs Time).

In the first part of the waveform graph the numbers of samples were 800 hundred (8 seconds at a sampling frequency of 100 Hz). Hence, the first 800 samples of the graph are converted to the final plot of the waveform using "curve fitting" signal processing techniques. The model of polynomial equation of order N is used. For the second part of the waveform graph having approximately total samples of 30,000, is converted to the final plot of the waveform using the same signal processing curve fitting tools as used in the first part but may be of different value of N. The third part is the same as the first part. So, after multipart parametric signal processing, the resultant waveform is shown in Figure 10-29, named "SG 0 Vs Time and Load Vs Time". The graph has two Y-axis, one is in Microstrain and other is in applied compressive load (k Newton). The graph is very clear and very



much similar in characteristics with the analogue output of the applied compressive load. The strain gauge is experiencing compression that's why the load Vs strain graph is inversely proportional (see Figure 10-29).

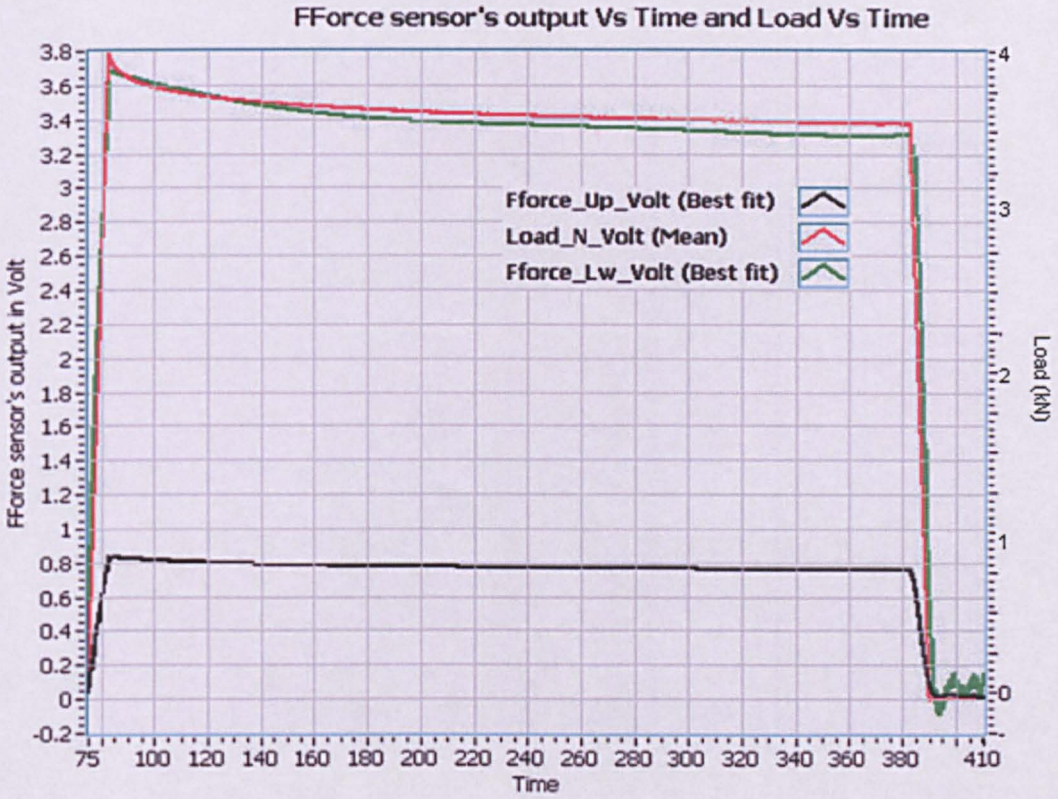


Figure 10-30: Outputs from the two Flexiforce® sensors and applied compressive load with respect to time.

Similarly, Figure 10-30 shows the graphical presentation of the two Flexiforce® sensors with respect to time. The graph has two Y-axis, similar to that shown in Figure 10-29, one is in Microstrain and the other is in applied compressive load (k Newton). The graphs are obtained using identical signal processing techniques for both the Flexiforce® sensors. The graphs are very clear and almost looking same with the analogue output of the applied compressive load. The outputs of the Flexiforce® sensors are excellent when compared to the outputs of the Flexiforce® sensors in the previous experiment, particularly in the 2<sup>nd</sup> part of the graph. Probably, the outputs of the Flexiforce® sensors are more stable when the signals are non-stationary. The signal processing techniques used in SG 0 Vs Time is also used for plotting all outputs of the eight strain gauges (SG 0 to SG 7) and the two Flexiforce® sensors (Flexiforce®\_Upper and



Flexiforce®\_Lower). For better comparison all outputs are plotted on a the same graph as shown in Figure 10-31.

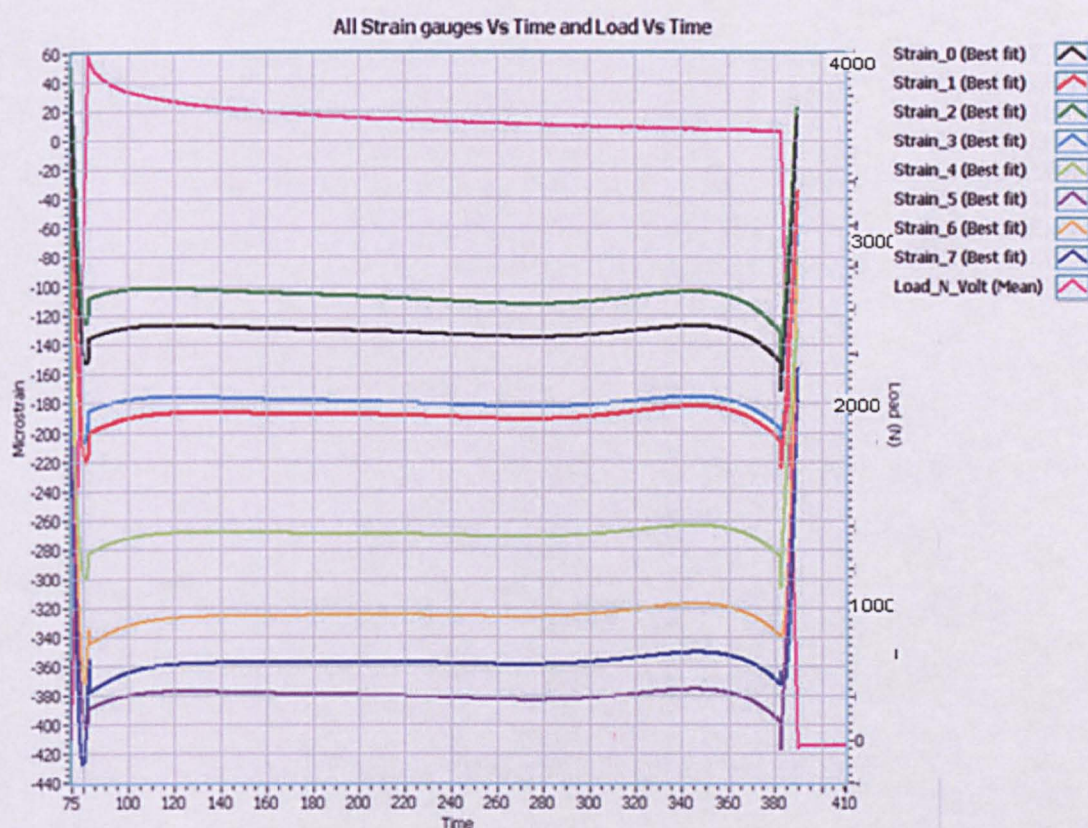


Figure 10-31: All SG output (Microstrain) & Load (N) Vs Time (S).

As explained before, the 1st and 3rd part of the graph which represents the sensor's output when loading and unloading has duration of 8-9 seconds only. This is less compare to the 2nd part of the graph which is 300 seconds. Hence, to clearly present the graph, the 1st and 3rd part of the graph in Figure 10-31 is magnified and shown in Figure 10-32 and 10-33 respectively.



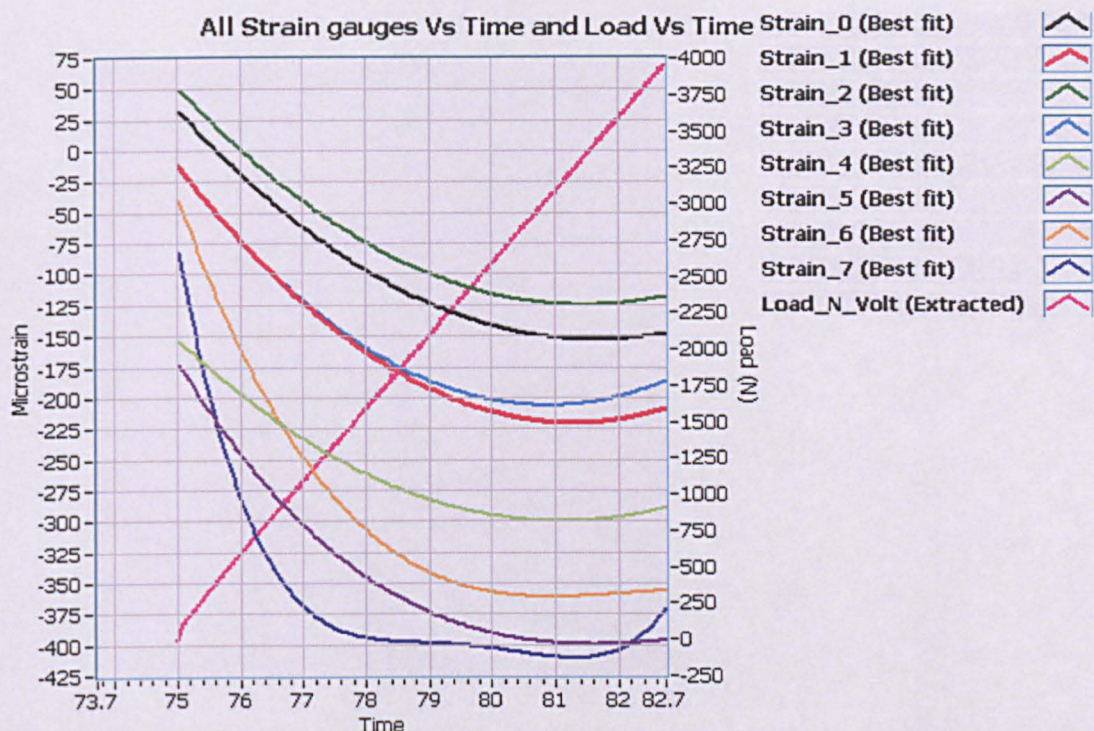


Figure 10-32: The 1st part of the graph for all strain gauge's output when loading from 0 to 4 kN.

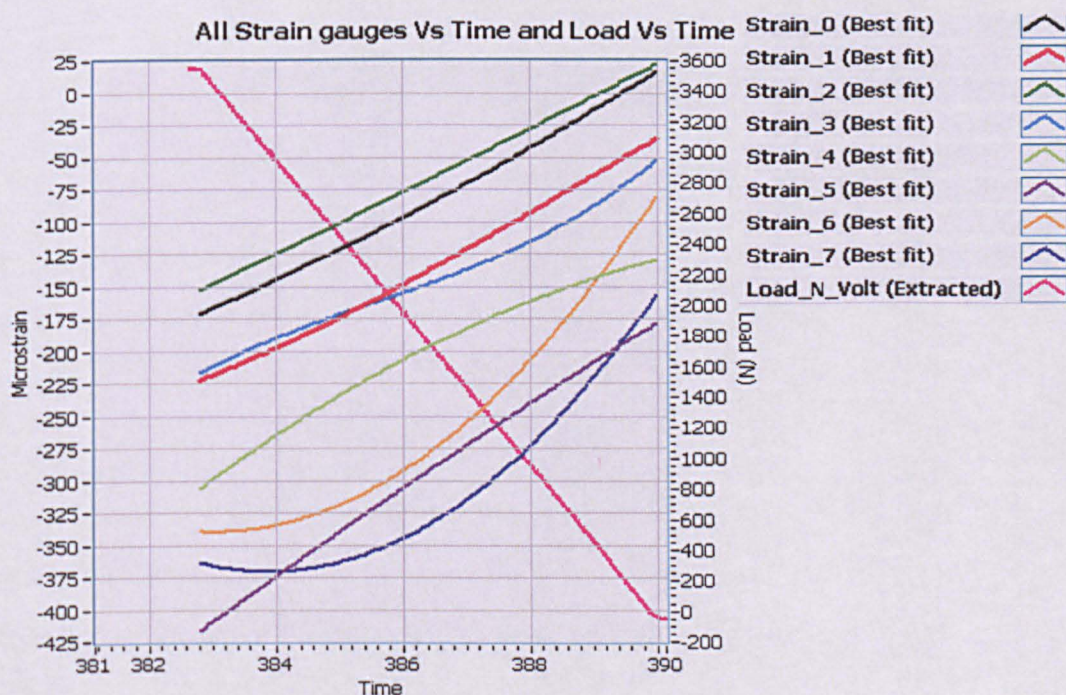


Figure 10-33: The 3rd part of the graph for all strain gauge's output when unloading from 4 to 0 kN.

It can be seen in Figure 10-32 and Figure 10-33 that all strain gauge's outputs are a somewhat non-linear in nature which is, as mentioned before



due to the visco-elastic inlay material of the disc. As the spinal disc exhibits visco-elastic behaviour, the sensors installed onto the artificial spinal disc should also exhibit visco-elastic behaviour. So, here it is reconfirmed that the strain gauges can be used in this application reliably.

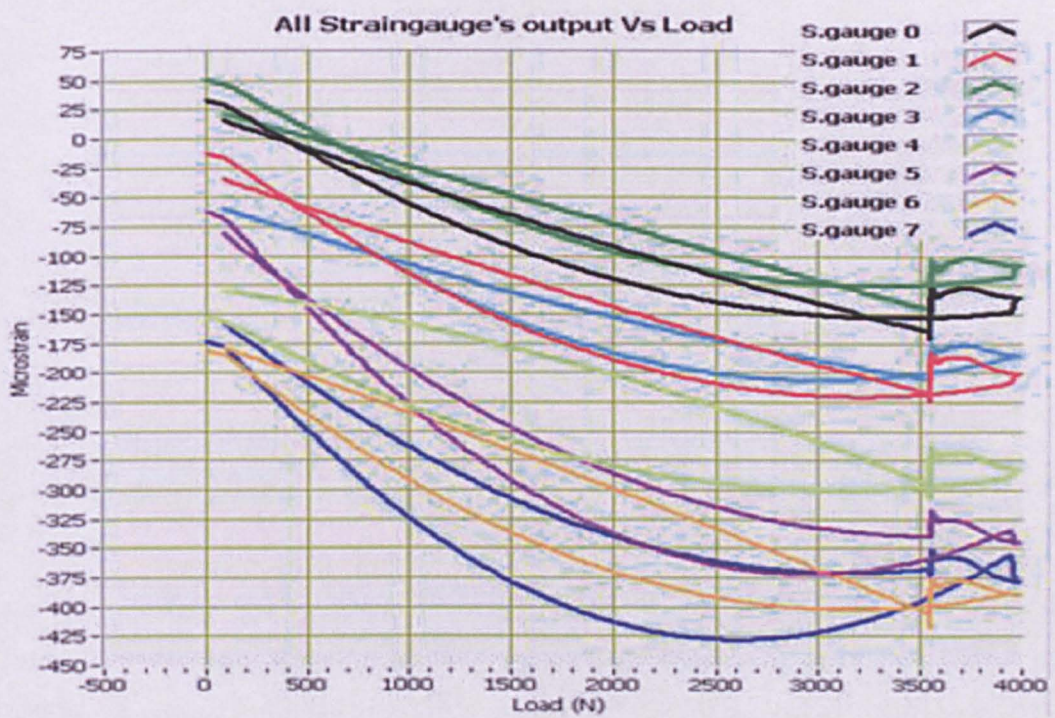


Figure 10-34: All strain gauges outputs with respect to applied compressive load.

Figure 10-34 shows the outputs from all strain gauges with respect to the applied compressive load. The applied compressive load in Newton is along the X-axis and the strain gauges output in Microstrain are along the Y-axis. The graph shows very clear and similar characteristics between the outputs, especially in the range of 500 N to 3500 N. The little irregularity in the graph between 3500 N to 4000 N is due to the decay in load from 4000 N to 3500 N in the 2<sup>nd</sup> part of the graph (holding for 300 seconds).

Figure 10-35 shows the outputs from the two Flexiforce® sensors with respect to the applied compressive load. The applied compressive load in Newton is along the X-axis and the Flexiforce® sensor's output in dc volt is along the Y-axis.



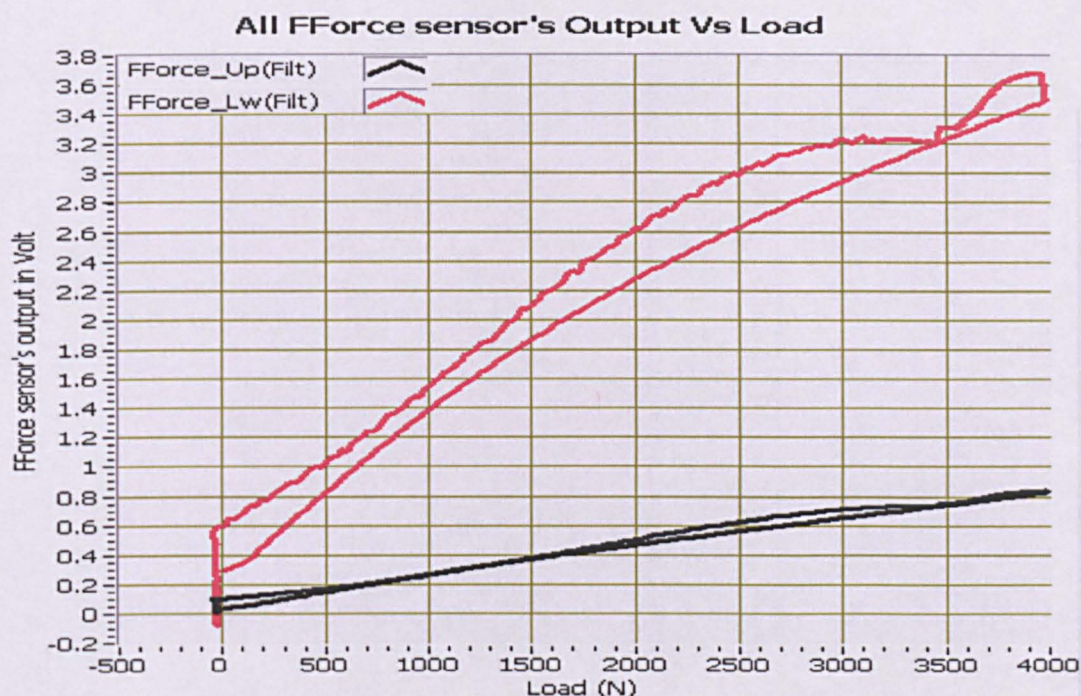


Figure 10-35: Two Flexiforce® sensor's output with respect to applied compressive load.

### 10.3.3 Results of Experiment 3: Exp\_4k\_500NPS\_NOH

Experiment 3 was performed as described in the protocol (section 10.2.3). The results are shown in graphical format; see Figure 10-36 and Figure 10-37. The graphs in Figure 10-36 present the outputs from all eight strain gauges (s.gauge 0 to s.gauge 7) and the outputs from the two piezoresistive- Flexiforce® sensors (Flexiforce®\_Upper and Flexiforce®\_Upper) when a compressive load is applied (with respect to time). The last graph depicted in Figure 10-36 entitled as "Load Vs Time" presents the analogue output of the applied compressive load by the universal testing machine. In the graphs, the outputs from all strain gauges are presented in Microstrain ( $\text{Microstrain} = \text{strain} \times 10^{-6}$ ) and the outputs from the two Flexiforce® sensors are in analogue dc volt (Y-axis). The time is in seconds (x-axis). The red colour portions in all graphs shows the noisy raw signal and the black line plots are the best fit lines.



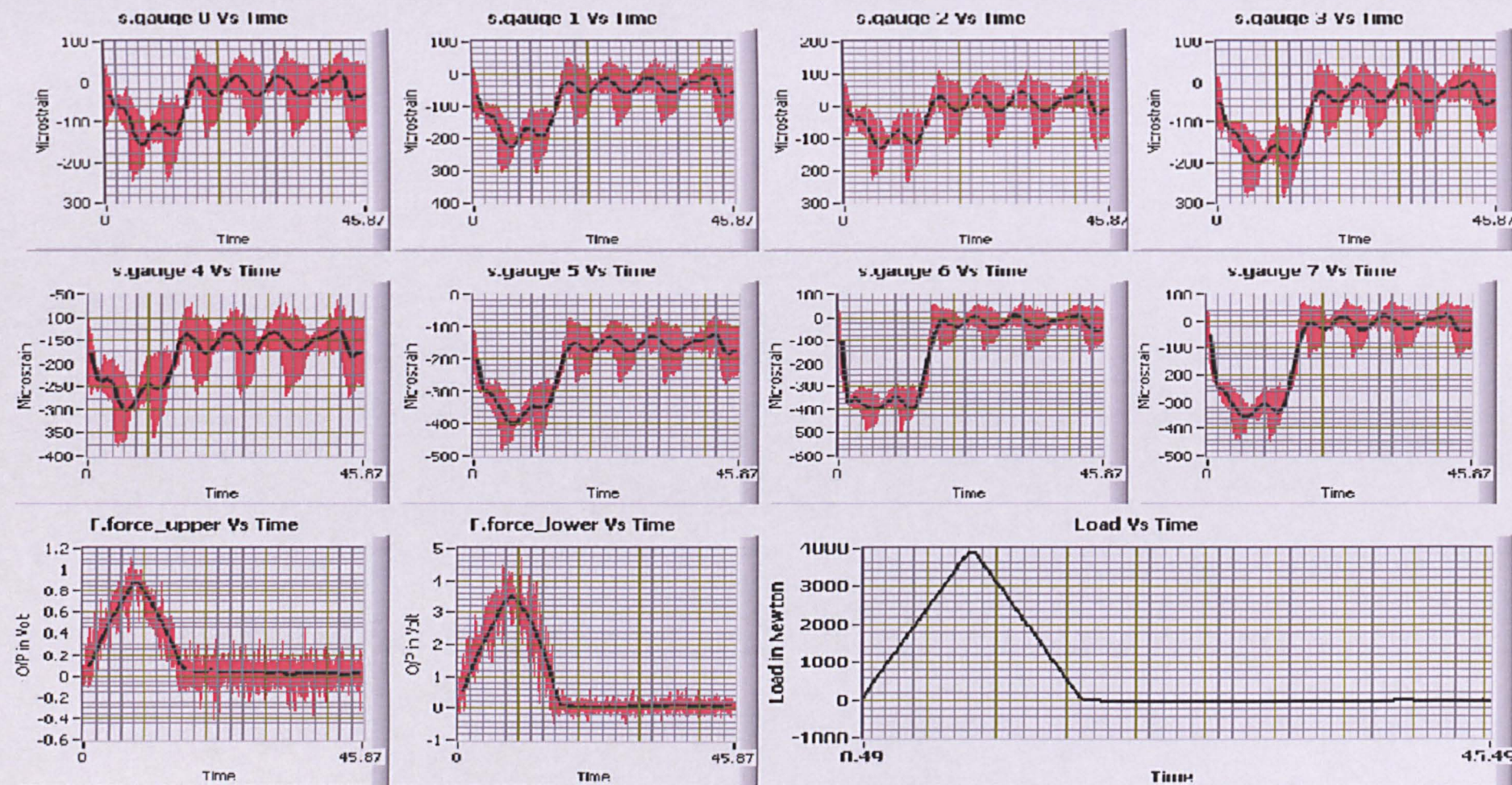


Figure 10-36: All eight strain gauge's outputs, two piezoresistive-Flexiforce® sensor's outputs and applied compressive load in Newton with respect to time in seconds. (Experiment protocol: Exp\_4k\_500NPS\_NOH).



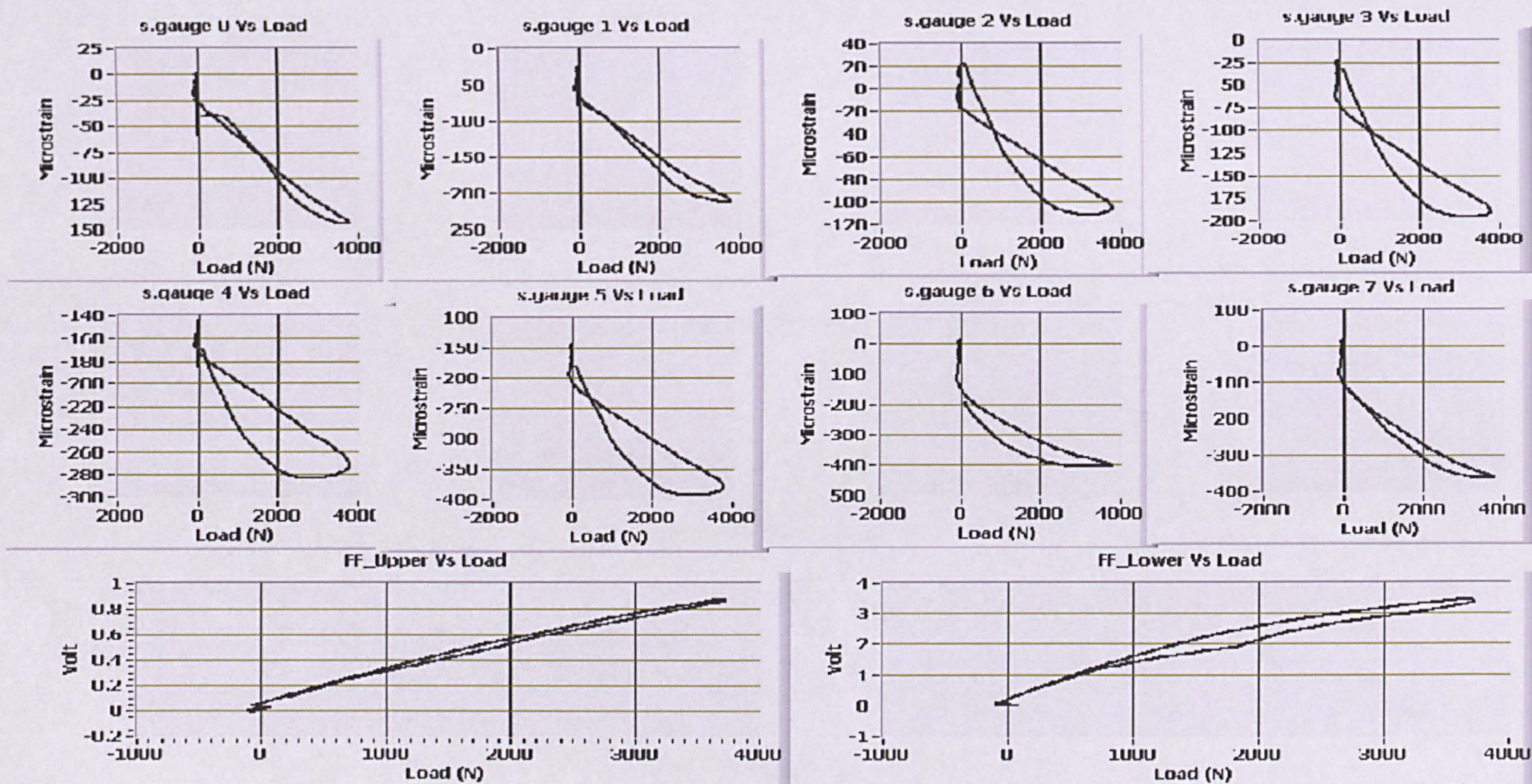


Figure 10-37: All eight strain gauge's outputs and two piezoresistive-Flexiforce® sensor's outputs with respect to applied compressive load in Newton. (Experiment protocol: Exp\_4k\_500NPS\_NOH).



Similarly in Figure 10-37, the graphs present the outputs from all eight strain gauges (s.gauge 0 to s.gauge 7) and the outputs from the two piezoresistive- Flexiforce® sensors (F.force\_upper and F.force\_lower) when a compressive load is applied (with respect to the applied compressive load). In the graphs outputs from all strain gauges are presented in Microstrain ( $\text{Microstrain} = \text{strain} \times 10^{-6}$ ) and outputs from the two Flexiforce® sensors are in analogue dc volt (Y-axis). The applied compressive load is in Newton (x-axis).

In Figure 10-36, a typical noise pattern similar to the previous experiments can be seen in the graphs representing outputs from all strain gauges. The only difference in noise in this experiment is its cyclic pattern. This cyclic pattern noise is possibly coming from the hydraulic pump motor vibrations and stroke pulsation. Similarly, a different noise pattern from the strain gauges can also be seen in the graphs representing outputs from the two Flexiforce® sensors. There are differences in the Flexiforce® sensor's output value range compare to previous experiments.

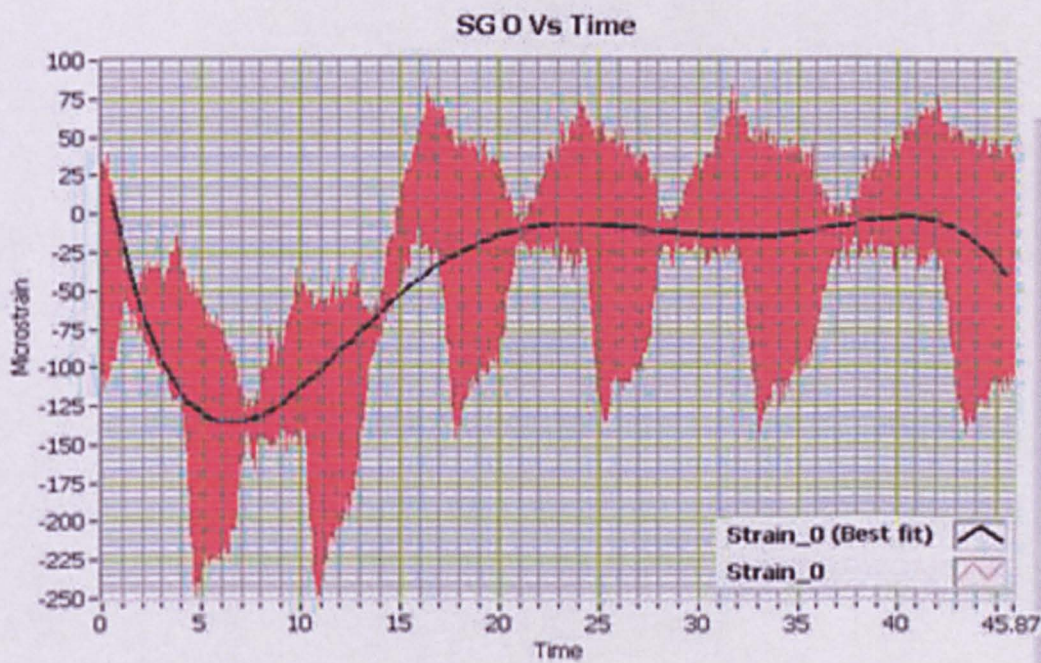


Figure 10-38: Raw Data with lots of typical noise of one typical strain gauge's output (SG 0 Vs Time) with respect to time.

As discussed in previous experiments, the same steps are taken for further noise analysis. Figure 10-38 shows a magnified view from the output (Microstrain) of one typical strain gauge (SG 0 Vs Time). In figure 10-38,



the raw data coloured in red contain the output of s.gauge 0 (SG 0) together noise which is similar as in the previous experiments.

To filter the noise the same Low Pass 3rd order Butterworth IIR Filter is used with a 5 Hz cutoff frequency. By applying FFT analysis the cut-off frequency of 5 Hz is selected here as well. The filtered signal is shown in Figure 10-32 which is very similar as in previous experiments, shown in Figure 10-11 and Figure 10-28.

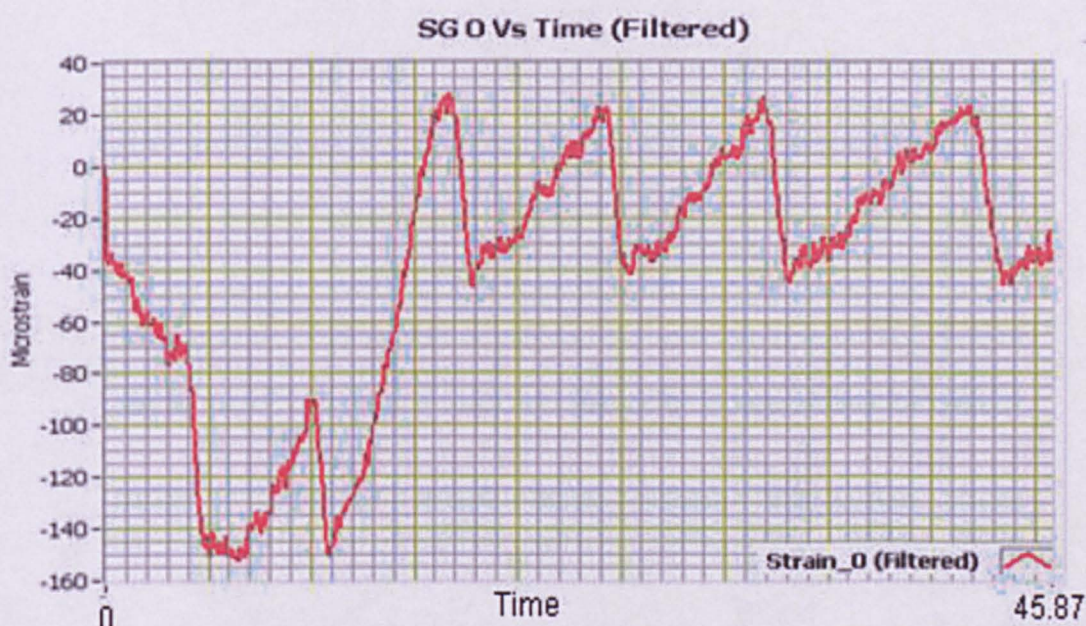


Figure 10-39: Filtered data of one typical strain gauge's output (SG 0 Vs Time) with respect to time. Low pass 3rd order Butterworth IIR filter-with cutoff frequency 5 Hz is used for filtering.

The signal processing techniques applied here are a little different than the ones used in the previous experiments. The signal processing technique used here is simpler than the previous experiments. The study protocol is also different from the previous experiments. So, in this experiment the graph is divided in two parts; the first part is when loading from 0 to 4 kN and the second part is unloading from 4 kN to 0 kN. There is no holding part (2nd part) in this experiment. According to the experiment protocol, the compressive load is applied from 0 to 4 kN in the first part with 500 NPS loading speed. Therefore, the duration of the first part is of about 8 seconds and the duration of second part is of about 8 seconds again when unloading from 4 to 0 kN with the same 500 NPS speed. Hence, both parts of the



graph are of non-stationary type and almost identical in loading and unloading speed.

In the first part of the waveform graph which as mentioned before is of 8-9 seconds the sampling speed of the experiment data acquisition system was set to 100 Hz. For 8 seconds, approximately the total samples of the first part are around 800 ( $8 \times 100$ ). Therefore, the first 800 samples of the waveform graph are converted to the final plot of the waveform using "curve fitting" signal processing technique. The model of polynomial equation of order N is used here and the value of N is either 1 or 2.

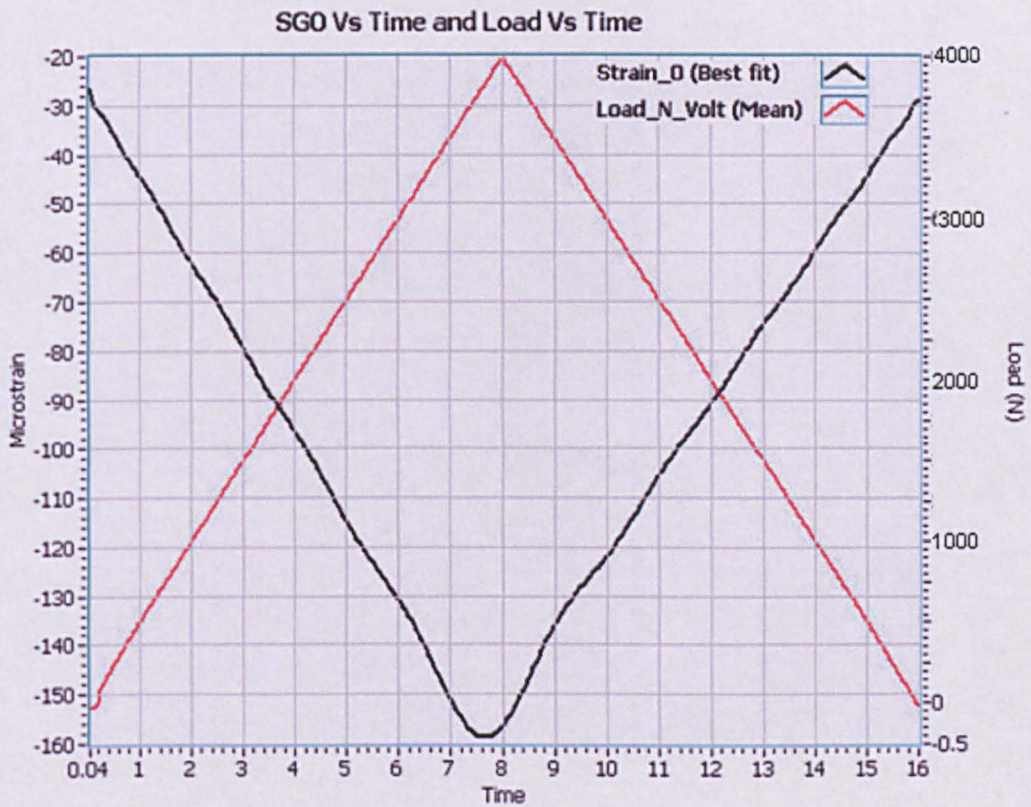


Figure 10-40: Typical strain gauge output and applied load graph with respect to time (SG 0 Vs Time and Load Vs Time).

For second part of the waveform graph having approximately total samples of 800 again, is converted to the final plot of the waveform using the same signal processing curve fitting tools as used in the first part. So, after multipart parametric signal processing the resultant waveform is shown in Figure 10-40, named "SG 0 Vs Time and Load Vs Time". The graph has two Y-axis, one is in Microstrain and the other is in applied compressive load (Newton). The graph is very clear and similar in characteristics with the



analogue output of applied compressive load. The strain gauge is experiencing compression that's why the load Vs strain graph is inversely proportional as can be seen in Figure 10-17, 10-29 and 10-40.

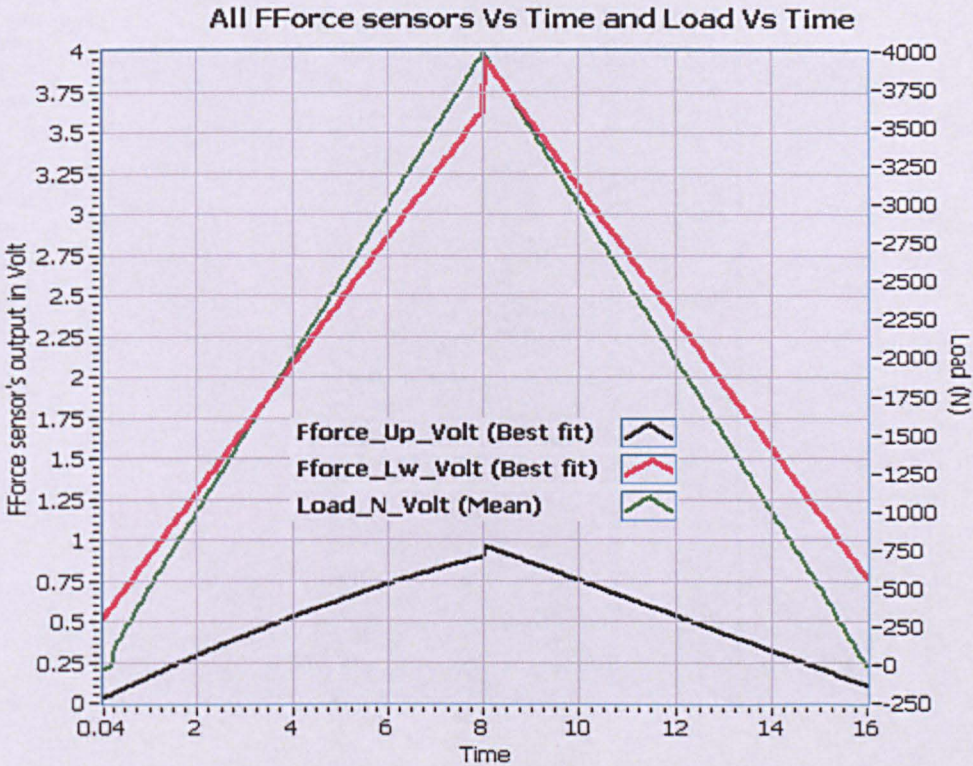


Figure 10-41: Outputs from two Flexiforce® sensors and applied load graph with respect to time.

Similarly, Figure 10-41 shows the graphical presentation of the two Flexiforce® sensors with respect to time. The graph has two Y-axis similar to those shown in Figure 10-40, one is in Microstrain and other is in applied compressive load (Newton). The graphs are obtained using identical signal processing techniques for both the Flexiforce® sensors.

The signal processing techniques used in SG 0 Vs Time are also used for plotting all outputs of the eight strain gauges (SG 0 to SG 7) and the two Flexiforce® sensors (Flexiforce®\_Upper and Flexiforce®\_Lower). For better comparison all outputs are plotted on a same graph as shown in Figure 10-42. All sensors' outputs look similar with the analogue output of the applied compressive load. The outputs from the Flexiforce® sensors are more linear than the outputs from the strain gauges (Figure 10-41, 10-42, 10-43 and 10-44).



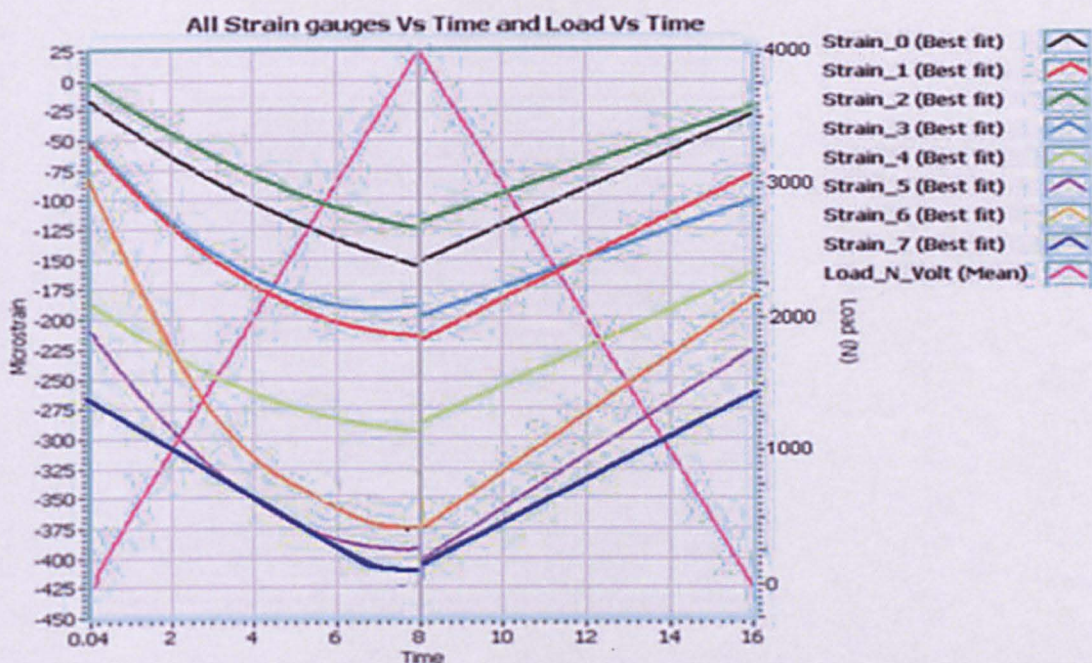


Figure 10-42: All SG output (Microstrain) & Load (N) Vs Time (S)

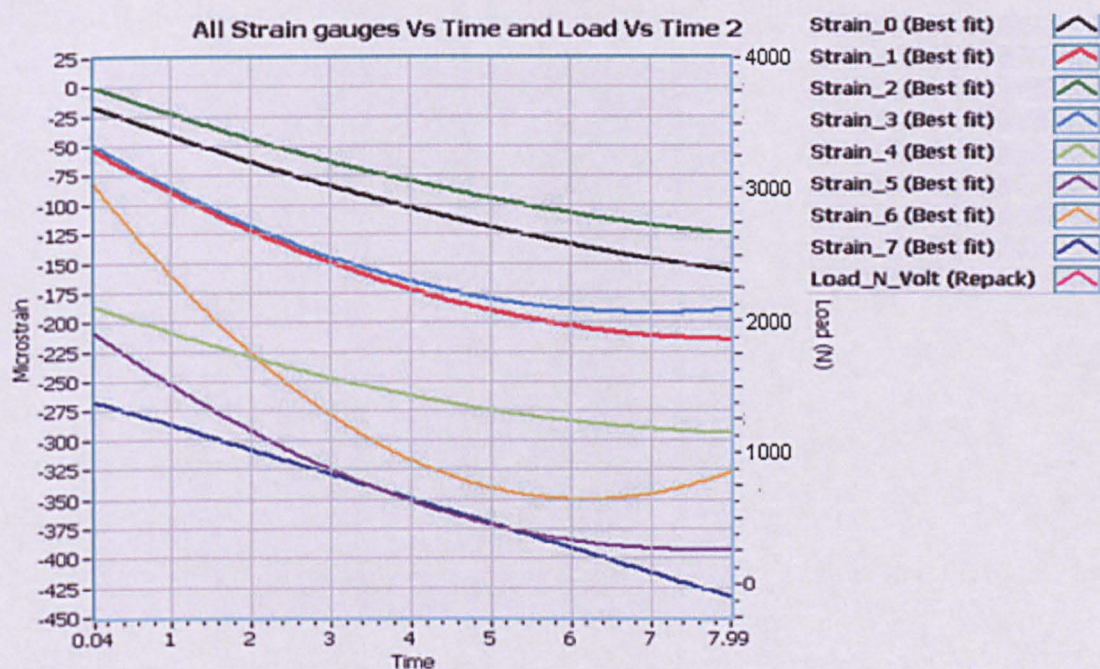


Figure 10-43: The 1st part of the graph for all strain gauge's output when loading from 0 to 4 kN.

The 1st and 2nd part of the graph which represents the sensor's output when loading and unloading has duration of 8-9 seconds. To clearly present the graph, the 1st and 2nd part of the graph in Figure 10-42 is magnified and shown in Figure 10-43 and 10-44 respectively.



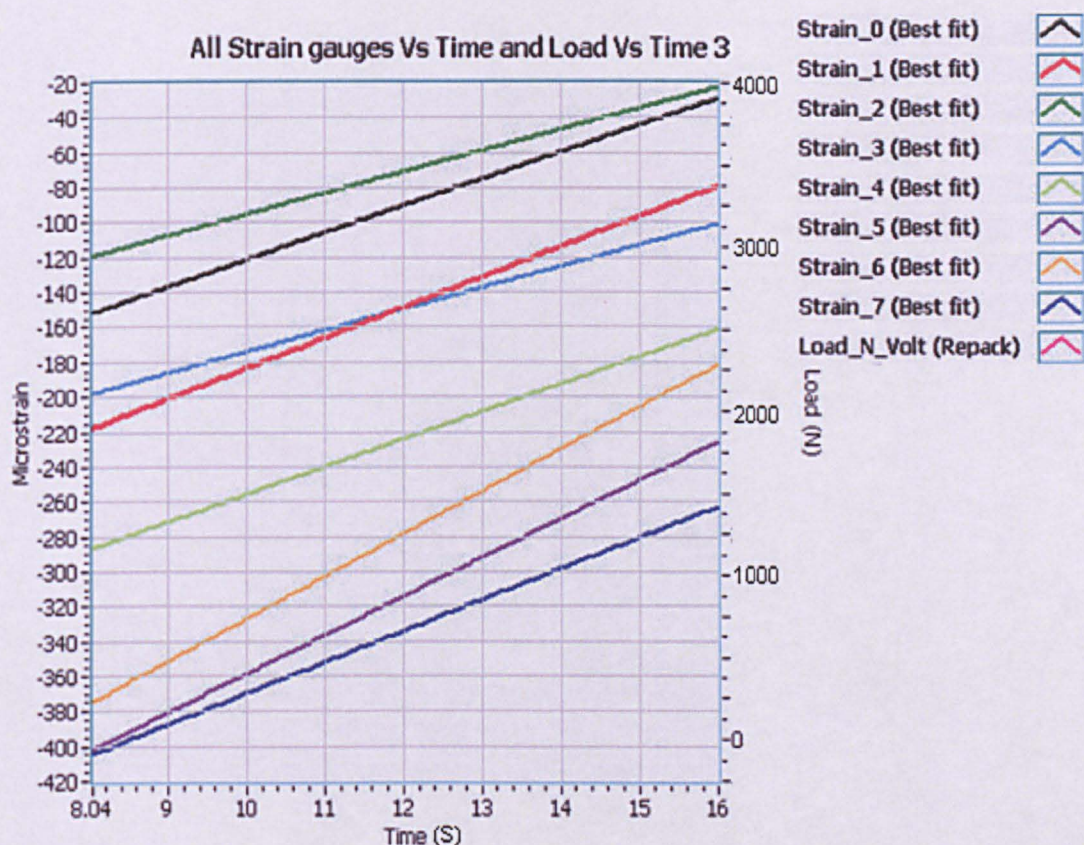


Figure 10-44: The 2nd part of the graph for all strain gauge's output when unloading from 4 to 0 kN.

Figure 10-45 shows the outputs from all strain gauges with respect to the applied compressive load. The applied compressive load in Newton is along the X-axis and the strain gauges output in Microstrain are along the Y-axis. The graph shows very clear and similar characteristics especially in the range of 500 N to 3500 N. An irregularity in the graph of strain gauge 5, between 3500 N to 4000 N, can be noticed in the graph of Figure 10-45.



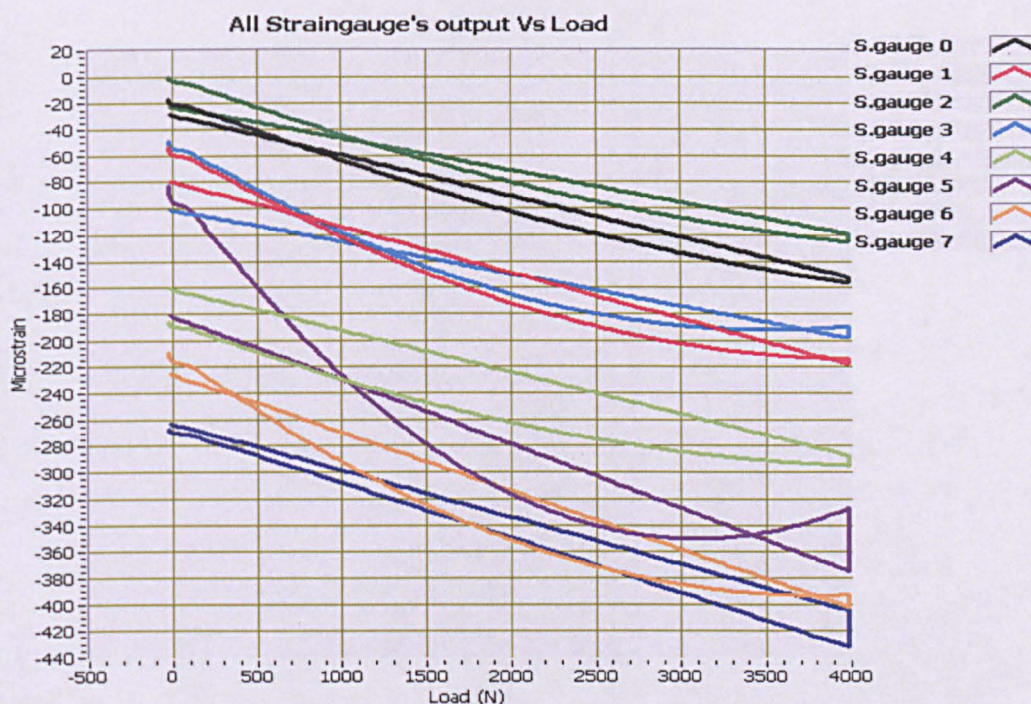


Figure 10-45: All strain gauges outputs with respect to applied compressive load.

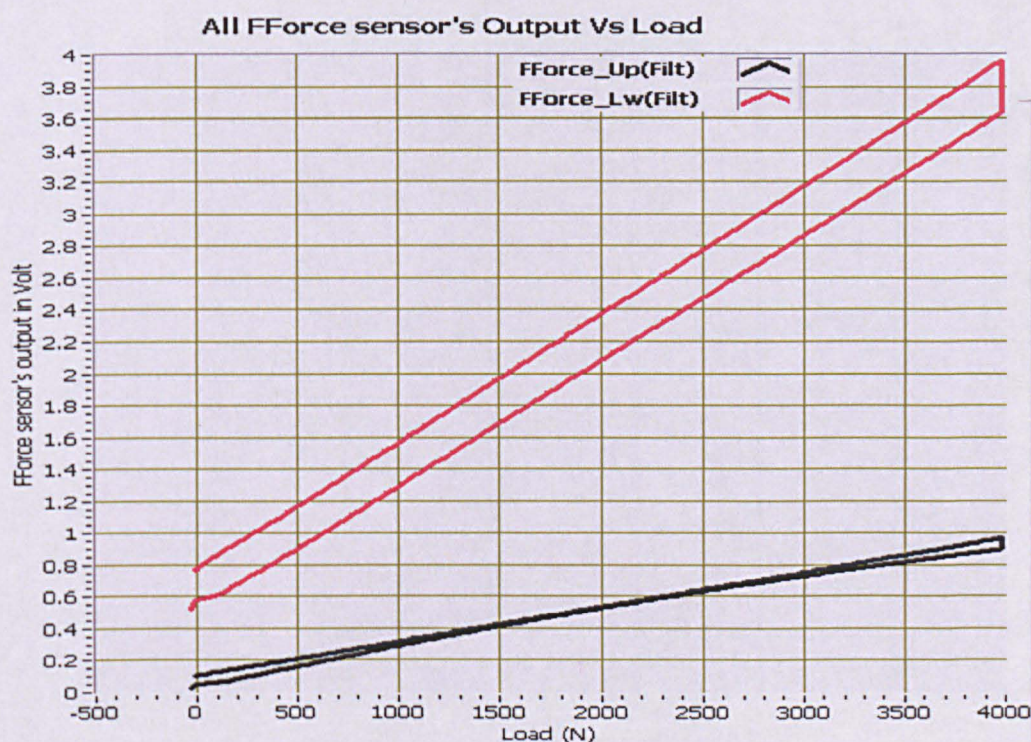


Figure 10-46: Two Flexiforce® sensor's output with respect to applied compressive load.

Figure 10-46 shows the outputs from the two Flexiforce® sensors with respect to the applied compressive load. The applied compressive load in Newton is along the X-axis and the Flexiforce® sensor's output in dc volt is

along the Y-axis. One of the important observations in this experiment is that the sensor's output is more non linear like quadratic curve in the loading cycle. This can be easily seen in Figure 10-42, 10-43, 10-44 and 10-45. In both Figures 10-45 and 10-46, the hysteresis can be found between plots of the loading and unloading cycle which is uniform in the case of the Flexiforce® sensors.

#### **10.3.4 Results of Experiment 4: Exp\_4k\_100NPS\_NOH**

---

Experiment 4 was performed as described in the protocol (section 10.2.4). The results are shown in graphical format; see Figure 10-47 and Figure 10-48. This experiment was similar in protocol to the previous experiment 3 except the loading speed is 100 NPS instead of 500 NPS. The loading and unloading speed has been programmed as per protocol in the universal testing machine. The graphs in Figure 10-47 present the outputs from all eight strain gauges (s.gauge 0 to s.gauge 7) and the outputs from the two piezoresistive-Flexiforce® sensors (F.force\_upper and F.force\_lower) when a compressive load is applied (with respect to time). The last graph depicted in Figure 10-47 titled as "Load Vs Time" presents the analogue output of the applied compressive load by the universal testing machine. In the graphs, outputs from all strain gauges are presented in Microstrain ( $\text{Microstrain} = \text{strain} \times 10^{-6}$ ) and outputs from the two Flexiforce® sensors are in analogue dc volt (Y-axis). The red colour portions in all graphs shows the noisy raw signal and the black line plots are the best fit lines. Similarly in Figure 10-48, the graphs present the outputs from all eight strain gauges (s.gauge 0 to s.gauge 7) and the outputs from the two piezoresistive-Flexiforce® sensors (F.force\_upper and F.force\_lower) when a compressive load is applied (with respect to the applied compressive load). In the graphs, outputs from all strain gauges are presented in Microstrain ( $\text{Microstrain} = \text{strain} \times 10^{-6}$ ) and outputs from the two Flexiforce® sensors are in analogue dc volt (Y-axis). The applied compressive load is in Newton (x-axis).



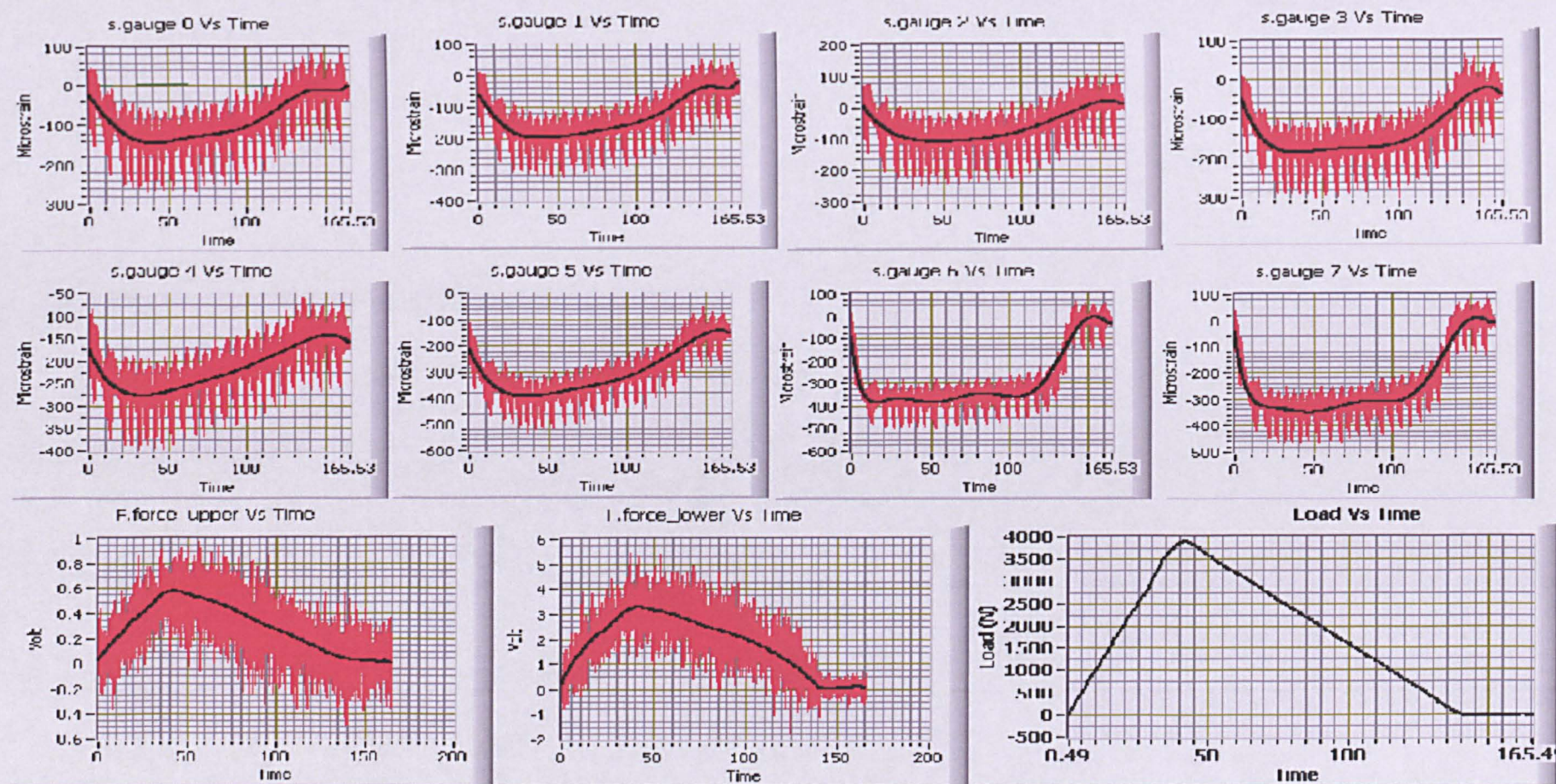


Figure 10-47: All eight strain gauge's outputs, two piezoresistive-Flexiforce® sensor's outputs and applied compressive load in Newton with respect to time in seconds. (Experiment protocol: Exp\_4k\_100NPS\_NOH).



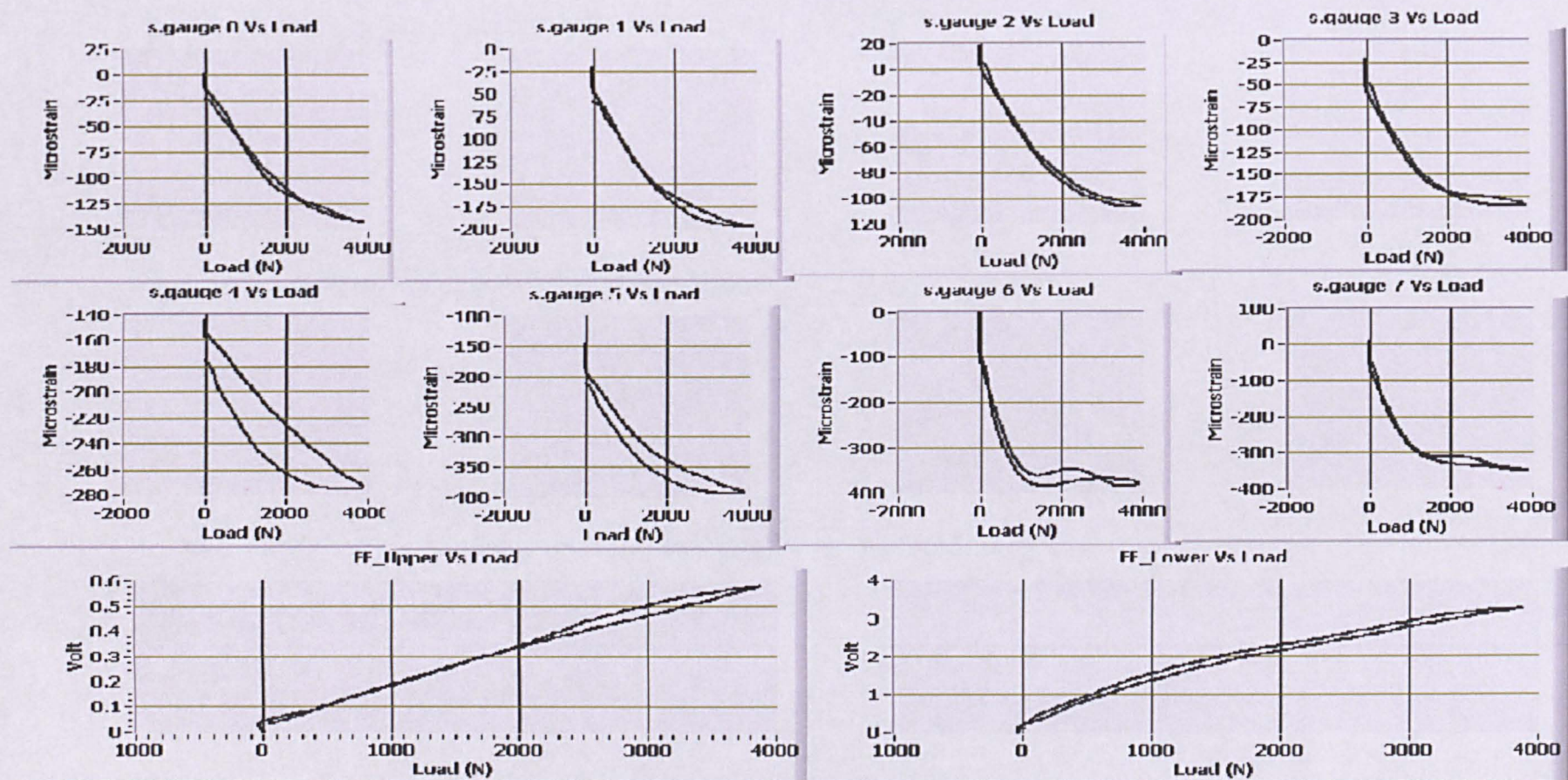


Figure 10-48: All eight strain gauge's outputs and two piezoresistive-Flexiforce® sensor's outputs with respect to applied compressive load in Newton. (Experiment protocol: Exp\_4k\_100NPS\_NOH).



In Figure 10-47, a typical noise pattern similar to the one from previous experiments.

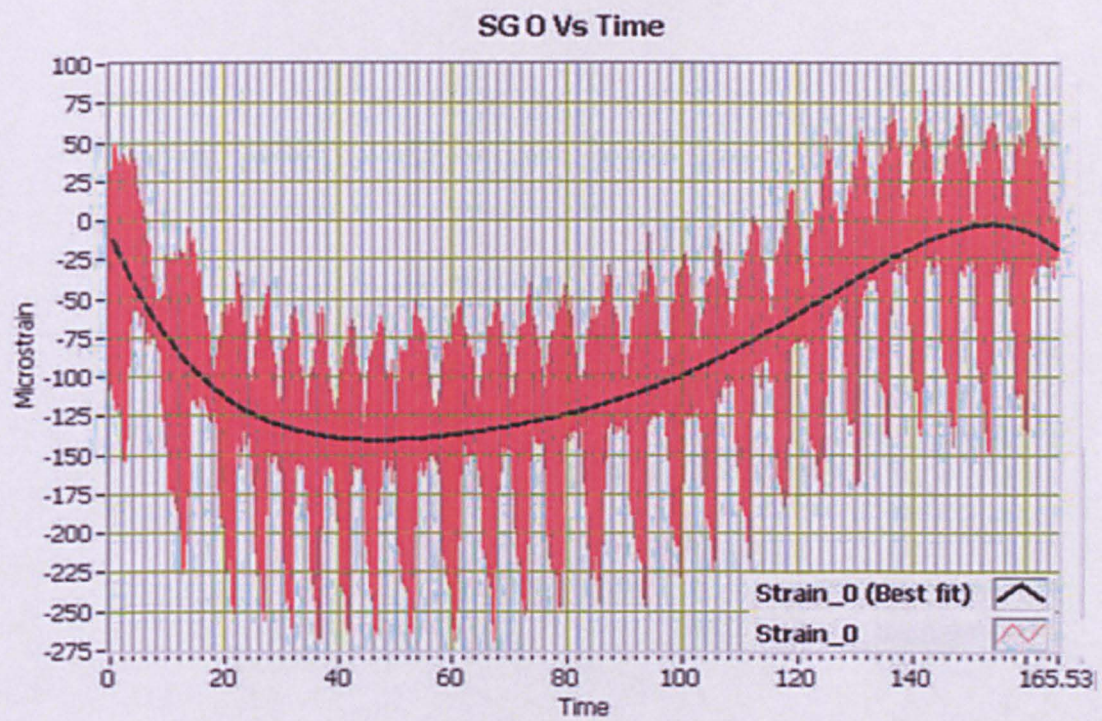


Figure 10-49: Raw Data with lots of typical noise of one typical strain gauge's output (SG 0 Vs Time) with respect to time.

As discussed in previous experiments, the same steps are taken for further noise analysis. Figure 10-49 shows a magnified view from the output (Microstrain) of one typical strain gauge (SG 0 Vs Time).

In figure 10-49, the raw data coloured in red contains the output of s.gauge 0 (SG 0) together with a typical noise which is similar as in previous experiments. The filtered signal is shown in Figure 10-50.



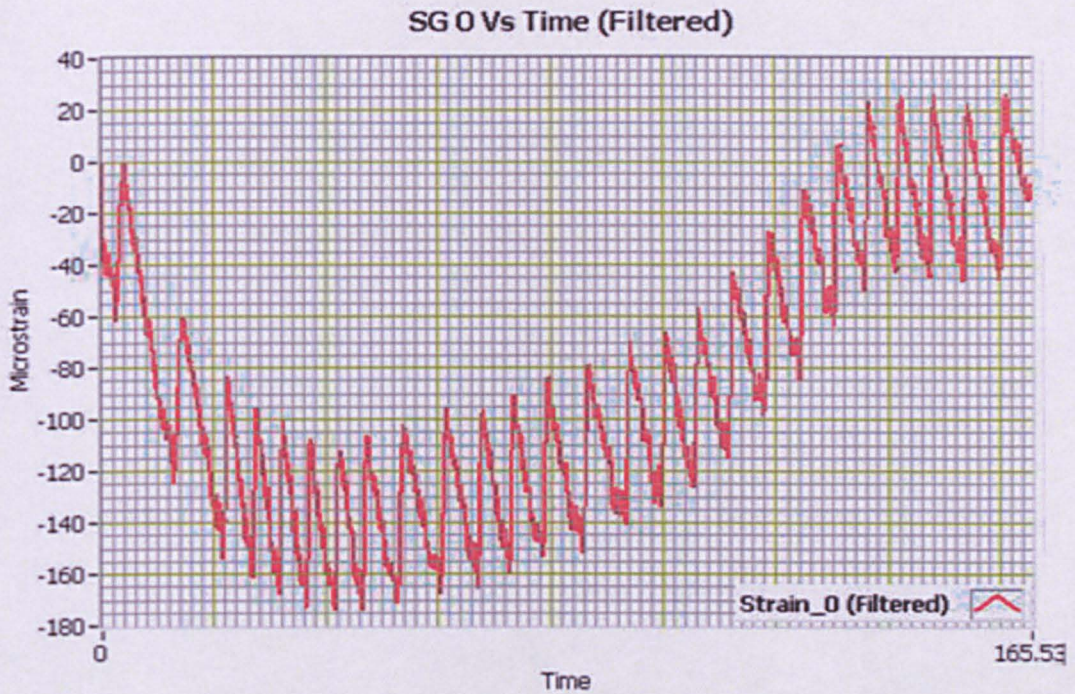


Figure 10-50: Filtered data of one typical strain gauge's output (SG 0 Vs Time) with respect to time. Low pass 3rd order Butterworth IIR filter-with cutoff frequency 5 Hz is used for filtering.

Here, the same signal processing techniques were applied as in the previous experiment 3. In this experiment the graph is divided in two parts; the first part is when loading from 0 to 4 kN and the second part is unloading from 4 kN to 0 kN. According to the experiment protocol, the compressive load is applied from 0 to 4 kN in the first part with 100 NPS loading speed compare to 500 NPS in the previous experiment 3. Therefore, the duration of the first part is of about 40 seconds and the duration of second part is of about 40 seconds again when unloading from 4 to 0 kN with the same 100 NPS speed. Hence, both parts of the graph are of non-stationary type.

The first 4000 samples of the waveform graph are converted to the final plot of the waveform using "curve fitting" signal processing technique. The model of polynomial equation of order N is used here and value of N is either 1 or 2 as in previous experiment 3. The second part of the waveform graph should have approximately a total number of samples of 4000 but here it is 10000, and is converted to the final plot of waveform using the same signal processing curve fitting tools as used in the first part. Hence, after multipart parametric signal processing, the resultant waveform is shown in Figure 10-51, named "SG 0 Vs Time and Load Vs Time". The graph



has two Y-axis, one is in Microstrain and other is in applied compressive load (Newton).

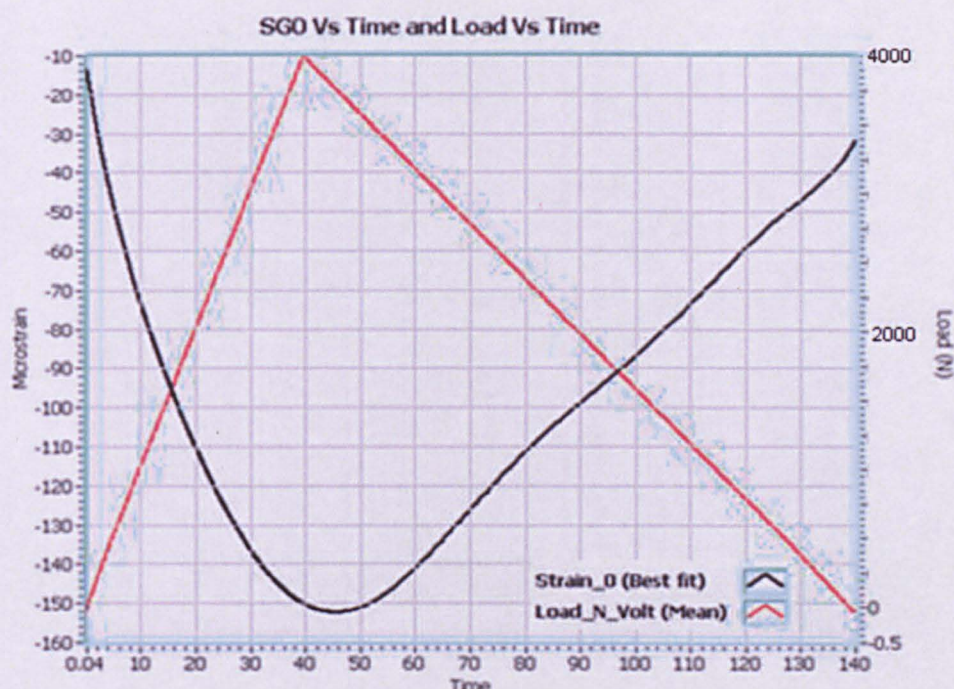


Figure 10-51: Typical strain gauge output and applied load graph with respect to time (SG 0 Vs Time and Load Vs Time).

Similarly, Figure 10-52 shows the graphical presentation of the two Flexiforce® sensors with respect to time. The graph has two Y-axis, similar to those shown in Figure 10-51, one is in Microstrain and other is in applied compressive load (Newton). The graphs are obtained using identical signal processing techniques for both the Flexiforce® sensors. The outputs of the Flexiforce® sensors are matching with the applied load graph in Figure 10-52.



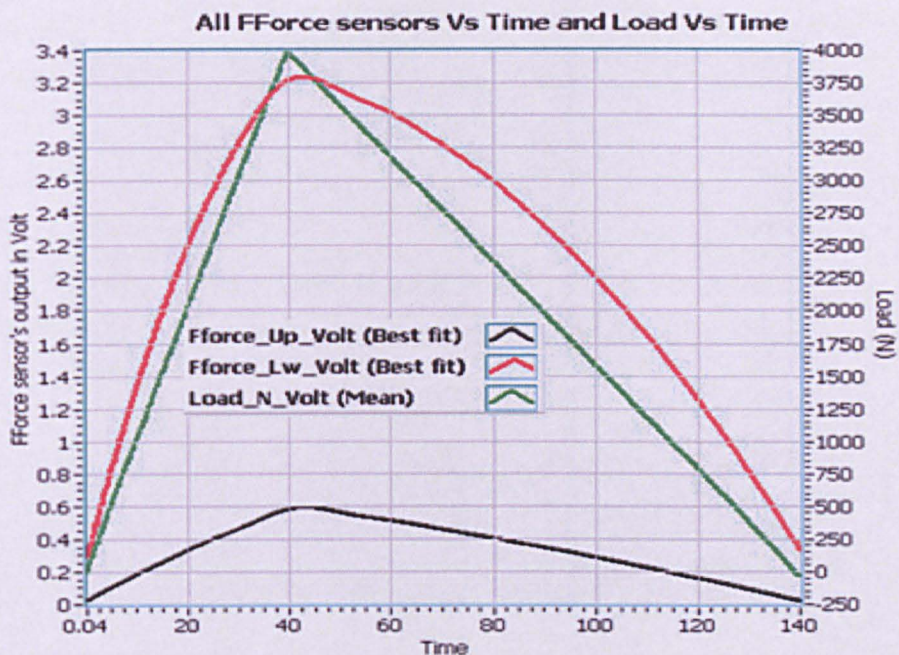


Figure 10-52: Outputs from two Flexiforce® sensors and applied load graph with respect to time.

The signal processing techniques used in SG 0 Vs Time are also used for plotting all the outputs of the eight strain gauges (SG 0 to SG 7) and the two Flexiforce® sensors (Flexiforce®\_Upper and Flexiforce®\_Lower). For better comparison all outputs are plotted on a same graph as shown in Figure 10-53.

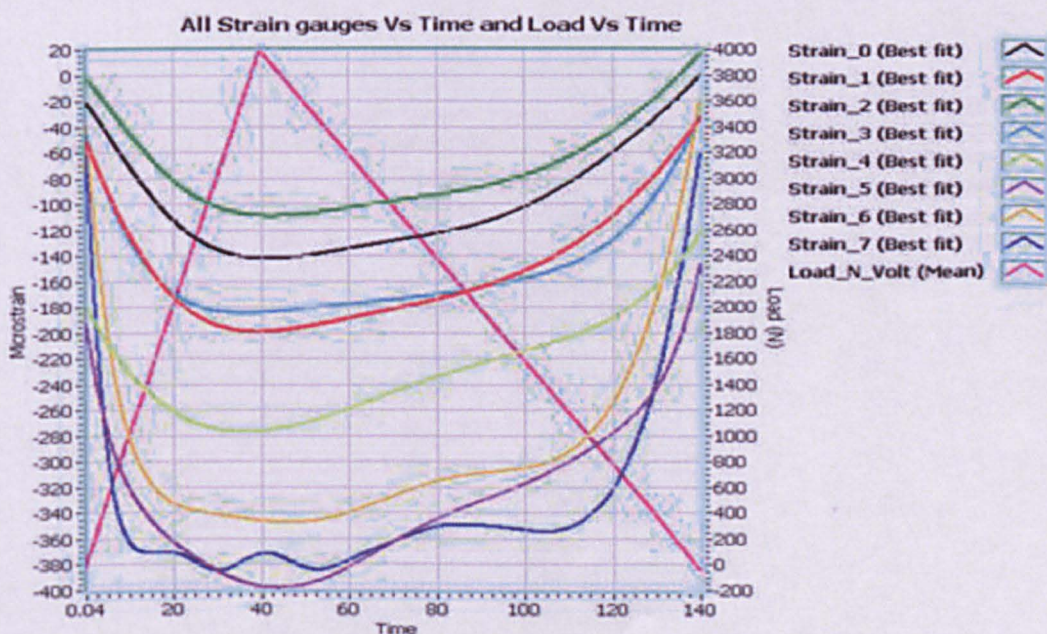


Figure 10-53: All SG output (Microstrain) & Load (N) Vs Time (S), Experiment protocol: Exp\_4k\_100NPS\_NOH.



All sensors' outputs are similar with the analogue output of the applied compressive load. One noticeable observation when compared to the graphs in the previous experiment 3 (Figure 10-40, 10-41 and 10-42), is that in this experiment the sensor's outputs are more non-linear (Figure 10-51, 10-52 and 10-53). This concluded that the less the speed of loading the behaviour is more visco-elastic in nature. This can also be seen in loading and unloading cycles of this experiment with different speeds.

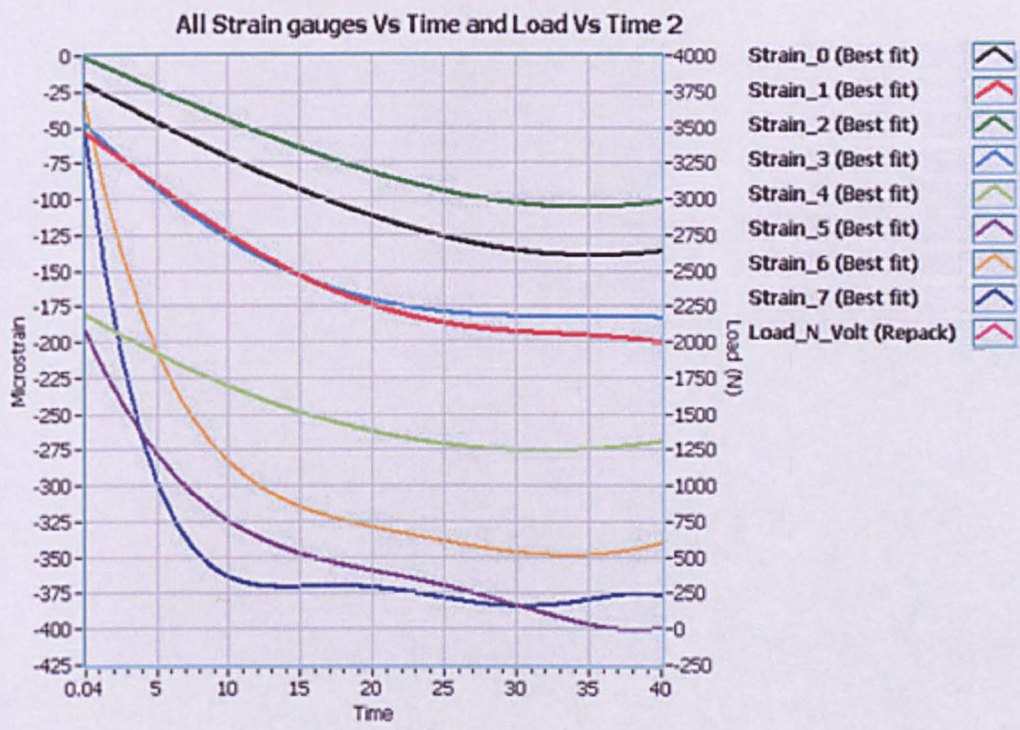


Figure 10-54: The 1st part of the graph for all strain gauge's output when loading from 0 to 4 kN.

Each part of Figure 10-53, is magnified and shown in Figure 10-54 and 10-55 separately. In every experiment the result output from strain gauge 7 is different from the other strain gauge's outputs.



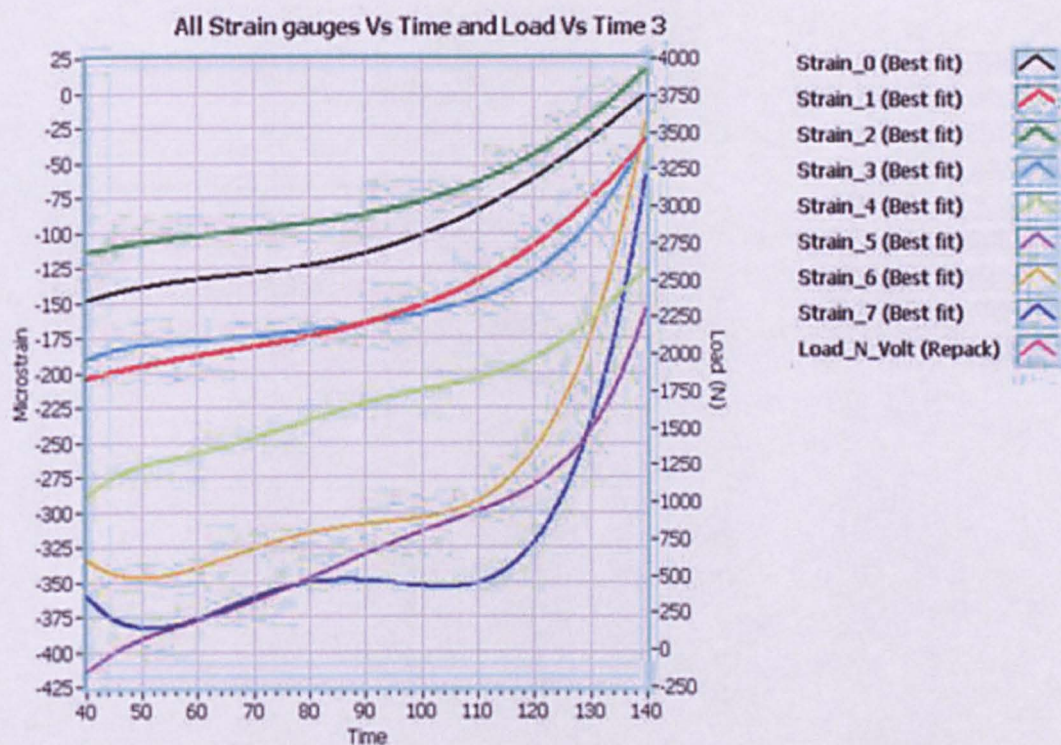


Figure 10-55: The 2nd part of the graph for all strain gauge's output when unloading from 4 to 0 kN.

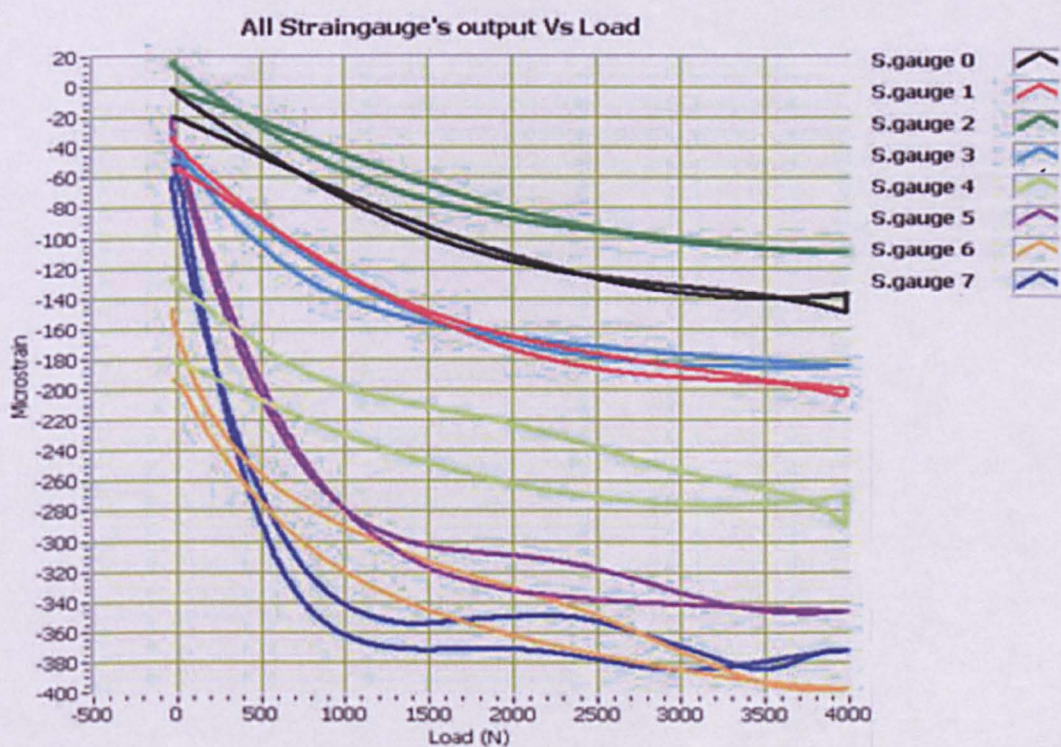


Figure 10-56: All strain gauges outputs with respect to applied compressive load.



Figure 10-56 shows the outputs from all strain gauges with respect to the applied compressive load. The applied compressive load in Newton is along the X-axis and strain gauges output in Microstrain are along the Y-axis. The graph shows similar characteristics especially in the range of 250 N to 3750 N. The little irregularity in the graph between 3750 N to 4000 N is due to change in loading speed and direction of loading i.e. from 100 NPS speed to 0 and again 0 to 40 NPS at the same time from compressive loading to unloading.

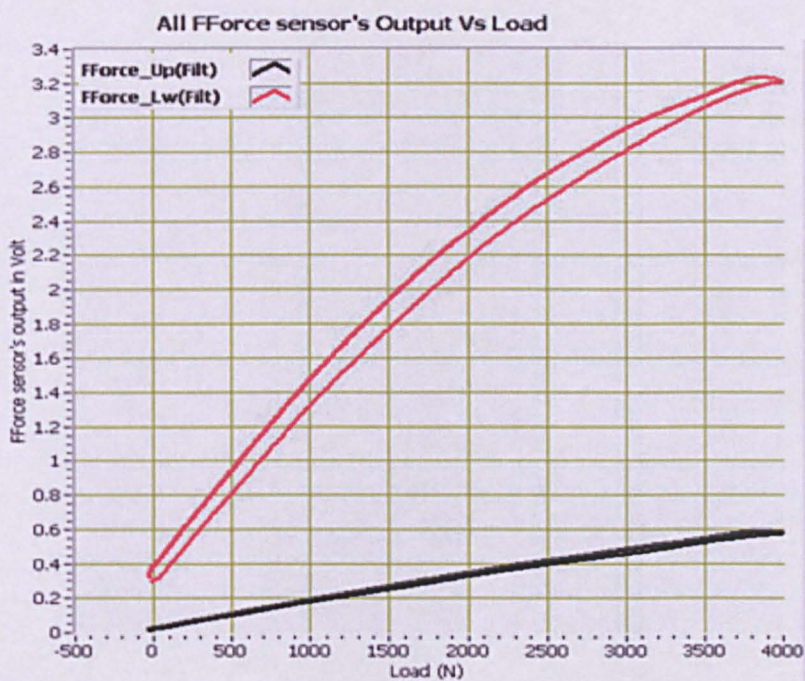


Figure 10-57: Two Flexiforce® sensor's output with respect to applied compressive load.

Figure 10-57 shows the outputs from the two Flexiforce® sensors with respect to the applied compressive load. The applied compressive load in Newton is along the X-axis and Flexiforce® sensor's output in dc volt is along the Y-axis. The graph shows very clear and similar characteristics. One noticeable observation in this experiment is that the output from the Flexiforce® sensor is more non-linear compare to experiment 3. The reason might be the difference in loading speed. In experiment 3 the loading speed was 500 NPS and in this experiment the loading speed is 100 NPS.

In both Figures 10-56 and 10-57, the hysteresis can be found between plots of the loading and unloading cycle. As mentioned in the previous experiments, the hysteresis shown in Figure 10-56 and 10-57 is smaller and much more uniform, especially for Flexiforce®. In Figure 10-57, the hysteresis shown by both Flexiforce® sensors is almost the same in percentage value but it looks higher in the Flexiforce® lower than Flexiforce® upper due to different scale of the output values from each Flexiforce® sensor.

#### **10.3.5 Results of Experiment 5: Exp\_4k\_10NPS\_NOH**

---

Experiment 5 was performed as described in the protocol (section 10.2.5) but with some modifications described below. The results are shown in graphical format (see Figure 10-58 and Figure 10-59). This experiment was similar in protocol to the previous experiments 3 and 4 except the loading speed is 10 NPS instead of 500 NPS and 100 NPS respectively. In this experiment, due to very low speed the overall experimental time increased significantly. For example, in the 1st part of the cycle i.e. loading from 0 to 4 kN, it took 400 seconds. The sampling speed is 100 Hz for all experiments, therefore, the total number of samples in the 1st part are 40000. For this reason the Virtual Instrument in Labview was not able to run the data acquisition. Hence, due to this technical issue this protocol is modified and the loading was done at 10 NPS designed speed but unloading cycle was done at a very high speed (500 NPS).

The graphs in Figure 10-58 present the outputs from all eight strain gauges (s.gauge 0 to s.gauge 7) and the outputs from the two piezoresistive-Flexiforce® sensors (F.force\_upper and F.force\_lower) when a compressive load is applied (with respect to time). The last graph depicted in Figure 10-58 titled as "Load Vs Time" presents the analogue output of the applied compressive load by the universal testing machine.



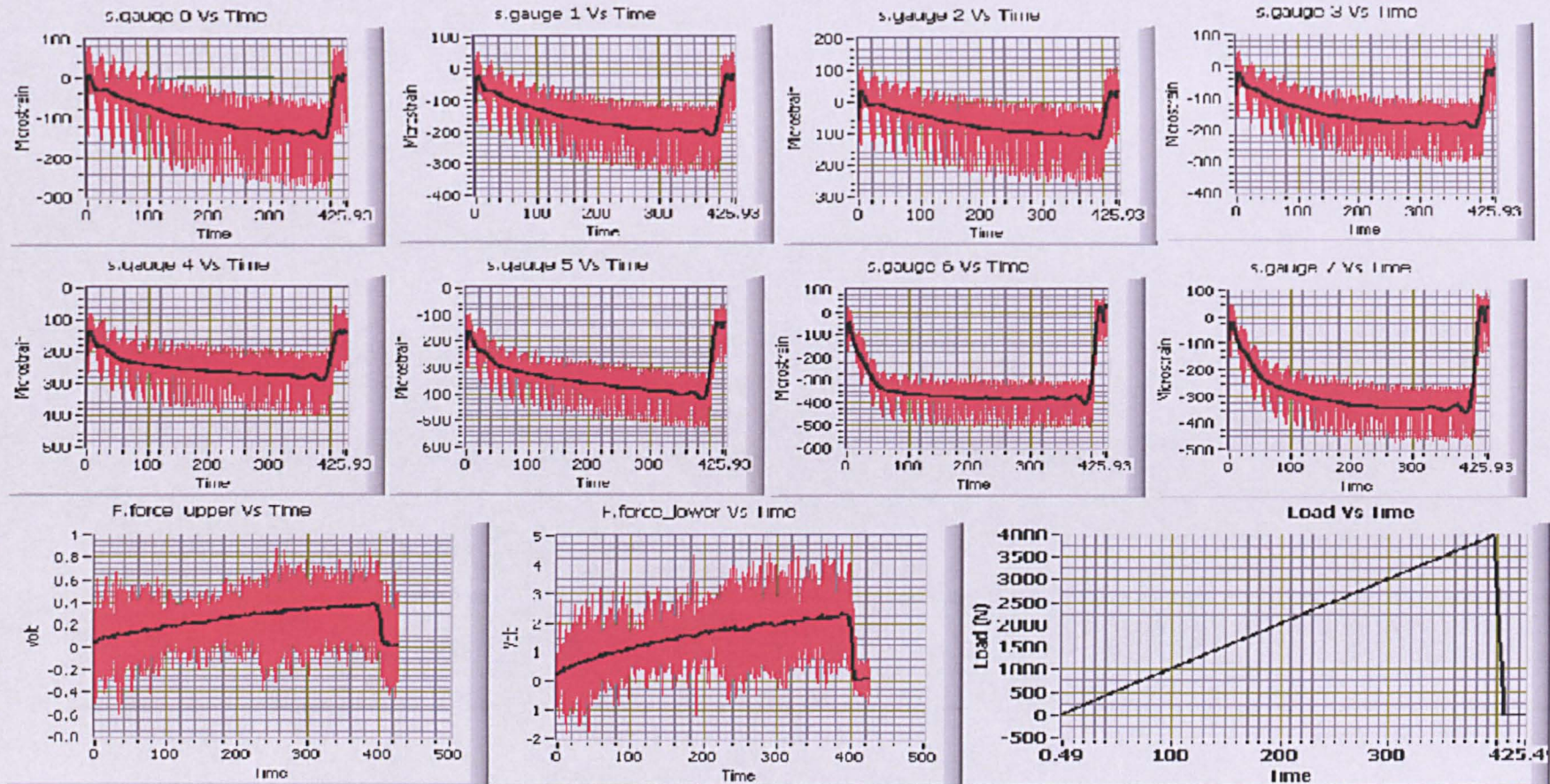


Figure 10-58: All eight strain gauge's outputs, two piezoresistive-Flexiforce® sensor's outputs and applied compressive load in Newton with respect to time in seconds. (Experiment protocol: Exp\_4k\_10NPS\_NOH).



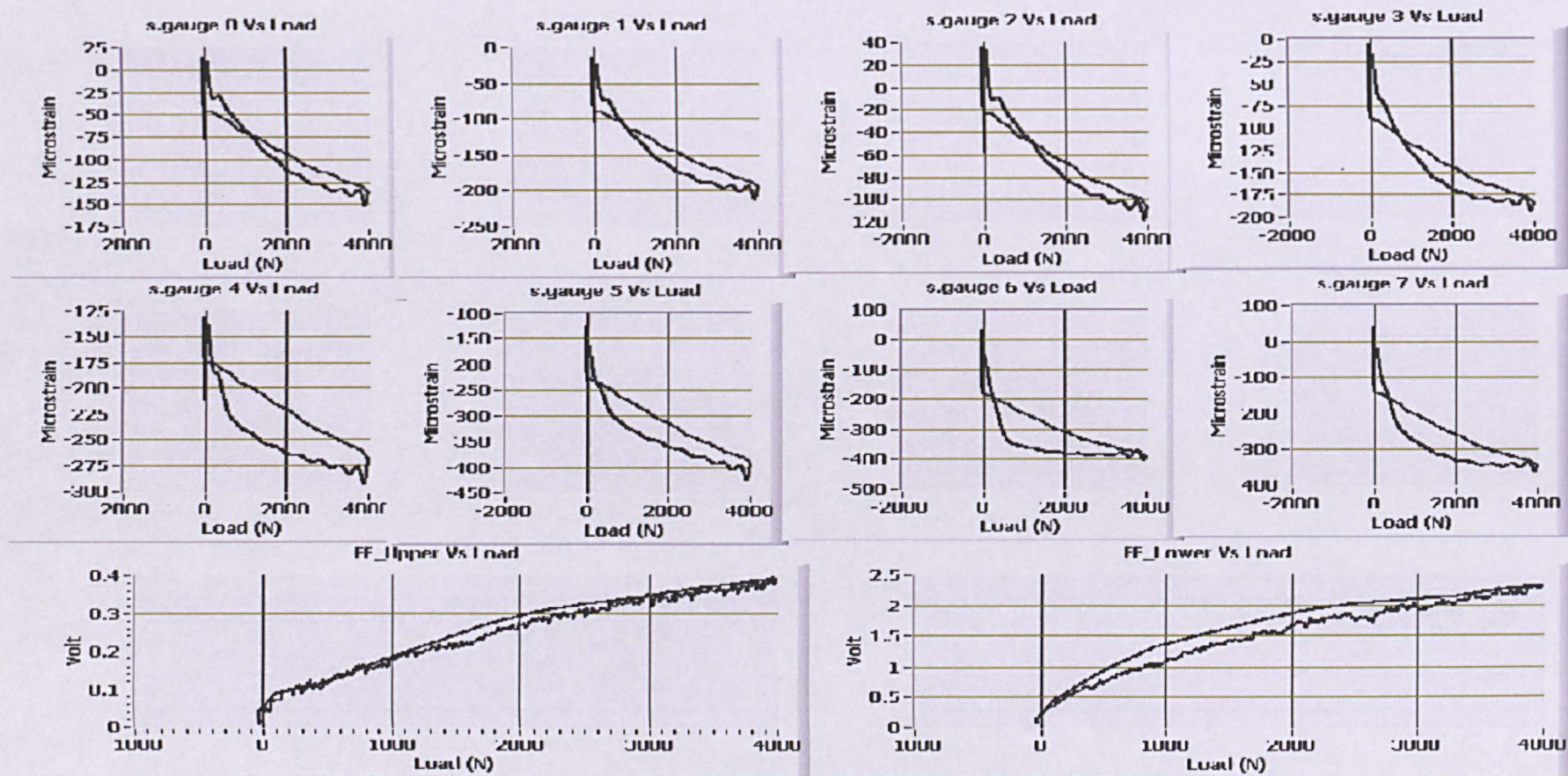


Figure 10-59: All eight strain gauge's outputs and two piezoresistive-Flexiforce® sensor's outputs with respect to applied compressive load in Newton. (Experiment protocol: Exp\_4k\_10NPS\_NOH).



In the graphs, outputs from all strain gauges are presented in Microstrain (Microstrain = strain  $\times 10^{-6}$ ) and outputs from the two Flexiforce® sensors are in analogue dc volt (Y-axis). The time is in seconds (x-axis). The red colour portions in all graphs shows the noisy raw signal and the black line plots are the best fit lines. Similarly in Figure 10-59, the graphs present the outputs from all eight strain gauges (s.gauge 0 to s.gauge 7) and the outputs from the two piezoresistive-Flexiforce® sensors (F.force\_upper and F.force\_lower) when a compressive load is applied (with respect to the applied compressive load).

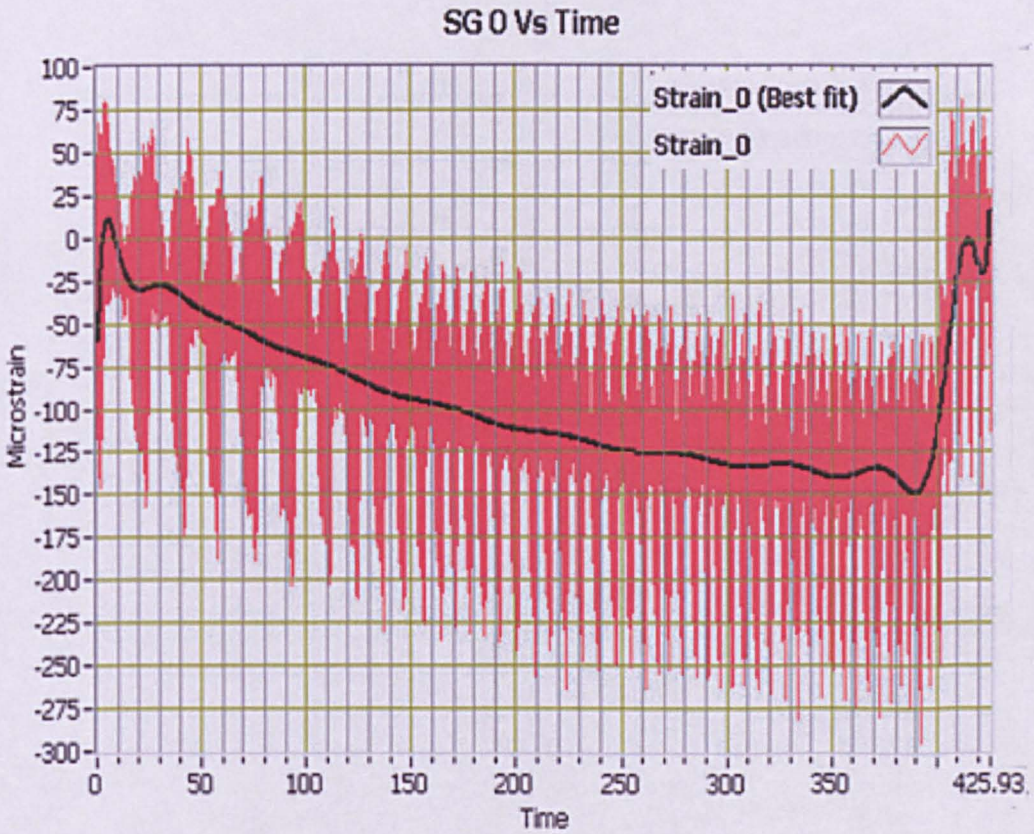


Figure 10-60: Raw Data with lots of typical noise of one typical strain gauge's output (SG 0 Vs Time) with respect to time.

In the graphs, outputs from all strain gauges are presented in Microstrain (Microstrain = strain  $\times 10^{-6}$ ) and outputs from the two Flexiforce® sensors are in analogue dc volt (Y-axis). The applied compressive load is in Newton (x-axis). In Figure 10-58, a typical noise pattern similar to previous experiments can be seen in the graphs representing outputs from all strain gauges. Similarly, a different noise pattern can also be seen in the graphs representing outputs from the two Flexiforce® sensors.



As discussed in previous experiments, the same steps were taken for further noise analysis. Figure 10-60 shows a magnified view from the output (Microstrain) of one typical strain gauge (SG 0 Vs Time).

In figure 10-60, the raw data coloured in red contain the output of s.gauge 0 (SG 0) together with a typical noise and which is similar as in previous experiments. Here again, to filter the noise the Low Pass 3rd order Butterworth IIR Filter is used with 5 Hz cutoff frequency.

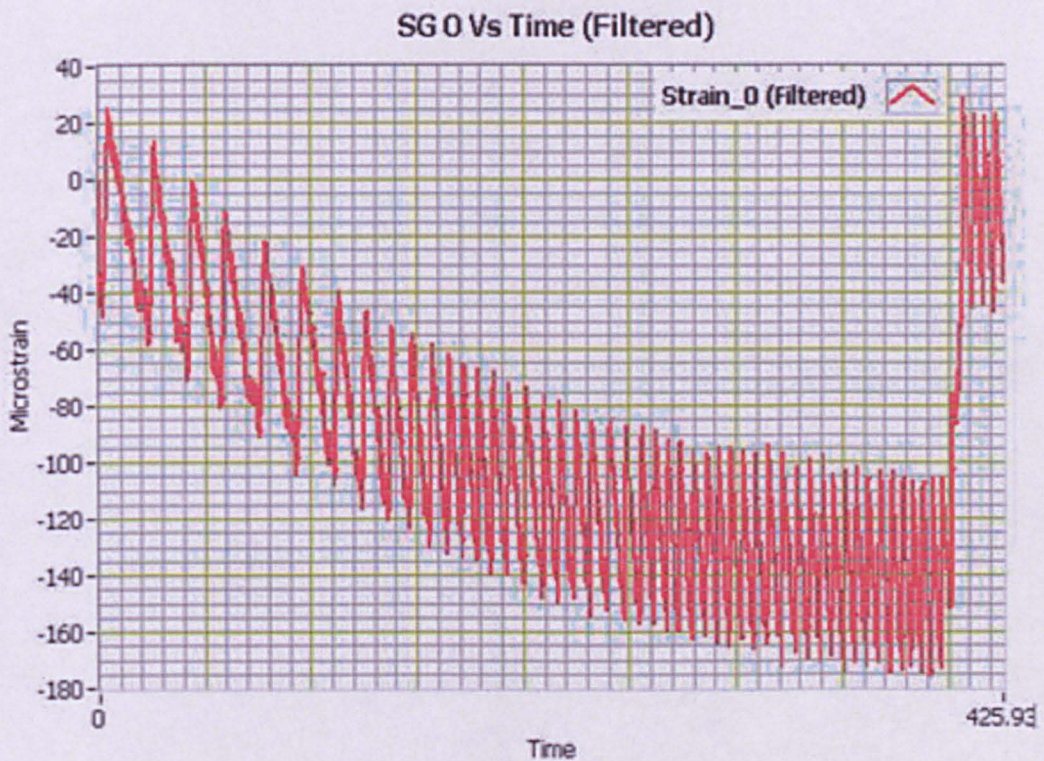


Figure 10-61: Filtered data of one typical strain gauge's output (SG 0 Vs Time) with respect to time. Low pass 3rd order Butterworth IIR filter-with cutoff frequency 5 Hz is used for filtering.

The filtered signal is shown in Figure 10-61 which is very much similar as in previous experiments. The same signal processing techniques were applied as in previous experiments with little modification in the "curve fitting" polynomial model. In this experiment the graph is divided into two parts; the first part is when loading from 0 to 4 kN and the second part is unloading from 4 kN to 0 kN. According to the modified experiment protocol, the compressive load is applied from 0 to 4 kN in the first part with 10 NPS loading speed compare to 100NPS in experiment 4 and 500



NPS in experiment 3. So, the duration of the first part is of about 400 seconds and the duration of the second part is of about 7-8 seconds. Therefore, both parts of the graph are of non-stationary type but with significantly different loading/unloading speed.

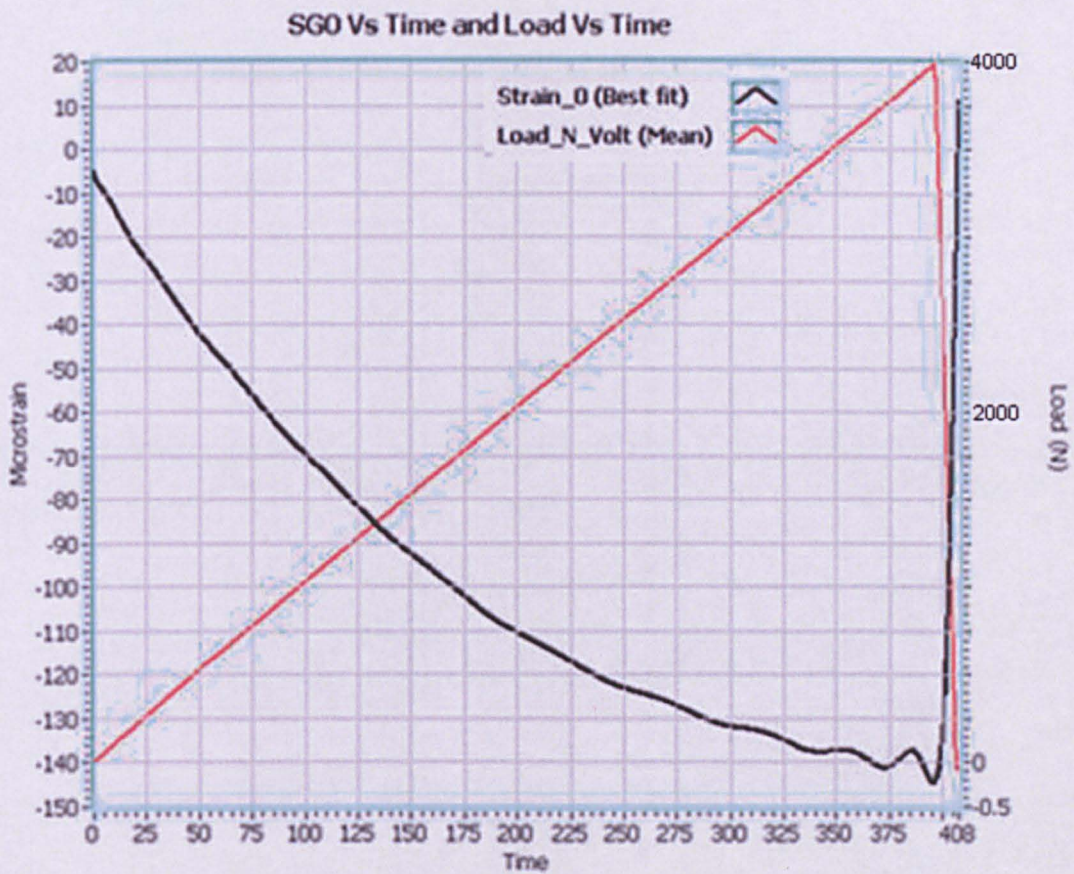


Figure 10-62: Typical strain gauge output and applied load graph with respect to time (SG 0 Vs Time and Load Vs Time).

The first part of the waveform graph is of 400 seconds and the sampling speed of the data acquisition system was set to 100 Hz. For 400 seconds, the approximate total samples are around 40000 (400 x 100). Hence, the first 40000 samples of waveform graph are converted to the final plot of the waveform using the "curve fitting" signal processing technique. The model of polynomial equation of order N is used here. For the second part of the waveform graph approximately 800 samples are converted to the final plot of the waveform using the same signal processing curve fitting tools as used in the first part but with different curve fitting model N value. So, after multipart parametric signal processing, the resultant waveform is shown in Figure 10-62, named "SG 0 Vs Time and Load Vs Time". The graph has two



Y-axis, one is in Microstrain and the other is in applied compressive load (Newton).

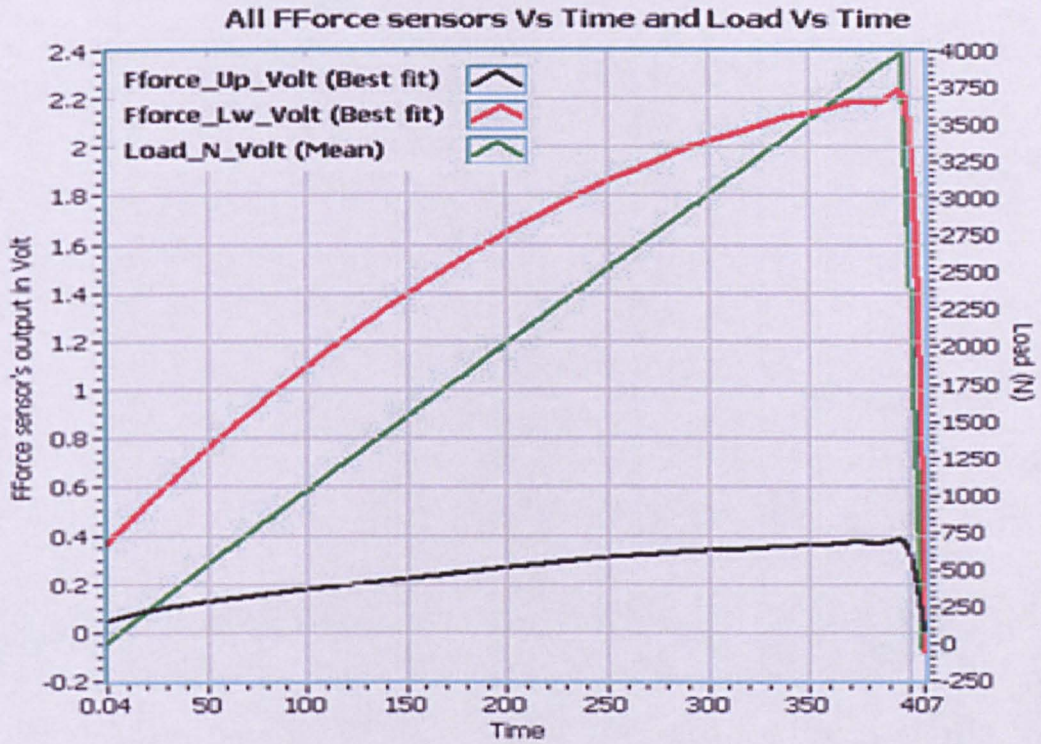


Figure 10-63: Outputs from two Flexiforce® sensors and applied load graph with respect to time.

Similarly, Figure 10-63 shows the graphical presentation of the two Flexiforce® sensors with respect to time. The graph has two Y-axis similar to Figure 10-62, one is in Microstrain and the other is in applied compressive load (Newton). The graphs are obtained using identical signal processing techniques for both the Flexiforce® sensors. The outputs of the Flexiforce® sensors match well with the analogue output of the applied compressive load.

The signal processing techniques used in SG 0 Vs Time is also used for plotting all outputs of the eight strain gauges (SG 0 to SG 7) and the two Flexiforce® sensors (Flexiforce®\_Upper and Flexiforce®\_Lower). For better comparison all outputs are plotted on a same graph as shown in Figure 10-64.



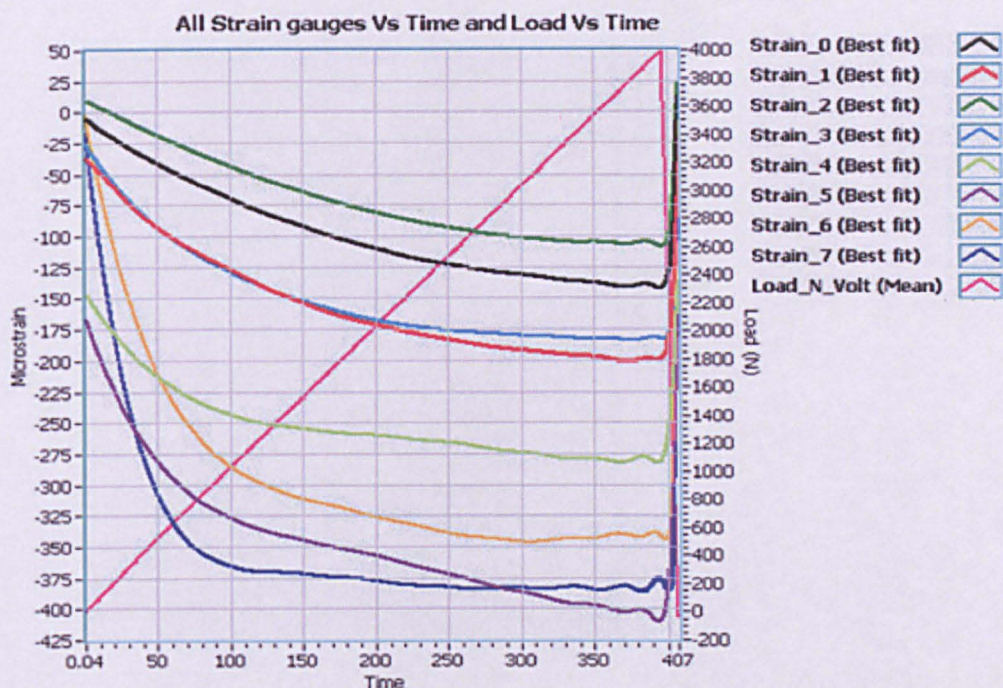


Figure 10-64: All SG output (Microstrain) & Load (N) Vs Time (S)

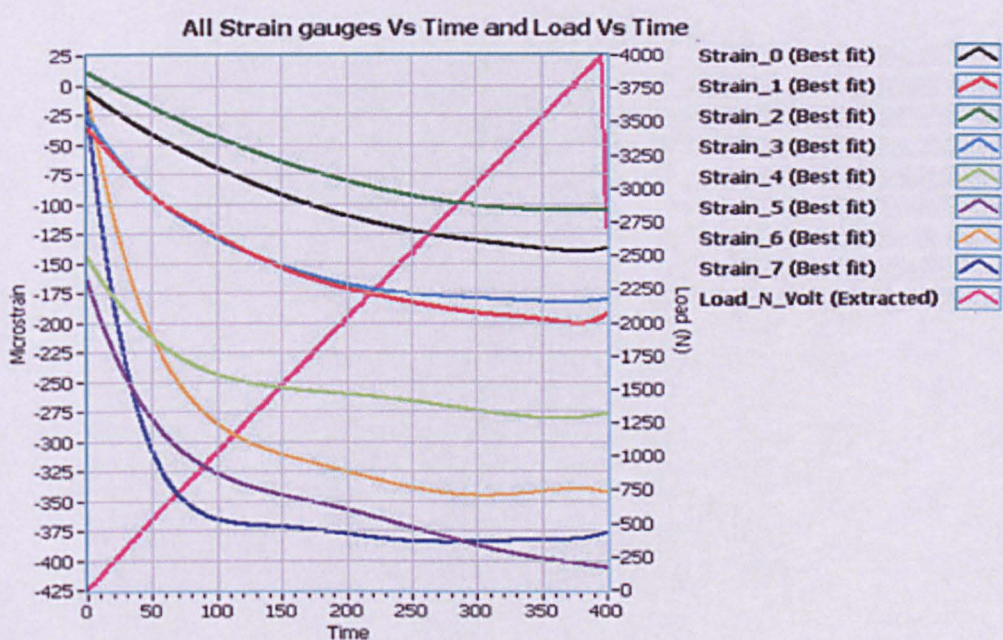


Figure 10-65: The 1st part of the graph for all strain gauge's output when loading from 0 to 4 kN.

The 2nd part of the graph which represents the sensor's output when unloading from 4 to 0 kN has duration of 7-8 seconds only. This is much less compared to the 1st part of the graph which is 400 seconds.



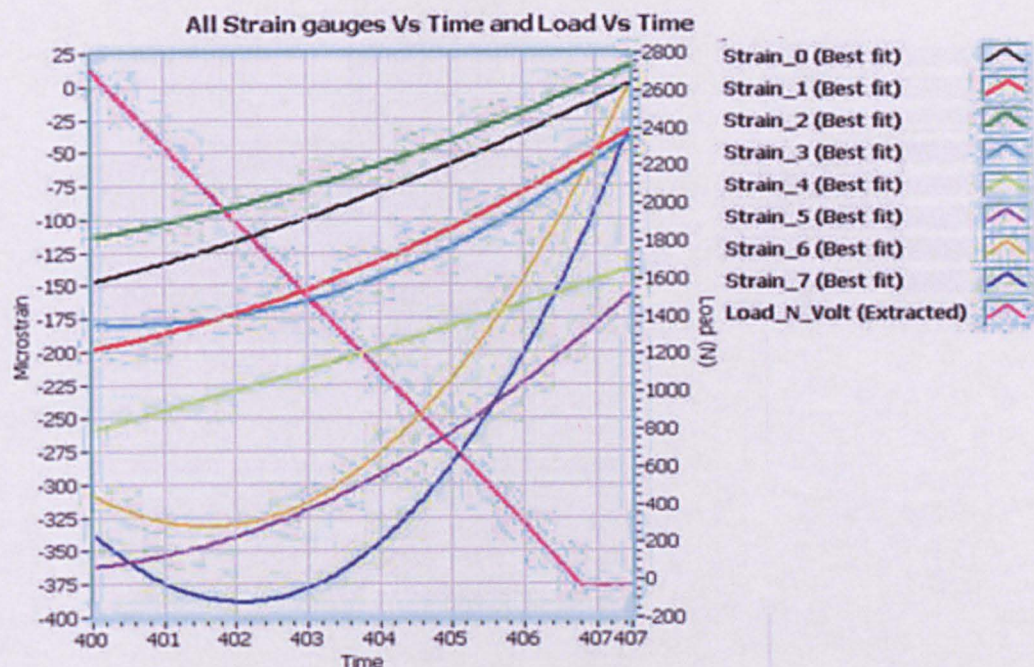


Figure 10-66: The 2nd part of the graph for all strain gauge's output when unloading from 4 to 0 kN.

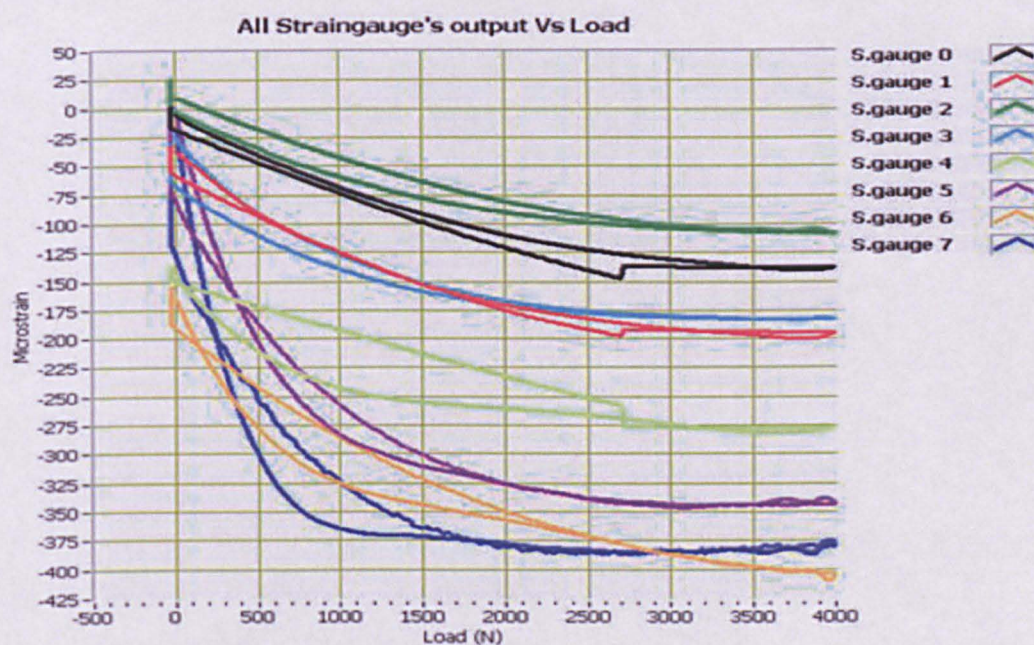


Figure 10-67: All strain gauges outputs with respect to applied compressive load.

Hence, to clearly present the graph, the 2nd and 1st part of the graph in Figure 10-64 is magnified and shown in Figure 10-65 and 10-66 respectively. It can be easily seen in the Figure 10-64 and Figure 10-62 that all strain gauge's outputs are a little non-linear in nature which is, as mentioned before due to the visco elastic inlay material of the disc.



Figure 10-67 shows the outputs from all strain gauges with respect to the applied compressive load. The applied compressive load in Newton is along the X-axis and strain gauges output in Microstrain are along the Y-axis. The graph shows very clear and similar characteristics in all graphs.

Figure 10-68 shows the outputs from the two Flexiforce® sensors with respect to the applied compressive load. The applied compressive load in Newton is along the X-axis and the Flexiforce® sensor’s output in dc volt is along the Y-axis.

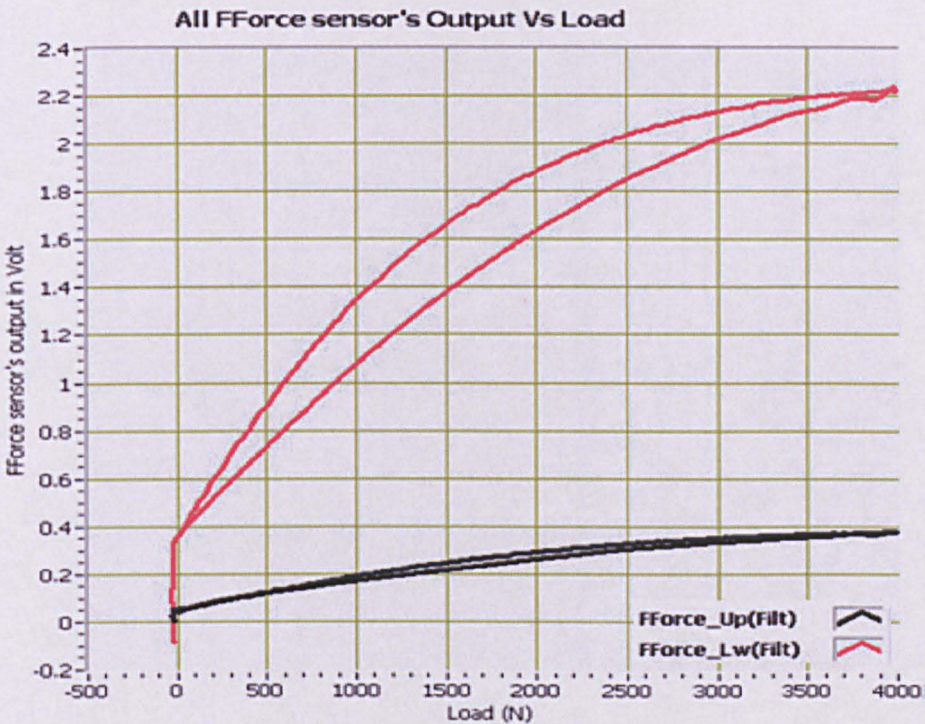


Figure 10-68: Two Flexiforce® sensor’s output with respect to applied compressive load.

The hysteresis in the graphs of the outputs from the Flexiforce® sensors in this experiment is higher than experiments 3 and 4. One of the reasons could be the significant difference in loading and unloading speed.

### 10.3.6 Result of Exp. 6: Exp\_4k\_step1k\_500NPS\_LH30S

Experiment 6 was performed as described in the protocol (section 10.2.5). The results are shown in graphical format; see Figure 10-69 and Figure 10-70. The graphs in Figure 10-69 present the outputs from all eight strain gauges (s.gauge 0 to s.gauge 7) and the outputs from the two



piezoresistive-Flexiforce® sensors (F.force\_upper and F.force\_lower) when a compressive load is applied (with respect to time).

The last graph depicted in Figure 10-69 entitled as “Load Vs Time” presents the analogue output of the applied compressive load by the universal testing machine. In the graphs, outputs from all strain gauges are presented in Microstrain ( $\text{Microstrain} = \text{strain} \times 10^{-6}$ ) and outputs from the two Flexiforce® sensors are in analogue dc volt (Y-axis). The red colour portions in all graphs show the noisy raw signal and the black line plots are the best fit lines.

Similarly in Figure 10-70, the graphs present the outputs from all eight strain gauges (s.gauge 0 to s.gauge 7) and the outputs from the two piezoresistive-Flexiforce® sensors (F.force\_upper and F.force\_lower) when a compressive load is applied (with respect to the applied compressive load). In the graphs, outputs from all strain gauges are presented in Microstrain ( $\text{Microstrain} = \text{strain} \times 10^{-6}$ ) and outputs from the two Flexiforce® sensors are in analogue dc volt (Y-axis). The applied compressive load is in Newton (x-axis). In Figure 10-69, a typical noise pattern similar to previous experiments can be seen in the graphs representing outputs from all strain gauges. Similarly, a different noise pattern can also be seen in the graphs representing outputs from the two Flexiforce® sensors.

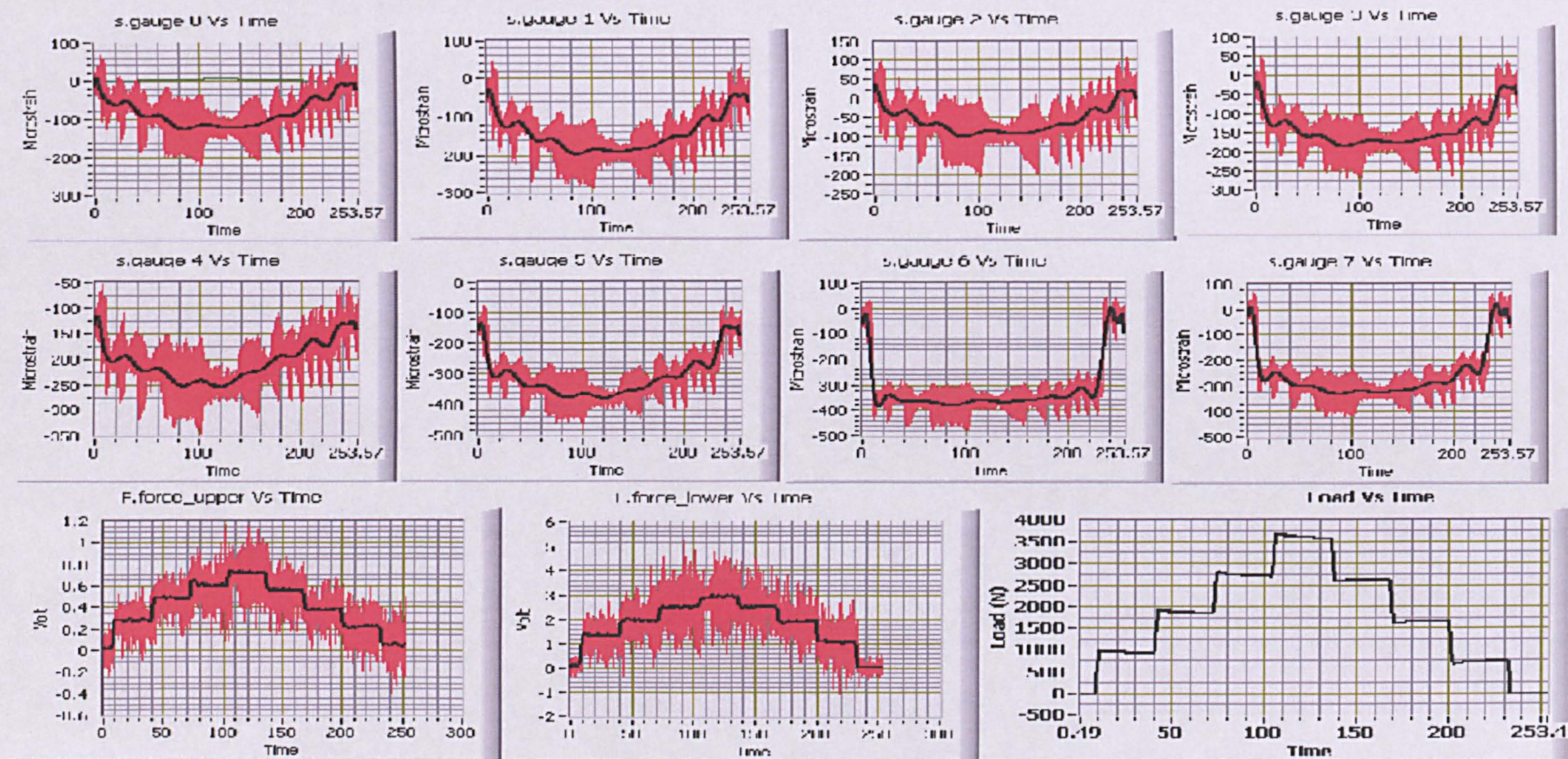


Figure 10-69: All eight strain gauge's outputs, two piezoresistive-Flexiforce® sensor's outputs and applied compressive load in Newton with respect to time in seconds. (Experiment protocol: Exp\_4k\_step1k\_500NPS\_LH30S).



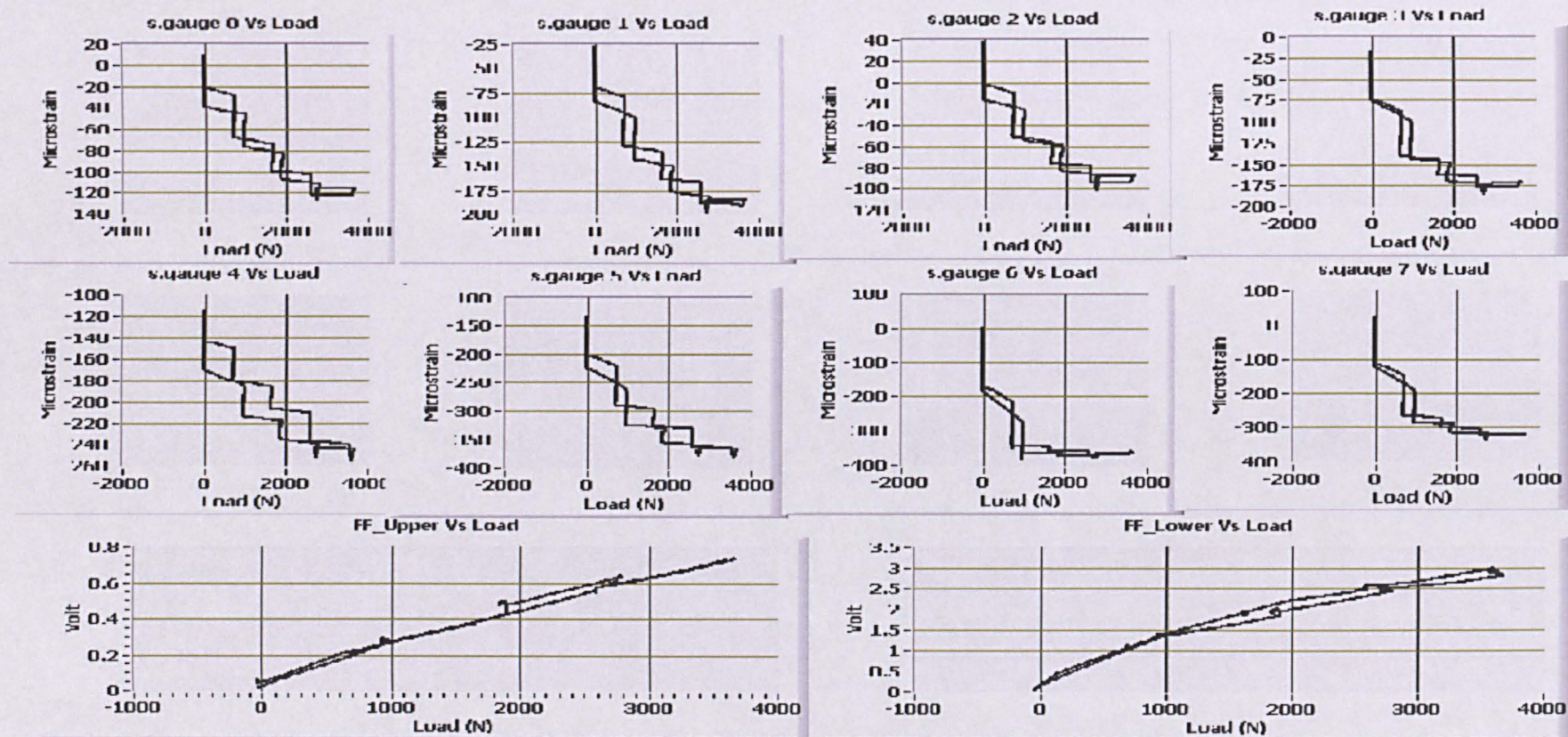


Figure 10-70: All eight strain gauge's outputs and two piezoresistive-Flexiforce® sensor's outputs with respect to applied compressive load in Newton. (Experiment protocol: Exp\_4k\_step1k\_500NPS\_LH30S).



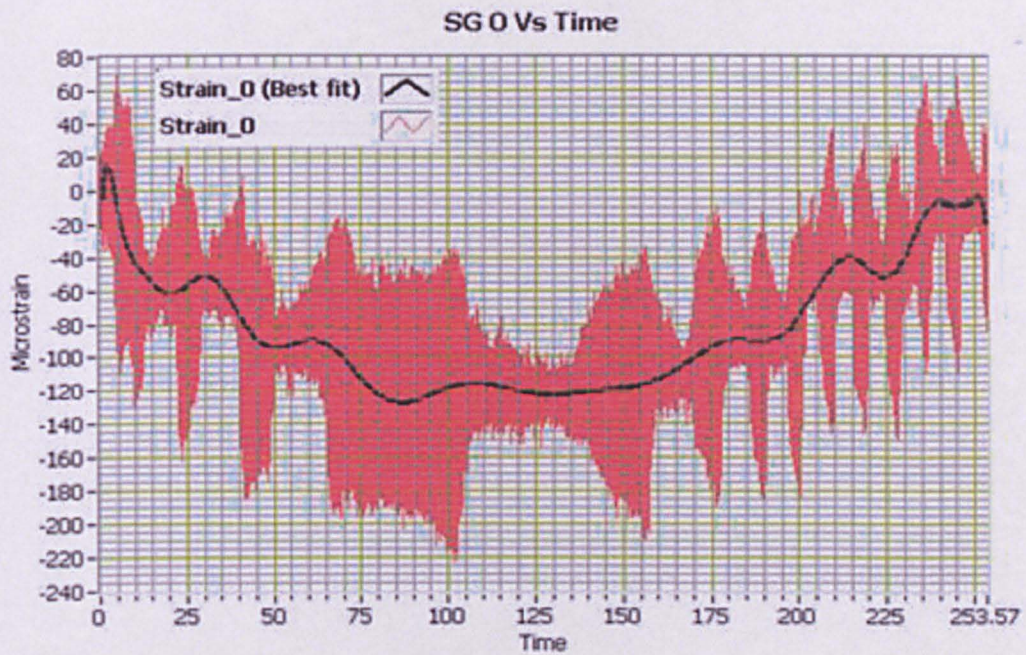


Figure 10-71: Raw Data with lots of typical noise of one typical strain gauge's output (SG 0 Vs Time) with respect to time.

In this experiment the noise filtering is extremely difficult because there are 15 parts of stationary and non-stationary types, out of which 8 parts are non-stationary type with 500 NPS loading/unloading speed and 7 parts are stationary type. Also, the duration of the parts are small which makes signal processing extremely difficult. As discussed in previous experiments, the same steps are taken for further noise analysis though they are not sufficient for this experiment looking at the complications explained before. Figure 10-71 shows a magnified view from the output (Microstrain) of one strain gauge out (SG 0 Vs Time).

In figure 10-71, the raw data coloured in red contains the output of s.gauge 0 (SG 0) together with a typical noise which is very much similar as in previous experiments. To filter the noise the Low Pass 3rd order Butterworth IIR Filter is used with 5 Hz cutoff frequency.

The filtered signal is shown in Figure 10-72 which is different from the previous experiments. For proper signal processing, the whole graph should be split in 15 parts as explained in the protocol. But, here the same signal processing techniques were used for the whole graph. The study protocol is, loading from 0 to 1 kN and then 30 seconds load holding, again after that



loading starts from 1 kN to 2kN then again load holding of 30 sec. Same way for unloading and upto 4 kN peak value.

The “curve fitting” signal processing is used for the whole graph with polynomial model of value N order. The value of N selected in the range of 15-23. The higher the value of N the resultant graph is sharper and near to the original raw data curve.

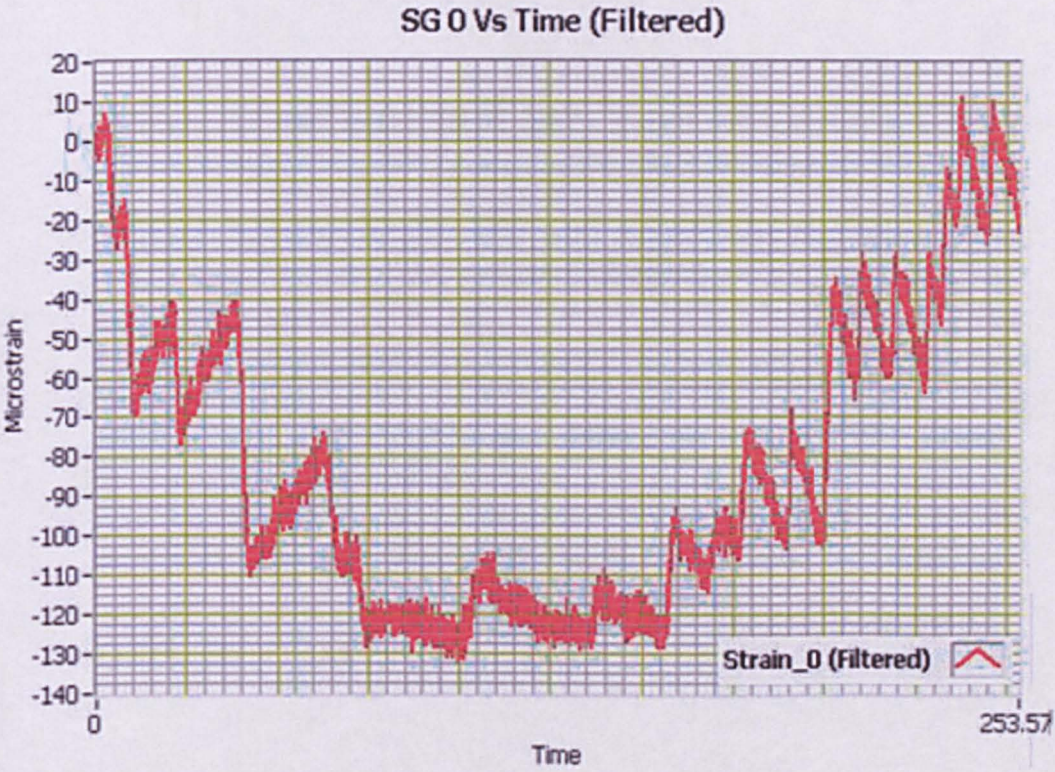


Figure 10-72: Filtered data of one typical strain gauge’s output (SG 0 Vs Time) with respect to time. Low pass 3rd order Butterworth IIR filter-with cutoff frequency 5 Hz is used for filtering.

Therefore, after parametric signal processing, the resultant waveform is shown in Figure 10-73, named “SG 0 Vs Time and Load Vs Time”.The graph has two Y-axis, one is in Microstrain and other is in applied compressive load (Newton). The graph is clear but not exactly matching with the analogue output of the applied compressive load in characteristics as in the previous experiments. The strain gauge is experiencing compression that is why the load Vs strain graph is inversely proportional as can be seen in Figure 10-73.



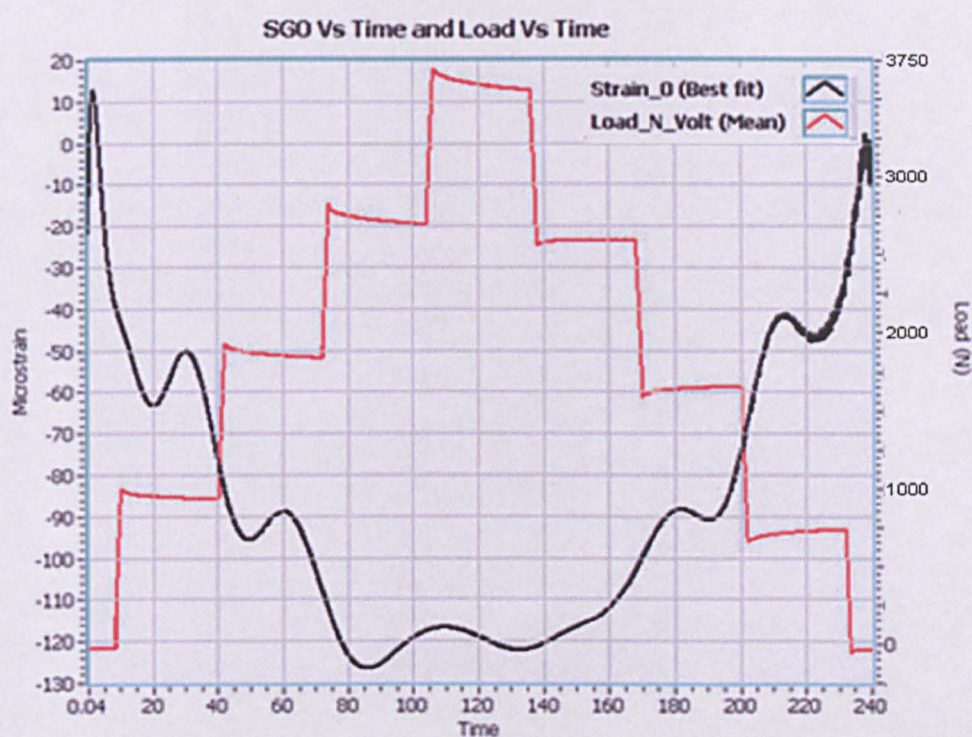


Figure 10-73: Typical strain gauge output and applied load graph with respect to time (SG 0 Vs Time and Load Vs Time).

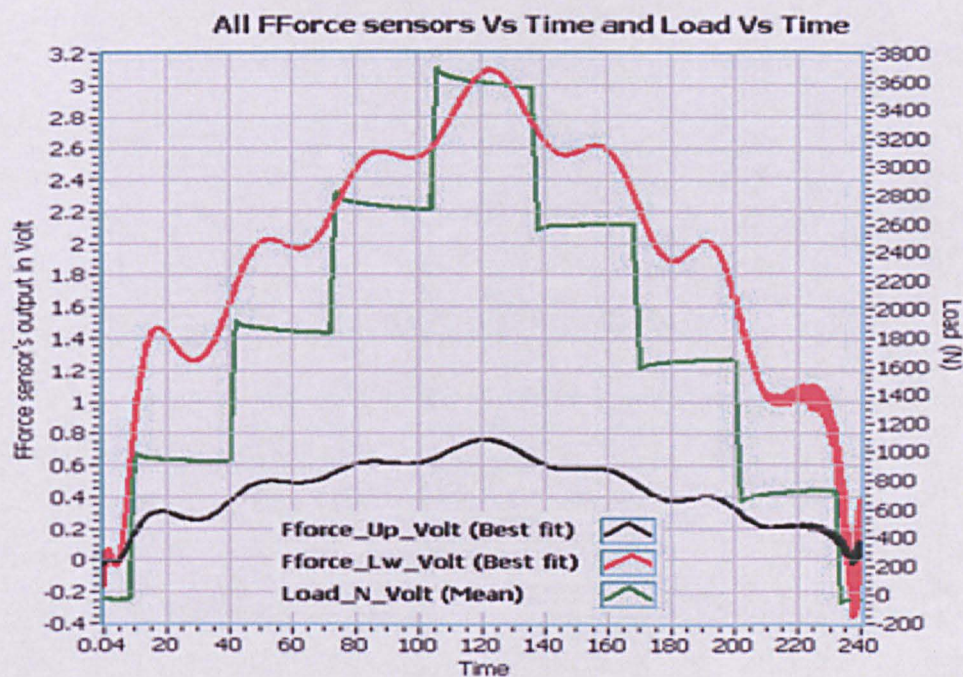


Figure 10-74: Outputs from two Flexiforce® sensors and applied load graph with respect to time.



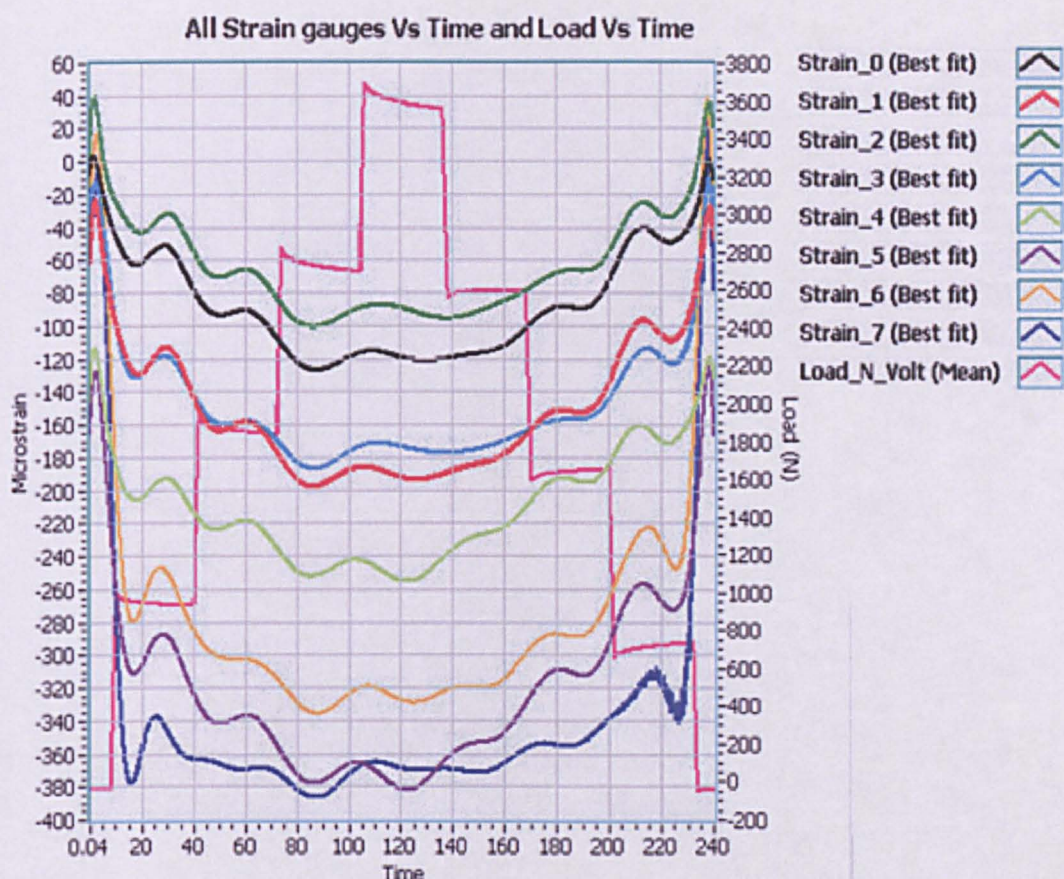


Figure 10-75: All SG output (Microstrain) & Load (N) Vs Time (S)

Similarly, Figure 10-74 shows the graphical presentation of the two Flexiforce® sensors with respect to time. The graph has two Y-axis as shown in Figure 10-74, one is in Microstrain and other is in applied compressive load (Newton). The graphs are obtained using identical signal processing techniques for both the Flexiforce® sensors.

The signal processing techniques used in "SG 0 Vs Time" graph (Figure 10-73) is also used for plotting all outputs from all eight strain gauges (SG 0 to SG 7). For better comparison of all outputs from all strain gauges, all graphs are plotted on the same graph as shown in Figure 10-75. Figure 10-76 shows a magnified view of the 1<sup>st</sup> part of the graph of Figure 10-75. Figure 10-77 shows a magnified view of the 2<sup>nd</sup> part of the graph of Figure 10-75.

Figure 10-78 shows the outputs from all strain gauges with respect to the applied compressive load. The applied compressive load in Newton is along the X-axis and the strain gauges output in Microstrain are along the Y-axis.



The graph shows very clear and similar characteristics especially in the range of 1000 N to 3500 N.

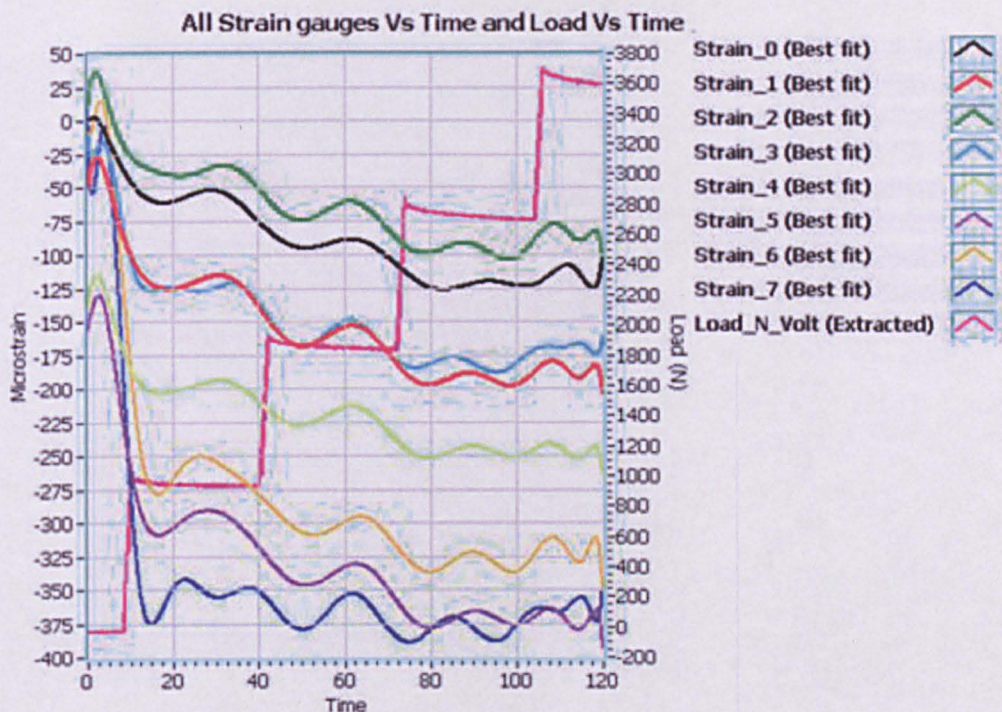


Figure 10-76: The 1st part of the graph for all strain gauge's output when loading from 0 to 4 kN.

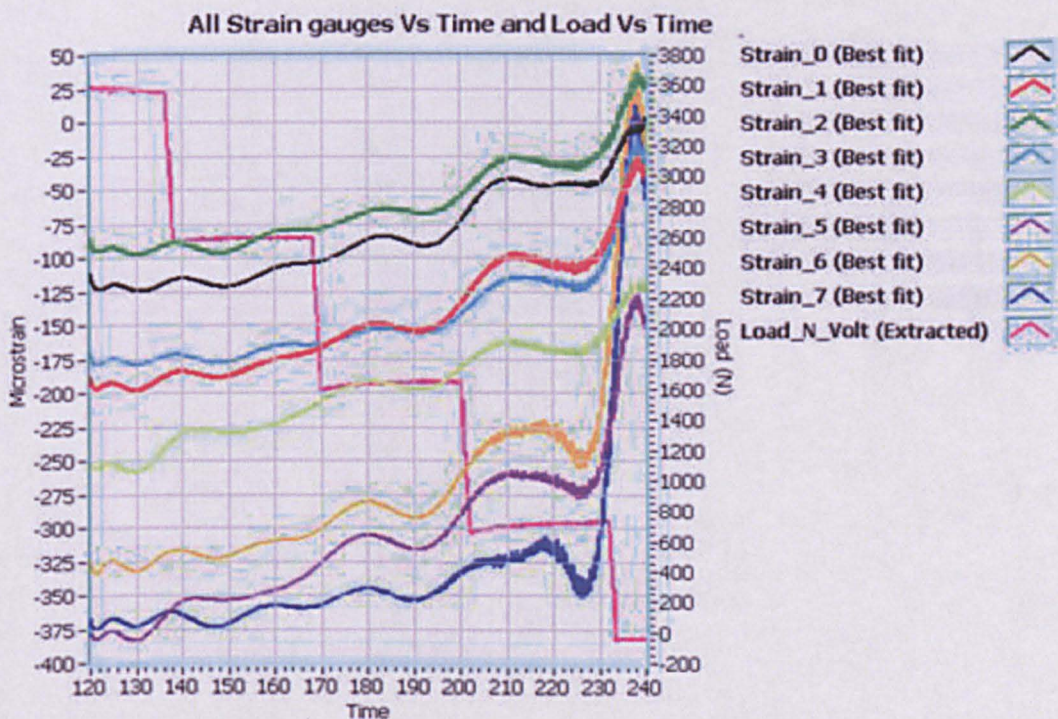


Figure 10-77: The 2nd part of the graph for all strain gauge's output when unloading from 4 to 0 kN.



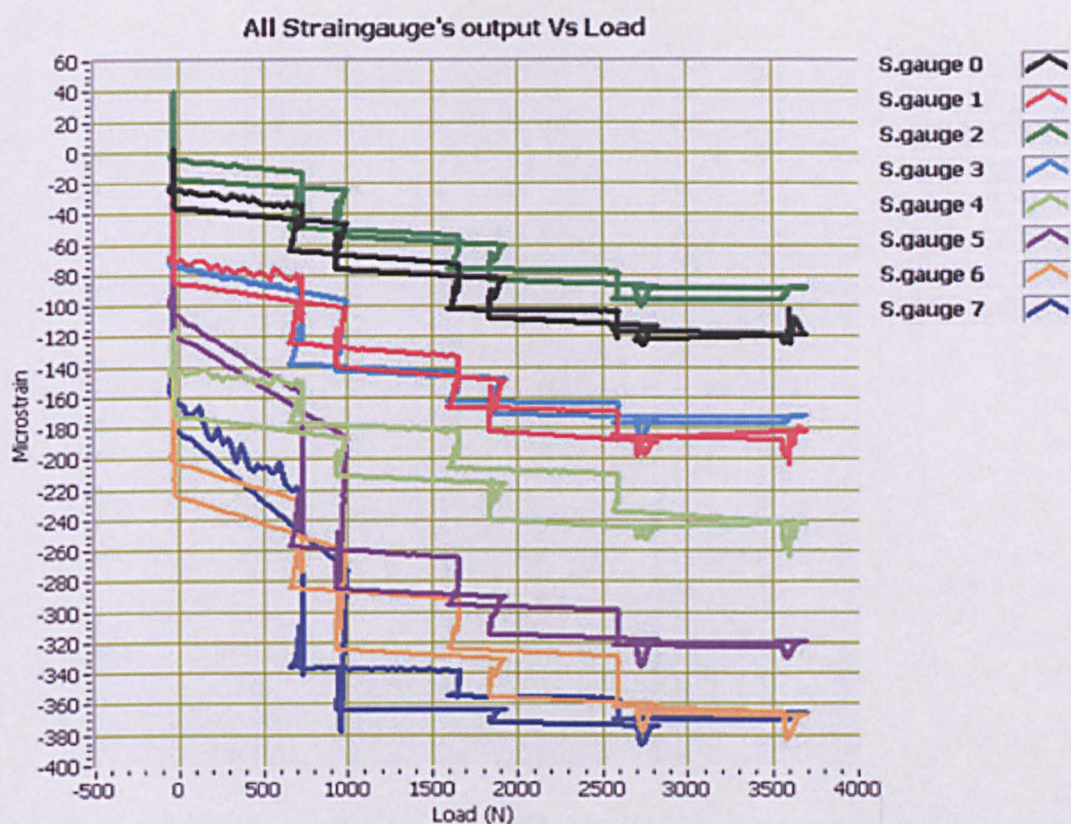


Figure 10-78: All strain gauges outputs with respect to applied compressive load.

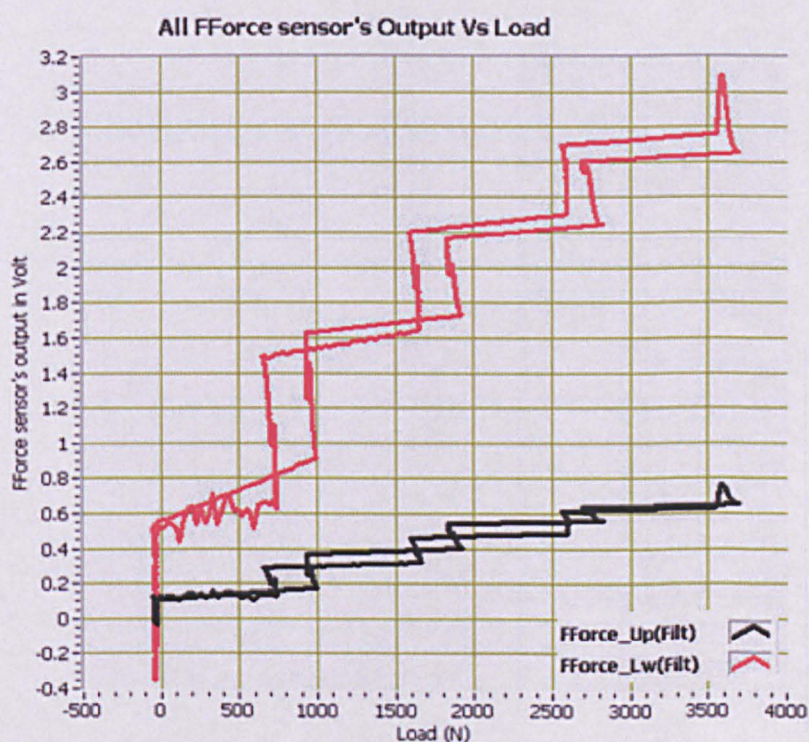


Figure 10-79: Two Flexiforce® sensor's output with respect to applied compressive load.

Figure 10-79 shows the outputs from the two Flexiforce® sensors with respect to the applied compressive load. The applied compressive load in Newton is along the X-axis and Flexiforce® sensor's output in dc volt are along the Y-axis.

In both Figures 10-78 and 10-79, the hysteresis is comparatively uniform and much less in the region of loading from 2700 N to 3700 N.

#### **10.3.7 Result of Exp. 7: Exp\_4k\_step1k\_10NPS\_LH30S**

---

Experiment 7 was performed as described in the protocol (section 10.2.3). The results are shown in graphical format; see Figure 10-80 and Figure 10-81. The graphs in Figure 10-80 present the outputs from all eight strain gauges (s.gauge 0 to s.gauge 7) and the outputs from the two piezoresistive-Flexiforce® sensors (F.force\_upper and F.force\_lower) when a compressive load is applied (with respect to time). The last graph depicted in Figure 10-80 entitled as "Load Vs Time" presents the analogue output of the applied compressive load by the universal testing machine. In the graphs, outputs from all strain gauges are presented in Microstrain ( $\text{Microstrain} = \text{strain} \times 10^{-6}$ ) and outputs from the two Flexiforce® sensors are in analogue dc volt (Y-axis). The time is in seconds (x-axis). The red coloured portions in all graphs shows the noisy raw signal and the black line plots are the best fit lines.

Similarly in Figure 10-81, the graphs present the outputs from all eight strain gauges (s.gauge 0 to s.gauge 7) and the outputs from the two piezoresistive-Flexiforce® sensors (F.force\_upper and F.force\_lower) when a compressive load is applied (with respect to the applied compressive load). In the graphs, outputs from all strain gauges are presented in Microstrain ( $\text{Microstrain} = \text{strain} \times 10^{-6}$ ) and outputs from the two Flexiforce® sensors are in analogue dc volt (Y-axis). The applied compressive load is in Newton (x-axis).

The outputs from all eight strain gauges look similar in characteristics as in the previous experiments. That reconfirms the suitability of the use of strain gauges for this application.



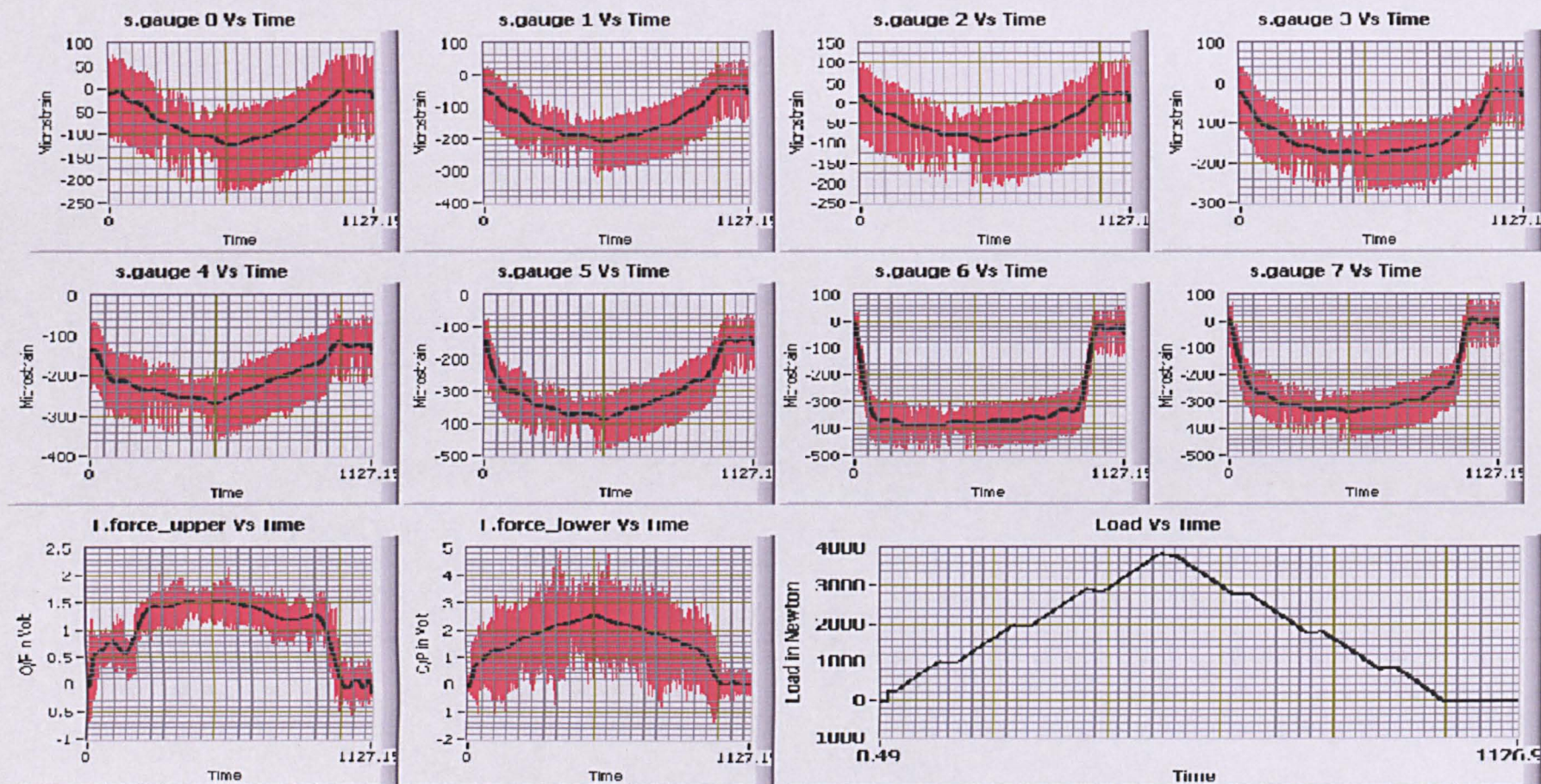


Figure 10-80: All eight strain gauge's outputs, two piezoresistive-Flexiforce® sensor's outputs and applied compressive load in Newton with respect to time in seconds. (Experiment protocol: Exp\_4k\_step1k\_10NPS\_LH30S).



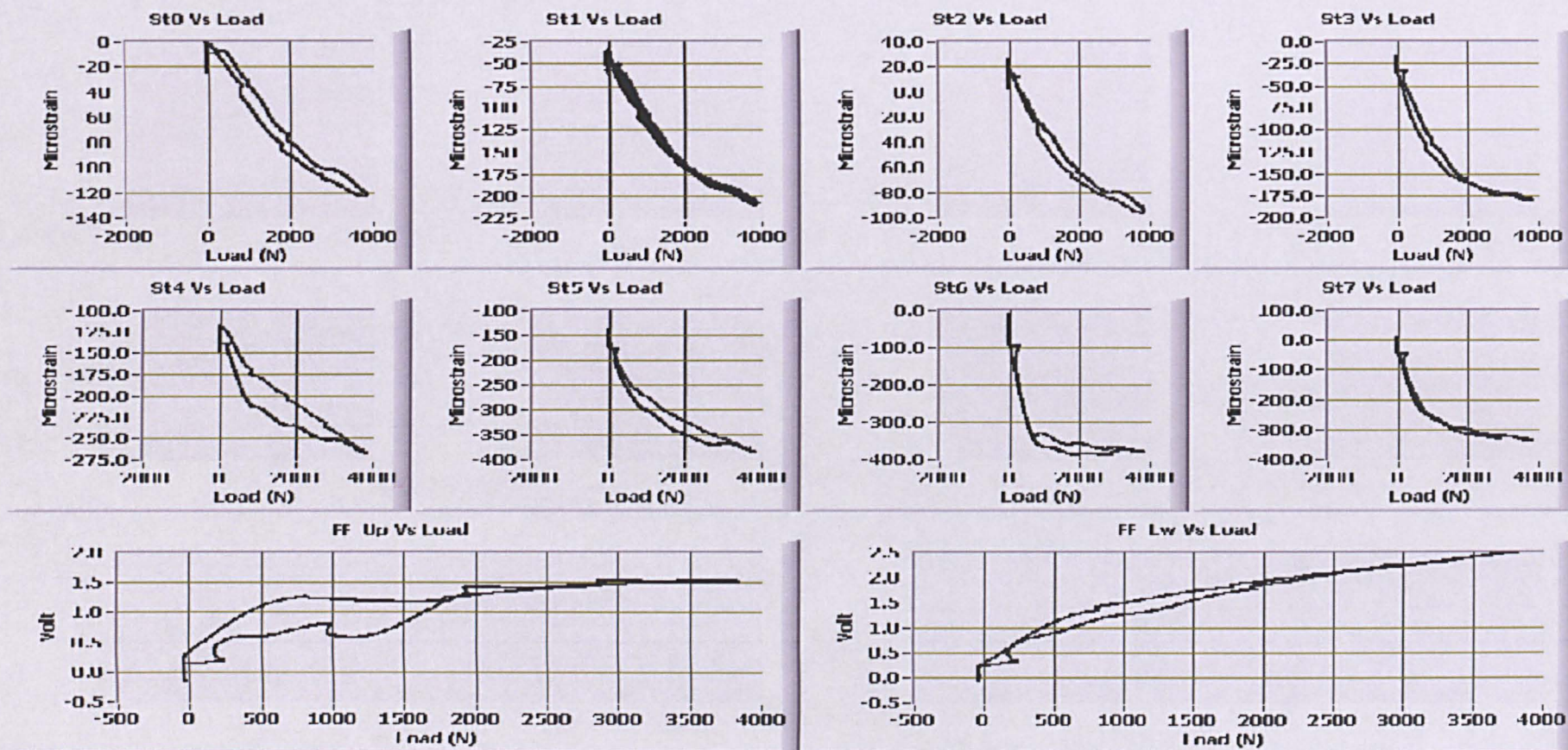


Figure 10-81: All eight strain gauge's outputs and two piezoresistive-Flexiforce® sensor's outputs with respect to applied compressive load in Newton. (Experiment protocol: Exp\_4k\_step1k\_10NPS\_LH30S).



In Figure 10-80, a typical noise pattern similar to previous experiments can be seen in the graphs representing outputs from all strain gauges. Similarly, a different noise pattern can also be seen in the graphs representing outputs from the two Flexiforce® sensors.

Again in this experiment the noise filtering is extremely difficult because there are 15 parts of stationary and non-stationary types. Out of which 8 parts are non-stationary type with 500 NPS loading/unloading speed and 7 parts are stationary type.

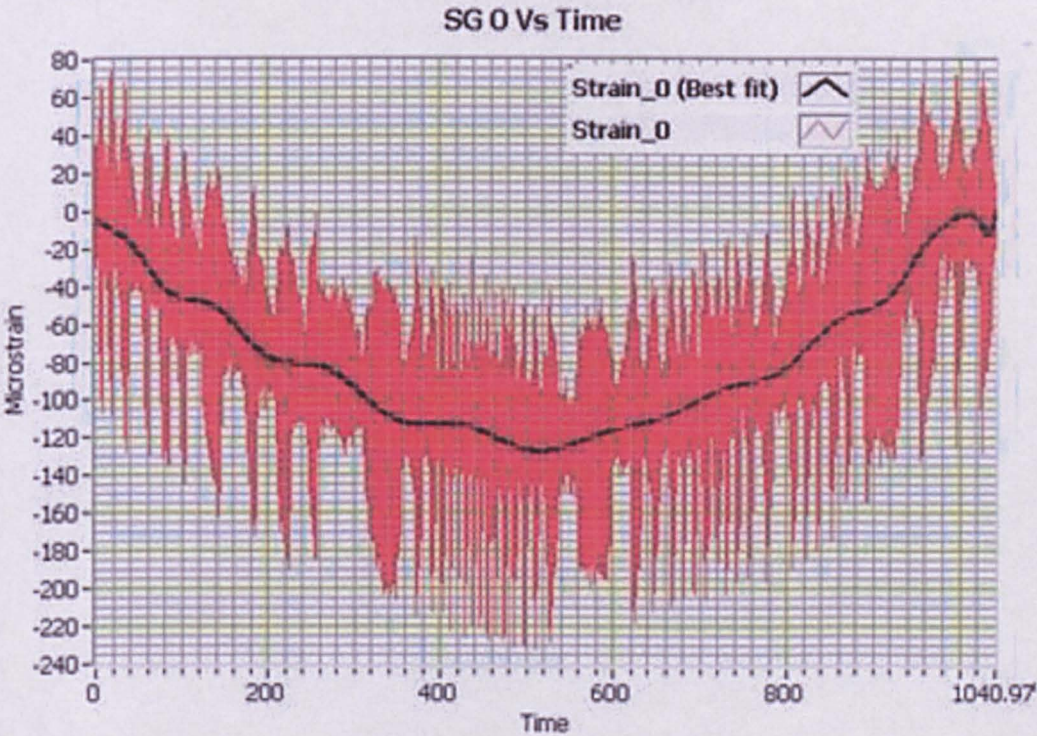


Figure 10-82: Raw Data with lots of typical noise of one typical strain gauge's output (SG 0 Vs Time) with respect to time.

As discussed in previous experiments, the same steps are taken for further noise analysis. Figure 10-82 shows a magnified view from the output (Microstrain) of one typical strain gauge out of all sensors (SG 0 Vs Time).

In figure 10-82, the raw data coloured in red contains the output of s.gauge 0 (SG 0) together with a typical noise which is very much similar as in previous experiments. To filter the noise the Low Pass 3rd order Butterworth IIR Filter is used with 5 Hz cutoff frequency. The filtered signal is shown in Figure 10-83 which is different from the previous experiments. In Figure 10-83, the filtered signal fluctuation range varies from 20 to 30



Microstrain which is somewhat contradictory when compared with Figure 10-82 which had a variation from 20 to 70 microstrain.

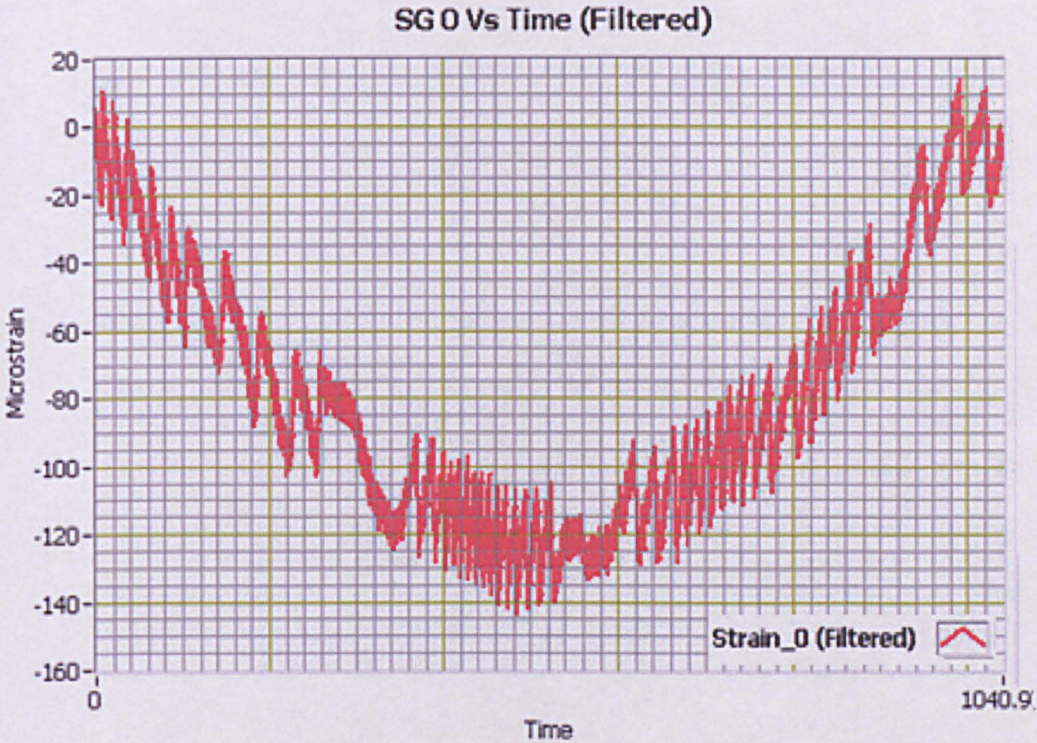


Figure 10-83: Filtered data of one typical strain gauge's output (SG 0 Vs Time) with respect to time. Low pass 3rd order Butterworth IIR filter-with cutoff frequency 5 Hz is used for filtering.

The same signal processing technique is used for whole graph. The "curve fitting" signal processing is used for whole graph with polynomial model of value N order. The value of N selected is in the range of 15-23. Therefore, after parametric signal processing, the resultant waveform is shown in Figure 10-84, named "SG 0 Vs Time and Load Vs Time". The graph has two Y-axis, one is in Microstrain and the other is in applied compressive load (Newton). The graph is clear but not exactly matching with the analogue output of the applied compressive load in characteristics as is in previous experiments. The strain gauge is experiencing compression that's why the load Vs strain graph is inversely proportional, as can be seen in Figure 10-84.



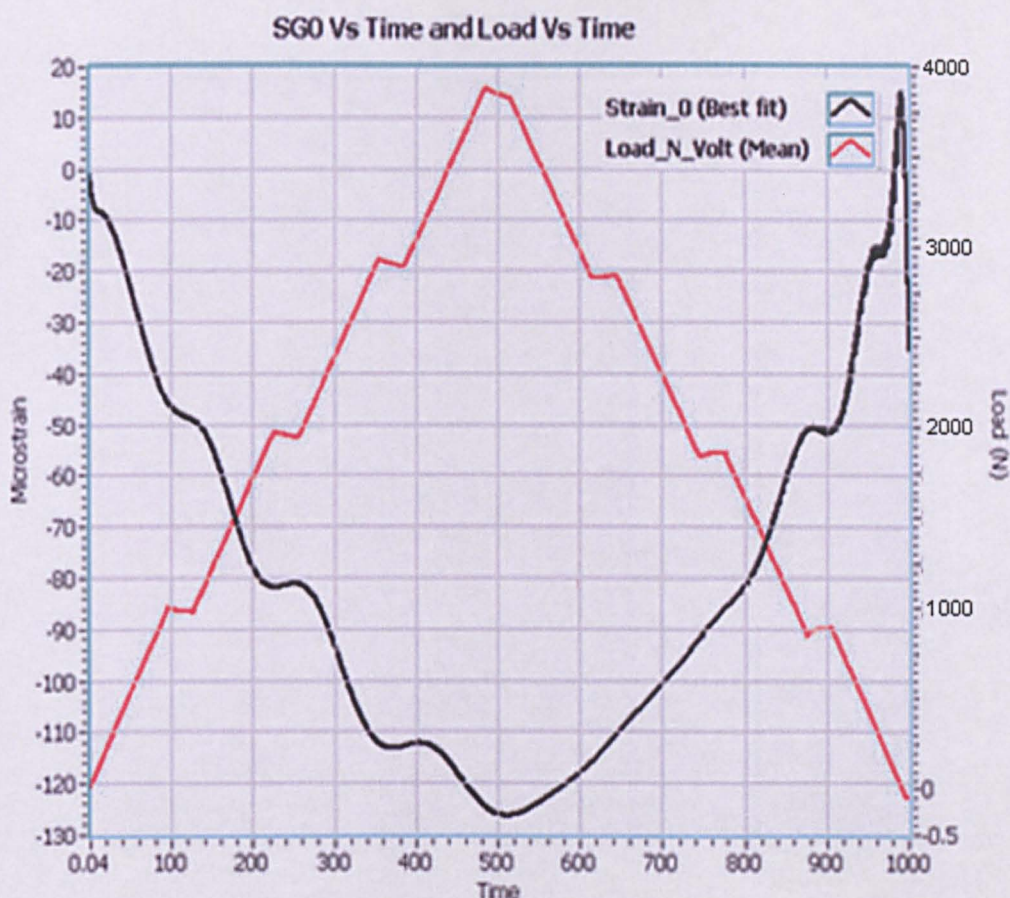


Figure 10-84: Typical strain gauge output and applied load graph with respect to time (SG 0 Vs Time and Load Vs Time).

Similarly, Figure 10-85 shows the graphical presentation of the two Flexiforce® sensors with respect to time. The graph has two Y-axis similar to shown in Figure 10-84, one is in Microstrain and the other is in applied compressive load (Newton). The graphs are obtained using identical signal processing techniques for both the Flexiforce® sensors. The signal processing techniques used in "SG 0 Vs Time" graph (Figure 10-84) are also used for plotting all outputs from all eight strain gauges (SG 0 to SG 7).



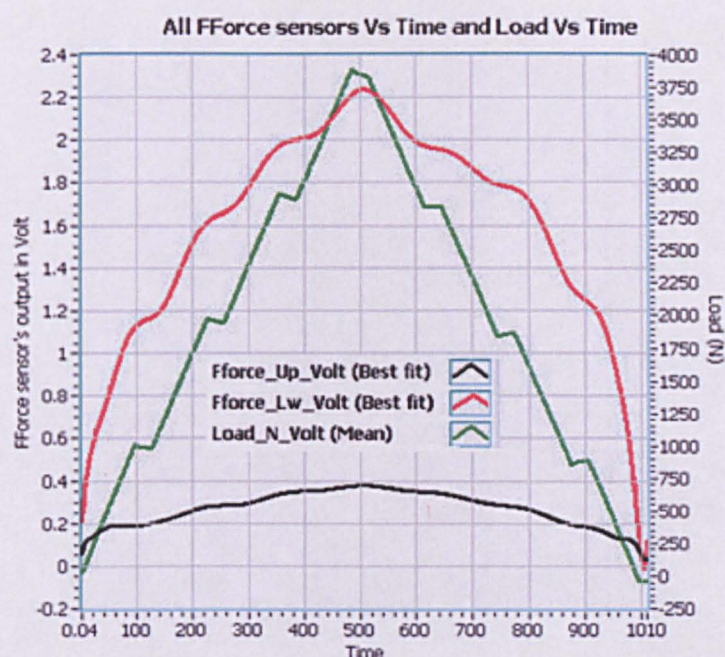


Figure 10-85: Outputs from two Flexiforce® sensors and applied load graph with respect to time.

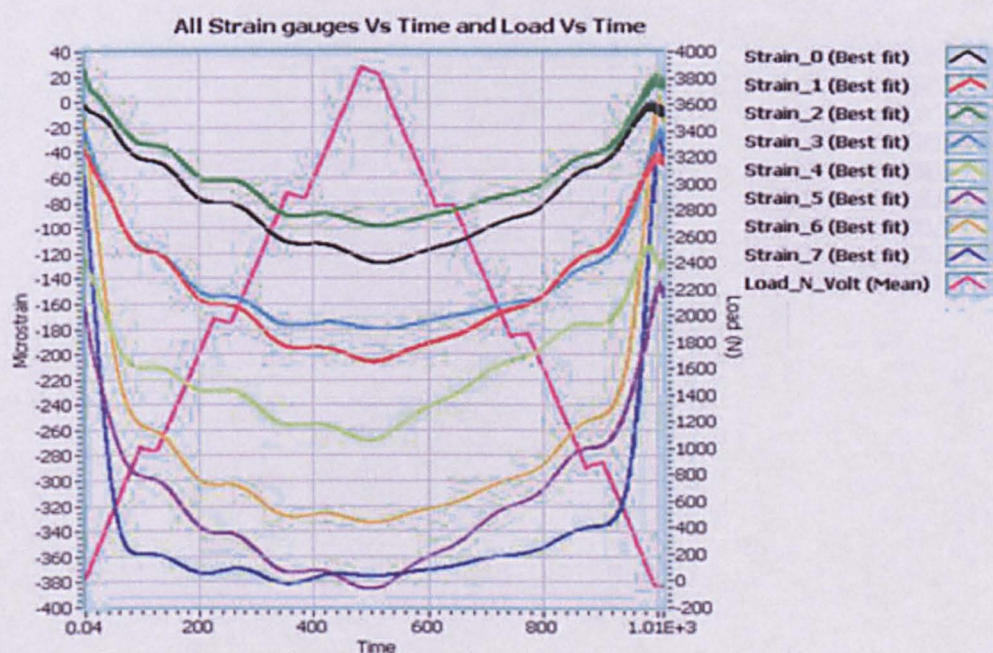


Figure 10-86: All SG output (Microstrain) & Load (N) Vs Time (S), Experiment protocol: Exp\_4k\_step1k\_10NPS\_LH30S.

For better comparison of all outputs from all strain gauges, all graphs are plotted on the same graph as shown in Figure 10-86. The analogue output of applied compressive load is shown by red coloured plot and that shows the linear ramp type application of compressive to the disc prosthesis whereas outputs of the sensors exhibit non-linear behaviour of the visco-



elastic artificial disc prosthesis. All sensors output looks very similar in characteristics in response to the linear ramp type applied compressive load.

For better clear view of the graphs from Figure 10-86, a magnified view of Figure 10-86 graphs is presented in Figure 10-87 and Figure 10-88. Figure 10-87 presents the 1st part of the graphs, i.e. from 0 to 4000 N loading cycle graph and Figure 10-88 presents the 2nd part of the graphs i.e. from 4000 N to 0 N unloading cycle graph.

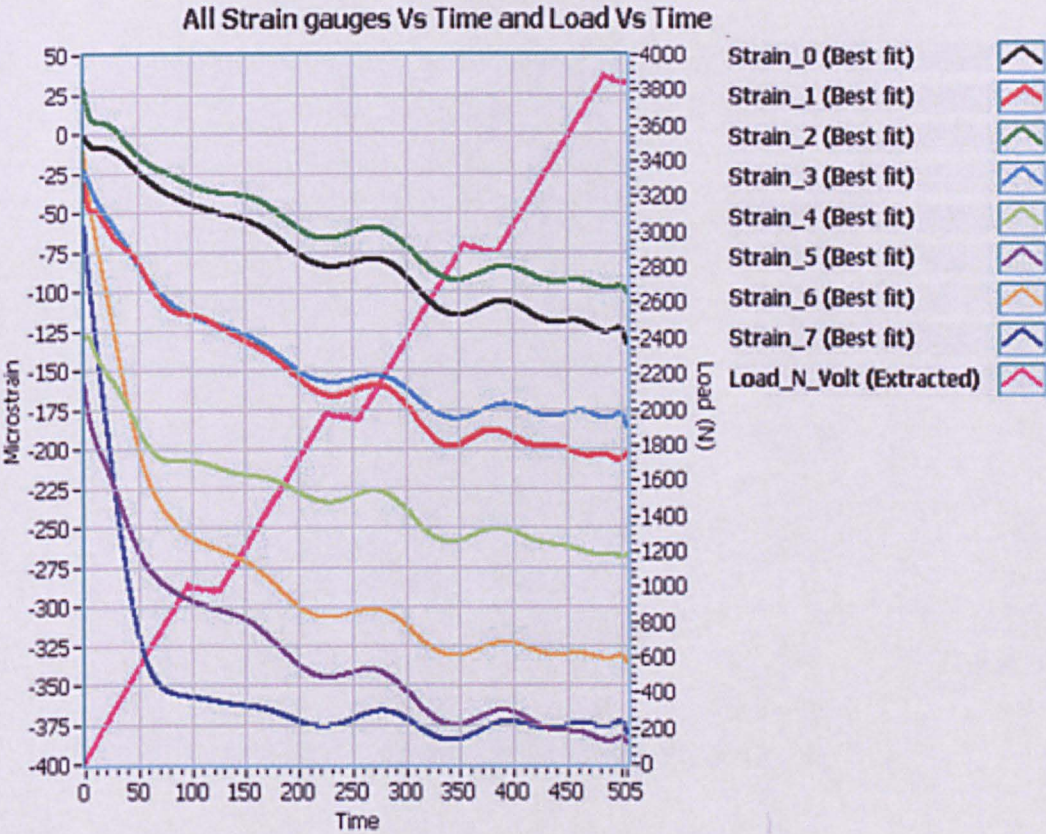


Figure 10-87: The 1st part of the graph for all strain gauge’s output when loading from 0 to 4 kN.

Figure 10-89 shows the outputs from all strain gauges with respect to the applied compressive load. The applied compressive load in Newton is along the X-axis and strain gauges output in Microstrain are along the Y-axis. The graph shows very clear and similar characteristics especially in the range of 500 N to 3800 N.

Figure 10-90 shows the outputs from the two Flexiforce® sensors with respect to the applied compressive load. The applied compressive load in



Newton is along the X-axis and Flexiforce® sensor's output in dc volt is along the Y-axis.

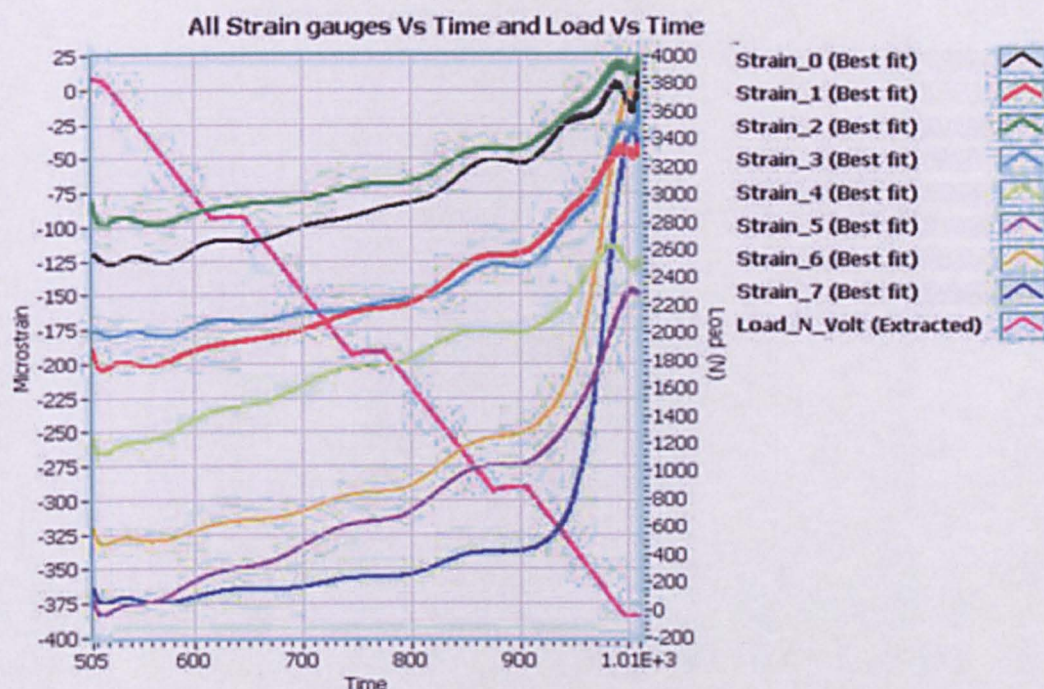


Figure 10-88: The 2nd part of the graph for all strain gauge's output when unloading from 4 to 0 kN.

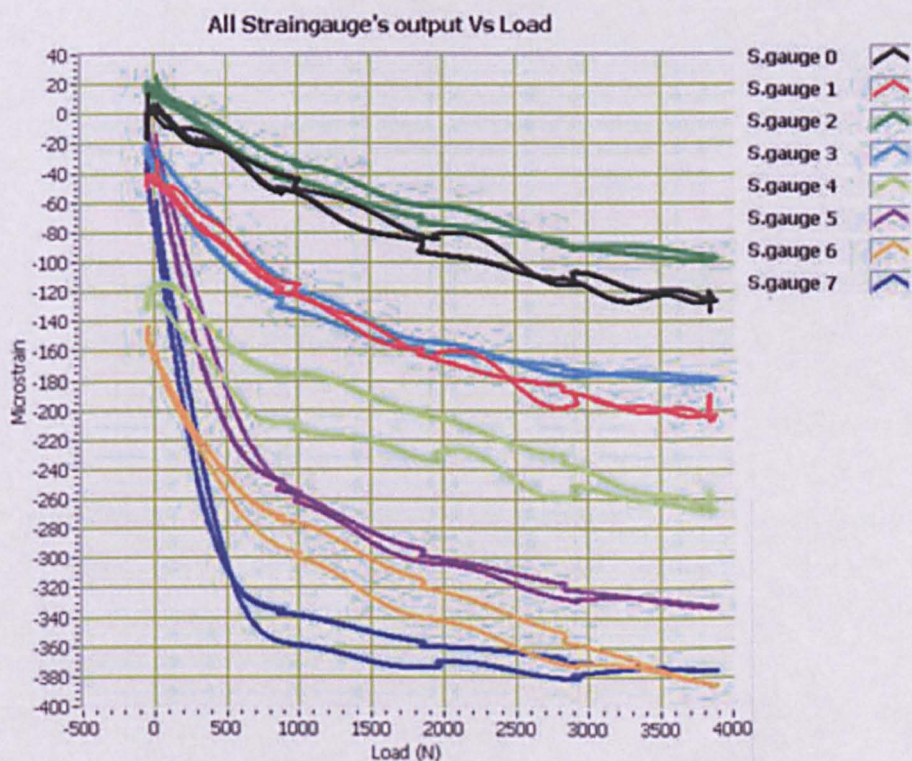


Figure 10-89: All strain gauges outputs with respect to applied compressive load.



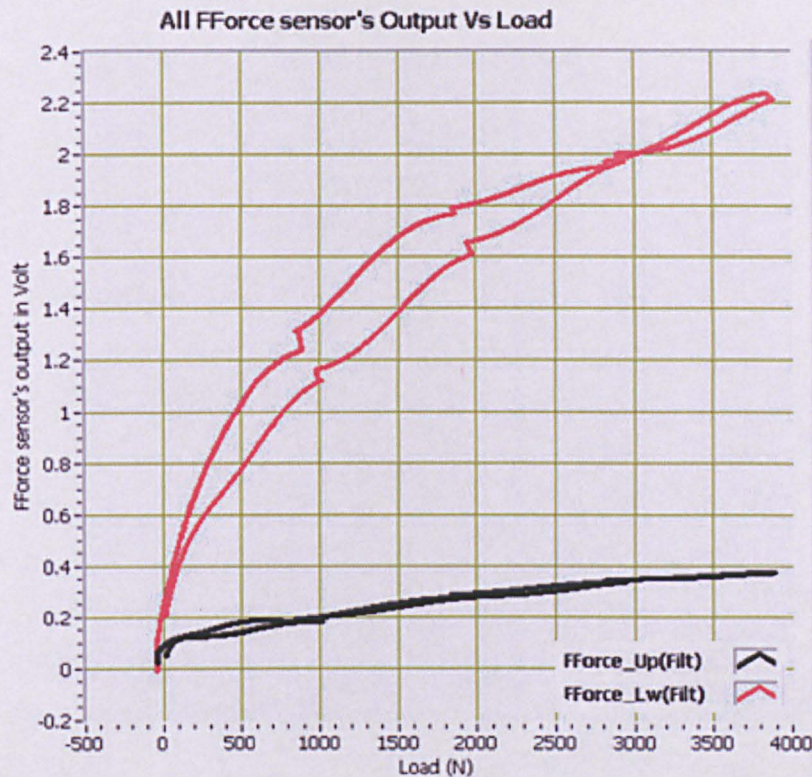


Figure 10-90: Two Flexiforce® sensor's output with respect to applied compressive load.

In both Figures 10-89 and 10-90, the hysteresis can be found between the plots of the loading and the unloading cycle. The hysteresis in all graphs is in the range of the applied compressive load of 250 N to 3000 N and especially significant in the load range of 1000 N to 2000 N which can be seen in Figure 10-89 and Figure 10-90.

## 10.4 SUMMARY

In these experiments, the study protocols were designed in such a way in order to investigate or answer the following questions:

- ✳ Does the designed load-cell and selected sensors provide adequately reliable, repeatable, accurate and precision results/outputs?
- ✳ Can the correct value of load/force and loading rate to the spinal disk be predicted from the result graphs?

All sensors showed almost identical and repeatable results with adequate tolerances. The results demonstrated adequately the visco-elastic behaviour

of the disc as the results recorded from all sensors did not exhibit a linear behaviour as the applied compressive load by UT machine.

Comparing the results of experiment-1 and experiment-2, it is found that experiment-1 results show more hysteresis than experiment-2. Moreover, in experiment-2, the value of peak load drops exponentially for 300 second due to the visco-elastic characteristic of the disk in-lay material. Comparing the results of experiments 3 and experiment-5, it is observed that the higher the loading rate the lower the non-linearity of the plot, which means that the higher the loading rate the less the visco-elasticity. In experiment-1, the loading cycle and unloading cycle are both continuous where in experiment-6, the loading and unloading cycles are in steps. In the result graphs of experiment-1 and experiment-6 this continuous and step-wise loading and unloading behaviour can be easily observed.



# **11 EXPERIMENTAL SET-UP, PROTOCOLS AND RESULTS FOR THE *EX VIVO* LOADING OF THE ARTIFICIAL SPINAL DISC PROSTHESIS – LOADING CELL WITH ANIMAL SPINE**

## **11.1 INTRODUCTION**

---

This chapter describes the development of *ex vivo* experimental set-up including a description of all conducted experiments and the results of the experiments. The *ex vivo* experiments mainly describe the loading of the loading cell as described in chapter 10 but with the animal spinal vertebrae included. This development begins with the selection of the animal spine, the harvesting of the spine, the cleaning of the spinal vertebrae and the removal of the spinal disc, and the preparation of the vertebra holding mechanical tools. All *ex vivo* experiments were done according to the study protocols mentioned here. All *ex vivo* experimental work took place at the clinical laboratory at The Royal Veterinary College of UCL at Potters' bar, Hertfordshire. The results of all *ex vivo* experiments are discussed in detail in section 11.3.

## **11.2 EXPERIMENTAL SET-UP AND STUDY PROTOCOLS**

---

In this section the *ex vivo* experimental set-up including selection of animal spine and its' harvesting are described. Also, this section presents the experimental protocol.

### **11.2.1 Selection of animal spine**

---

For the correct mechanical loading, the artificial lumbar spinal disc-load cell must be dimensionally set between two animal spinal vertebrae. The vertebrae surface adjacent to the spinal disc should be big enough in size to properly anchor the load cell end-plates. Firstly, a pig spine was selected for the experiments, however it was found that the pig spinal vertebrae size

was smaller than the load cell end-plates (size of 28 mm X 34.5 mm) and therefore was not deemed suitable. Therefore, a sheep spine was then proposed for the experiments. Unfortunately, the sheep's spinal vertebrae size was also proved to be small. Finally, a calf spine was selected for the experiments. One and half year old calf's spine was harvested and kept in the freezer at the laboratory (Figure 11-1).

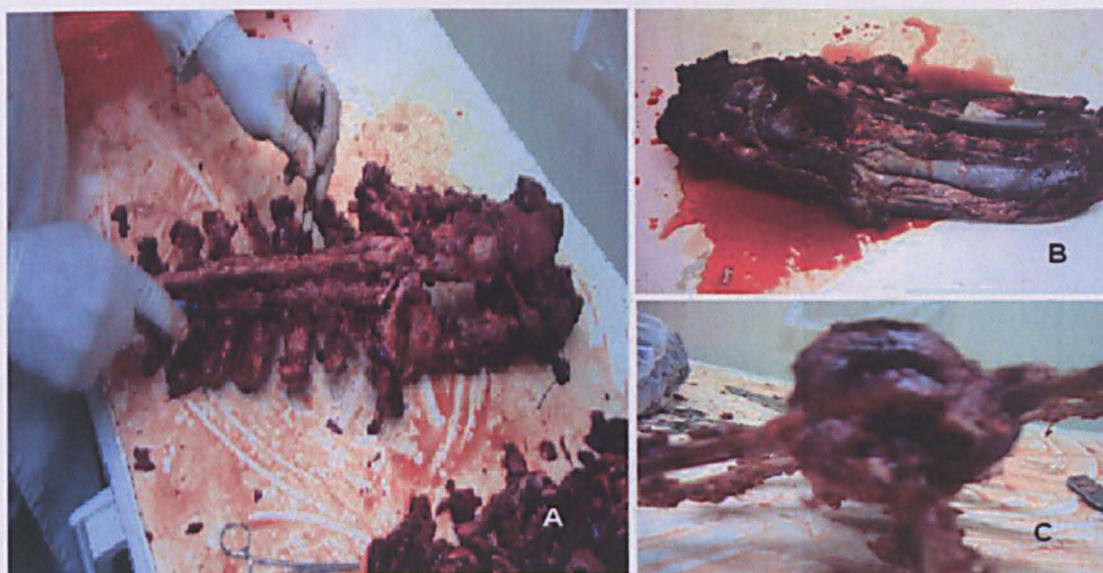


Figure 11-1: Photographs of the preparation of the animal spinal vertebrae for experimentation at the Royal Veterinary College clinical lab, UCL, Potters' Bar, UK (A) Cleaning of harvested animal spine (B) Freshly harvested unclean animal spine (C) Cross-section view of spinal vertebra

### 11.2.2 Preparation of the animal spinal vertebrae

A day before the commencement of the *ex vivo* experiments the calf's spine was brought at room temperature in order to make the surrounding tissues soft enough for removing (Figure 11-1(B)). The skeletal spine was first cleaned from the surrounding tissue using surgical tools like scissors, forceps, etc (Figure 11-1(A)). Then, two to four spinal vertebrae were removed by cutting through the spinal disc. The spinal disc was removed from the spinal vertebrae (figure 11-1(C)). The spinal canal was also cleaned from the spinal cord and that part was also removed from the main vertebrae body. Finally the main spinal vertebrae body was left without any surrounding tissues.



### 11.2.3 *Ex vivo* experimental set-up

The protocol from the *in vitro* experimental set-up (chapter 10) was repeated with some required modifications explained in section 11.2.4. As shown in Figure 11-3 and Figure 11-5(A), for this experiment the Universal Testing Machine was used with the loading cell (artificial spinal disc with all embedded sensors) placed between the calf's spinal vertebrae. The vertebrae were held by custom made mechanical tools and a X-Y movable compressive platen. The detail of the UT machine and the X-Y movable compression platen were explained in chapter-10. In this *ex vivo* experiment a spinal vertebrae holding mechanical tool was specially designed and developed and is described below.

#### Development of the vertebrae holding mechanical tool

This mechanical tool was developed in order to strongly hold the calf's spinal vertebrae with the anchored artificial spinal disc prosthesis-load cell end-plates as shown in Figure 11-2, 11-3 and 11-5(B)(C). One of the important requirements of this tool was that it facilitates the correct central installation of the vertebrae for the correct compressive loading of the load cell.

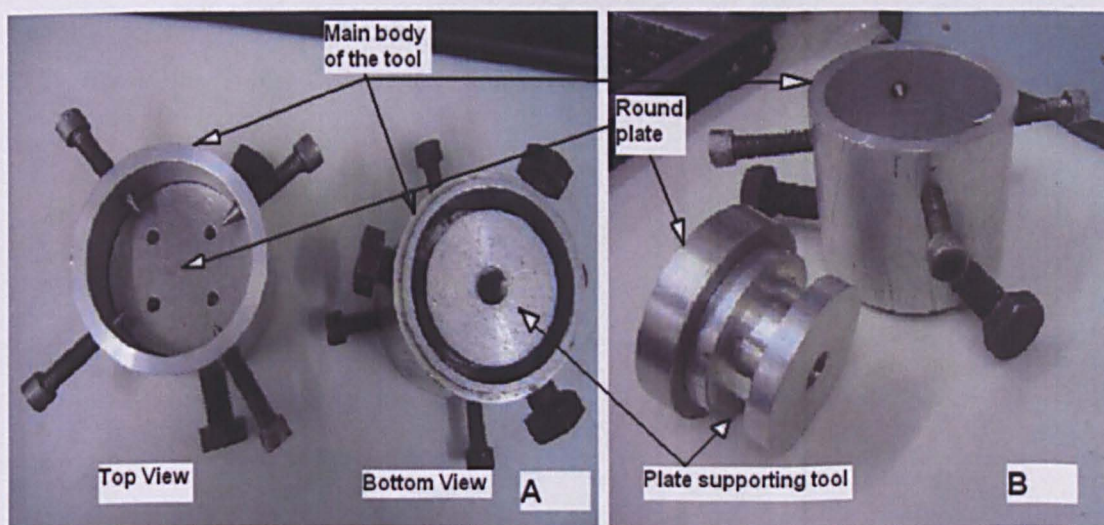


Figure 11-2: Photographs of the specially designed and developed spinal vertebrae holding mechanical tool (A) Top and bottom view of the tool (B) Three parts of the tool-(1) main holding body with positioning and locking screws (2) simple round plate (3) Plate supporting tool



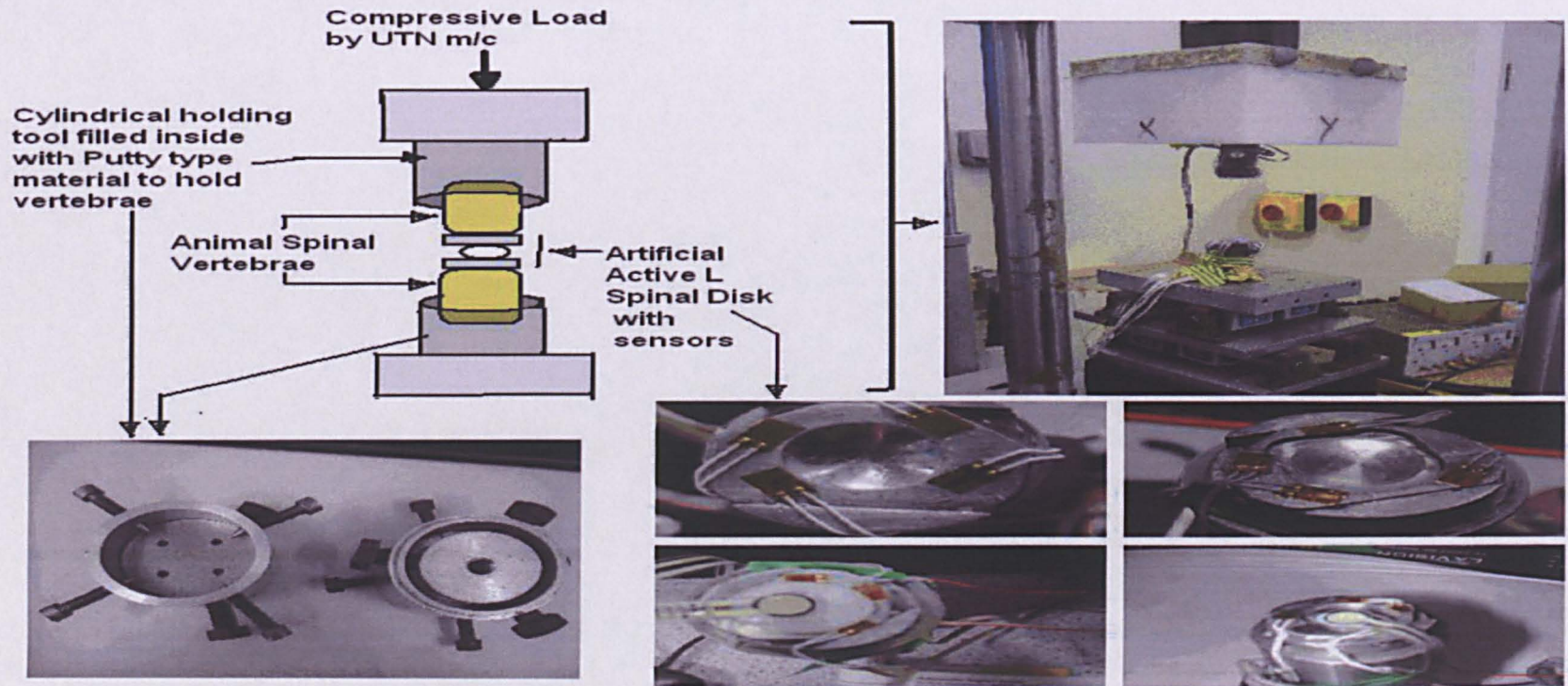


Figure 11-3: *Ex vivo* experimental set-up with photographs of the main components like load cell, Universal Testing machine, vertebrae holding tool etc.



As shown in Figure 11-2 and 11-4 it consists of 3-parts:

- ✳ Main body of the tool
- ✳ Adjustable round plate
- ✳ Plate supporting tool

The whole tool is made-up of aluminium except from the seven positioning and holding screws. The dimensions of all three parts of the tool are shown in Figure 11-4.

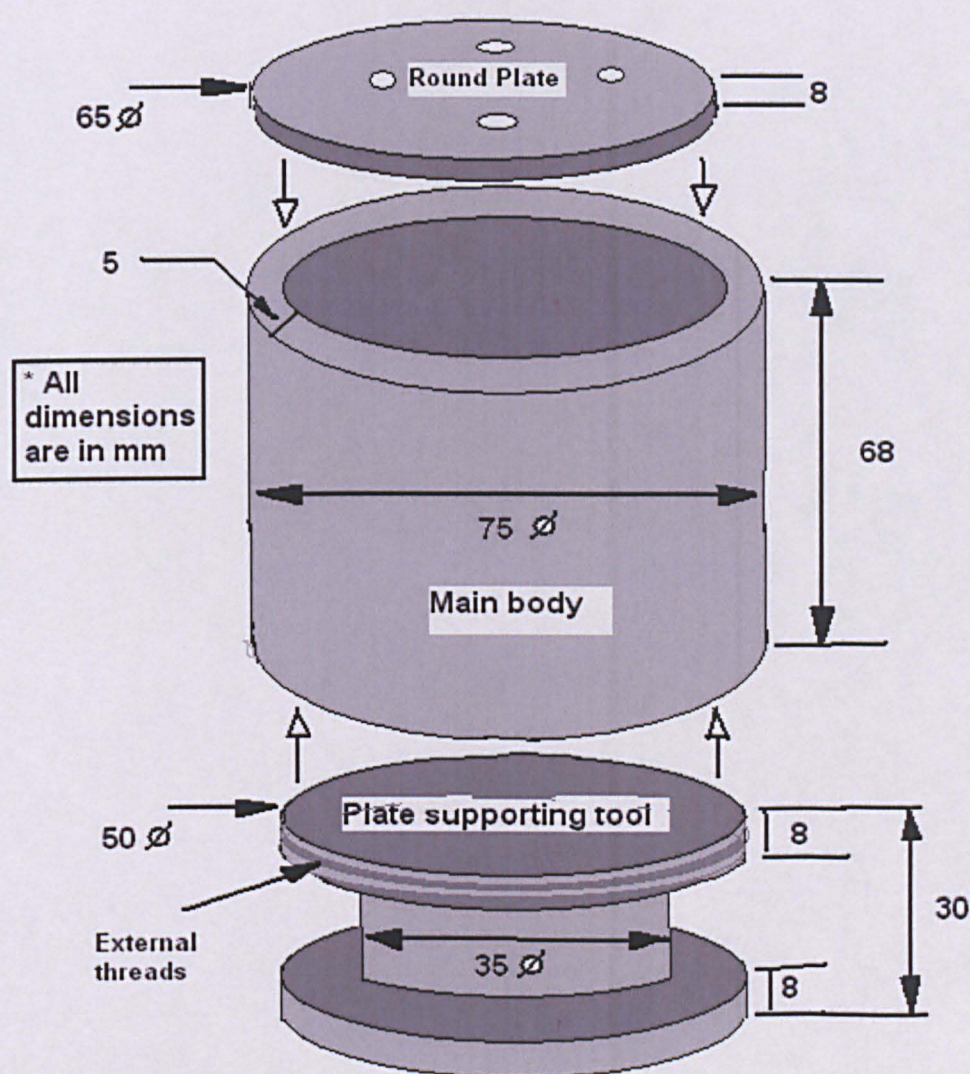


Figure 11-4: Schematic diagram of the spinal vertebrae holding tool including all three parts and necessary dimensions.

The main function of the tool is to hold the vertebrae strongly in the centre as per experiment's requirements. The details of the tool and their functions are given below.



**Main body of the tool:** The main body of the tool is a hollow cylinder made up of aluminium with 5mm wall thickness with four positioning screws and three plate supporting holding screws as shown in Figure 11-2, 11-3 and 11-4. The tool houses inside the remaining two parts i.e. round aluminium plate and plate supporting tool. The four positioning screws are designed for holding and positioning the vertebrae firmly in the centre of the tool (Figure 11-2, 11-3 and Figure 11-4).

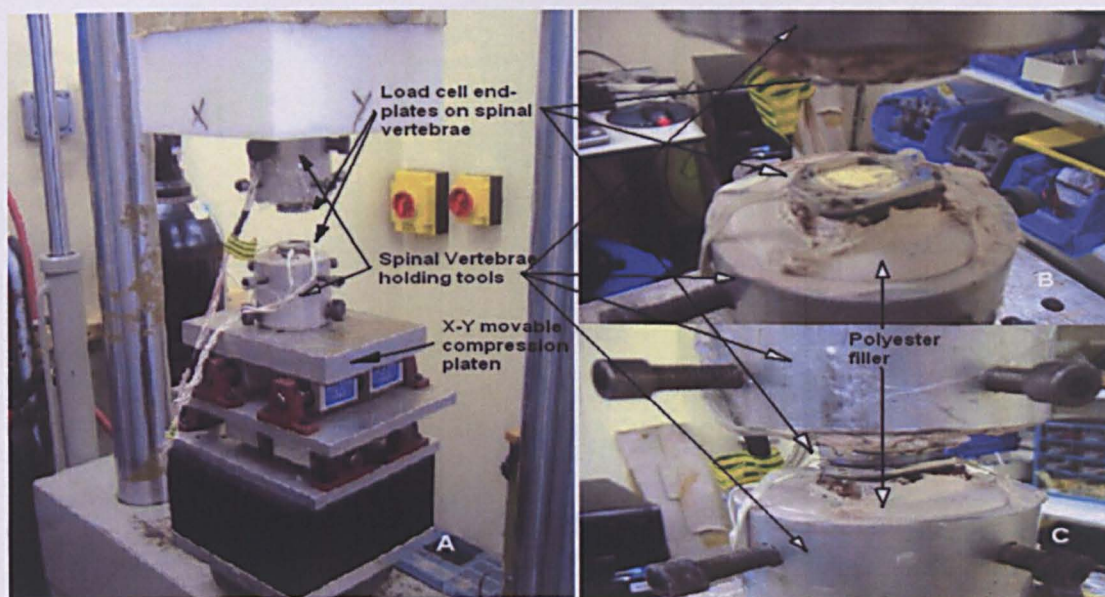


Figure 11-5: Photographs of the mechanical experimental set-up (A) UT machine with all required mechanical tools & accessories (B) Zoom in view of the animal spinal vertebrae with mounted load cell end-plates fixed in specially designed holding tool (C) Zoom in view at the time of the load cell loading during experiment.

As shown in Figure 11-5(A), for correct normal compressive loading, the alignment of the two parts of the Universal Testing Machine (Upper and lower) is critical. Hence, the proper positioning of the vertebrae at the centre of the main body of the tool is crucial. Furthermore, the top surface of the vertebrae must be as horizontal as possible for correct loading. Accordingly the four screws were tightened enough to firmly hold the vertebrae at the required position. To provide further mechanical holding to support the vertebrae the surrounding cavity was filled with polyester filler. After overnight curing the putty type filler became solid and held the vertebrae very firmly (Figure 11-5 (B) and Figure 11-5 (C)).



**Round plate:** The round plate is made-up of aluminium with dimensions as shown in Figure 11-4 and Figure 11-6.

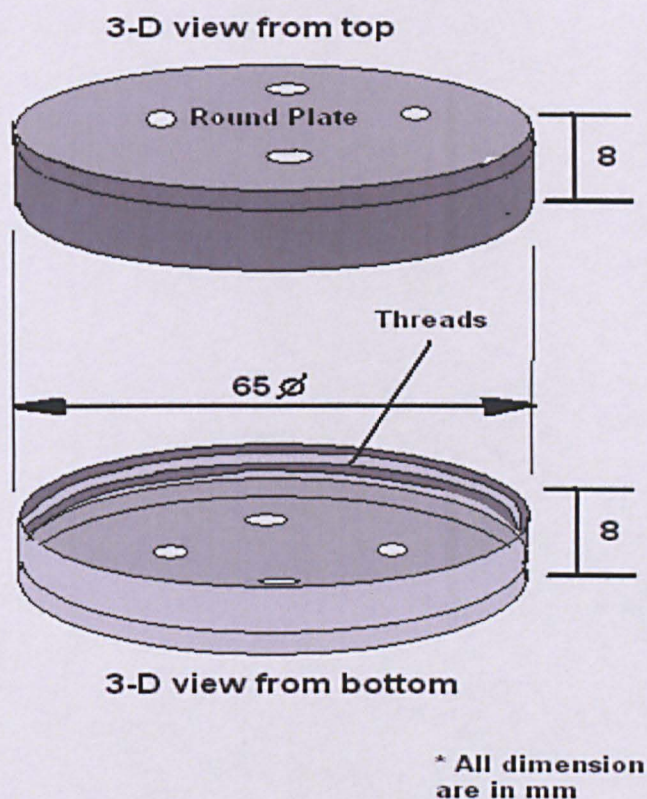


Figure 11-6: Schematic 3-D views of the round plate vertebrae holding tool

The inside threads are used to couple the plate with the supporting tool.

**Plate supporting tool:** The primary function of the plate supporting tool is to mechanically support the round aluminium plate. The plate supporting tool schematic diagram with dimensions is shown in Figure 11-4. The actual photograph of the plate supporting tool is shown in Figure 11-2. The plate supporting tool's external threads are coupled with the internal threads of the round aluminium plates and make one assembly as shown in Figure 11-2(B). The bottom surface of the plate supporting tool has an internal threaded hole of diameter of 12mm exactly at the centre (see Figure 11-2(A)). That threaded hole is used to fix the lower part of the UT machine with the externally threaded suitable size rod. The plate supporting tool can also be strongly gripped by the three screws.

#### 11.2.4 *Ex vivo* study protocols

The study protocols for the *ex vivo* experiments are explained below. The study protocols are similar with the *in vitro* experiments but with some minor required modifications. Only, three experiments were performed in *ex vivo* and their study protocols are given below. It is worth mentioning that during some trial runs of *ex vivo* experiments the artificial disc plates started to shift/slip when the compressive load reached around 1000 N. This was due to the lack of enough anchoring power of the disc plate studs onto the spinal vertebrae surfaces. Hence, all *ex vivo* experiments were conducted up to 1000 N load. Another issue which was experienced during the trial runs was the difficulty to hold the load or position on the artificial disc plates for some time and for that reason this was abandoned in the formal *ex vivo* experiments, although in the last *ex vivo* experiment efforts have been made to introduce some holding. Details of the three *ex vivo* experiments can be found below.

##### **Experiment 1: Exp\_1k\_10NPS\_NOH**

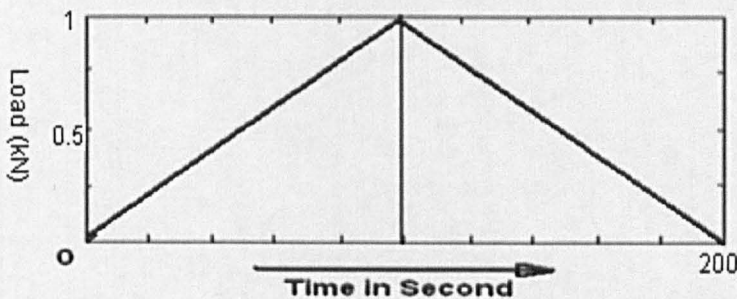


Figure 11-7: Event description diagram of Experiment 1.

Figure 11-7 describes the events in this Experiment 1. The specifications for this experiment are as follows:

- ✦ Loading range: 0 – 1 – 0 kN
- ✦ Loading speed: 10 Newton per second
- ✦ No Holding interval



## Experiment 2: Exp\_1k\_100NPS\_NOH

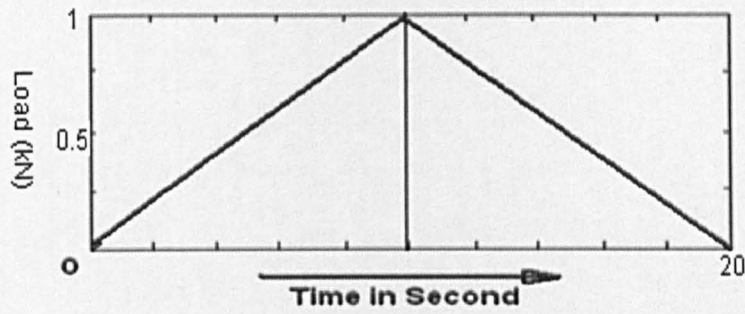


Figure 11-8: Event description diagram of Experiment 2.

Figure 11-8 describes the events in this Experiment 2. The specifications for this experiment are as follows:

- ✦ Loading range: 0 – 1 – 0 kN
- ✦ Loading speed: 100 Newton per second
- ✦ No Holding interval

## Experiment 3: Exp\_750N\_step250N\_10NPS\_LH10S

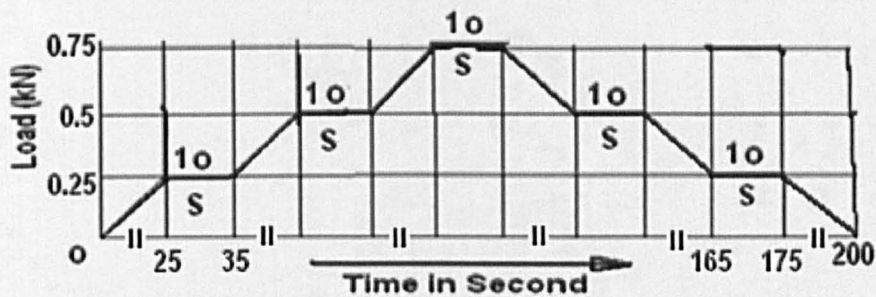


Figure 11-9: Even description diagram of Experiment 3

Figure 11-9 describes the events in this Experiment 3. The specifications for this experiment are as follows:

- ✦ Loading range: 0 – 0.25 – 0.5 – 0.75 – 0.5 – 0.25 – 0 kN
- ✦ Loading speed: 10 Newton per second
- ✦ Holding interval: 10 seconds between each step of 250 N with load holding

## 1 1.3 RESULTS OF THE EX VIVO EXPERIMENTS

This section presents the results from the *ex vivo* experiments

### 11.3.1 Results of Exp. 1: Exp\_1k\_10NPS\_NOH

---

Experiment 1 was performed as described in the protocol (section 11.2.4). The results are shown in graphical format; see Figure 11-10 and Figure 11-11. The loading and unloading speed has been programmed as per protocol in the universal testing machine. The graphs in Figure 11-10 present the outputs from all eight strain gauges (s.gauge 0 to s.gauge 7) and the outputs from the two piezoresistive-Flexiforce® sensors (F.force\_upper and F.force\_lower) when a compressive load is applied (with respect to time). The last graph depicted in Figure 11-10 titled as "Load Vs Time" presents the analogue output of the applied compressive load by the universal testing machine. In the graphs, outputs from all strain gauges are presented in Microstrain ( $\text{Microstrain} = \text{strain} \times 10^{-6}$ ) and outputs from the two Flexiforce® sensors are in analogue dc volt (Y-axis). The time is in seconds (x-axis). The red coloured portions in all graphs shows the noisy raw signal and the black line plots are the best fit lines. Similarly in Figure 11-11, the graphs present the outputs from all eight strain gauges (s.gauge 0 to s.gauge 7) and the outputs from the two piezoresistive-Flexiforce® sensors (F.force\_upper and F.force\_lower) when a compressive load is applied (with respect to the applied compressive load). In the graphs, outputs from all strain gauges are presented in Microstrain ( $\text{Microstrain} = \text{strain} \times 10^{-6}$ ) and outputs from the two Flexiforce® sensors are in analogue dc volt (Y-axis). The applied compressive load is in Newton (x-axis). In Figure 11-10 a typical noise pattern, similar to the previous in vitro experiments described in chapter-10, can be seen in the graphs. Similarly, a different noise pattern can also be seen in the graphs representing the outputs from the two Flexiforce® sensors.



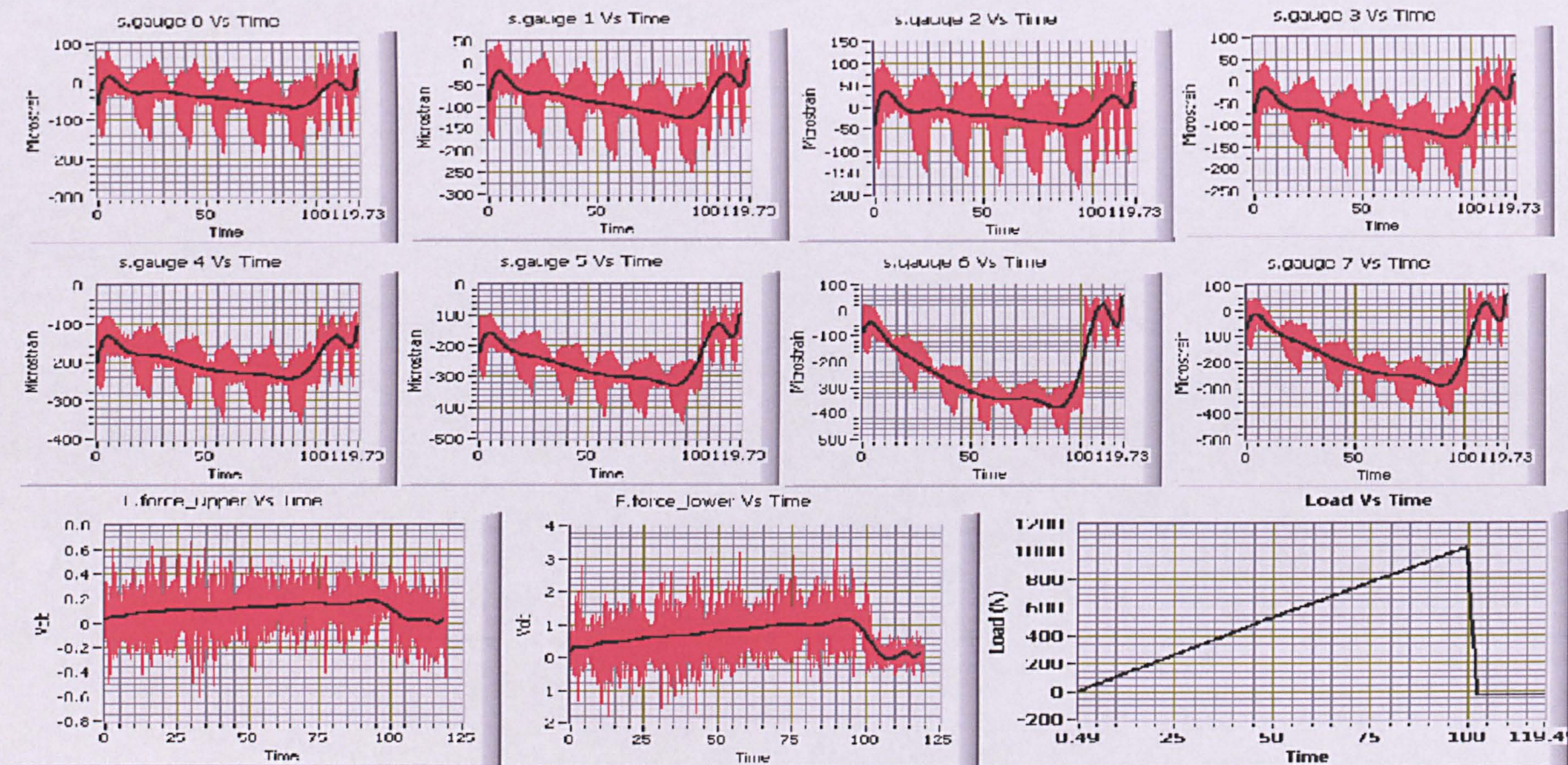


Figure 11-10: All eight strain gauge's outputs, two piezoresistive-Flexiforce® sensor's outputs and applied compressive load in Newton with respect to time in seconds. (Experiment protocol: Exp\_1k\_10NPS\_NOH).



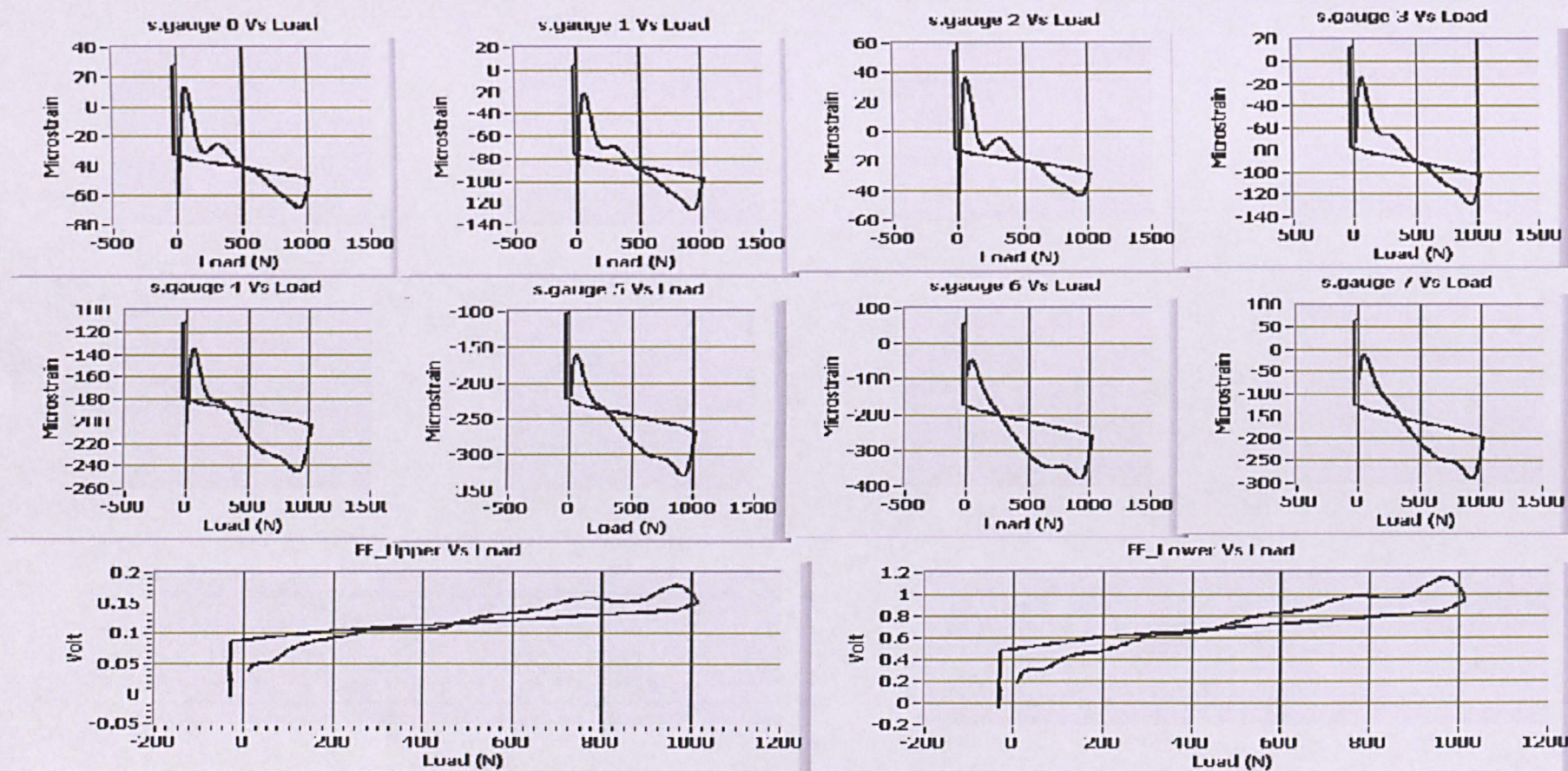


Figure 11-11: All eight strain gauge's outputs and two piezoresistive-Flexiforce® sensor's outputs with respect to applied compressive load in Newton. (Experiment protocol: Exp\_1k\_10NPS\_NOH).



As discussed in chapter-10, the same steps were taken for the noise analysis. Figure 11-12 shows a magnified view from the output (Microstrain) of one typical strain gauge (SG 0 Vs Time).

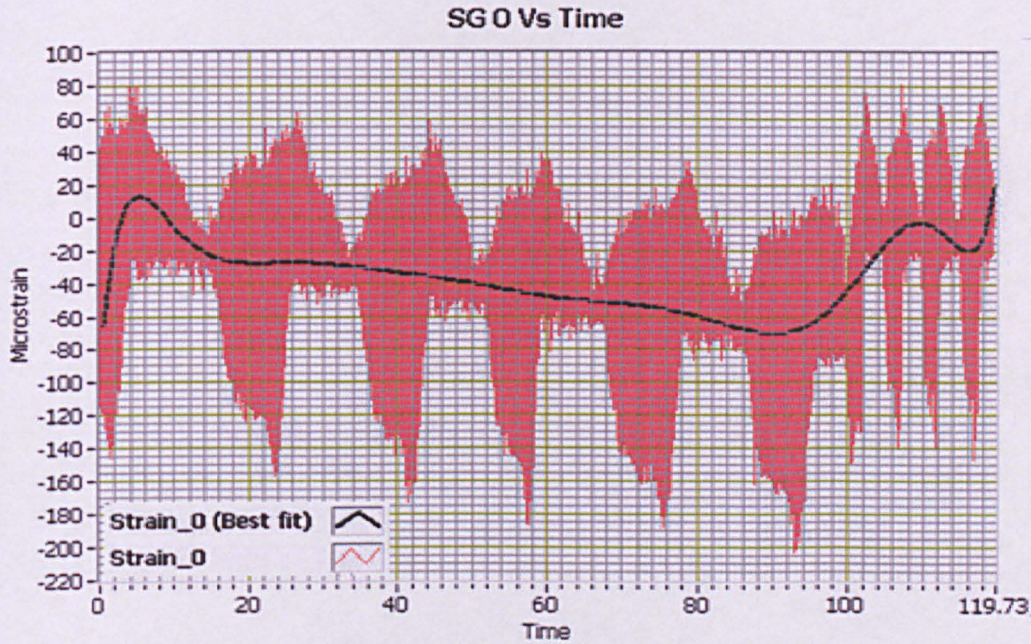


Figure 11-12: Raw Data with lots of typical noise of one typical strain gauge's output (SG 0 Vs Time) with respect to time.

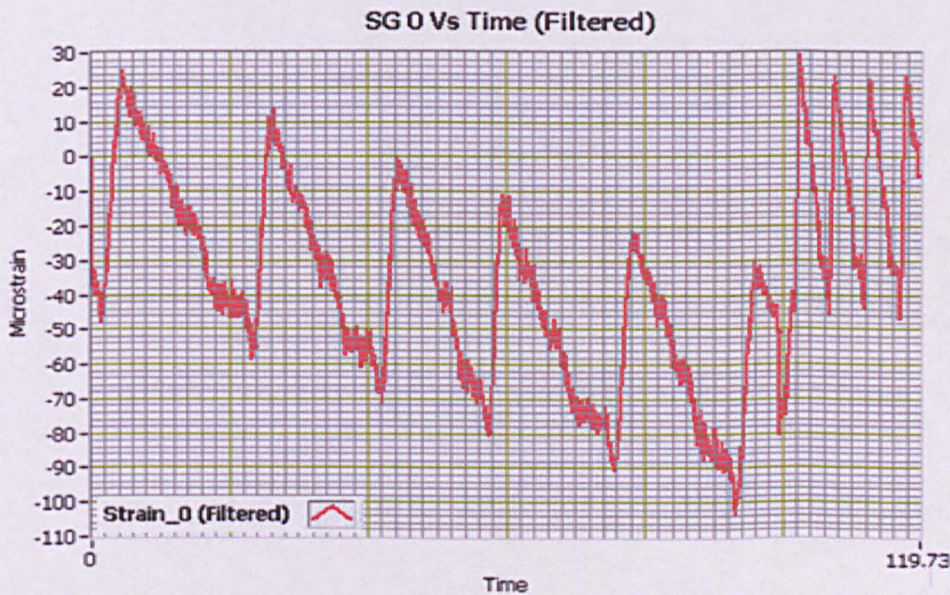


Figure 11-13: Filtered data of one typical strain gauge's output (SG 0 Vs Time) with respect to time. Low pass 3rd order Butterworth IIR filter-with cutoff frequency 5 Hz is used for filtering.



In figure 11-12, the raw data coloured in red contain the output of s.gauge 0 (SG 0) together with a typical noise. To filter the noise the Low Pass 3rd order Butterworth IIR Filter with 5 Hz cut-off frequency is used. The filtered signal is shown in Figure 11-13.

In this experiment the graph is divided into two parts; the first part is when loading from 0 to 1 kN and the second part is unloading from 1 kN to 0 kN. According to the experiment protocol, the compressive load is applied from 0 to 1 kN in the first part with 10 NPS loading speed. So, the duration of the first part is of about 100 seconds and the duration of the second part is of about 3-8 seconds, because unloading is done at very high speed around 500NPS. So, both parts of the graph are of non-stationary type.

In the first part of the waveform graph which comprises of approximately 10,000 samples (100 seconds loading at sampling frequency of 100Hz) the “curve fitting” signal processing technique (as described in chapter 10) was employed. A similar approach was performed on the second part of the graph (which comprises of approximately 300 to 800 samples).

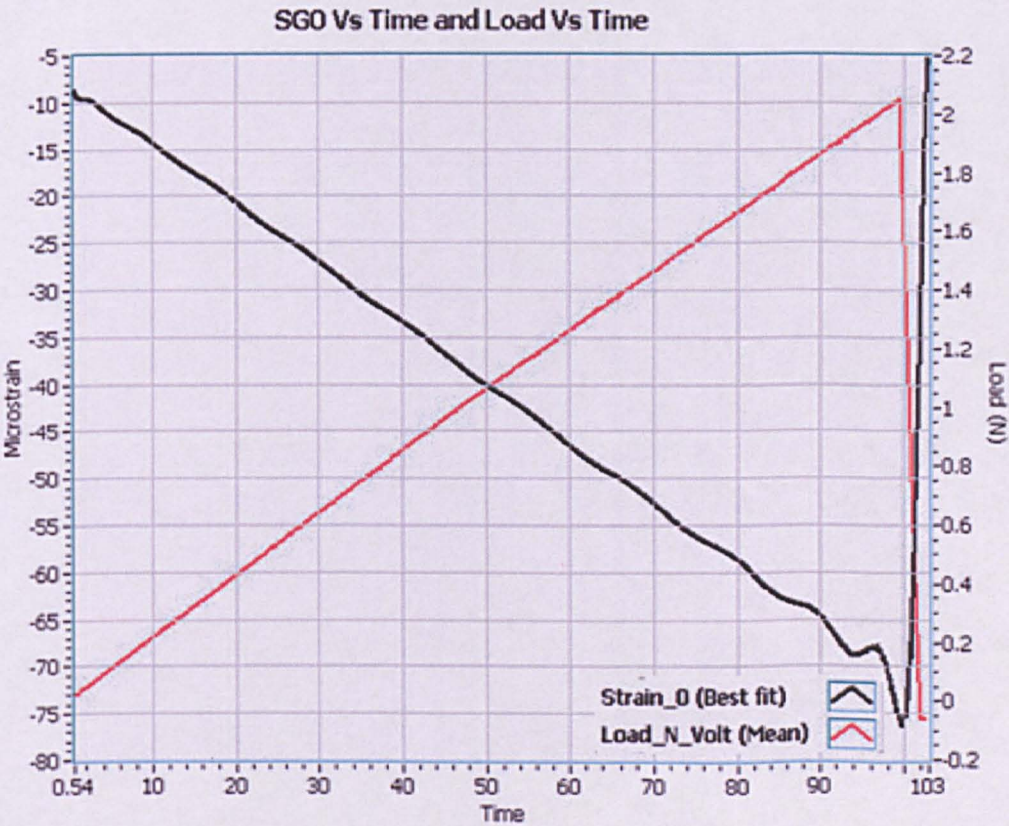


Figure 11-14: Typical strain gauge output and applied load graph with respect to time (SG 0 Vs Time and Load Vs Time).



After multipart parametric signal processing, the resultant waveform is shown in Figure 11-14, named "SG 0 Vs Time and Load Vs Time". The graph has two Y-axis, one is in Microstrain and the other is in applied compressive load (Newton). The graph is very clear and very much similar in characteristics of the analogue output of applied compressive load. The strain gauge is experiencing compression that's why the load Vs strain graph is inversely proportional (as seen in all previous experiments, Chapter-10).

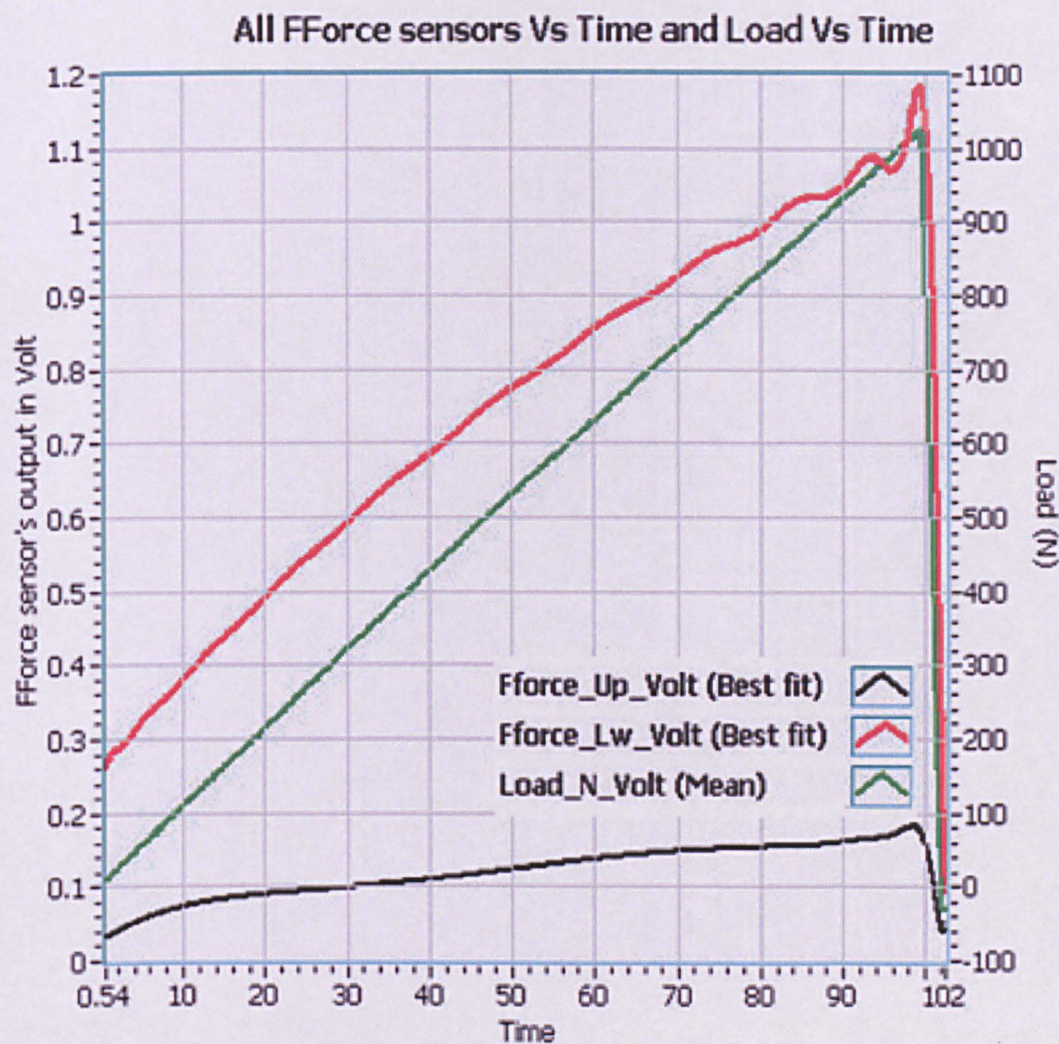


Figure 11-15: Outputs from two Flexiforce® sensors and applied load graph with respect to time.

Similar results as the ones depicted in Figure 11-14 were obtained from all strain gauges. Figure 11-15 shows the graphical presentation of the two Flexiforce® sensors with respect to time. The graph again has two Y-axis as shown in Figure 11-14, one is in dc volt and the other is in applied



compressive load (Newton). The graphs were obtained by using identical signal processing techniques for both the Flexiforce® sensors. The graphs are very clear and almost look the same in characteristics with the analogue output of the applied compressive load. The outputs of the Flexiforce® sensors are excellent in matching with the applied load graph shown in Figure 11-15. This suggests that the outputs of Flexiforce® sensors are more stable when signals are non-stationary.

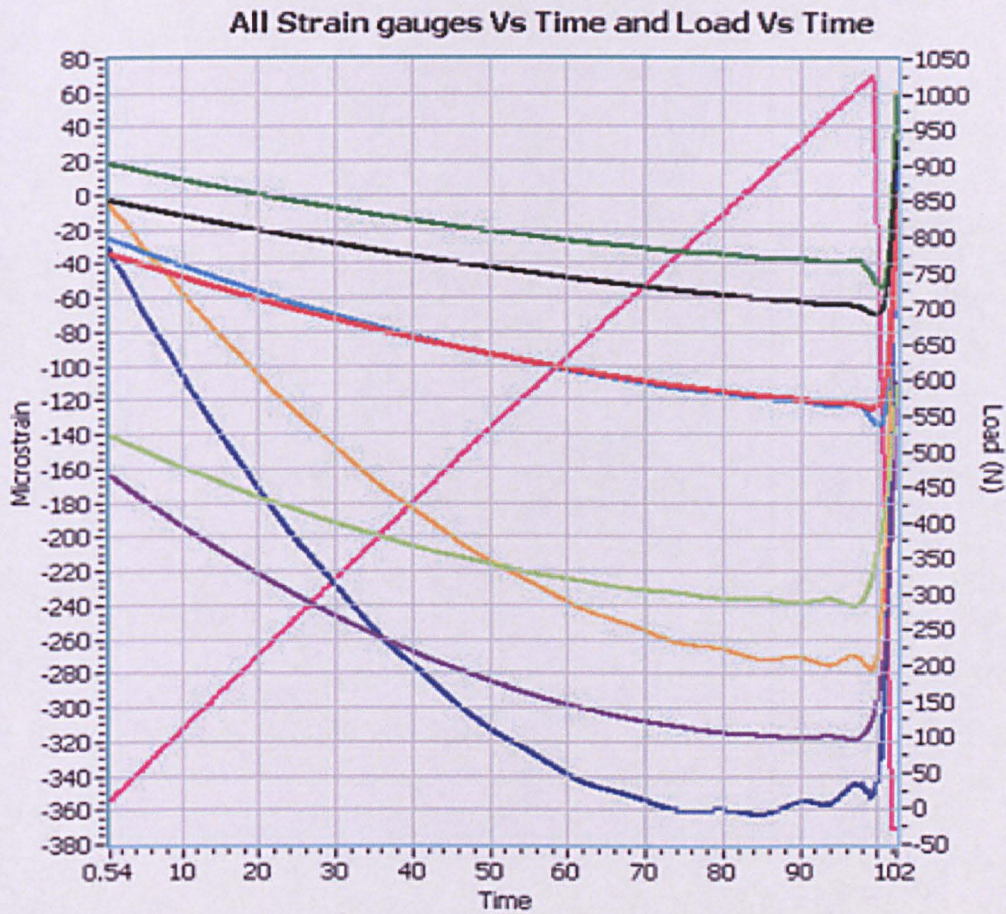


Figure 11-16: The 1st part of the graph for all strain gauge's output when loading from 0 to 4 kN.

The signal processing techniques used in SG 0 Vs Time are also used for plotting all outputs of all the eight strain gauges (SG 0 to SG 7) and the two Flexiforce® sensors (Flexiforce®\_Upper and Flexiforce®\_Lower). For better comparison all outputs are plotted on the same graph as shown in Figure 11-16. All sensors' outputs graphs look similar in characteristics with the analogue output of the applied compressive loads. One noticeable observation is that there is more non-linearity in the loading cycle compare to the unloading cycle. Hence, the lower the speed of loading a more visco-



elastic behavior is observed. This can also be seen in loading and unloading cycles of this experiment with different speed. The sensor's output graphs are more non-linear in a loading slow cycle than in an unloading fast cycle.

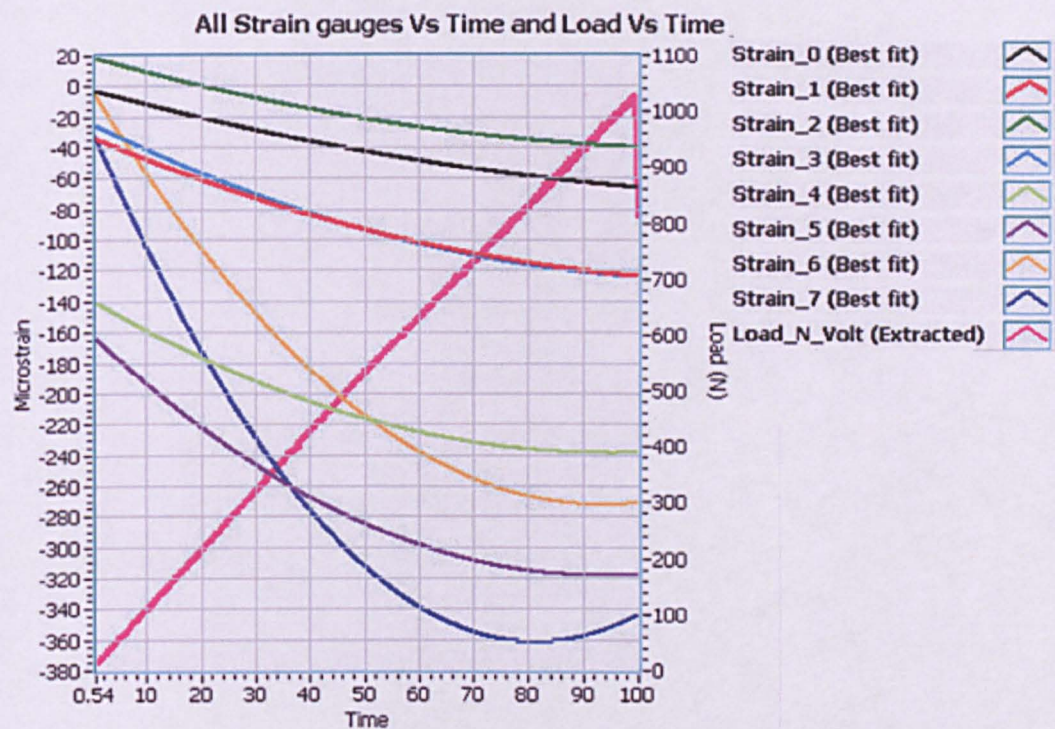


Figure 11-17: The 3rd part of the graph for all strain gauge’s output when unloading from 4 to 0 kN.

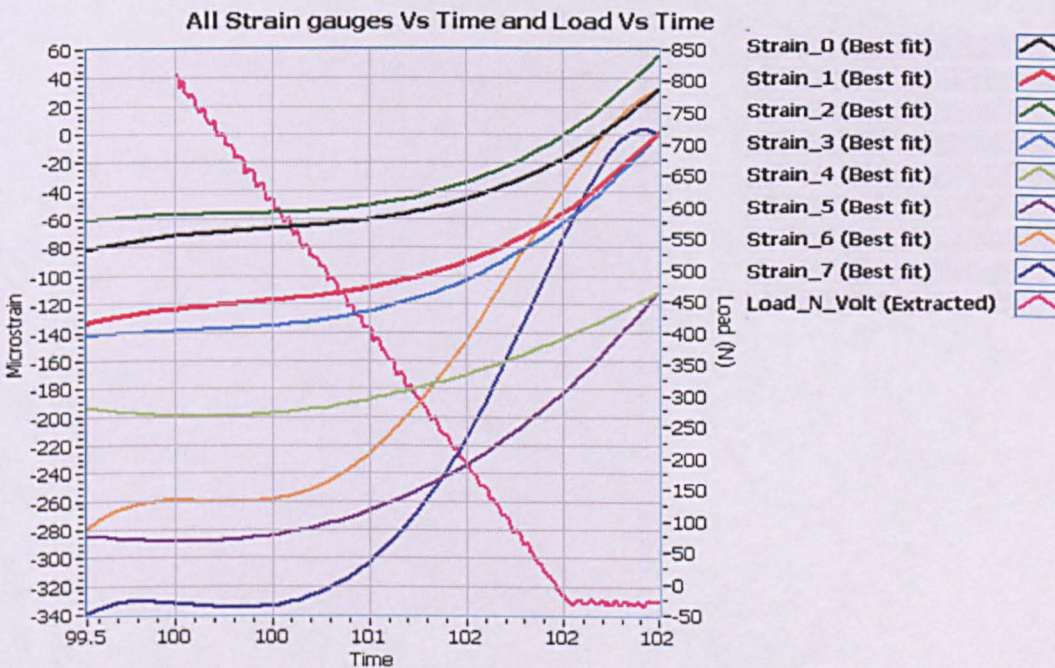


Figure 11-18: The 3rd part of the graph for all strain gauge’s output when unloading from 4 to 0 kN.



The 2nd part of the graph which represents the sensor's output when unloading from 1 to 0 kN has a duration of 3-8 seconds only. In order to clearly present the graph, the 2nd and 1st part of the graph in Figure 11-16 is magnified and shown in Figure 11-17 and 11-18 respectively.

It can be seen in Figure 11-17 and Figure 11-18 that all strain gauge's outputs are a little non-linear in nature which is, as mentioned before, due to the visco- elastic inlay material of the disc. So, here it is reconfirmed that the strain gauges can be used in this application reliably.

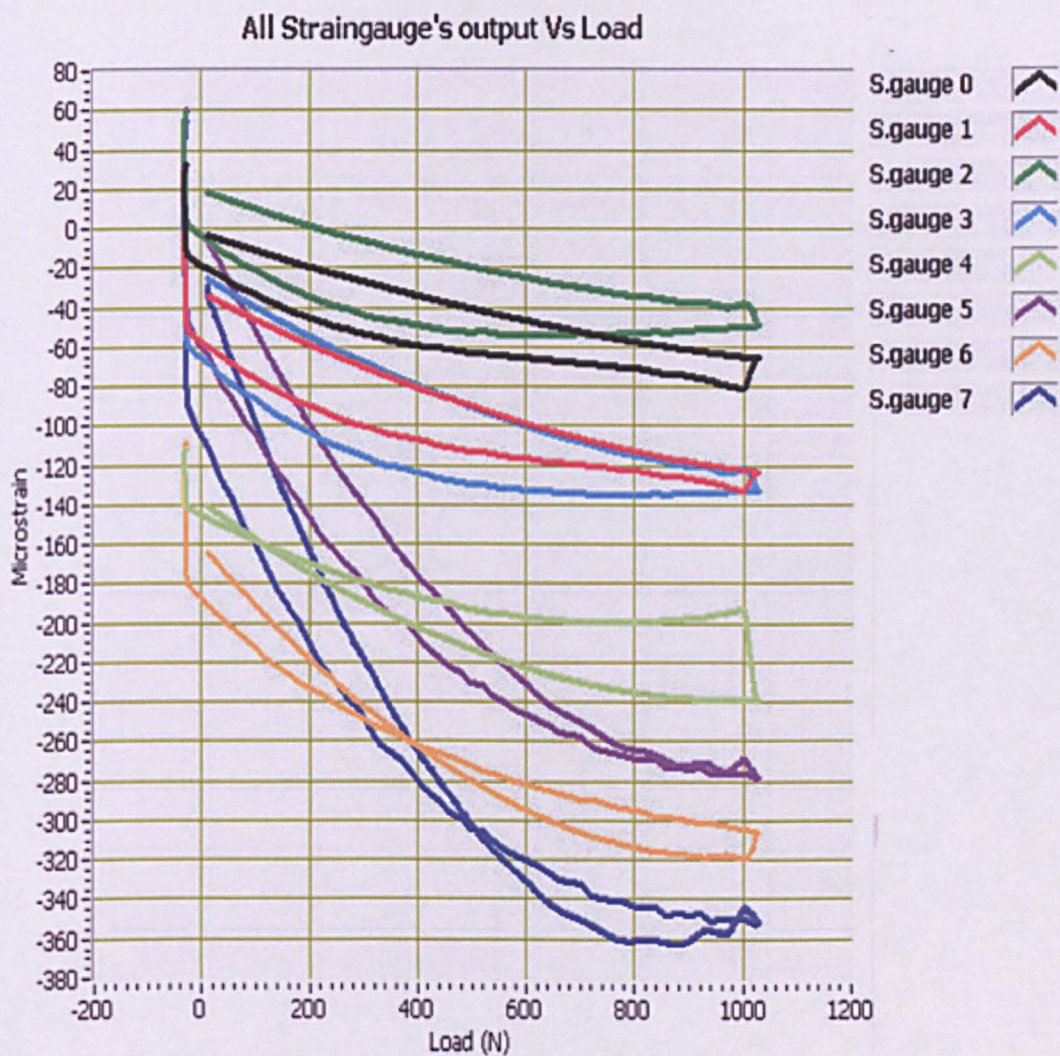


Figure 11-19: All strain gauges outputs with respect to applied compressive load.

Figure 11-19 shows the outputs from all strain gauges with respect to the applied compressive load. The applied compressive load in Newton is along the X-axis and strain gauges' output in Microstrain is along the Y-axis. The graph shows very clear the similarity in the characteristics in all the range.



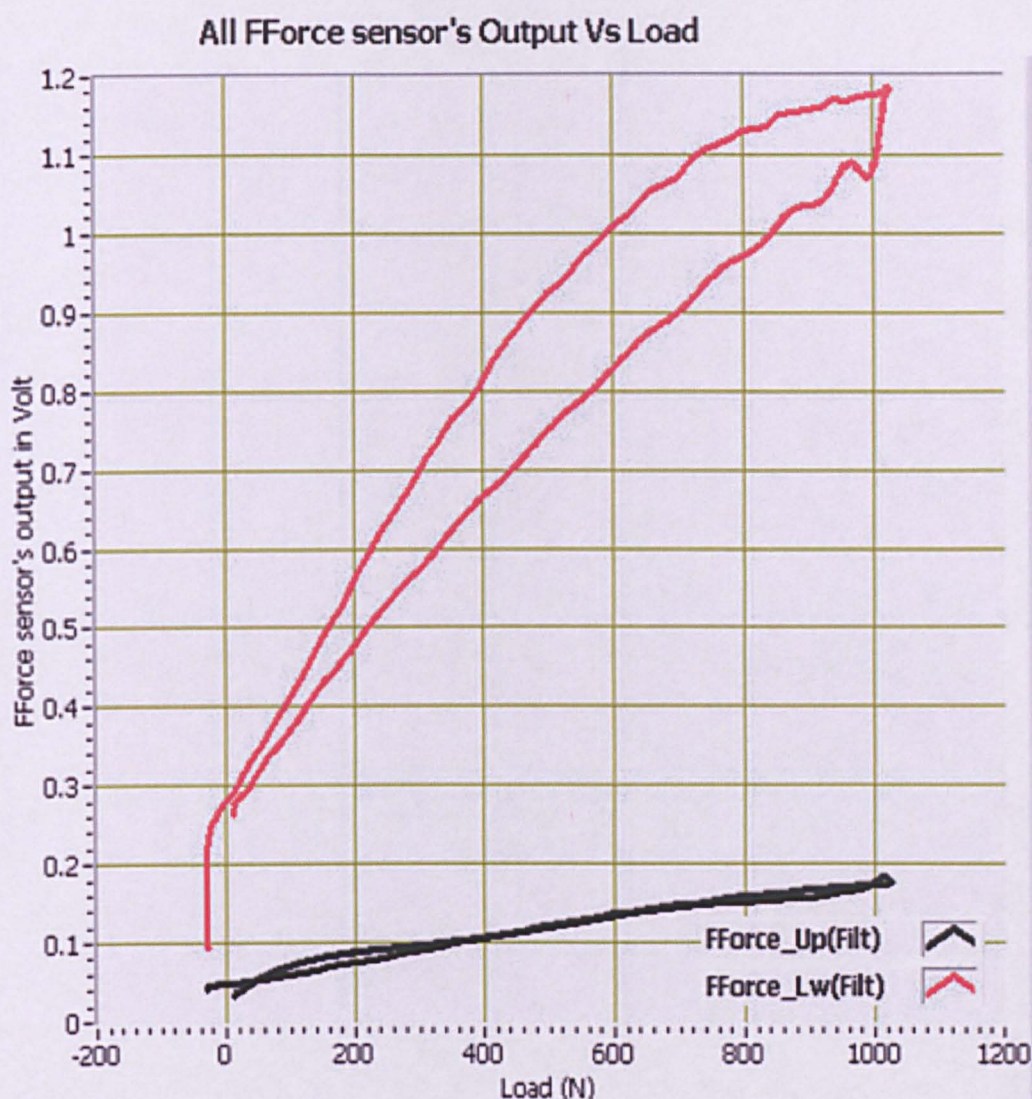


Figure 11-20: Two Flexiforce® sensors's output with respect to applied compressive load.

Figure 11-20 shows the outputs from the two Flexiforce® sensors with respect to the applied compressive load. The applied compressive load in Newton is along the X-axis and the Flexiforce® sensor's output in dc volt is along the Y-axis. In both Figures 11-19 and 1-20, the hysteresis can be found between the plots of the loading and unloading cycle.

### 11.3.2 Results of Exp. 2: Exp\_1k\_100NPS\_NOH

Experiment 2 was performed as described in the protocol (section 11.2.4). The results are shown in graphical format; see Figure 11-21 and Figure 11-22. The loading and unloading speed has been programmed as per protocol

in the universal testing machine. The graphs in Figure 11-21 present the outputs from all eight strain gauges (s.gauge 0 to s.gauge 7) and the outputs from the two piezoresistive-Flexiforce® sensors (F.force\_upper and F.force\_lower) when a compressive load is applied (with respect to time). The last graph depicted in Figure 11-21 titled as "Load Vs Time" presents the analogue output of the applied compressive load by the universal testing machine. In the graphs outputs from all strain gauges are presented in Microstrain ( $\text{Microstrain} = \text{strain} \times 10^{-6}$ ) and outputs from the two Flexiforce® sensors are in analogue dc volt (Y-axis). The time is in seconds (x-axis). The red coloured portions in all graphs shows the noisy raw signal and the black line plots are the best fit lines.

Similarly in Figure 11-22, the graphs present the outputs from all eight strain gauges (s.gauge 0 to s.gauge 7) and the outputs from the two piezoresistive-Flexiforce® sensors (F.force\_upper and F.force\_lower) when a compressive load is applied (with respect to the applied compressive load). In the graphs, outputs from all strain gauges are presented in Microstrain ( $\text{Microstrain} = \text{strain} \times 10^{-6}$ ) and outputs from the two Flexiforce® sensors are in analogue dc volt (Y-axis). The applied compressive load is in Newton (x-axis).

Also, the same "curve fitting" signal processing technique were utilized to both parts of the graph (loading and unloading). Therefore after multipart parametric signal processing, the resultant waveform is shown in Figure 11-23, named "SG 0 Vs Time and Load Vs Time". The graph has two Y-axis, one is in Microstrain and the other is in applied compressive load (Newton). The graph is very clear and very much similar in characteristics of the analogue output of the applied compressive load. The strain gauge is experiencing compression that's why the load Vs strain graph is inversely proportional. Similarly, Figure 11-24 shows the graphical presentation of the two Flexiforce® sensors with respect to time. The graph has two Y-axis as shown in Figure 11-24, one is in dc volt and the other is in applied compressive load (Newton). The graphs are obtained using identical signal processing techniques for both the Flexiforce® sensors. The outputs of the Flexiforce® sensors match well with the applied load graph shown in Figure 11-24.



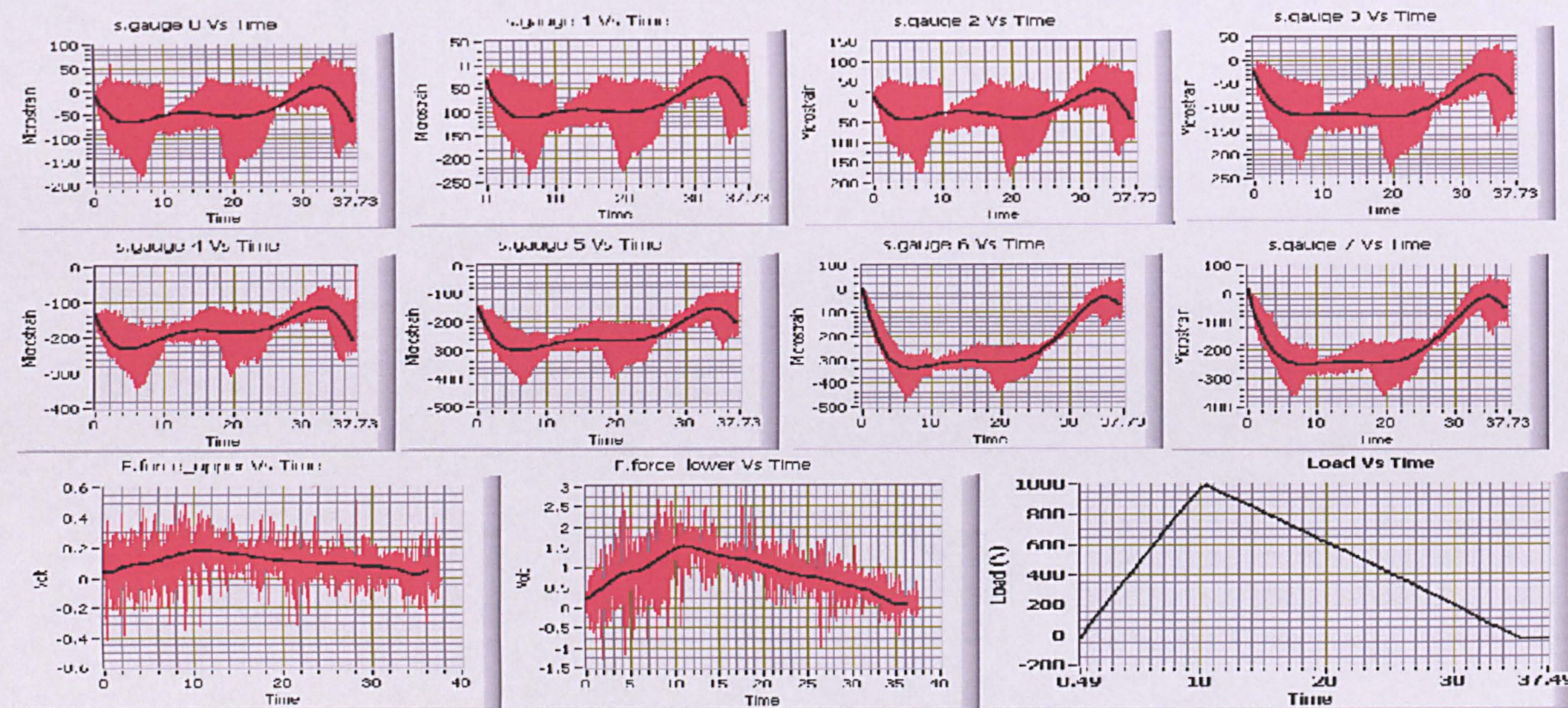


Figure 11-21: All eight strain gauge's outputs, two piezoresistive-Flexiforce® sensor's outputs and applied compressive load in Newton with respect to time in seconds. (Experiment protocol: Exp\_1k\_100NPS\_NOH).



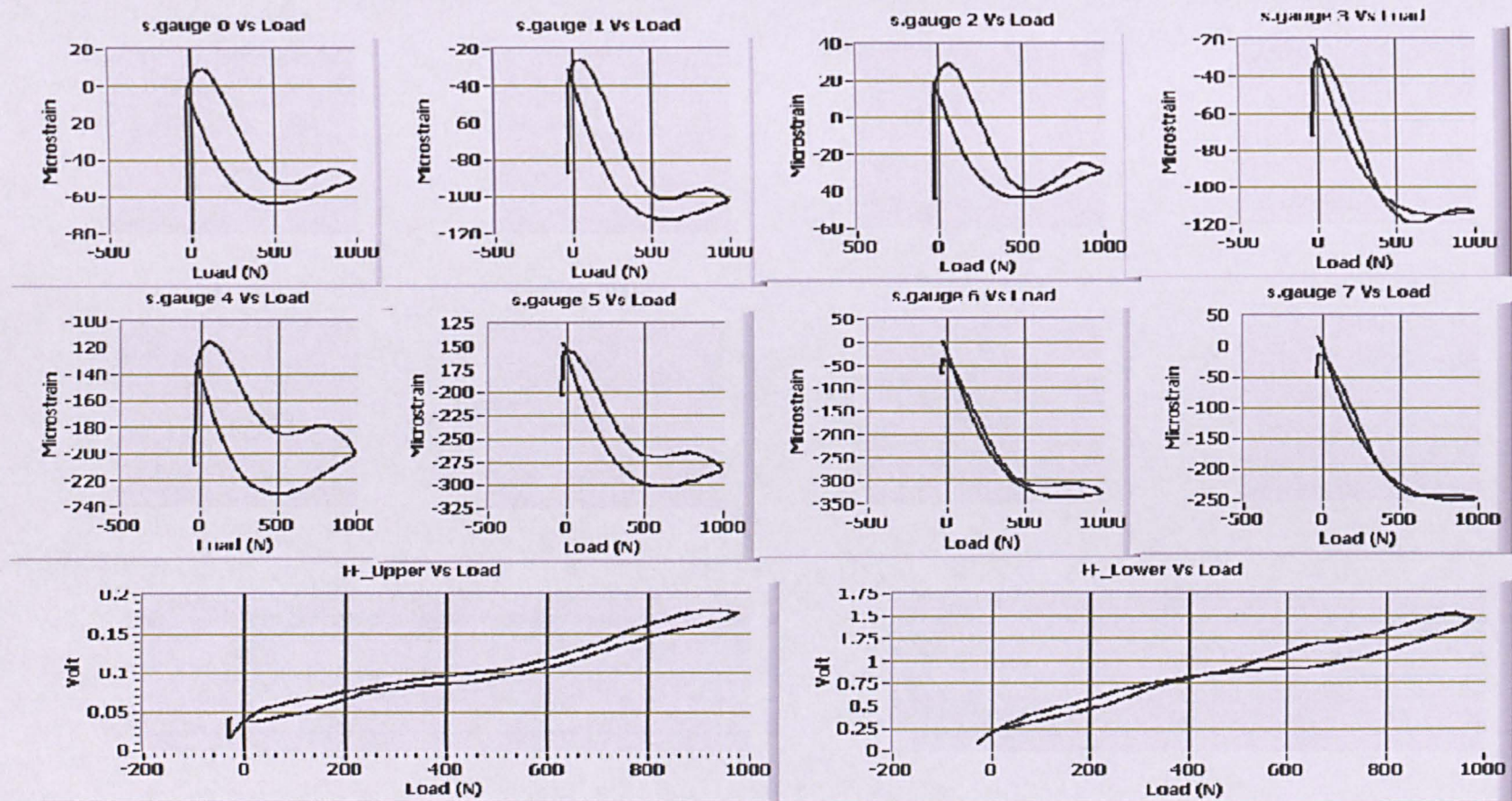


Figure 11-22: All eight strain gauge's outputs, two piezoresistive-Flexiforce® sensor's outputs and applied compressive load in Newton with respect to time in seconds. (Experiment protocol: Exp\_1k\_100NPS\_NOH).





Figure 11-23: Typical strain gauge output and applied load graph with respect to time (SG 0 Vs Time and Load Vs Time).

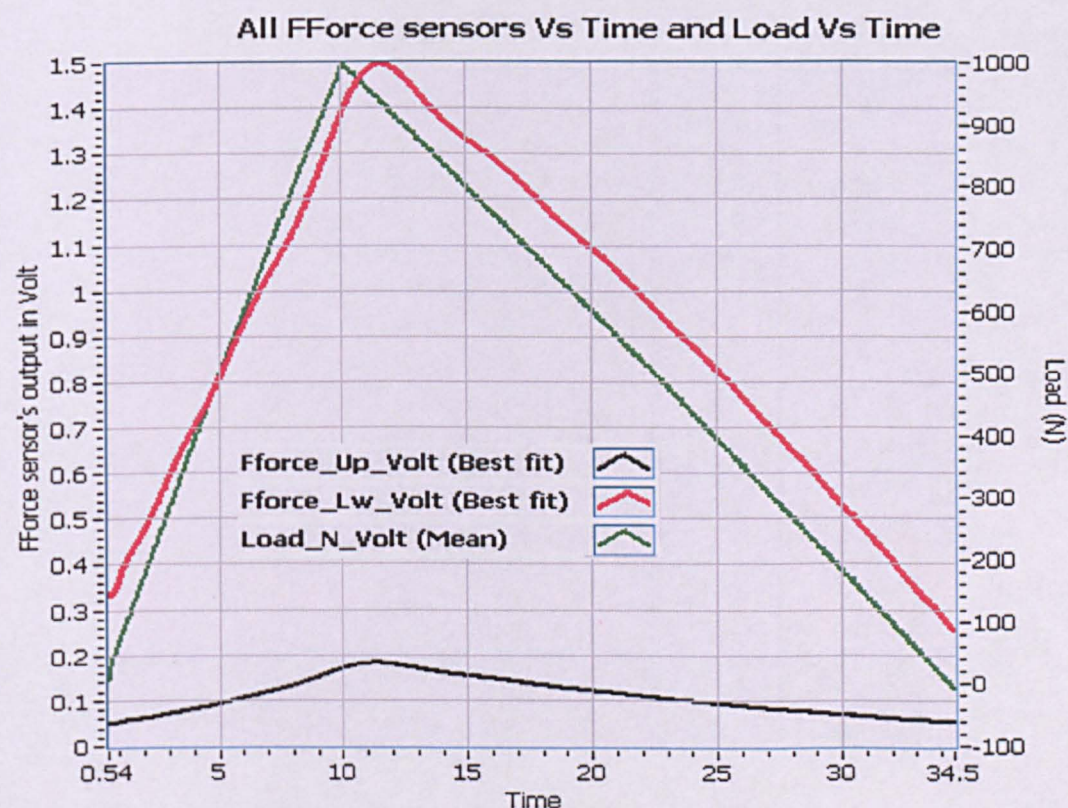


Figure 11-24: Outputs from two Flexiforce® sensors and applied load graph with respect to time.



The signal processing technique used in SG 0 Vs Time is also used for plotting all outputs of all the eight strain gauges (SG 0 to SG 7) and the two Flexiforce® sensors (Flexiforce®\_Upper and Flexiforce®\_Lower). For better comparison all outputs are plotted on a same graph as shown in Figure 11-25. All sensors' outputs with analogue output of the applied compressive load look very similar in characteristics. One noticeable observation when compared with experiment 1 is that there is less non-linearity in the loading cycle compare to the unloading cycle. Hence, the lower the speed of loading the more visco-elastic behaviour is observed. This can also be seen in loading and unloading cycles of this experiment with different speeds. The sensor's output graphs are more non-linear in a loading slow cycle than in an unloading slow cycle.

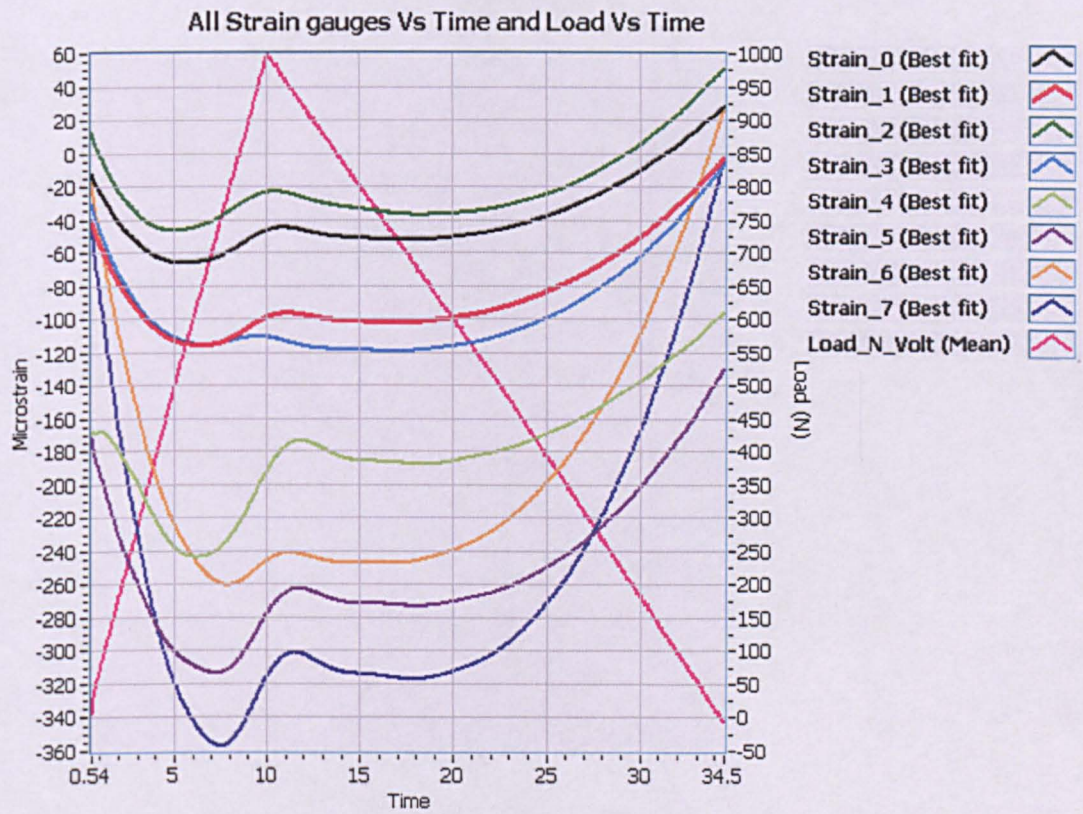


Figure 11-25: All strain gauge's output when loading from 0 to 1 kN.

The 2nd part of the graph which represents the sensor's output when unloading from 1 to 0 kN has a duration of 25 seconds only. This is higher compare to the 1st part of the graph which is only 10 seconds. Hence, to clearly present the graph, the 2nd and 1st part of the graph of Figure 11-23 is magnified and shown in Figure 11-26 and 11-27 respectively.



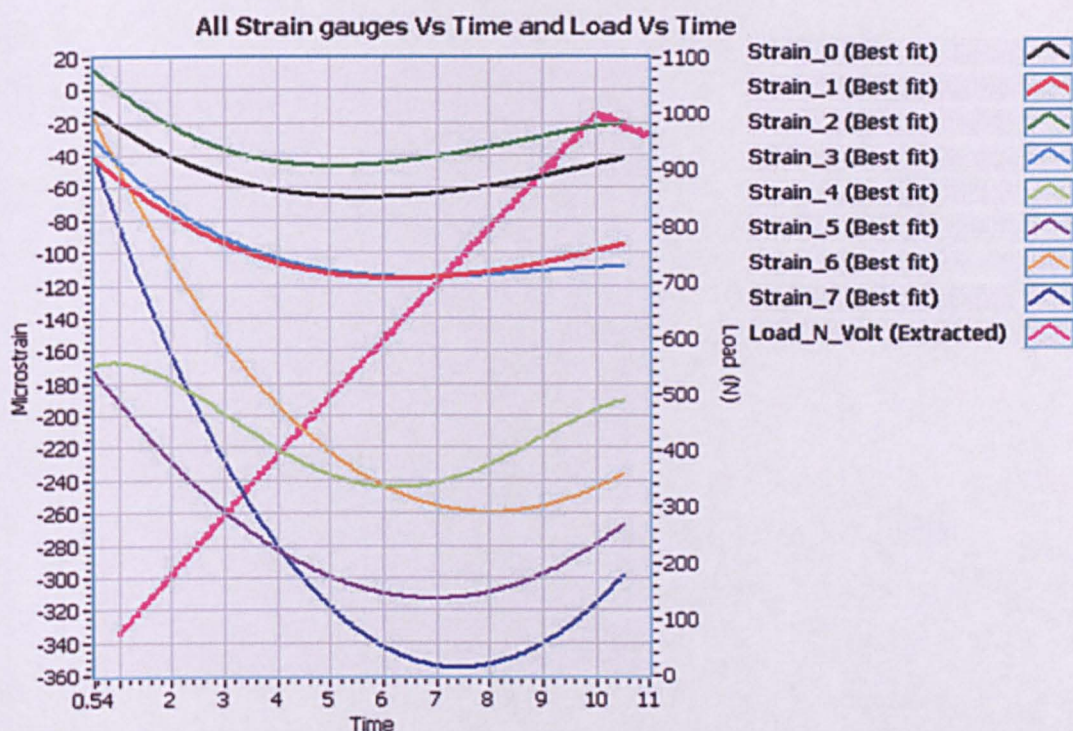


Figure 11-26: The 1st part of the graph for all strain gauge's output when loading from 0 to 1 kN.

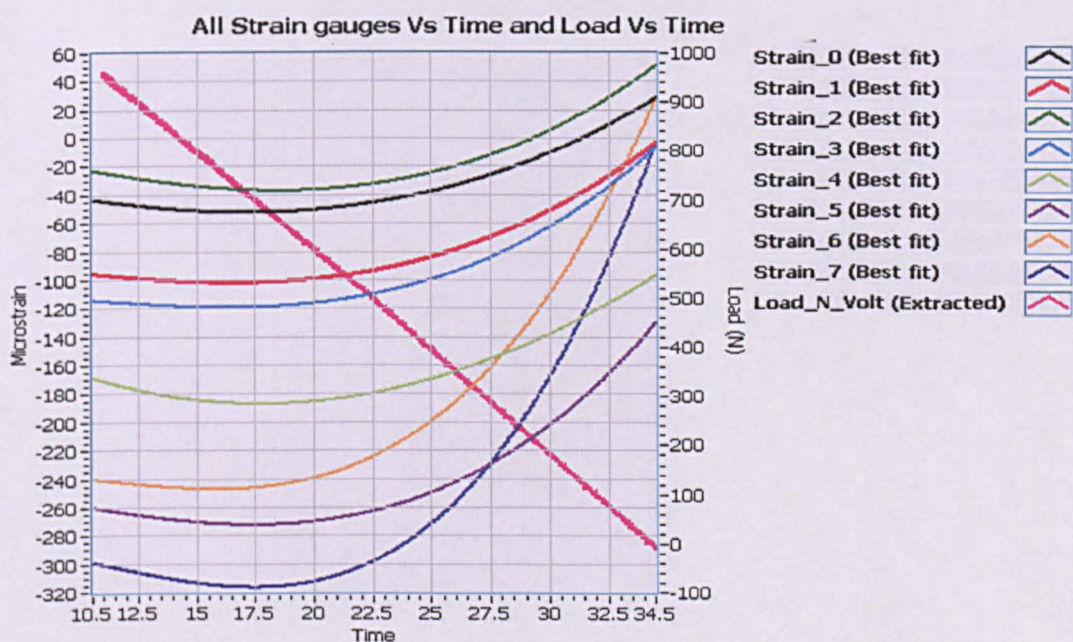


Figure 11-27: The 3rd part of the graph for all strain gauge's output when unloading from 1 to 0 kN.

Figure 11-28 shows the outputs from all strain gauges with respect to the applied compressive load. The applied compressive load in Newton is along the X-axis and the strain gauges output in Microstrain are along the Y-axis.



The graph shows very clear and similar characteristics throughout the range.

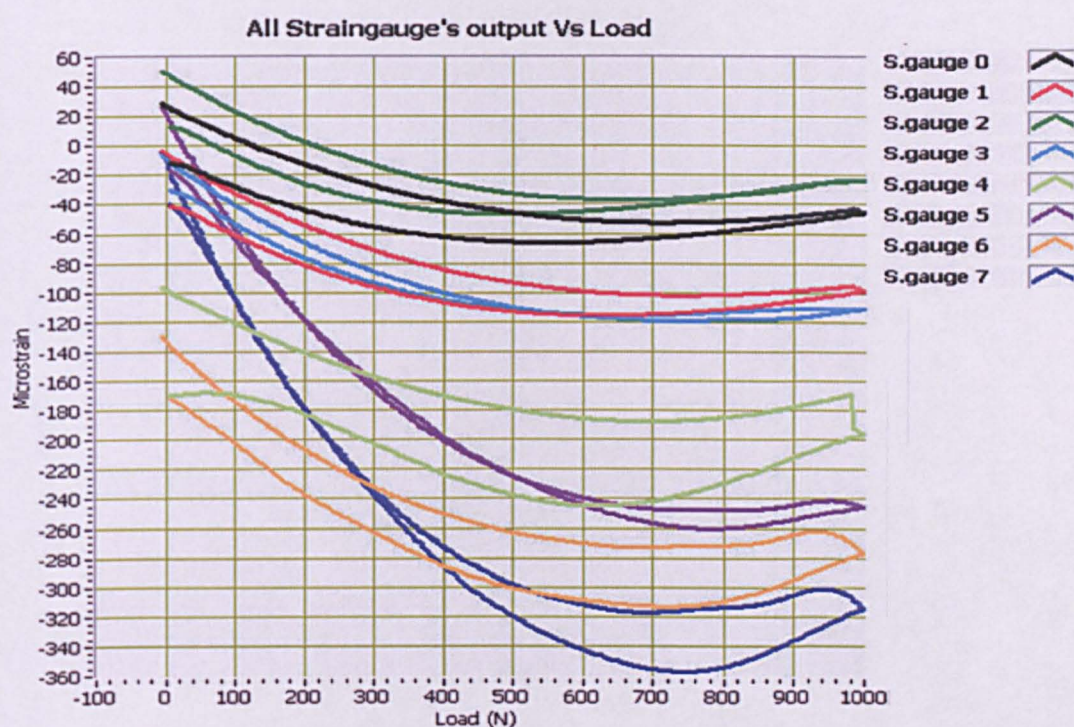


Figure 11-28: All strain gauges outputs with respect to applied compressive load.

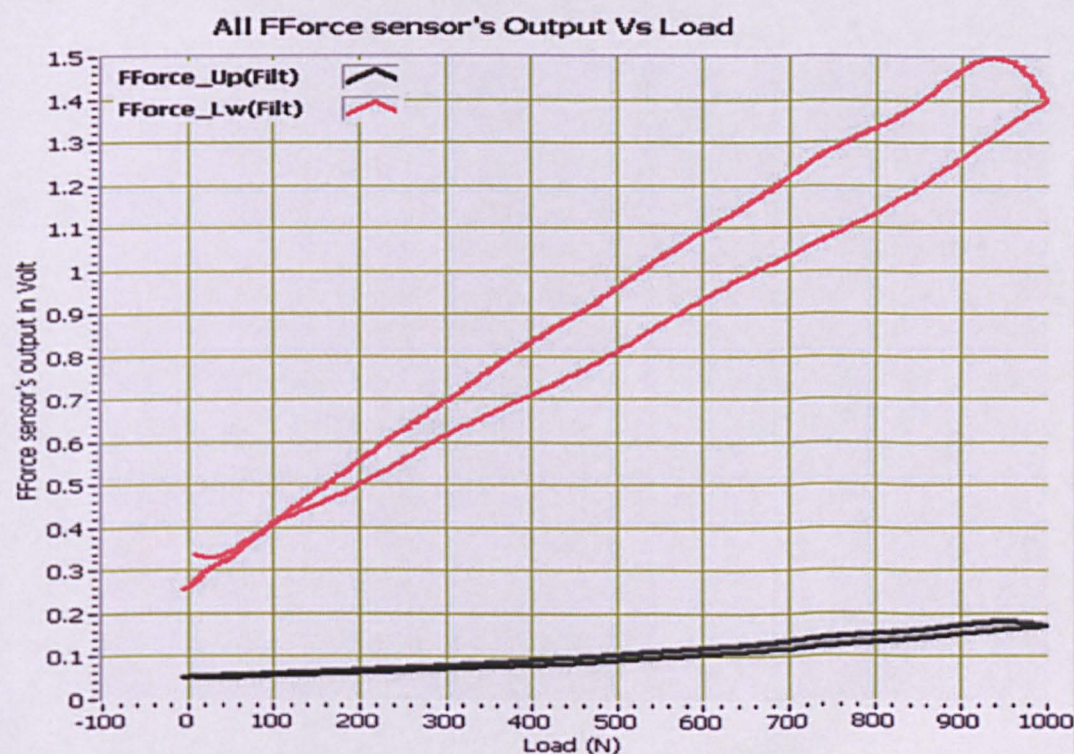


Figure 11-29: Two Flexiforce® sensor's output with respect to applied compressive load.



Figure 11-29 shows the outputs from the two Flexiforce® sensors with respect to the applied compressive load. The applied compressive load in Newton is along the X-axis and the Flexiforce® sensor's output in dc volt is along the Y-axis. The graph shows very clear and similar characteristics. In both Figures 11-28 and 11-29, the hysteresis can be found between the plots of the loading and unloading cycle. In this experiment, the loading speed is 100 NPS and the unloading speed is 40 NPS, where as in the previous experiment the loading speed was 10 NPS and unloading speed was 500 NPS.

### **11.3.3 Results of Exp. 3: Exp\_750N\_step250N\_10NPS\_LH10S**

---

Experiment 3 was performed as described in the protocol (section 11.2.4). The results are shown in graphical format; see Figure 11-30 and Figure 11-31. The graphs in Figure 11-30 present the outputs from all eight strain gauges (s.gauge 0 to s.gauge 7) and the outputs from the two piezoresistive-Flexiforce® sensors (F.force\_upper and F.force\_lower) when a compressive load is applied (with respect to time). The last graph depicted in Figure 11-30 titled as "Load Vs Time" presents the analogue output of the applied compressive load by the universal testing machine. In the graphs, outputs from all strain gauges are presented in Microstrain ( $\text{Microstrain} = \text{strain} \times 10^{-6}$ ) and outputs from the two Flexiforce® sensors are in analogue dc volt (Y-axis). The red coloured portions in all graphs shows the noisy raw signal and the black line plots are the best fit lines.

Similarly in Figure 11-31, the graphs present the outputs from all eight strain gauges (s.gauge 0 to s.gauge 7) and the outputs from the two piezoresistive-Flexiforce® sensors (F.force\_upper and F.force\_lower) when a compressive load is applied (with respect to the applied compressive load). In the graphs, outputs from all strain gauges are presented in Microstrain ( $\text{Microstrain} = \text{strain} \times 10^{-6}$ ) and outputs from the two Flexiforce® sensors are in analogue dc volt (Y-axis). The applied compressive load is in Newton (x-axis).

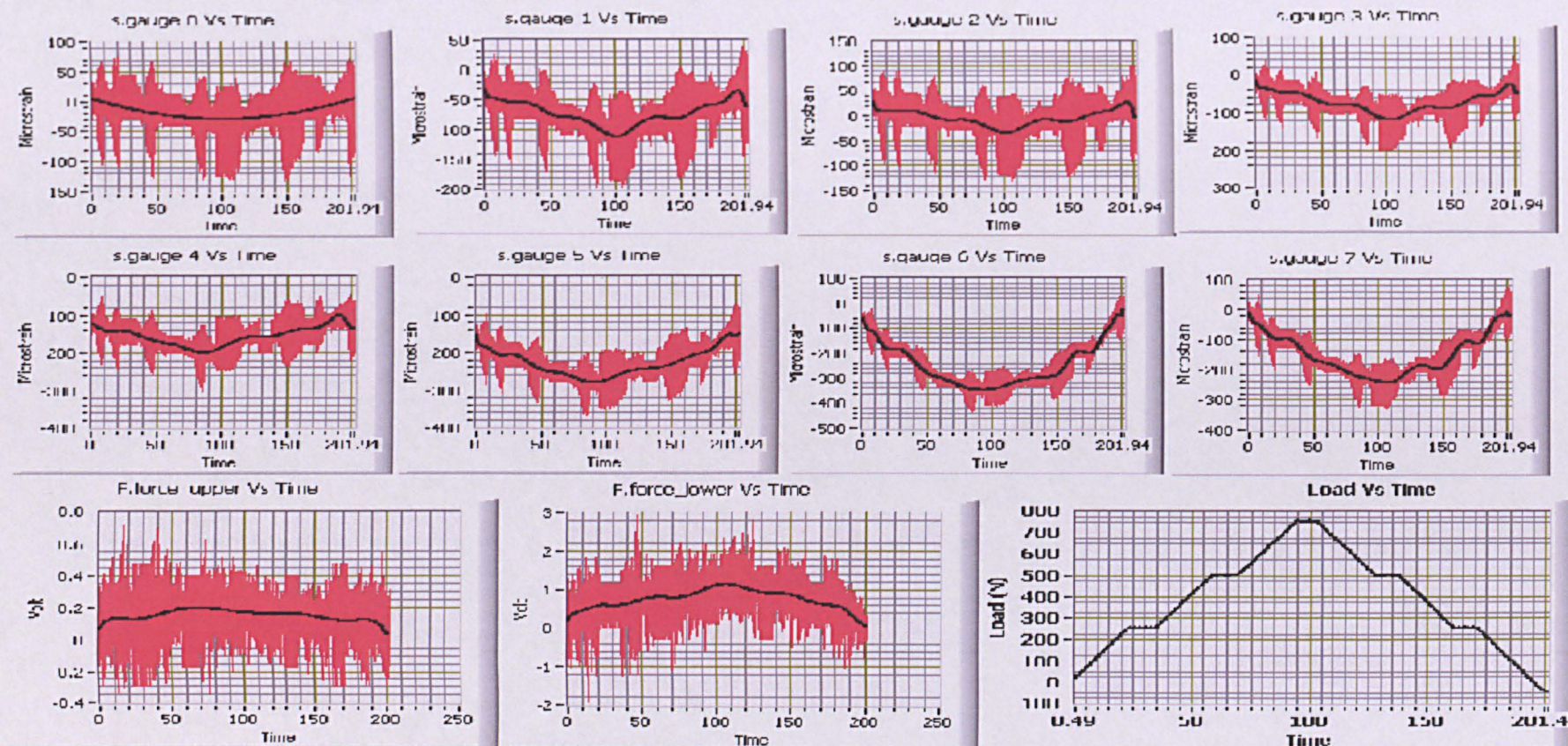


Figure 11-30: All eight strain gauge's outputs, two piezoresistive-Flexiforce® sensor's outputs and applied compressive load in Newton with respect to time in seconds. (Experiment protocol: Exp\_750N\_step250N\_10NPS\_LH10S).



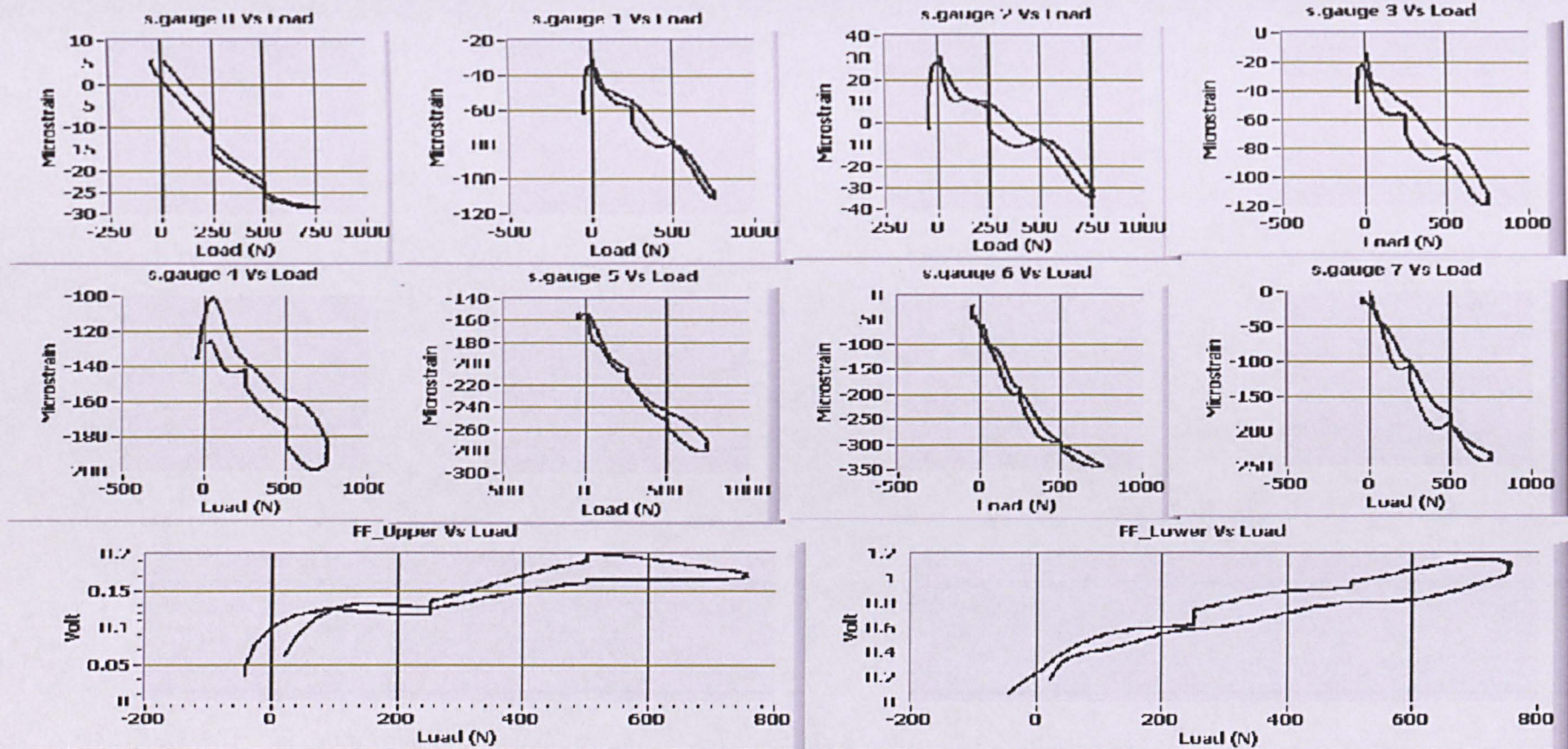


Figure 11-31: All eight strain gauge's outputs, two piezoresistive-Flexiforce® sensor's outputs and applied compressive load in Newton with respect to time in seconds. (Experiment protocol: Exp\_750N\_step250N\_10NPS\_LH10S).



The outputs from all the eight strain gauges look similar in characteristics as in previous experiments. In Figure 11-30, a typical noise pattern similar to previous experiments can be seen in the graphs representing outputs from all strain gauges. Similarly, a different noise pattern can also be seen in the graphs representing outputs from the two Flexiforce® sensors.

In this experiment the noise filtering is extremely difficult because there are 11 parts of stationary and non-stationary types. Out of which 6 parts are non-stationary type with 10 NPS loading/unloading speed and 5 parts are stationary type. The same signal processing techniques described before were applied to remove the noise from the signals.

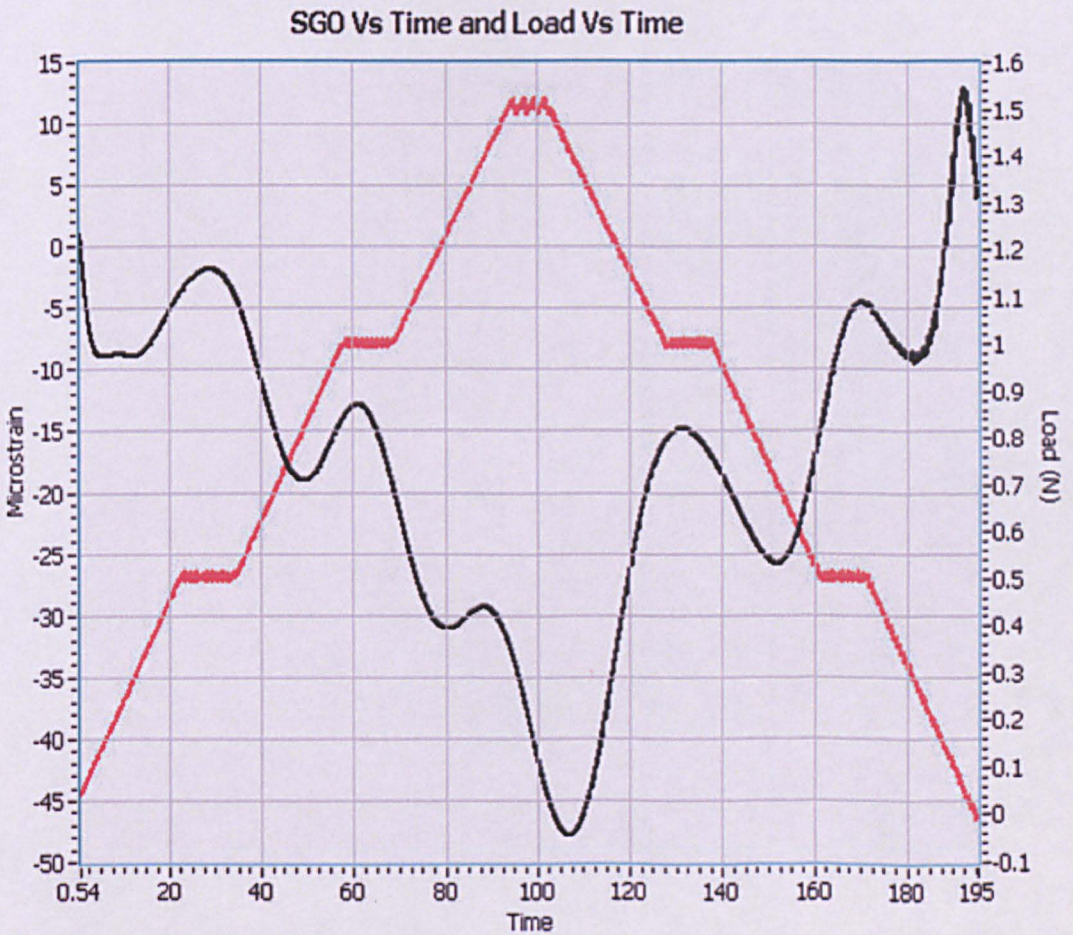


Figure 11-32: Typical strain gauge output and applied load graph with respect to time (SG 0 Vs Time and Load Vs Time)

Also, the same "curve fitting" signal processing technique were utilized to all parts of the graph (loading, holding, and unloading). Therefore, after parametric signal processing, the resultant waveform is shown in Figure 11-32, named "SG 0 Vs Time and Load Vs Time". The graph has two Y-axis,



one is in Microstrain and other is in applied compressive load (Newton). The graph is clear but not exactly matching with the characteristics of the analogue output of the applied compressive load as is in previous experiments. The strain gauge is experiencing compression that's why the load Vs strain graph is inversely proportional.

Similarly, Figure 11-33 shows the graphical presentation of the two Flexiforce® sensors with respect to time. The graph has two Y-axis as shown in Figure 11-32, one is in dc-volt and other is in applied compressive load (Newton). The graphs are obtained using identical signal processing techniques for both the Flexiforce® sensors.

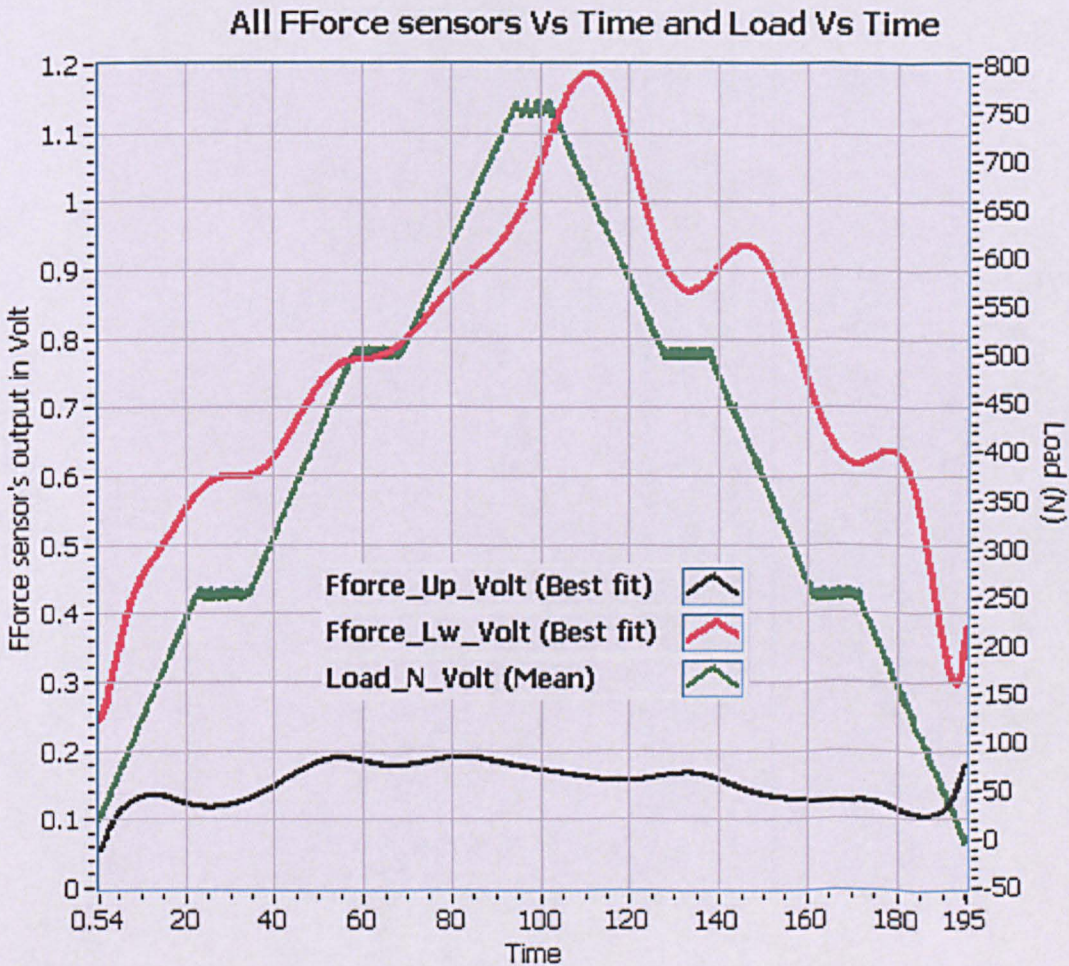


Figure 11-33: Outputs from two Flexiforce® sensors and applied load graph with respect to time.



The signal processing technique used in "SG 0 Vs Time" graph (Figure 11-32) is also used for plotting all outputs from all eight strain gauges (SG 0 to SG 7).

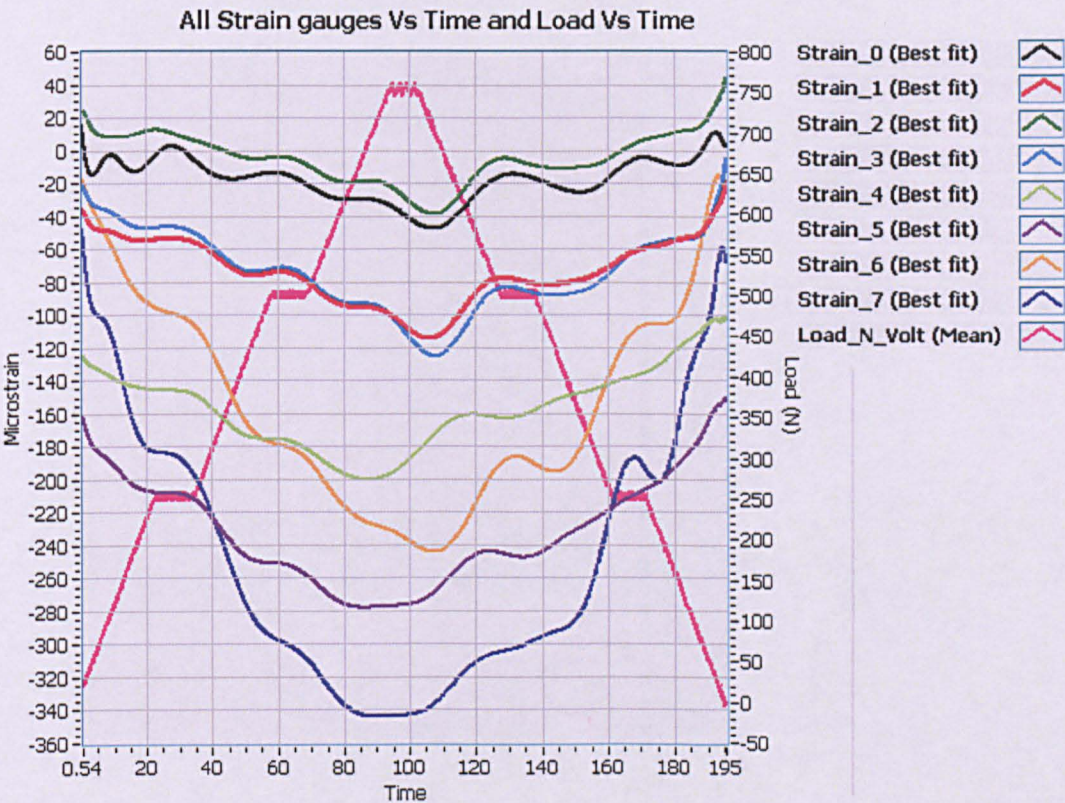


Figure 11-34: All strain gauges outputs with respect to applied compressive load.

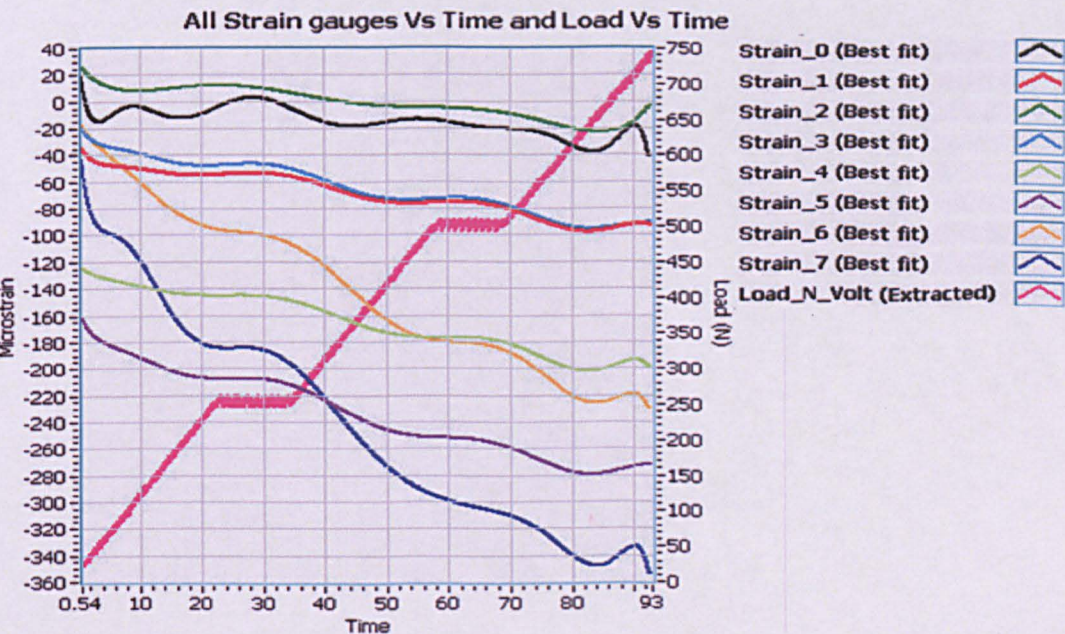


Figure 11-35: The 1st part of the graph for all strain gauge's output when loading from 0 to 750 N.



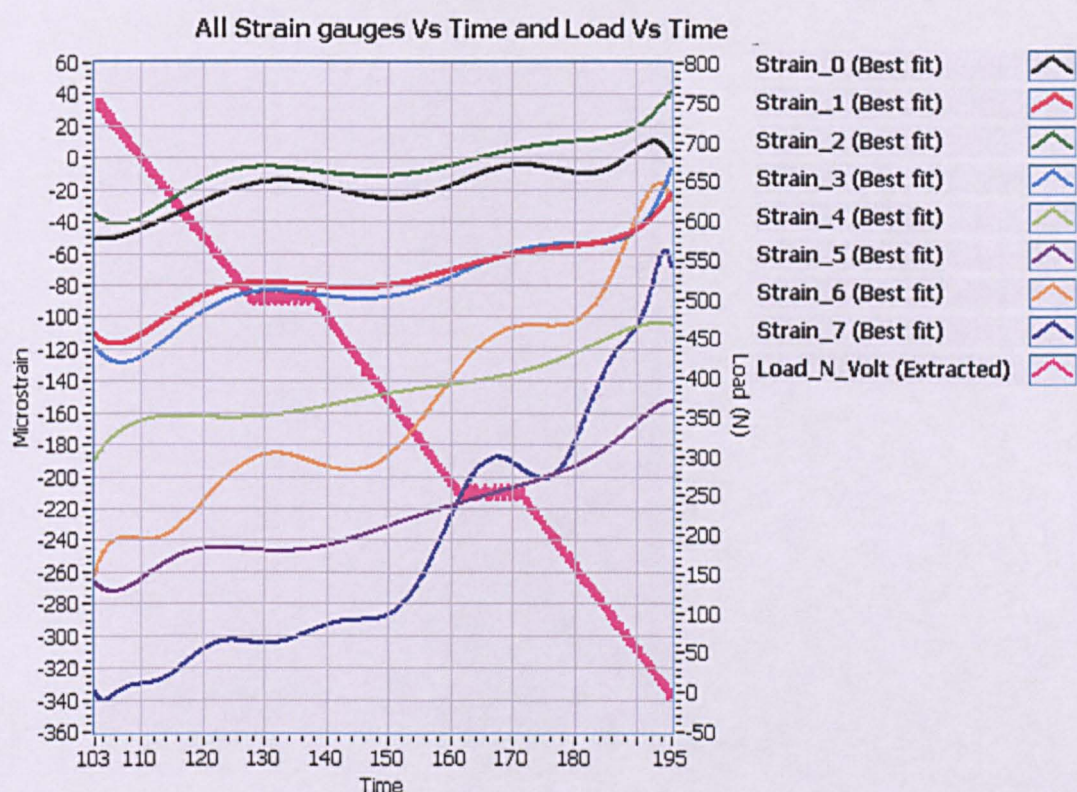


Figure 11-36: The 3rd part of the graph for all strain gauge's output when unloading from 750 to 0 N.

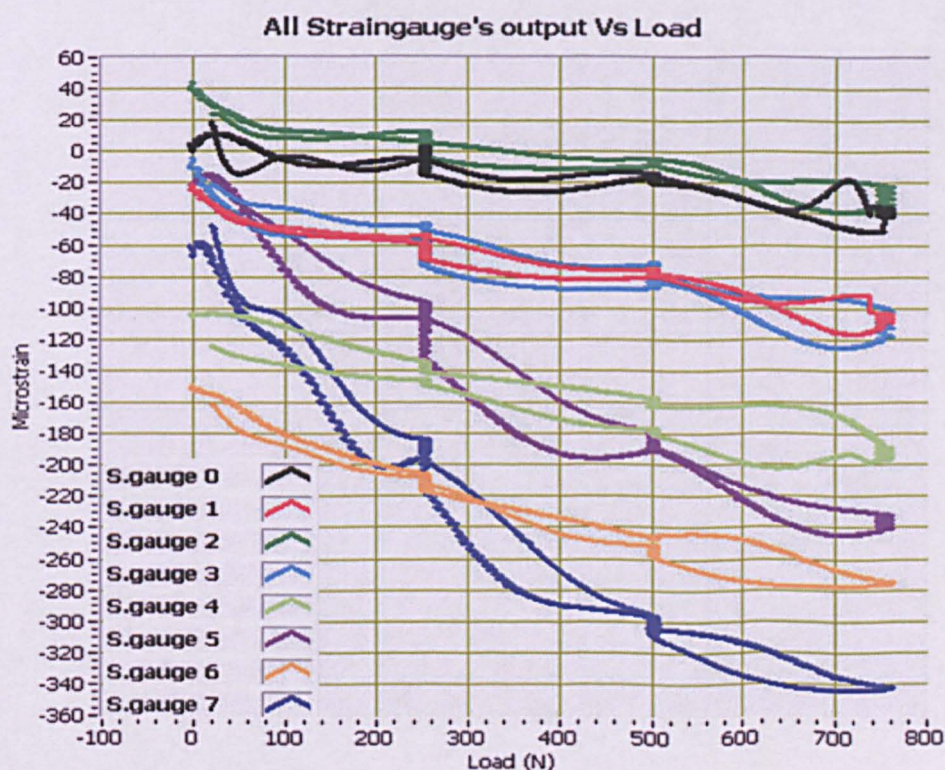


Figure 11-37: shows the outputs from all strain gauges with respect to the applied compressive load. The applied compressive load in Newton is along the X-axis and strain gauges output in Microstrain are along the Y-axis.



For better comparison of all outputs from all strain gauges, all graphs are plotted on the same graph as shown in Figure 11-34. All sensors' outputs look similar with the analogue output of the applied compressive load. For a better clear view of the graphs a magnified view of Figure 11-34 is presented in Figure 11-35 and Figure 11-36. Figure 11-35 presents the 1st part of the graphs i.e. from 0 to 750 N loading cycle graph and Figure 13-27 presents the 3rd part of the graphs i.e. from 750 N to 0 N unloading cycle graph.

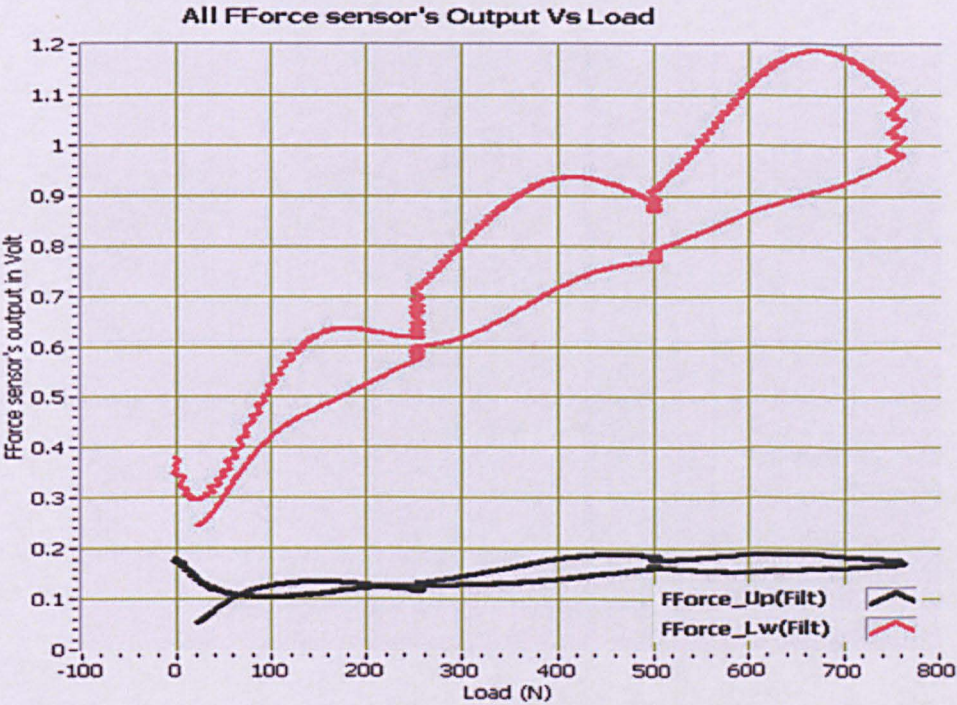


Figure 11-38: Two Flexiforce® sensors's output with respect to applied compressive load.

Figure 11-37 shows the outputs from all strain gauges with respect to the applied compressive load. The applied compressive load in Newton is along the X-axis and the strain gauge's output in Microstrain is along the Y-axis.

Figure 11-38 shows the outputs from the two Flexiforce® sensors with respect to the applied compressive load. The applied compressive load in Newton is along the X-axis and the Flexiforce® sensor's output in dc volt is along the Y-axis.



## 1 1.4 SUMMARY

---

All the results of the three *ex vivo* experiments show more irregular and unstable behaviour when compared to *in vitro* experiments. This might be due to the difficulty in the grip of the disc (load cell). However, overall all *ex vivo* results produced outputs which are comparable with the *in vitro* results despite the difficulties with the experimental set-up.

# **12 DISCUSSIONS, CONCLUSIONS AND FUTURE WORK**

---

## **12.1 INTRODUCTION**

---

This chapter covers discussion, conclusions and recommendations for future work on this research project.

## **12.2 DISCUSSION AND CONCLUSION**

---

Low back pain is an economic and social burden to the society. Its total solution requires a systematic, long term and multi-disciplinary approach. Low back pain which is due to degenerative disc and damaged vertebrae is considered to be a chronic problem and in many cases requires a surgical intervention. The main causes for degenerative disc are extremely complex and still not well understood, although in their majority are strongly related to the acute and frequent mechanical loading on the spine (Cholewicki, et al., 1991; Stokes, et al., 2004; Liuke, et al., 2005; Kyriacou, et al., 2009). Knowledge that might shed more light in such pathologies is the availability of *in vivo* data of loading of the human spinal disc, which at the moment does not exist. Many efforts had been made by researchers to investigate and understand the *in vivo* loading of human spinal discs. All such techniques were not true *in vivo* techniques and hence, their findings are questionable (Nachemson, et al., 1970; Cholewicki, et al., 1991; Schultz, et al., 1991; McGill, 1992; Han, et al., 1995; Rohlmann, et al., 1997; Dolan, et al., 1998; Morlock, et al., 1998; Patwardhan, et al., 1999; Ledet, et al., 2000; Ledet, et al., 2005; (Kyriacou et al., 2009). Not only a complete understanding of the *in vivo* loading of the human spine, but also the distribution of the loading on the spinal disc are of prime importance in order to comprehensively understand the biomechanics of the human spine and its parts, and therefore, enable the creation of solutions (surgical, technological) for low back pain pathologies. Such new knowledge will also be helpful in treatment of the vertebrae compression fractures due to low



bone mineral density or multiple myeloma, etc. Finally such new knowledge will aid in the further improvement of current implantable spinal technologies.

The aim of this work was to engage towards such preliminary investigation by developing and evaluating a prototype artificial spinal disc with the capability of mapping the loads applied to the disc when is loaded in an *in vitro* and *ex vivo* environment. Therefore, in this research project, for the first time an artificial intervertebral disc prosthesis was designed and developed as a base for a load-cell with a primary focus of investigating *in vivo* loading on the spinal disc.

Following a comprehensive critical review of possible suitable sensors (strain, pressure) to be embedded within the artificial spinal disc, it was concluded that two types of sensors will be used. These sensors were:

- ★ Strain gauge
- ★ Piezoresistive thin layer sensor

Strain gauge technologies have been used in the past in similar investigations however this is the first time that piezoresistive thin layer sensors and strain gauges are incorporated within the body of an artificial spinal disc. These two different sensing modalities offer unique advantages for correctly measuring the *in vivo* loading on the spinal disc. The working principles of both sensing modalities are fundamentally different as the strain gauge measures load on the basis of surface strain measurement and the piezoresistive thin layer sensor measures load on the basis of change in the resistance of the sensor. Hence, the strain gauge is an indirect sensor whereas the piezoresistive thin layer sensor is a direct sensor for measuring load.

The loading cell has been successfully designed and developed comprising of eight strain gauges and two piezoresistive sensors encapsulated inside the body of a commercial artificial spinal disc. Four strain gauges were placed on the upper metal plate of the spinal disc and the other four were placed on the bottom plate. The two piezoresistive sensors were placed above and below the inlay material of the disc. Further instrumentation and software were developed in order to interface the loading cell with a data acquisition system. A universal testing machine was used for all loading

experiments. *In vitro* and *ex vivo* (using a cadaveric animal spine) were conducted in order to evaluate the developed technology and also to rigorously investigate the loading behaviour of the new loading cell.

Comprehensive study protocols were designed in order to simulate various loading scenarios. All *in vitro* experiments were conducted by applying 0-4 kN compressive load in normal directions only. All sensor outputs with respect to the applied compressive load were repeatable, consistent, accurate and more importantly predictable by fitting into certain regression models with acceptable tolerances. In the graphs shown in chapter-10 (raw data) a noticeable signal noise element was present which compromised somewhat the results. It was very difficult to point out the main reasons for this noise; however this could be due to the electric line and/or other types of inductive loads and/or electromagnetic interferences, etc. At the time of the experiments the noticeable reasons for noise could also be the Universal Testing Machine, which uses a hydraulic motor. It was also observed that at the time of the ON period the amplitude of noise increased significantly, around 200 Microstrain, in all output signals of the strain gauges. The artificial intervertebral disc used in the experiment has one typical characteristic, which could have some contribution on the generated noise. The inlay material of the disc between the two end-plates moved minutely by around 1 mm in both X and Y directions depending upon the direction of the application of the compressive load. That sudden unpredictable movement of the inlay material generated a sudden mechanical thrust on the disc end-plates. Due to that temporary unstable mechanical condition, the sensor's output showed typical spikes or movement which are unpredictable. The noise that was due to the movement of the inlay material was only noticeable on the strain gauges and not the piezoresistive sensors. This might be due to the fact that the strain gauge operates on the principle of measuring surface strain on the end-plates where the piezoresistive sensors measures resistance changes as the load changes and the load is passing through the sensor. Hence, the piezoresistive sensors are less sensitive to force other than normal force. Strain gauges are more sensitive than the piezoresistive sensors and they along with their signal conditioning circuits can easily pick-up surrounding noise.



Following the *in vitro* loading experiments it is concluded that strain gauges are suitable for this application. The main reasons that aid their suitability are - they are rugged, consistent, long life, reliable and provide the possibility of usability at very low power requirements. Some of the undesirable characteristics of strain gauges such as sensitivity and susceptibility to noise can be overcome by advanced signal processing techniques and better mechanical design of the whole system. The *in vitro* results showed poor correlation during the period of load holding. For example, in Experiment-2, the value of correlation coefficient is higher than Experiment-1, during the period of constant load. The main reason for that is that in Experiment-1 the load is kept constant where in Experiment-2, the position is kept constant but the load decreases slowly with time due to the visco-elastic characteristic of the inlay material. Furthermore, the value of correlation coefficient is higher and more consistent during the loading period when compared to the unloading period. The Flexiforce sensor (piezoresistive sensor) exhibits high correlation except in some experimental instances like in Experiment-1. It is also observed that the higher the speed of loading the better the correlation. Following the *in vitro* investigations the loading cell was used for *ex vivo* loading investigations using an animal spine. In these experiments one significant anatomical difference of the spinal vertebrae used was that the animal spinal disc was bigger in length compared to a human spinal disc. The reason for this is because the human spine posture is vertical in the body where for a four legged animal (used in this study) the spine posture is horizontal and hence their loading pattern is different. In this experiment each plate of the artificial spinal disc was anchored by three studs on the animal vertebrae. However, during the *ex vivo* experiment this anchorage was not strong enough to provide mechanical stability. It was observed that at or after 1000 N of applied compressive loading the disc end-plates started dislocating. The failures in loading at high loading pressures (>1000 N) were due to the lack of tissue support to the spinal vertebrae as is in real life where our spinal discs are supported by tissues/muscles and therefore higher loading is possible. This observation can be of significant importance as it can prove one of the main areas of total disc failure after surgical procedures. These failures according to our observations can be due to dislocation of the artificial spinal disc prosthesis.

The results of the *ex vivo* experiments were described in Chapter-11. The hypothesis of these experiments was the generation of a more realistic loading environment (similar to *in vivo*) where more details in relation to the visco-elasticity of the spine could be observed. The results (sensor outputs) from these experiments do not fully support the hypothesis. The main reason could be that the vertebrae bones are not that visco-elastic in nature like the spinal disc. That's why the spinal disc is solely responsible in the spine for absorbing the mechanical shocks and vibrations. All the results from the three *ex vivo* experiments are not very different with their corresponding *in vitro* experiments. An overall important observation from the *in vitro* and *ex vivo* experiments was that all sensors outputs are almost identical in characteristics in all different loading experiments and all results are very much predictable with moderate level of tolerances, uncertainty, accuracy and repeatability.

### 12.3 FUTURE WORK

---

In the quest for *in vivo* spinal loading the efforts of future work could be focused in the further evaluation of the loading cell using a cadaveric human spine and conducting loading with 6-degrees of freedom. Such experiments will provide more realistic results. This can be done by using a loading machine with 6-degrees of freedom, for example using a spine simulator. Further miniaturisation of the technology and the introduction of telemetry will lead in to an animal study (preferable a two legged standing animal) for a true *in vivo* evaluation. Of course there are more challenges before such a device can be implanted in the human spine, such as biocompatibility, making this area of research very challenging but simultaneously very exciting. In summary, a prototype artificial intervertebral disc prosthesis for the assessment of spinal loading/stresses has been developed and evaluated both *in vitro* and *ex vivo*. The development of this new stress/ strain technology could allow the *in vivo* investigation of loading on the human spine in the lumbar region and therefore enable the continuous postoperative assessment of patients that had a spinal disc surgical intervention.



# REFERENCES

- ★ Aesculap, B.Braun Ltd. , 2005. *Active-L Product Brochure*. Product Catalogue. Tuttingen, Germany: Aesculap-B.Braun.
- ★ Albee, F.H., 1911. Transplantation of a portion of the tibia into the spine for Pott's disease: A preliminary report. *Journal of the american medical association*, 57, p.885.
- ★ American association of neurological surgeons, 2010. *Conditions: back-pain: spineuniverse.com*. [Online] Available at: <http://www.spineuniverse.com/conditions/back-pain/low-back-pain/low-back-pain-getting-root-problem> [Accessed 5th July 2010].
- ★ Andersson, G.B.J. & Schultz, A.B., 1979. Effects of fluid injection on mechanical properties of intervertebral discs. *Journal of biomechanics*, 12, p.453.
- ★ Arnau, A., 2004. *Piezoelectric transducers and applications*. Berlin: Springer-verlag.
- ★ Ashida, H., Yotsunomiya, K. & Okamoto, A., 1990. An attempt to develop artificial nuclei pulposi in lumbar intervertebral disc. *Journal of Japan Orthopaedic Assoc.*, 64, p.S947.
- ★ B.Braun Inc., 2010. *products: bbraun.com*. [Online] Available at: <http://www.bbraun.com/cps/rde/xchg/bbraun-com/hs.xsl/products.html?id=00020741510000000431&pid=PRID00004594> [Accessed 15th September 2010].
- ★ backpain-guide.com, 2011. *backpainguide.com/spine anatomy*. [Online] Available at: [http://www.backpain-guide.com/Chapter\\_Fig\\_folders/Ch05\\_Anatomy\\_Folder/Ch5\\_Images/05-4\\_Overall\\_Spine.jpg](http://www.backpain-guide.com/Chapter_Fig_folders/Ch05_Anatomy_Folder/Ch5_Images/05-4_Overall_Spine.jpg) [Accessed 2011 25 May].
- ★ backpain-guide.com, 2011. *backpain-guide.com/spine anatomy*. [Online] Available at: [http://www.backpain-guide.com/Chapter\\_Fig\\_folders/Ch05\\_Anatomy\\_Folder/Ch5\\_Images/05-4\\_Overall\\_Spine.jpg](http://www.backpain-guide.com/Chapter_Fig_folders/Ch05_Anatomy_Folder/Ch5_Images/05-4_Overall_Spine.jpg) [Accessed 25 May 2011].
- ★ Bao, M.-H., 2000. Micro-Mechanical transducers, pressure sensors, accelerometers and gyroscopes. In Middelhoek, S. *Handbook of sensors and actuators*. Amsterdam: Elsevier. p.8: 1 to 371.
- ★ Bao, Q.B. & Higham, P.A., 10 September, 1991. *Hydrogel intervertebral disc nucleus*. Patent No: 5,047,055. USA.
- ★ Bao, Q.B. & Higham, P.A., 9 March, 1993. *Hydrogel bead intervertebral disc nucleus*. Patent No: 5,192,326. US.

- ★ Bartleson, J.D. & Gordon Deen, H., 2010. Spine disorders: Medical and surgical management. *Journal of bone and joint surgery*, 92-B(8), pp.1182-83.
- ★ Bell, G.H., Dunbar, O., Beck, J.S. & Gibb, A., 1967. Variation in strength of Vertebrae with age and their relation to Osteoporosis.. *Calcif. Tissue Res.*, 1, p.75.
- ★ Benzel, E.C., 2005. *Spine surgery: Techniques, Complications, Avoidance and Management*. 2nd ed. Elsevier Churchill Livingstone.
- ★ Bernick, S. & Cailliet, R., 1982. Vertebrae End-plate Changes with ageing of Human Vertebrae. *Spine*, 7(2), p.97.
- ★ Bertagnoli, R. & Schonmayr, R., 2002. Surgical and clinical results with the PDN prosthetic disc-nucleus device. *European Spine Journal*, pp.11:S143-8.
- ★ Bogduk, N. & Twomey, L., 1991. *Clinical Anatomy of the Lumbar Spine*. 2nd ed. Churchill Livingstone.
- ★ Bono, C. & Garfin, S., 2004. History and evolution of disc replacement. *The Spine Journal*, 4, pp.145S-50S.
- ★ Bono, C.M. & Grafin, S.R., 2004. *Orthopaedic surgery essential: spine*. Lippincott Williams and Wilkison.
- ★ Boulder neurosurgical associates, 2010. *patient-resources-neck-pain: bnasurg*. [Online] Available at: <http://www.bnasurg.com/patient-resources-neck-pain.php> [Accessed 30th October 2010].
- ★ Bradford, D.S. & Zdeblick, T.A., 2004. *Master technique in orthopaedic surgery: The spine*. 2nd ed. Lippincott Williams & Wilkins.
- ★ Brinckmann, P., Fobin, W., Hierholzer, E. & Horst, M., 1983. Deformation of the vertebral end-plate under axial loading of the spine. *Spine*, 8, p.851.
- ★ Broberg, K.B., 1983. On the mechanical behaviour of the intervertebral discs. *Spine*, 8, p.151.
- ★ Brodgesell, A., Liptak, B. & Silva Girao, P., 2003. Torque and Force Transducers. In Liptak, B.G. *Instrument Engineers' Handbook: Process Measurement and Analysis, Volume I*. Boca Raton, Florida.: CRC Press. pp.1051-60.
- ★ Brown, T., Hanson, R. & Yorra, A., 1957. Some Mechanical test on the lumbo-sacral spine with particular reference to intervertebral discs.. *Journal of bone and joint surgery*, 39A, p.1135.
- ★ Burton Report , 2010. *SurgArtificialDiscs: infspine: burtonreport*. [Online] Available at: <http://www.burtonreport.com/infspine/SurgArtificialDiscs.htm> [Accessed 24th October 2010].
- ★ Busch-Vishniac, I., 1999. *Electromechanical sensors and actuators*. Newyork: Springer.
- ★ Cholewicki, J., Juluru, K. & McGill, S.M., 1999. Intra-abdominal pressure mechanism for stabilizing the lumbar spine. *Journal of biomechanics*, 32, pp.13-17.



- ★ Cholewicki, J., McGill, S. & Norman, R., 1991. Lumbar spinal load during the lifting of extremely heavy weights. *Medical Science Sports Exercise*, 23(10), pp.1179-86.
- ★ Cummins, B., Robertson, J. & Gill, S., 1998. Surgical experience with an implanted artificial cervical joint. *Journal of Neurosurgery*, 88, p.943-948.
- ★ Demetropoulos, C.K., Morgan, C.R., Sengupta, D.K. & Herkowitz, H.N., 2009. Development of 4-axis load cell used for lumbar interbody load measurements. *Medical engineering & physics*, 31(7), pp.846-51.
- ★ Doebelin, E.O., 1989. *Measurement systems*. New York: McGraw-Hill.
- ★ Dolan, P. & Adams, M., 1998. Repetitive lifting tasks fatigue the back muscles and increase the bending moment acting on the lumbar spine. *Journal of biomechanics*, 31, pp.713-21.
- ★ Dove, J., Hardcastle, P., Davis, J. & King, B., 27 February, 1990. *Spinal Implants*. Patent No: 49,04,261. USA.
- ★ Downey, E., 17 October, 1989. *Replacement disc*. Patent No: 4,874,389. USA, US.
- ★ Downey, E.L., 30 July, 1991. *Replacement Disc*. Patent No: 5,035,716. USA, US.
- ★ Drafts, B., 2000. *sensors: acoustic ultrasound: acoustic-wave-technology-sensors-936: sensormag*. [Online] Questex Media Group LLC Available at: <http://www.sensormag.com/sensors/acoustic-ultrasound/acoustic-wave-technology-sensors-936> [Accessed 26 August 2010].
- ★ Edeland, H., 1989. Some additional suggestions for an intervertebral disc prosthesis. *J Biomed Mater Resources: Appl Biomaterial*, 23, pp.189-94.
- ★ Eismont, F.J. & Simeone, F.A., 1981. Bone overgrowth (hypertrophy) as a cause of late paraphrases after scoliosis fusion.. *Journal of bone and joint surgery*, 63A, p.1016.
- ★ Elbestawi, M.A., 1999. Forec Measurement. In Webster, J.-E.-i.-c. *The measurement, instrumentation and sensors handbook*. Boca Raton, FL: CRC Press. pp.23-1 to 23-16.
- ★ Enker, P., Steffee, A. & McMillin, C., 1993. Artificial disc replacement Preliminary report with a 3 year minimum follow-up. *Spine*, 18, pp.1061-80.
- ★ Fardon, D.F. & Millet, P.C., 2001. *Nomenclature and Classification of Lumbar Disc Pathology: Recommendations of the Combined Task Forces of the North American Spine Society, American Society of Spine Radiology, and American Society of Neuroradiology*. Case Report. Lippincott Williams & Wilkinson Inc.
- ★ Farfan, H.F.P.-d.L.&F., 1973. Mechanical Disorder of the Low Back.
- ★ Farfan, H., 1995. Form and function of the musculoskeletal system as revealed by mathematical analysis of the lumbar spine. *Spine*, 20(13), pp.1462-74.

- ★ Farfan, H.F. et al., 1970. The Effects of Torsion on The Lumbar Intervertebral Joints: the Role of Torsion in the production of disc degeneration. *Journal of bone and joint surgery*, 52A, p.468.
- ★ Fassio, B. & Ginestie, J., 1978. Prothese discale en silicone. Etude experimentale. *Nouv Press Med*, 21, p.207.
- ★ Fernström, U., 1964. Metallic disk prosthesis for lumbar disc rupture. *Nord Med*, p.71: 160.
- ★ Fernström, U., 1965. Metallic disk prosthesis for lumbar and cervical disc rupture. *Nord Med*, 73, pp. 272-273.
- ★ Fernström, U., 1966. Arthroplasty with intercorporal endoprosthesis in herniated disc and in painful disc. *Acta Orthopaedica Scand. Suppl.*, 10, pp.287-89.
- ★ Fernström, U., 1966. Arthroplasty with intercorporal endoprosthesis in herniated disc and in painful disc. *Acta Chir Scand*, 355 (Suppl), pp.154-59.
- ★ Fischer, H., 8 December, 1987. Patent No: DE-OS 3,741,493. West Germany, West Germany.
- ★ Fletcher, R., 1996. Force transduction materials for human-technology interfaces. *IBM systems journal*, pp.Vol.(3-4) 630 to 638.
- ★ Fraden, J., 1997. *Handbook of modern sensors: physics, designs and applications*. Woodbury, New York: AIP Press.
- ★ Frey, O.K.R., 11 September, 1990. Patent No: 4,955,908. USA.
- ★ Frey, O.K.R.P.H.M.F., 12 June, 1990. Patent No: 4,932,969. USA.
- ★ Frey, O. & Koch, R., 17 April, 1990. Patent No: 4.917.704. USA.
- ★ Froning, E.C., 8 April, 1975. *Intervertebral disc prosthesis and instruments for locating same*. Patent no: 3,875,595. USA.
- ★ Fuhrmann, G. et al., 26 March, 1991. 5,002,576. USA.
- ★ Gautschi, G., 2002. *Piezoelectric sensorics: force, Strain, pressure, Acceleration and acoustic emission sensors, materials and amplifiers*. Berlin: Springer.
- ★ Gertzbein, S.D., Wolfson, N. & King, G., 1988. The diagnosis of segmental instability in vivo by centrodome length. In *Trans. Int. Soc. For study of lumbar spine*. Miami, 1988. Int. Soc. For study of lumbar spine.
- ★ Goel, V.K. & Weinstein, J.N., 1990. *Biomechanics of the spine: clinical and surgical perspective..* Boca raton: CRC press.
- ★ Granhed, H., Johnson, R. & Hansson, T., 1987. The loads on the lumbar spine during extreme weight lifting. *Spine*, 12(2), pp.146-49.
- ★ Han, J.S. et al., 1995. Loads in the spinal structures during lifting: development of a three-dimensional comprehensive biomechanical model. *Euro spine journal*, 4, pp.153-68.



- ★ Hayes, M.A., Howard, T.C., Gruel, C.R. & Kopta, J.A., 1989. Roentgenographic evaluation of lumbar spine flexion-extension in asymptomatic individuals. *Spine*, 14(3), p.327.
- ★ HBM Ltd., 2005. *Strain gauge and Accessories brochure*. Product Catalogue.
- ★ Health and Safety Executive, 2006. *Backs! 2005 initiative - Final Report*. 3 year Musculoskeletal Disorders Reduction Programme. HSE.
- ★ health.com, 2011. *health.com/spinal cord*. [Online] Available at: <http://www.health.com/health/static/hw/media/medical/hw/n5551554.jpg> [Accessed 25 May 2011].
- ★ Hedman, T., Kostuik, J., Fernie, G. & Hellier, W., 1991. Design of an intervertebral disc prosthesis. *Spine*, 16, pp.5256-60.
- ★ Herkowitz, H.N. et al., 2004. *The lumbar spine*. 3rd ed. Philadelphia, PA, USA: Lippincott Williams and Wilkins.
- ★ Hibbs, R.A., 1911. An operation for progressive spinal deformities: A preliminary report from three cases from the service of the orthopaedic hospital.. *New York State Medical Journal*, 93, p.1013.
- ★ Hirayama, Y., Ikata, H., Ojim, S. & Matsuzaki, H., 7 August, 1990. Patent No: 4,946,378. USA.
- ★ Hirsch, C., 1955. The Reaction of Intervertebral Discs to Compression Forces. *Journal of bone and joint surgery*, 37A, p.1188.
- ★ Hirsch, C. & Lewin, T., 1968. Lumbosacral synovial joints in flexion-extension. *Acta Orthop.Scand.*, 39, p.303.
- ★ Hou, T.S., 1994. *Changzhen Hospital, Shanghai, China*. Interview by communication personnel.
- ★ Hsiu, A., Issac, K. & Katz, J., 2000. Cauda equine syndrome from intradiscal electro thermal therapy. *Neurology*, 55(2), p.320.
- ★ Hunter, L.Y., Braunstein, E.M. & Bailey, R.W., 1980. Radiographic changes following anterior cervical spine fusions. *Spine*, 5, p.399.
- ★ indyspinemd.com, 2011. *indyspinemd.com/vertebra.jpg*. [Online] Available at: <http://indyspinemd.com/Images/normalAnat/Vertebra.jpg> [Accessed 25 May 2011].
- ★ Jirout, J., 1957. The normal mobility of the lumbosacral spine.. *Acta radiology*, 47, p.345.
- ★ Kazarian, L.E., 1975. Creep Characteristics of the Human Spinal Column. *Clin. Orthop. North Am.*, 6, p.3.
- ★ Khvisyuk, N., Prodan, A. & Lygun, L., 7 January, 1982. Patent No: 895,433. USSR.
- ★ Kings, A.I., Prasad, P. & Ewing, C.L., 1975. Mechanism of Spinal Injury due to caudocephalad acceleration. *Orthop. Clin. North Am.*, 6, p.19.

- ★ Knowles, F.L., 4th May, 1954. *Apparatus for treatment of the spinal column*. Patent No: 2,677,369. USA.
- ★ Knutsson, f., 1944. The instability associated with disc degeneration in the lumbar spine.. *Acta Radiology.*, 24, pp.593-609.
- ★ Korge, A., Nydegger, T. & Polard, J., 2002. A spiral implant as nucleus prosthesis in the lumbar spine. *Euro Spine Journal*, p.11:S149–53.
- ★ Kotsuik, J.P., 1997. Intervertebral disc replacement. Experimental study. *Clinical Orthopaedics*, 337, p.27–41.
- ★ Kromodihardjo, S. & Mital, A., 1987. A biomechanical analysis of manual lifting tasks. *Journal of biomechanics*, 109, pp.132-38.
- ★ Kuntz, J.D., 21 september, 1982. *Intervertebral disc prosthesis*. Patent No: 4,349,921. USA.
- ★ Kyriacou, P., Pancholi, M. & Yeh, J., 2009. Investigation of the in-vitro loading of the artificial disk prosthesis. In *Journal of Physics*. Edinburgh, 2009. IOP Publishing Ltd..
- ★ Langrana, N., Parsons, J. & Lee, C., 1994. Materials and design concepts for an intervertebral disc spacer. I. Fiber-reinforced composite design. *Journal of Applied Biomaterials*, 5, p.125–132.
- ★ Laurent, J., Bisson, E. & Hadley, M., 2006. Spinal Reconstruction: Quo Vadis? *Clinical neurosurgery*, pp.229-37.
- ★ Ledet, E.H. et al., 2000. Real time in vivo loading in the lumbar spine. Part 1: interbody implant load cell design and preliminary data. *Spine*, 25(20), pp.2595-600.
- ★ Ledet, E.H. et al., 2005. Direct Real-Time measurement of in vivo forces in the lumbar spine. *The Spine Journal*, 5, pp.85-94.
- ★ Lee, C.K. & Langrana, N.A., 1984. Lumbosacral spinal fusion: A biomechanical study. *Spine*, 9, p.574.
- ★ Leskinen, T., Stalhammar, H., Kuorinka, I. & Troup, J., 1983. A dynamic analysis of spinal compression with different lifting techniques. *Ergonomics*, 26, pp.595-604.
- ★ Lewis, D.R., 2007. *Report for City University on the market and potential partners for a Wireless Implantable Stress/Strain Sensor for Intervertebral Disc Prostheses*. Market and potential partners. London: Dialogue Resources Ltd.
- ★ Linders, D.R. & Nuckley, D.J., 2007. Deduction of spinal loading from vertebral body surface strain measurements. *Experimental mechanics*, 47, pp.303-10.
- ★ Liptak, B.G., 2003. Electronic pressure sensors. In Liptak, B.G. *Instrument engineers' handbook: Process measurement analysis (Vol-I)*. Boca Raton, FL.: CRC Press. p.751 to 761.
- ★ Liuke, M. et al., 2005. Disc degeneration of the lumbar spine in relation to overweight. *International Journal of Obesity*, pp.29, 903-908.



- ★ Liuke, M. et al., 2005. Disc degeneration of the lumbar spine in relation to overweight. *International Journal of Obesity*, 29(doi:10.1038/sj.ijo.0802974), pp.903-08.
- ★ Main, J.A., Wells, M.E. & Keller, T.S., 12 june, 1990. Patent no: 4,932,975. USA.
- ★ Maniadakis, A. & Gray, A., 2000. The economic burden of back pain in UK. *Pain*, 84, pp.95-103.
- ★ Markolf, K.L., 1970. Stiffness and Dampening Characteristic of the Thoracic-Lumbar Spine. In *Proceedings on Workshop on Bio-Engineering Approaches to the Problems of The Spine.*, 1970. NIH.
- ★ McGill, S.M., 1990. Loads on the lumbar spine and associated tissues. cited in: Goel VK, Weinstein JN, editors. *Biomechanics of the spine: clinical and surgical perspective.*
- ★ McGill, S., 1992. A myoelectrically based dynamic three-dimensional model to predict loads on lumbar spine tissues during lateral bending. *Journal of Biomechanics*, 25(4), pp.395-414.
- ★ mcm.edu, 2011. [mcm.edu/vertebrainerve.gif](http://www.mcm.edu/~wvatta/wordpress/wp-content/uploads/vertebralnerves.gif). [Online] Available at: <http://www.mcm.edu/~wvatta/wordpress/wp-content/uploads/vertebralnerves.gif> [Accessed 25 May 2011].
- ★ Medtronic Inc., 2010. *newsroom: content: 1244729914384.high\_resolution.jpg*. [Online] Available at: [http://www.medtronic.com/newsroom/content/1244729914384.high\\_resolution.jpg](http://www.medtronic.com/newsroom/content/1244729914384.high_resolution.jpg) [Accessed 30th October 2010].
- ★ Mensor, M.C. & Duvall, G., 1959. Absence of motion at the fourth and fifth lumbar interspaces in patients with and without low-back pain. *Journal of joint and bone surgery*, 41A, p.1047.
- ★ Merriam-Webster Inc., 2010. *facetectomy: medical : merriam-webster Inc.*. [Online] Available at: <http://www.merriam-webster.com/medical/facetectomy> [Accessed 02 October 2010].
- ★ Merriam-webster Inc., 2010. *laminotomy: medical: merriam-webster.com*. [Online] Available at: <http://www.merriam-webster.com/medical/laminotomy> [Accessed 2nd October 2010].
- ★ Microspine inc., 2010. *disc1.gif: doctorbuzz.com*. [Online] Available at: <http://www.doctorbuzz.com/disc1.gif> [Accessed 24th October 2010].
- ★ Milette, P.C., 1997. The proper terminology for reporting lumbar intervertebral disk disorders. *AJNR Am J Neuroradiol*, 18, p.1859–1866.
- ★ Milette, P.C., 2000. Classification, diagnostic imaging and imaging characterization of a lumbar herniated disc. *Radiol Clinical North America*, 38, pp.1267-92.
- ★ Miller, J.A.A., Schmatz, C. & Schultz, A.B., 1988. : Lumbar Disc Degeneration: Correlation with Age, Sex and Spine level in 600 Autopsy Specimens. *Spine*, 13(2), p.173.
- ★ Monson, G.L., 5 September, 1989. *Synthetic intervertebral disc prosthesis*. Patent no: 4,863,477. USA.

- ★ Morlock, M.M. & Schneider, E., 1998. Determination of the magnitude of lumbar spinal loading during different nursing activities. In *Proceedings of the 44th Annual Meeting of the Orthopaedic Research Society*. New Orleans, Louisiana, Chicago, 1998. Orthopaedic research society.
- ★ Murtagh, R.D. et al., 2010. *contents: radiographics*. [Online] Available at: <http://radiographics.rsna.org/content/29/1/105.figures-only> [Accessed 24th October 2010].
- ★ Nachemson, A., 1960. Lumbar Intradiscal Pressure. *Acta Orthop.Scand.*, p.suppl. 43.
- ★ Nachemson, A., 1965. The effect of forward leaning on lumbar intradiscal pressure. *Acta orthop. scandinav.*, 35, pp.314-28.
- ★ Nachemson, A., 1966. The load on the lumbar disks in different positions of the body. *Clinical Orthopaedics*, 45, pp.45-122.
- ★ Nachemson, A.L., 1981. Disc pressure measurements. *Spine*, 6(1), pp.93-97.
- ★ Nachemson, A. & Elfstrom, G., 1970. Intravital dynamic pressure measurements in lumbar discs.. *Scand J Rehabil Med Suppl*, S1, pp.1-40.
- ★ Nachemson, A. & Morris, J.M., 1964. In vivo Measurement of Intradiscal Pressure. *Journal of bone and joint surgery*, 46, p.1077.
- ★ National Instruments Corporation, 2010. *NI Developer Zone: Natinal Instruments Corporation*. [Online] (May 21, 2010) Available at: <http://zone.ni.com/devzone/cda/tut/p/id/3642> [Accessed 24 August 2010].
- ★ Neurocirgia inc., 2010. *CHARITE.jpg: images: instrumental: neurocirugia*. [Online] Available at: [http://www.neurocirugia.com/instrumental/images/CHARITÉ\\*.jpg](http://www.neurocirugia.com/instrumental/images/CHARITÉ*.jpg) [Accessed 24th October 2010].
- ★ Neurocirguia Contemporanea, 2010. *dynardi.jpg: images: instrumental: neurocirugia*. [Online] Available at: <http://www.neurocirugia.com/instrumental/images/dynardi.jpg> [Accessed 24th October 2010].
- ★ Noltingk, B.E., 1996. *Instrumentation reference book*. Oxford: Butterworth-Heinemann.
- ★ Norton, H.N., 1982. *Sensor and analyzer handbook*. Englewood Cliffs: Prentice hall.
- ★ Nuchiro, 2011. *Nuchiro disc*. [Online] Available at: <http://nuchiro.files.wordpress.com/2011/04/disc.jpg> [Accessed 25 May 2011].
- ★ Nuvasive inc., 2010. *XL-TDR-Device: images: xlmotion: nuvasive*. [Online] Available at: <http://www.nuvasive.com/xlmotion/images/XL-TDR-Device.jpg> [Accessed 15th September 2010].
- ★ Oka, M., Gen, S., Ikada, Y. & Okimatsu, H., 24 May, 1994. 5,314,478. USA.



- ★ Olsson, T.H., Selvik, G. & Willner, S., 1977. Mobility in the lumbosacral spine after fusion studied with the aid of roentgen stereophotogrammetry. *Clinical orthopaedics*, 129, pp.181-90.
- ★ Panagiotacopulos, N.D., Pope, M.H., Block, R. & Krag, M.H., 1987. Water Content in Human Vertebral Discs. Part II. Viscoelastic behaviour. *Spine*, 12, p.918.
- ★ patientsites.com, 2011. *patientssite.com/neural foramina*. [Online] Available at: [http://patientsites.com/media/img/1281/thoracic\\_spine\\_anatomy06.jpg](http://patientsites.com/media/img/1281/thoracic_spine_anatomy06.jpg) [Accessed 25 May 2011].
- ★ Patil, A.A., 12th January, 1982. *Artificial Intervertebral Disc*. Patent No: 4,309,777. USA.
- ★ Patwardhan, A., Meade, K. & Lee, B., 1999. A “follower load” increases the load carrying capacity of the lumbar spine in axial compression. *Spine*, 24(10), pp.1003-09.
- ★ Pearcy, M.J., Portek, I. & Shepherd, J., 1984. Three-dimensional X-ray analysis of normal movement in the lumbar spine.. *Spine*, 9(3), pp.294-97.
- ★ Perey, O., 1957. Fracture of the vertebral end-plate in the lumbar spine. ; . *Acta Orthop Scand*, S25(2), p.101.
- ★ Perey, O., 1957. Fracture of the vertebral end-plate in the lumbar spine.. *Acta Orthop Scand*, S25, pp.2-101.
- ★ Pisharodi, M., 23 June, 1992. *Artificial Spinal Prosthesis*. Patent no: 5,123,926. USA.
- ★ Prasad, P., King, A.I. & Ewing, C.L., 1974. The Role of Articular facets during +Gz Acceleration. *Journal of applied mechanics*, 41, p.321.
- ★ Punjabi, M.M., Brown, M., Lindahl, s. & Irstam, L., 1988. Intrinsic disc pressure as a measure of integrity of the lumbar spine. *Spine*, 13(8), p.913.
- ★ Quinnel, R.C. & Stockdale, H.R., 1983. Observations of pressure within normal disc in the lumbar spine.. *Spine*, 8, p.166.
- ★ Ray, C., 2002. The PDN prosthetic disc-nucleus device. *Euro Spine Journal*, pp.11: S137-42.
- ★ Ray, C.D. & Corbin, T.P., 20 September, 1988. *Prosthetic disc and method of implanting*. Patent No: 4,772,287. US.
- ★ Reitz, H. & Joubert, M., 1964. Intractable headache and cervicobrachial giabrachialgiaintervertebral discs with a metal prosthesis. *South African Medical Journal*, 38, pp.881-884.
- ★ Rohlmann, A., Bergmann, G. & Graichen, F., 1997. Loads on an internal spinal fixation device during walking.. *Journal of biomechanics*, 30(1), pp.41-47.
- ★ Rohlmann, A., Bergmann, G., Graichen, F. & Weber, U., 2000. Changes in the loads on an internal spinal fixator iliac crest autograft. *J Bone Joint Surg*, 82-B, pp.445-49.

- ★ Rohlmann, A. et al., 2008. Loads on a telemetrized vertebral body replacement measured in two patients. *Spine*, 33(11), pp.1170-79.
- ★ Rolander, S.D., 1966. Motion of the lumbar spine with special reference to the stabilizing effect of posterior fusion. *Acta Orthop. Scand.*, (Thesis), p.99 [Suppl.].
- ★ Rolander, S.D. & Blair, W.E., 1975. Deformation and fracture of a lumbar vertebral end-plate,. *Clinical Orthopaedics North America*, 6, p.75.
- ★ Roy-Camille, R., Saillant, G. & Lavaste, F., 1978. study of lumbar disc replacement. *Rev Chir Ortho Reparatr Appar Mot (Suppl II)*, 64, pp.106-07.
- ★ Schlapfer, F., Magerl, F. & Jacobs, R., 1980. In Vivo Measurements of Loads on an External Fixation Device for Human Lumbar Spine Fractures. *London: The Institute of Mechanical Engineers*, C131/80, pp.59-64.
- ★ Schneider, P.G. & Oyen, R., 1974a. Intervertebral disc replacement.Experimental studies, clinical consequences. *Journal of Orthopaedics*, 112, pp.791-192.
- ★ Schneider, P. & Oyen, R., 1974b. Plastic surgery on intervertebral disc. Part I: Intervertebral disc replacement in the lumbar region with silicone rubber. Theoretical and Experimental studies. *Journal of Orthopaedics*, 112, pp.1078-86.
- ★ Schultz, A.B. et al., 1982a. Analysis and measurement of lumbar trunk loads in tasks involving bends and twists. *Journal of biomechanics*, 15(9), pp.669-75.
- ★ Schultz, A. et al., 1982b. Loads on the lumbar spine: validation of biomechanical analysis by measurements of intradiscal pressure and myoelectric signals. *Journal of bone and joint surgery*, 64-A(5), pp.713-20.
- ★ Sekhon, L., 2003. Cervical arthroplasty in the management of spondylotic myelopathy. *Journal of Spinal Disord Tech*, pp.16:307-13.
- ★ Shirazi-Adl, Srivastava, S.C. & Ahmed, A.M., 1984. Stress analysis of the lumbar disc-body unit in compression: a three-dimensional non-linear finite element study.. *Spine*, 9(2), p.120.
- ★ Sijbrandij, s., 1962. The value of anterior inter-body vertebral fusion in the treatment of lumbosacral insufficiency with the special reference to spondylolisthesis. *Acta Chir. Neer land.*, 14, p.37.
- ★ Slack Inc.-Orthosupersite, 2008. [Online] Available at: <http://www.orthosupersite.com/view.aspx?rid=28657> [Accessed 30th October 2010].
- ★ spineuniverse.com, 2011. *spineuniverse.com/disc & spine*. [Online] Available at: [http://www.spineuniverse.com/sites/default/files/legacy-images/dp\\_latcutaway-BB.jpg](http://www.spineuniverse.com/sites/default/files/legacy-images/dp_latcutaway-BB.jpg) [Accessed 25th May 2011].



- ★ spineuniverse.com, 2011. *spineuniverse.com/facetjoints2\_250-BB.jpg*. [Online] Available at: [http://www.spineuniverse.com/sites/default/files/legacy-images/facetjoints2\\_250-BB.jpg](http://www.spineuniverse.com/sites/default/files/legacy-images/facetjoints2_250-BB.jpg) [Accessed 25 May 2011].
- ★ Stokes, I.A.F. & Iatridis, J.C., 2004. Mechanical conditions that accelerate intervertebral disk degeneration: Overload Versus Immobilization. *Spine*, 29(23), pp.2724-32.
- ★ Stone, K.R., 28 April, 1992. *Prosthetic intervertebral disc*. Pataent no: 5,108,438. USA.
- ★ Stubstad, J., Urbaniak, J. & Kahn, P., 25 February, 1975. *Prosthesis for spinal repair*. Patent No: 3,867,728. USA.
- ★ Szpalski, M., Gunzburg, R. & Mayer, M., 2002. Spine arthroplasty: a historical review. *Euro Spine Journal*, 11, pp.565-84.
- ★ Tadano, S. et al., 1992. Structure and materials for a synthetic intervertebral disc. In *Proceedings of the 7th International Conference on Biomedical Engineering*. Singapore, 1992.
- ★ Tanz, S.S., 1953. Motion of the lumbar spine. A roentgenologic study. *Journal of Roentgenol.*, 69, p.399.
- ★ Tekscan Inc., 2007. *Flexiforce Product Brochure*. Product Catalogue.
- ★ Truchly, G. & Thompson, W.A.L., 1970. Posterior lateral fusion: 14 years' experience with a salvage procedure for failure of spine fusion. *Journal of bone and joint surgery*, 52A, p.826.
- ★ Urbaniak, J., Bright, D. & Hopkins, J., 1973. Replacement of intervertebral discs in chimpanzees by silicon-dacron implants: a preliminary report. *Journal of Biomedical Mater Res*, p.7:165–86.
- ★ Van Steenbrugghe, M., 28th May, 1956. *Improvements in joint prosthesis*. Patent No: 1,122,634. France.
- ★ Virgin, W., 1951. Experimental Investigations into Physical Properties of the Intervertebral disc. *Journal of bone and joint surgery*, 33 B(4), pp.607-11.
- ★ Vuono-Hawkins, M., Zimmerman, M. & Lee, C., 1994. Mechanical evaluation of a canine intervertebral disc spacer: in situ and in vivo studies. *Journal of Ortho. Res.*, 12, pp.119-27.
- ★ Waris, W., 1948. Lumbar disc herniation. *Acta Chir. Scandiv.[Suppl]*, 140, pp.1-134.
- ★ Waugh, T., 1966. Intravital measurements during instrumental correction of idiopathic scoliosis. *Acta Orthop Scand*, 93(S), pp.58-75.
- ★ Weber, B.G., 21 June, 1980. Patent No: DE 3,023,353. West Germany, West Germany.
- ★ Weber, B., 6 February, 1978. Patent No: DE-OS 2,804,936. West Germany, West Germany.
- ★ White, A.A. & Panjabi, M.M., 1978. *Clinical biomechanics of the spine*. 1st ed. Philadelphia: J.B.Lippincott.

- ★ White, A.A.I. & Punjabi, M.M., 1990. *Clinical Biomechanics of The Spine (2nd Ed.)*. 2nd ed. Lippincott Williams & Wilkins.
- ★ Wikimedia Foundation Inc., 2008. *wiki: corpectomy: wikipedia.org*. [Online] Available at: <http://en.wikipedia.org/wiki/Corpectomy> [Accessed 2nd October 2010].
- ★ Wikimedia Foundation Inc., 2010. *Intervertebral\_disc\_arthroplasty*. [Online] Available at: [http://en.wikipedia.org/wiki/Intervertebral\\_disc\\_arthroplasty](http://en.wikipedia.org/wiki/Intervertebral_disc_arthroplasty) [Accessed 15th November 2010].
- ★ Wikimedia Foundation Inc., 2010. *Spinal\_fusion: wiki: wikipedia*. [Online] Available at: [http://en.wikipedia.org/wiki/Spinal\\_fusion](http://en.wikipedia.org/wiki/Spinal_fusion) [Accessed 14th September 2010].
- ★ Wikimedia Foundation Inc., 2010. *wiki: surface\_acoustic\_wave: wikipedia.org*. [Online] Available at: [http://en.wikipedia.org/wiki/surface\\_acoustic\\_wave](http://en.wikipedia.org/wiki/surface_acoustic_wave) [Accessed 1 November 2010].
- ★ Wikimedia Inc., 2010. *Disectomy: wiki: wikimedia inc*. [Online] Available at: <http://www.en.wikipedia.org/wiki/Disectomy> [Accessed 2nd October 2010].
- ★ Wilke, H.-J., 1992. *Biomed Technik*, 37, pp.78-85.
- ★ Woody, J. et al., 1988. Excessive translation on flexion-extension radiographs in asymptomatic populations. In *Trans. Int. Soc. For study of lumbar Spine*. Miami, 1988. Int. Soc. For study of lumbar Spine.
- ★ Wu, K.K., 1975. Surgical technique for arthrodesis of two to four adjacent spinal vertebrae throughout the entire spinal column. *Henry Ford Hospital Medical Journal*, 23, p.39.
- ★ Yamamoto, I. et al., 1989. Three dimensional movements of the whole lumbar spine and lumbosacral joint.. In *Trans. Int. Soc. For study of Lumbar Spine*. Kyoto, Japan., 1989. Int. Soc. For study of Lumbar Spine.
- ★ Zimmer Inc., 2010. *template: Mp: navid: 5889: zimmerspine*. [Online] Available at: <http://www.zimmerspine.eu/z/ctl/op/global/action/1/id/9035/template/MP/navid/5889> [Accessed 24th October 2010].



## **PUBLICATIONS AND PATENTS**

---

### **Patent:**

P003017GB: An Intelligent Artificial Intervertebral Disk Prosthesis (Filed April 03, 2009)

(Patent Application No: 0905804.1)

Inventors: Mehul Pancholi (GB), Kyriacou Panayiotis (GB).

### **Research Papers:**

- ❖ "In-vitro spinal loading experiments on an animal spine utilizing an intelligent spinal artificial disk prosthesis", published in an international peer reviewed journal "Applied Bionics and Biomechanics" (<http://www.tandf.co.uk/journals/titles/11762322.asp> ).
- ❖ "Investigation of the in-vitro loading of the artificial disk prosthesis", Journal of Physics: Conference Series 178 (2009) 012023, IOP Publishing Ltd.

# GLOSSARY

---

- ★ **Acupuncture:** Acupuncture is an alternative medicine that treats patients by insertion and manipulation of needles in the body. Its proponents variously claim that it relieves pain, treats infertility, treats disease, prevents disease, or promotes general health.
- ★ **Anatomy:** Anatomy is a branch of biology and medicine that is the consideration of the structure of living things. It is a general term that includes human anatomy, animal anatomy (zootomy) and plant anatomy (phytotomy). In some of its facets anatomy is closely related to embryology, comparative anatomy and comparative embryology, through common roots in evolution.
- ★ **Apophyses:** A natural protuberance from a bone, or inside the shell or exoskeleton of a sea urchin or insect, for the attachment of muscles.
- ★ **Ayurvedic:** Ayurveda or ayurvedic medicine is a system of traditional medicine native to India and a form of alternative medicine. In Sanskrit, words āyus, meaning "longevity", and veda, meaning "related to knowledge" or "science". Evolving throughout its history, of medicine in South Asia. The earliest literature on Indian medical practice appeared during the *Vedic period in India*.
- ★ **Bending moment:** A bending moment exists in a structural element when a moment is applied to the element so that the element bends. Moments and torques are measured as a force multiplied by a distance so they have as unit newton-metres (N·m) , or foot-pounds force (ft·lbf). The concept of bending moment is very important in engineering (particularly in civil and mechanical engineering) and physics.
- ★ **Biocompatibility:** The extent to which a foreign, usually implanted, material elicits an immune or other response in a recipient. OR The ability to coexist with living organisms without harming them.
- ★ **Biomechanics:** The application of mechanical laws to living structures, especially to the musculoskeletal system and locomotion; biomechanics addresses mechanical laws governing structure, function, and position of the human body.
- ★ **BNC connector:** The BNC connector (Bayonet Neill-Concelman connector) is a common type of RF connector used for the coaxial cable which connects much radio, television, and other radio-frequency electronic equipment.
- ★ **Cervical region (Spine):** The neck region of the spine is known as the Cervical Spine. This region consists of seven vertebrae, which are abbreviated C1 through C7 (top to bottom). These vertebrae protect the brain stem and the spinal cord, support the skull, and allow for a wide range of head movement.
- ★ **Chiropractic:** Chiropractic is a form of alternative medicine[1] that emphasizes diagnosis, treatment and prevention of mechanical disorders of the musculoskeletal system, especially the spine, under the hypothesis that these disorders affect general health via the nervous system.
- ★ **Compression platen:** Designed to be centred on the loading axis of an electromechanical or hydraulic universal test machine load frame, compression platens provide a hardened surface (Rockwell HRC 58/60) for complex compression tests in which uniform stress distribution is critical.
- ★ **Craniocaudal view:** In a system of nomenclature of radiographic positioning used in animals, means the path that the beam takes from the x-ray tube to the film, passing from the head end of the animal towards its tail.
- ★ **Visco-elasticity:** The time dependent property of a material (e.g. hysteresis, creep, relaxation) to show sensitivity to rate of loading or deformation.



- ★ **Degeneration of the intervertebral disc:** Degeneration of the intervertebral disc, often called "degenerative disc disease" (DDD) of the spine, is a condition that can be painful and can greatly affect the quality of one's life. While disc degeneration is a normal part of aging and for most people is not a problem, for certain individuals a degenerated disc can cause severe constant chronic pain.
- ★ **Degrees of freedom:** In mechanics, degrees of freedom (DOF) are the set of independent displacements and/or rotations that specify completely the displaced or deformed position and orientation of the body or system. This is a fundamental concept relating to systems of moving bodies in mechanical engineering, aeronautical engineering, robotics, structural engineering, etc. A rigid body that moves in three dimensional space has three translational displacement components as DOFs, while a rigid body would have at most six DOFs including three rotations. Translation is the ability to move without rotating, while rotation is angular motion about some axis.
- ★ **Discogenic pain:** Discogenic pain is an orthopaedic pain related to the damaged spinal disc.
- ★ **Dynamics:** In the field of physics, the study of the causes of motion and changes in motion is dynamics. In other words the study of forces and why objects are in motion. Dynamics includes the study of the effect of torques on motion. These are in contrast to Kinematics, the branch of classical mechanics that describes the motion of objects without consideration of the causes leading to the motion.
- ★ **Elastic deformation (range):** Elastic deformation is reversible. Once the forces are no longer applied, the object returns to its original shape. Elastomers and shape memory metals such as Nitinol exhibit large elastic deformation ranges, as does rubber. Soft thermoplastics and conventional metals have moderate elastic deformation ranges, while ceramics, crystals, and hard thermosetting plastics undergo almost no elastic deformation.
- ★ **Elastic instability/stability:** Elastic instability is a form of instability occurring in elastic systems, such as buckling of beams and plates subject to large compressive loads.
- ★ **Electromyography:** Electromyography (EMG) is a diagnostic procedure to assess the health of muscles and the nerve cells that control them (motor neurons). Motor neurons transmit electrical signals that cause muscles to contract. An EMG translates these signals into graphs, sounds or numerical values that a specialist interprets. An EMG uses tiny devices called electrodes to transmit or detect electrical signals. During a needle EMG, a needle electrode inserted directly into a muscle records the electrical activity in that muscle. A nerve conduction study, another part of an EMG, uses surface electrodes — electrodes taped to the skin — to measure the speed and strength of signals traveling between two or more points. EMG results can reveal nerve dysfunction, muscle dysfunction or problems with nerve-to-muscle signal transmission.
- ★ **EMG:** See Electromyography.
- ★ **End-plates (spinal vertebral):** Vertebral end plates are the top and bottom portions of the vertebral bodies that interface with the vertebral discs. The vertebral end plate is composed of a layer of thickened cancellous bone.
- ★ **Epidural:** The term epidural is often short for epidural analgesia, a form of regional analgesia involving injection of drugs through a catheter placed into the epidural space. The injection can cause both a loss of sensation (anaesthesia) and a loss of pain (analgesia), by blocking the transmission of signals through nerves in or near the spinal cord.
- ★ **Ex vivo:** Ex vivo (Latin: "out of the living") means that which takes place outside an organism. In science, ex vivo refers to experimentation or measurements done in or on tissue in an artificial environment outside the organism with the minimum alteration of natural conditions. Ex vivo conditions allow experimentation under more controlled

conditions than possible in *in vivo* experiments (in the intact organism), at the expense of altering the "natural" environment.

- ★ **Fatigue:** In materials science, fatigue is the progressive and localized structural damage that occurs when a material is subjected to cyclic loading. The nominal maximum stress values are less than the ultimate tensile stress limit, and may be below the yield stress limit of the material.
- ★ **Fixture:** A fixture is a work-holding or support device used in the manufacturing industry. What makes a fixture unique is that each one is built to fit a particular part or shape. The main purpose of a fixture is to locate and in some cases hold a work-piece during either a machining operation or some other industrial process.
- ★ **Fusion cage (interbody):** An interbody fusion cage (colloquially known as a "spine cage") is a prosthesis used in spinal fusion procedures to maintain foraminal height and decompression. They are cylindrical or square-shaped devices, and usually threaded. There are several varieties: the Harms cage, Ray cage, Pyramesh cage, InterFix cage, and lordotic LT cage, all of which are made from titanium; the Brantigan cage, made from carbon fibre; and the Cortical Bone Dowel, which is cut from allograft femur. The cages can be packed with autologous bone material in order to promote arthrodesis.
- ★ **Hysteresis:** Hysteresis refers to systems that may exhibit path dependence, or "rate-independent memory". In a deterministic system with no dynamics or hysteresis, it is possible to predict the system's output at an instant in time given only its input at that instant in time. In a system with hysteresis, this is not possible; the output depends in part on the internal state of system and not only on its input. There is no way to predict the system's output without looking at the history of the input (to determine the path that the input followed before it reached its current value) or inspecting the internal state of the system.
- ★ **IIR (Filter):** See Infinite Impulse Response (filter).
- ★ **In vitro:** In vitro (Latin: within glass) refers to studies in experimental biology that are conducted using components of an organism that have been isolated from their usual biological context in order to permit a more detailed or more convenient analysis than can be done with whole organisms.
- ★ **In vivo:** In vivo (Latin for "within the living") is experimentation using a whole, living organism as opposed to a partial or dead organism, or an in vitro ("within the glass", i.e., in a test tube or Petri dish) controlled environment. Animal testing and clinical trials are two forms of in vivo research. In vivo testing is often employed over in vitro because it is better suited for observing the overall effects of an experiment on a living subject.
- ★ **Infinite Impulse Response (filter):** Infinite impulse response (IIR) is a property of signal processing systems. Systems with this property are known as IIR systems or, when dealing with filter systems, as IIR filters. IIR systems have an impulse response function that is non-zero over an infinite length of time. This is in contrast to finite impulse response (FIR) filters, which have fixed-duration impulse responses. The simplest analogue IIR filter is an RC filter made up of a single resistor (R) feeding into a node shared with a single capacitor (C). This filter has an exponential impulse response characterized by an RC time constant. Example IIR filters include the Chebyshev filter, Butterworth filter, and the Bessel filter.
- ★ **Inflammation:** A local response to cellular injury that is marked by capillary dilatation, Leukocytic infiltration, redness, heat and pain that serve as a mechanism initiating the elimination and of noxious agents and of damaged tissues.
- ★ **Instantaneous axis of rotation:** In a body which has motions both of translation and rotation, is a line, which is supposed to be rigidly united with the body, and which for the instant is at rest. The motion of the body is for the instant simply that of rotation about the instantaneous axis.



- ★ **Jig:** In metalworking and woodworking, a jig is a type of tool used to control the location and/or motion of another tool. A jig's primary purpose is to provide repeatability, accuracy, and interchange-ability in the manufacturing of products. A jig is often confused with a fixture; a fixture holds the work in a fixed location. A device that does both functions (holding the work and guiding a tool) is called a jig.
- ★ **Kyphosis:** Kyphosis (Greek - kyphos, a hump), also called hunchback or roundback, is a common condition of a curvature of the upper back. It can be either the result of degenerative diseases (such as arthritis), developmental problems (the most common example being Scheuermann's disease), osteoporosis with compression fractures of the vertebrae, and/or trauma.
- ★ **Lesions:** A lesion is any abnormal tissue found on or in an organism, usually damaged by disease or trauma. Lesion is derived from the Latin word laesio which means injury.
- ★ **Load-cell:** A load cell is a transducer that is used to convert a force into electrical signal. This conversion is indirect and happens in two stages. Through a mechanical arrangement, the force being sensed deforms a strain gauge. The strain gauge measures the deformation (strain) as an electrical signal, because the strain changes the effective electrical resistance of the wire. A load cell usually consists of four strain gauges in a Wheatstone bridge configuration. Load cells of one strain gauge (quarter bridge) or two strain gauges (half bridge) are also available.
- ★ **Lumbar region (spine):** The Lumbar Spine has 5 vertebrae abbreviated L1 through L5 (largest). The size and shape of each lumbar vertebra is designed to carry most of the body's weight. Each structural element of a lumbar vertebra is bigger, wider and broader than similar components in the cervical and thoracic regions.
- ★ **Magnetic Resonance Imaging:** Magnetic resonance imaging (MRI), nuclear magnetic resonance imaging (NMRI), or magnetic resonance tomography (MRT) is a medical imaging technique used in radiology to visualize detailed internal structures. MRI makes use of the property of nuclear magnetic resonance (NMR) to image nuclei of atoms inside the body. An MRI machine uses a powerful magnetic field to align the magnetization of some atoms in the body, and radio frequency fields to systematically alter the alignment of this magnetization. This causes the nuclei to produce a rotating magnetic field detectable by the scanner—and this information is recorded to construct an image of the scanned area of the body. Strong magnetic field gradients cause nuclei at different locations to rotate at different speeds. 3-D spatial information can be obtained by providing gradients in each direction. MRI provides good contrast between the different soft tissues of the body, which make it especially useful in imaging the brain, muscles, the heart, and cancers compared with other medical imaging techniques such as computed tomography (CT) or X-rays. Unlike CT scans or traditional X-rays, MRI uses no ionizing radiation.
- ★ **Morphology:** In biology, morphology is a branch of bioscience dealing with the study of the form and structure of organisms and their specific structural features. This includes aspects of the outward appearance (shape, structure, colour, pattern)[8] as well as the form and structure of the internal parts like bones and organs. This is in contrast to physiology, which deals primarily with function. Morphology is a branch of life science dealing with the study of gross structure of an organism or Taxon and its component parts.
- ★ **MRI :** See Magnetic Resonance Imaging.
- ★ **Mucin:** Any of a group of protein-containing glycoconjugates with high sialic acid or sulfated polysaccharide content that compose the chief constituent of mucus. OR Any of a wide variety of glycoconjugates, including mucoproteins, glycoproteins, glycosaminoglycans, and glycolipids.
- ★ **Neoplasia:** The abnormal proliferation of benign or malignant cells.
- ★ **Orthotics:** Orthotics (Greek: Opθός, ortho, "to straighten" or "align") is a specialty within the medical field concerned with the design, manufacture and application of

orthoses. An orthosis (plural: orthoses) is an orthopedic device that supports or corrects the function of a limb or the torso.

- ★ **Osteoblast/Osteoblastic process:** A cell from which bone develops; a bone-forming cell is known as Osteoblast and forming process is known as Osteoblastic process.
- ★ **Osteochondrosis:** Osteochondrosis is a family of orthopaedic diseases of the joint.
- ★ **Osteophytes (Bone spur):** Osteophytes also known as, Bone spurs, are bony projections that form along joints. Bone spurs form due to the body's increase of a damaged joint's surface area; most commonly from the onset of arthritis. Bone spurs usually limit joint movement and typically cause pain.
- ★ **Osteotomy:** Osteotomy is a surgical operation whereby a bone is cut to shorten, lengthen, or change its alignment.
- ★ **Pathology:** Pathology is the study and diagnosis of disease. The word pathology is from Greek, pathos, "feeling, suffering"; and -logia.
- ★ **Physiology:** Physiology is the science of the function of living systems. It is a subcategory of biology. In physiology, the scientific method is applied to determine how organisms, organ systems, organs, cells and bio-molecules carry out the chemical or physical function that they have in a living system.
- ★ **Physiotherapy:** Physical therapy (or physiotherapy), often abbreviated PT, is the art and science of physical care and rehabilitation.
- ★ **Posterior rami syndrome:** Posterior Rami Syndrome, also referred to as Thoracolumbar Junction Syndrome, Maigne Syndrome and Dorsal Ramus Syndrome is caused by the unexplained activation of the primary division of a posterior ramus of a spinal nerve (Dorsal ramus of spinal nerve). This nerve irritation causes referred pain in a well described tri-branched pattern.
- ★ **Prosthesis:** In medicine, prosthesis, prosthetic, or prosthetic limb is an artificial device extension that replaces a missing body part. It is part of the field of biomechatronics, the science of using mechanical devices with human muscle, skeleton, and nervous systems to assist or enhance motor control lost by trauma, disease, or defect. Prostheses are typically used to replace parts lost by injury (traumatic) or missing from birth (congenital) or to supplement defective body parts. Inside the body, artificial heart valves are in common use with artificial hearts and lungs seeing less common use but under active technology development. Other medical devices and aids that can be considered prosthetics include artificial spinal disc, artificial eyes, palatal obturator, gastric bands, and dentures.
- ★ **Pseudoarthrosis:** A joint formed by fibrous tissue bridging the gap between the two fragments of bone of an old fracture that have not united.
- ★ **Radiculopathy:** Radiculopathy is not a specific condition, but rather a description of a problem in which one or more nerves are affected and do not work properly (a neuropathy). The emphasis is on the nerve root (Radix = "root"). This can result in pain (radicular pain), weakness, numbness, or difficulty controlling specific muscles.
- ★ **Roentgen stereophotogrammetry:** Roentgen stereophotogrammetry is a highly accurate technique for the assessment of three-dimensional migration of prostheses.
- ★ **Sagittal:** Relating to the suture between the parietal bones of the skull OR Relating to, situated in, or being the median plane of the body or any plane parallel to it
- ★ **Scoliosis:** Scoliosis is a medical condition in which a person's spine is curved from side to side. Although it is a complex three-dimensional deformity, on an X-ray, viewed from the rear, the spine of an individual with scoliosis may look more like an "S" or a "C" than a straight line.
- ★ **Signal conditioning:** In electronics, signal conditioning means manipulating an analogue signal in such a way that it meets the requirements of the next stage for further processing. Most common use is in analogue-to-digital converters. In control engineering applications, it is common to have a sensing stage (which consists of a sensor), a signal conditioning stage (where usually amplification of the signal is done)



and a processing stage (normally carried out by an ADC and a micro-controller). Operational amplifiers (op-amps) are commonly employed to carry out the amplification of the signal in the signal conditioning stage.

- ★ **Spondylitis:** Spondylitis is an inflammation of the vertebra.
- ★ **Spondylolisthesis:** Spondylolisthesis is a spinal pathological condition. It is a forward displacement of a lumbar vertebra on the one below it and especially of the fifth lumbar vertebra on the sacrum producing pain by compression of nerve roots
- ★ **Spondylosisdeformans:** Spondylosisdeformans is a chronic disease of the vertebrae, especially in the lumbar area.
- ★ **Standard deviation:** Standard deviation is a widely used measurement of variability or diversity used in statistics and probability theory. It shows how much variation or "dispersion" there is from the average (mean, or expected value). A low standard deviation indicates that the data points tend to be very close to the mean, whereas high standard deviation indicates that the data are spread out over a large range of values.
- ★ **Stiffness:** Stiffness is the resistance of an elastic body to deformation by an applied force along a given degree of freedom (DOF) when a set of loading points and boundary conditions are prescribed on the elastic body. It is an extensive material property.
- ★ **Subchondral:** Subchondral means below the cartilage.
- ★ **Thoracic region (spine):** Beneath the last cervical vertebra are the 12 vertebrae of the Thoracic Spine. These are abbreviated T1 through T12 (top to bottom). T1 is the smallest and T12 is the largest thoracic vertebra.
- ★ **Variance:** In probability theory and statistics, the variance is used as a measure of how far a set of numbers are spread out from each other. It is one of several descriptors of a probability distribution, describing how far the numbers lie from the mean (expected value). In particular, the variance is one of the moments of a distribution. The value of variance is square of value of the standard deviation.